

QUANTITATIVE IMAGING OF COCAINE AND ITS METABOLITES IN
BRAIN TISSUE BY MATRIX-ASSISTED LASER DESORPTION/IONIZATION
LINEAR ION TRAP TANDEM MASS SPECTROMETRY

By

RICHARD FRED REICH, JR.

A DISSERTATION PRESENTED TO THE GRADUATE SCHOOL
OF THE UNIVERSITY OF FLORIDA IN PARTIAL FULFILLMENT
OF THE REQUIREMENTS FOR THE DEGREE OF
DOCTOR OF PHILOSOPHY

UNIVERSITY OF FLORIDA

2010

© 2010 Richard Fred Reich, Jr.

To my best friend and wife, Erica,
who displayed incredible patience, support,
and sacrifice throughout my educational journey.
God gave me the greatest gift in the world
by placing you in my life.

ACKNOWLEDGMENTS

First, I would like to thank my research advisor, Rick Yost, who welcomed me back into his research group again. I have learned to appreciate the free environment that you allow your students to thrive in during graduate school. You have allowed me to think independently and to mature with minimal guidance in your research laboratory. I know that the experiences that I have gained under your mentorship will serve me well in the future.

I thank my USAFA co-worker and retired forensic toxicologist, Joseph Levisky, for providing me tissue samples from the El Paso County Coroner's Office in Colorado Springs, Colorado. I thank my undergraduate research assistants, Kasia Cudzilo and Kyle Cromwell, who helped prepare samples and served as a soundboard for brainstorming research ideas. I would also like to thank the Yost research group, past and present, for all their help and support. I hope to continue to see you at future ASMS conferences. You made the hospitality suites a lot of fun.

I thank my good friend Pat Castle, who encouraged me throughout my PhD program. Even from out-of-state, you were able to keep me physically and spiritually fit. I love you, brother.

I thank the parishioners of St. Augustine Catholic Church, who served as my family away from home. I must also thank my brother Knights from Council 13900. Thank you for providing me the opportunity to serve you as Grand Knight. You have helped me to further develop my leadership skills and provided me experiences that will last a lifetime.

Last, thanks go to my wife and my parents. I am very grateful for their patience with my effort and support when I needed them. Erica, you are the love of my life. Thank you for understanding who I am and allowing me to be myself. I look forward to our adventures together at our next assignment at Patrick AFB.

TABLE OF CONTENTS

	<u>page</u>
ACKNOWLEDGMENTS	4
LIST OF TABLES	8
LIST OF FIGURES	9
ABSTRACT	13
CHAPTER	
1 INTRODUCTION	15
Cocaine	15
Cocaine Metabolism	15
Neurobiological Mechanism of Cocaine	16
Analysis of Drugs of Abuse in Tissue	16
Tissue Imaging Techniques	17
MALDI-MS Imaging (MALDI-MSI)	19
Spatial Resolution	20
Tissue Preparation	21
Excision of Tissue	22
Tissue Sectioning and Mounting	22
Sample Transfer	23
MALDI Matrix	24
Matrix selection	24
Matrix deposition	25
Tissue washing	25
Quantitative MALDI-MS	26
Internal Standards	26
Tandem Mass Spectrometry	27
MALDI-MSI Instrumentation	27
Linear Ion Trap Mass Spectrometry	28
Mass-Selective Instability	29
Ion Storage	30
Automatic Gain Control	31
Helium Buffer Gas	31
Resonance Ejection	32
Mass Analysis	33
Isolation	33
Activation	34
Overview of Dissertation	35
2 WIDE ISOLATION	48

Introduction.....	48
Experimental.....	50
Chemicals.....	50
Tissue Collection.....	51
Tissue Sectioning and Sample Preparation.....	51
Mass Spectrometry.....	52
Results and Discussion.....	53
MS ² and MS ³ Mass Spectra of COC and COC-d ₃	53
Improving Signal Reproducibility with Internal Standards.....	54
Increasing Analyte Selectivity with MS ⁿ	54
Combining Internal Standards with MS ⁿ using a Wide Isolation Window.....	56
Isolation Window Width and Automatic Gain Control.....	58
Quantification of Cocaine in Postmortem Human Brain Tissue.....	60
Conclusions.....	63
3 SWIFT ISOLATION.....	74
Introduction.....	74
Experimental.....	77
Chemicals.....	77
Tissue Collection.....	77
Tissue Sectioning and Sample Preparation.....	78
Mass Spectrometry.....	78
SWIFT Calculation.....	79
Inverse Fourier transform.....	79
Quadratic phase modulation.....	80
Temporal spectral inhomogeneity.....	80
Apodization.....	82
SWIFT Application to LTQ.....	83
Results and Discussion.....	83
Optimization of a Dual-Notch SWIFT.....	83
Frequency optimization.....	83
Burst count optimization.....	84
Amplitude optimization.....	86
Selective Ion Isolation of Standards on MALDI Plate.....	87
Improving MALDI Precision with SWIFT.....	87
Selective Ion Isolation of Standards on Tissue.....	89
Conclusions.....	90
4 QUANTITATIVE ANALYSIS OF DRUGS IN BRAIN TISSUE.....	100
Introduction.....	100
Experimental.....	101
Chemicals.....	101
Tissue Collection.....	101
Tissue Sectioning and Sample Preparation.....	101
Tissue Homogenization.....	102

Preparation of Standard Solutions	102
Preparation of Unknown Sample Solution	103
Solid-Phase Extraction	103
Mass Spectrometry	104
SWIFT Calculation	105
SWIFT Application to LTQ	106
Results and Discussion	106
Hexa-Notch SWIFT Isolation	106
SWIFT Isolation on Tissue	108
Ion Ejection	109
Two-Stage Isolation	112
High Mass Filter (HMF)	113
Combining HMF with Hexa-Notch SWIFT	114
MS/MS with Two-Stage Isolation	116
Comparing Wide Isolation and Two-Stage SWIFT Isolation	118
Two-Stage SWIFT MALDI-MS/MS Quantification	120
SPE-MALDI-MS/MS Quantification	121
Conclusions	124
5 CONCLUSIONS AND FUTURE WORK	160
Conclusions	160
Future Work	164
APPENDIX	
A BETA CALCULATION	165
B C++ SWIFT PROGRAM	168
C LTQ MODIFICATIONS	185
LIST OF REFERENCES	202
BIOGRAPHICAL SKETCH	209

LIST OF TABLES

<u>Table</u>		<u>page</u>
4-1	Hexa-notch SWIFT properties based on m/z 305.8 at $q = 0.830$	127
4-2	Hexa-notch SWIFT properties based on m/z 290.2 at $q = 0.830$	134
4-3	Hexa-notch SWIFT properties based on m/z 290.2 at $q = 0.791$	136
4-4	Quantification of BE, COC, and CE from Unspiked Human Brain Tissue.....	156

LIST OF FIGURES

<u>Figure</u>	<u>page</u>
1-1 Metabolism of cocaine.....	38
1-2 Cocaine's mechanism of action	39
1-3 Dopaminergic pathway.....	40
1-4 Cocaine imaging in tissue.....	41
1-5 Tissue preparation and MALDI-MS imaging protocol.....	42
1-6 Schematic of the LTQ with MALDI source.....	43
1-7 Basic design of the two-dimensional linear ion trap.....	44
1-8 Scheme for application of DC, RF trapping, and AC excitation voltages necessary for operation of the 2D ion trap.....	45
1-9 Mathieu stability diagram for the linear ion trap.....	46
1-10 A simplified scan function for the quadrupole ion trap showing the prescan and the analytical scan which makes up one microscan.....	47
2-1 Cocaine dissociation pathway.....	65
2-2 MALDI-MS signal variability with and without internal standards.....	66
2-3 Comparing mass spectra of COC and COC-d ₃ on MALDI plate and on brain tissue.....	67
2-4 Fragmentation of the benzyldimethyldodecylammonium ion. ¹⁰²	68
2-5 Wide isolation MALDI-MS ²	69
2-6 Images of standards spiked on brain tissue.....	70
2-7 Calibration curves for alternating scans MS ² and wide isolation MS ²	71
2-8 Mass spectrometric image of cocaine in brain tissue.....	72
2-9 Cocaine quantification	73
3-1 Temporal spectral inhomogeneity of SWIFT.....	91
3-2 Effects of apodization on SWIFT.....	92
3-3 Optimization of frequency notches.....	93

3-4	Optimization of burst counts.....	94
3-5	Optimization of SWIFT amplitude.....	95
3-6	SWIFT isolation and wide isolation comparison.....	96
3-7	SWIFT isolation and wide isolation calibration curves.....	97
3-8	Quad-notch SWIFT isolation of standards on MALDI plate.....	98
3-9	Quad-notch SWIFT isolation of standards on brain tissue.....	99
4-1	Solid-phase extraction scheme.....	126
4-2	Frequency domain of hexa-notch SWIFT isolation waveform.....	128
4-3	Relationship between secular frequency (ω) and q -space.....	129
4-4	Variable hexa-notch SWIFT amplitude (m/z 305.8 at $q = 0.830$).....	130
4-5	Mass spectra (m/z 80 to 2000) of hexa-notch SWIFT at different amplitudes.....	131
4-6	Mass spectra (m/z 280 to 330) of hexa-notch SWIFT at different amplitudes.....	132
4-7	Pseudopotential well depth (D_x) of the ion trap.....	133
4-8	Isolation window width (Da) determined by the preset q of isolation.....	135
4-9	Hexa-notch SWIFT applied at variable q of isolation.....	137
4-10	Variable hexa-notch SWIFT amplitude (m/z 290.2 at $q = 0.791$).....	138
4-11	Mass spectra (m/z 280 to 330) of hexa-notch SWIFT at different amplitudes.....	139
4-12	Mass spectra (m/z 80 to 2000) of hexa-notch SWIFT at different amplitudes.....	140
4-13	Frequency domain of high mass filter (HMF).....	141
4-14	Variable amplitude of HMF.....	142
4-15	Mass spectra (m/z 80 to 2000) of HMF at different amplitudes.....	143
4-16	Mass spectra (m/z 280 to 330) of HMF at different amplitudes.....	144
4-17	Frequency domain of two-stage SWIFT isolation.....	145
4-18	The time domain of the two-stage SWIFT isolation.....	146
4-19	Variable amplitude of two-stage SWIFT isolation.....	147

4-20	Mass spectra (m/z 80 to 2000) of two-stage SWIFT isolation at different amplitudes....	148
4-21	Mass spectra (m/z 280 to 330) of two-stage SWIFT isolation at different amplitudes....	149
4-22	MS/MS product spectra from the application of a two-stage isolation.	150
4-23	Comparison of MS/MS with wide isolation and two-stage SWIFT isolation	151
4-24	Mass spectra comparison of wide isolation and two-stage SWIFT isolation..	152
4-25	BE calibration curve for BE spiked on intact brain tissue.	153
4-26	COC calibration curve for COC spiked on intact brain tissue.	154
4-27	CE calibration curve for CE spiked on intact brain tissue.	155
4-28	BE calibration curve for BE standards spiked in blank brain tissue homogenate.	157
4-29	COC calibration curve for COC standards spiked into blank brain tissue homogenate. .	158
4-30	CE calibration curve for CE standards spiked into blank brain tissue homogenate.	159
A-1	LabView block diagram of subVI aqb_conf.	165
A-2	Trap Calculator LabView program used to calculate β through an iterative process.	166
A-3	Iterative calculation of β using the LabView program Trap Calculator.	167
B-1	Program introductory comments.	168
B-2	Definition of constants and declaration of variables.	169
B-3	Variable definitions.	170
B-4	Initialize variables for notches 1 through 4.	171
B-5	Initialize variables for notches 5 and 6.	172
B-6	Test initialized variables	173
B-7	Setup output files.	174
B-8	Build components 1, 2, 3, 4, 5, 7, 9 and 11 of excitation waveform.	175
B-9	Build components 6, 8, 10 and 12 of excitation waveform.	176
B-10	Build components 1 through 5 of isolation waveform.	177
B-11	Build components 6 through 10 of isolation waveform.	178

B-12	Build components 11 through 13 of isolation waveform.....	179
B-13	Create data array for frequency data.....	180
B-14	Inverse Fourier transform, midpoint time reflection, and apodization.....	181
B-15	Normalize waveform and download to function generator.....	182
B-16	Write waveform data to output files.....	183
B-17	Fast Fourier transform function.....	184
C-1	Adding SWIFT waveform to AD734 chip (U64) on LTQ Analog PCB.....	189
C-2	Analog PCB modification to apply SWIFT waveform.....	190
C-3	LTQ programmable trigger.....	191
C-4	Programmable trigger locations.....	192
C-5	Digital PCB modifications to access programmable trigger.....	193
C-6	Trigger at beginning of scan.....	194
C-7	Trigger at injection.....	195
C-8	Trigger at isolation.....	196
C-9	Toggling LTQ isolation waveform on and off.....	197
C-10	Mass spectra of cocaine with isolation waveform toggled.....	198
C-11	Trigger at isolation with isolation toggled.....	199
C-12	Trigger at activation.....	200
C-13	Trigger at scan out.....	201

Abstract of Dissertation Presented to the Graduate School
of the University of Florida in Partial Fulfillment of the
Requirements for the Degree of Doctor of Philosophy

QUANTITATIVE IMAGING OF COCAINE AND ITS METABOLITES IN
BRAIN TISSUE BY MATRIX-ASSISTED LASER DESORPTION/IONIZATION
LINEAR ION TRAP TANDEM MASS SPECTROMETRY

By

Richard Fred Reich, Jr.

August 2010

Chair: Richard Alan Yost

Major: Chemistry

Detection of drugs in tissue typically requires extensive sample preparation in which the tissue is first homogenized, followed by drug extraction, before the extracts are finally analyzed by liquid chromatography/mass spectrometry (LC/MS). Directly analyzing drugs in intact tissue would eliminate any complications introduced by sample preparation. A matrix-assisted laser desorption/ionization tandem mass spectrometry (MALDI-MSⁿ) method has been developed for the quantification of cocaine and its metabolites present in postmortem brain tissue of a chronic human cocaine user. It is shown that tandem mass spectrometry (MSⁿ) increases selectivity, which is critical for differentiating analyte ions from background ions such as matrix clusters and endogenous compounds found in brain tissue. It is also shown that the use of internal standards corrects for signal variability during quantitative MALDI, which can be caused by inhomogeneous crystal formation, inconsistent sample preparation, and laser shot-to-shot variability. The MALDI-MSⁿ method developed allows for a single MS² experiment that uses a wide isolation window to isolate both analyte and internal standard target ions. This method is shown to provide improved precision (~10-20 times reduction in percent relative standard

deviation) for quantitative analysis compared to using two alternating MS² experiments that separately isolate the target analyte and internal standard ions.

A wide isolation window reduces signal variability when the analyte and internal standard signals are ratioed. However, the wide isolation window not only isolates the analyte and internal standard ions, but also other ions that are not of interest. These ions fill up the finite storage capacity of the ion trap and may lead to space-charge effects, which result in reduced resolution and peak shifts that interfere with detection of the target ions. Since the current instrument software only allows for one isolation window during MSⁿ, a multi-notch isolation waveform that selectively isolates the analyte and internal standard ions was created to remove the effects of background interferences and boost the sensitivity for analyte and internal standard ions. A multi-notch stored waveform inverse Fourier transform (SWIFT) pulse was calculated with frequency notches corresponding to the secular frequencies of the [M+H]⁺ ions of cocaine (COC), benzoylecgonine (BE), cocaethylene (CE), and their trideuterated analogs, COC-d₃, BE-d₃, and CE-d₃. Multi-notch SWIFT isolation was found to have lower precision than wide isolation, which may be caused by frequency shifts of the analyte and internal standard ions from space-charge effects caused by high *m/z* background ions from the tissue (e.g., lipids).

Finally, a two-stage SWIFT isolation method was developed that uses a high-mass filter to eject high *m/z* background ions before the multi-notch SWIFT isolation is applied. The two-stage SWIFT isolation showed similar precision to wide isolation for the MALDI-MS² analysis of cocaine and its metabolites in brain tissue. The two-stage SWIFT isolation and wide isolation were used to quantitatively image cocaine and its metabolites in postmortem human brain tissue, and were compared to the quantitative analysis of human brain tissue homogenate using MALDI-MS².

CHAPTER 1 INTRODUCTION

Cocaine

Postmortem toxicology is a special field of forensic toxicology that is used to determine whether alcohol, drugs, or other poisons may have caused or contributed to the death of a person. Cocaine is the most frequent cause of drug-related deaths in the United States, either as the direct cause of death or as a contributing factor.¹ According to the federal Drug Abuse Warning Network survey, 40% of the 11,942 drug-related deaths reported in 2007 involved cocaine.² This explains why cocaine analysis is of particular interest to the field of postmortem toxicology.

Cocaine Metabolism

Understanding the metabolism of cocaine (COC) and the relative proportion of COC to its detectable metabolites can provide valuable forensic inferences about the extent of prior abuse. For example, an individual with a brain concentration of 8 mg/kg of COC and 0.5 mg/kg of benzoylecgonine (BE; a metabolite of COC) must have taken the drug just before death, because BE does not cross the blood/brain barrier as freely as its lipophilic parent compound (COC).¹ Conversely, addicts who have ingested large amounts of COC over several days are usually found to have only modest COC concentrations, but high concentration of BE.¹

The major route of cocaine metabolism (Figure 1-1) is hydrolysis of COC by hepatic and plasma esterases, with loss of a benzoyl group to give ecgonine methyl ester (EME). The secondary route is spontaneous hydrolysis, probably non-enzymatic, which leads to BE by demethylation. The final degradation of COC, which is a sequel to both the principal and secondary routes of metabolism, leads to ecgonine. N-demethylation of COC is a minor route leading to norcocaine. The principal metabolites are therefore BE, EME, and ecgonine itself, which are inactive; and norcocaine which is active, and may be relevant after acute intoxication.¹

In the presence of alcohol, a further active metabolite, cocaethylene (CE) is formed in the liver by a transesterification reaction which adds an extra methyl group to COC.¹

Neurobiological Mechanism of Cocaine

Under normal conditions, dopamine (DA) is released by a neuron into the synapse, where it can bind with DA receptors on neighboring neurons³ (Figure 1-2). Normally DA is then recycled back into the transmitting neuron by a specialized protein called the dopamine transporter (DAT). If COC is present, it attaches to the DAT and blocks the normal recycling process, resulting in a build-up of DA in the synapse which contributes to the pleasurable effects of COC. DA-rich brain regions such as the ventral tegmental area (VTA), nucleus accumbens (NAc), and prefrontal cortex are frequent targets of COC addiction research. Of particular interest is the pathway consisting of dopaminergic neurons originating in the VTA that terminate in the NAc (Figure 1-3). This projection may function as a “reward center”, in that it seems to show activation in response to drugs of abuse like COC in addition to natural rewards like food or sex. Note that research was performed on tissue sections from the NAc, a DA-rich area of the striatum, which may contain an accumulation of COC due to its affinity to bind with the DAT.

Analysis of Drugs of Abuse in Tissue

A large variety of specimens are collected in the field of postmortem toxicology including blood, liver, brain, and urine.⁴ For the analysis of drugs of abuse, brain samples show several advantages over all other specimens in postmortem toxicology.⁵ One advantage is due to the brain being an isolated compartment, which delays putrefaction after death.⁶ Also, the metabolic activity is lower in the brain than in other tissues or in blood, resulting in slower decomposition.⁷ Finally, drugs of abuse establish their effects through the central nervous system. Therefore, it can be assumed that concentrations of drugs of abuse found in the brain better reflect drug concentrations at their site of action at the time of death.⁸

Analysis of drugs of abuse in the brain has applications in forensic and postmortem toxicology. Drug concentrations in the brain may be needed to substantiate fatal overdoses⁹ and support neurotoxicity studies.¹⁰ Direct measurement of drug and metabolite concentrations in discrete brain regions can also be used to study the mechanisms of drug action,¹¹ regional distribution,¹² and preferential accumulation of drugs.¹³

Conventional drug analysis in tissue involves homogenization of the tissue prior to subsequent chromatographic analysis.¹⁴ Such sample pretreatments are known to introduce variation in detection due to inhomogeneity of the analyte within the sample matrix.¹⁵ Also, homogenization of tissue eliminates the opportunity to acquire detailed anatomical and histological information for *in situ* drug distribution. Imaging techniques that include mass spectrometric imaging can help provide this information.

Tissue Imaging Techniques

A number of analytical techniques are capable of imaging drugs *in vivo* and *ex vivo*, including positron emission tomography (PET),¹⁶ single photon emission computed tomography,¹⁷ magnetic resonance imaging,¹⁸ x-ray computed tomography,¹⁹ optical fluorescence imaging,²⁰ optical bioluminescence imaging,²¹ ultrasound,²² whole body autoradiography (WBA),²³ infrared imaging,²⁴ and magnetically labeled nanoparticles.²⁵ However, disadvantages of these imaging methods include low sensitivity, low specificity, limited functional and molecular information, poor spatial resolution, and the need for the drug to be labeled with either a radioactive isotope or a fluorescent tag, which can be time-consuming and costly.²⁶ Figure 1-4 shows cocaine imaging in tissue using PET to image [¹¹C]cocaine and WBA to image [³H]cocaine. A specific disadvantage for those techniques that require a chemical tag is the need to monitor the tag rather than the intact drug, and therefore, the ability to differentiate the drug from a metabolite that may have retained the tag is difficult. In addition, a

chemical tag may alter the pharmacological properties of the compound, which could affect both bioavailability and localization within the tissue.

Mass spectrometric imaging (MSI) has higher molecular specificity compared to other tissue imaging techniques, particularly when used in combination with tandem mass spectrometry (MS/MS).²⁷ The high selectivity of the instrument eliminates the need for labeling, because the ion (or product ion as in tandem mass spectrometry) is monitored directly and leaves the drug molecule of interest functionally unmodified. An unmodified drug compound also removes the potential interference of fluorescent/radioactive labels with the biological function (e.g., when the drug must pass through the blood/brain barrier). This analyte specificity of the instrument also provides the ability to simultaneously image drugs and their metabolites due to the parallel detection of multiple analytes. With MSI, an image can be produced for each of the hundreds of detected analytes within the mass spectral data set. Another advantage is its high sensitivity. Unfortunately, MSI is a destructive imaging technique, although only a few molecular monolayers of sample are affected by the analysis. This characteristic precludes MSI from being used for *in vivo* studies.

MSI collects chemical data normally associated with mass spectrometry, but in a spatially defined manner, and processes that information into chemical image maps. Secondary ion mass spectrometry (SIMS)²⁸ and matrix-assisted laser desorption/ionization (MALDI) mass spectrometry (MS)²⁹ are the two main techniques used with MSI. MALDI-MS has been shown to be very effective for the direct analysis of drugs and their metabolites in tissues.³⁰⁻⁴⁴ MALDI-MS is currently the most common MSI technique used for mapping pharmaceuticals in tissue, although new MSI techniques may emerge as new surface ionization methods are developed. Ambient ionization methods such as desorption electrospray ionization (DESI)⁴⁵ and laser

ablation electrospray ionization (LAESI)⁴⁶ show potential for the *in vivo* analysis on the surface of skin of organisms with high specificity. DESI has been used for the *in vivo* detection of the antihistamine Loratadine from the finger of a person who had taken 10 mg of the drug, 40 min prior to analysis.⁴⁵ DESI has also been used to localize clozapine directly from histological sections of brain, lung, kidney, and testis without prior chemical treatment.⁴⁷

MALDI-MS Imaging (MALDI-MSI)

The most commonly used ionization source for mass spectrometric imaging is MALDI. Unlike SIMS and DESI, MALDI requires the addition of a matrix to the sample. An advantage of the matrix is that the solvent used to apply the matrix is used to extract the analyte out of the tissue, not just analyte at the surface. However, the matrix solvent allows the potential for analyte migration. MALDI is a soft ionization technique in which laser energy is applied for an instant to a co-crystallized mixture of a compound (called a matrix) and the analyte molecules. A typical matrix is a small organic compound that absorbs at the wavelength of the laser and consequently promotes desorption of the analyte. The ionization mechanisms of MALDI are not fully understood, but have been critically reviewed.⁴⁸ In brief, the chromophore of the matrix couples with the laser energy and causes a rapid vibrational excitation that desorbs matrix and analyte molecules from the solid solution. The photo-excited matrix molecules are then stabilized through proton transfer to the analyte (e.g., $[M+H]^+$). Figure 1-5 illustrates the overall protocol of a MALDI-MSI experiment. The first step in sample preparation for MALDI-MSI involves application of a homogeneous layer of matrix to the sample (Figure 1-5D). The sample is then analyzed by moving it step-wise beneath a pulsed laser beam (Figure 1-5E) and MALDI mass spectra are acquired from each point (Figure 1-5F). Two-dimensional images may then be obtained by plotting the relative or absolute ion abundance (considered to be proportional to analyte concentration) versus spatial dimensions of X and Y (Figure 1-5G).

Laser wavelength is an important parameter in MALDI. The most commonly used wavelength is 337 nm from the nitrogen laser, but harmonics of the Nd:YAG laser 1065 nm fundamental (3x, 355 nm and 4x, 266 nm), various excimer laser lines that include XeCl (308 nm), KrF (248 nm), and ArF (193 nm), and infrared lasers such as carbon dioxide (10.6 μm) and Er:YAG (2.94 μm) lasers have been employed.⁴⁸ It has been shown that MALDI mass spectra obtained from UV and IR laser wavelengths are similar.⁴⁹ However, IR MALDI requires higher laser pulse energy due to lower MALDI matrix absorption, and the sample consumption is also higher.⁵⁰ Characteristics of IR-MALDI that have been reported include a greater tendency to form multiply charged high-mass ions, less metastable fragmentation, and adduct ion formation.⁵¹

Spatial Resolution

Spatial resolution for MALDI-MSI experiments is limited by laser spot size, laser step size, matrix crystal size, and analyte migration. Spatial resolution increases with decreasing laser spot size, but MALDI mass spectrometers are usually equipped with N₂ (337 nm) or tripled Nd:YAG (355 nm) lasers having relatively large spot sizes (about 100 μm diameter). The rate of energy redistribution rapidly increases with smaller laser spot sizes and higher laser fluences are required for MALDI to occur.⁵² These higher laser fluences can cause extensive fragmentation. Laser spot sizes focused to 7-8 μm in diameter lead to a decrease in ion yields of two orders of magnitude compared to a normal (100 μm) laser spot,⁵³ since the cross sectional area analyzed is approximately 100 times smaller. In addition, high spatial resolution experiments are more sensitive to analyte migration during the matrix application step and dramatically increase analysis time for whole tissue section analysis.

An alternate approach to increase spatial resolution is by oversampling (using a step size that is smaller than the laser spot width). This method involves first, the complete ablation of the MALDI matrix coating the sample at each sample position and second, moving the sample target a distance less than the diameter of the laser beam before repeating the process. The reported method enabled commercial MALDI instruments with large laser spots sizes (100 μm) to image with approximately 25 μm imaging spatial resolution.⁵⁴

Another factor that determines spatial resolution for MALDI-MSI is the size of the matrix crystals formed during the matrix deposition process. The size of the sample-matrix co-crystals grown is strongly dependent on the sample-matrix solution composition and the rate at which the crystals are grown.⁵⁵ For the majority of MALDI-MSI experiments, the spot size of the laser is such that multiple crystals are sampled in each laser shot, thus the spatial resolution is limited by the laser spot size and not the crystals formed. However, it is still important to avoid non-uniformities in the matrix layer (crystals), which can cause ionization yields to vary across the sample and hinder the interpretation of spatial information. Some approaches for MALDI matrix application, such as inkjet printing,^{56,57} can produce a uniform coating of small crystals. Different approaches for the application of MALDI matrix will be discussed further in the matrix deposition section.

Tissue Preparation

MALDI-MSI of intact tissue involves preparation procedures with minimal sample handling, which decreases analyte losses compared to analyses that involve the preparation of tissue homogenates followed by extraction. Nonetheless, tissue preparation for MALDI-MSI is critical to maintain the integrity of the spatial arrangement of drug and metabolite compounds within tissue. Mishandling or improperly storing tissue samples in the early sample preparation

steps may cause delocalization or degradation of the analytes. Experimental procedures that should be considered include excision of tissue, tissue sectioning, sample transfer to MALDI target plate or glass microscope slide, matrix application, and tissue storage after sectioning.

Excision of Tissue

Tissue samples should be surgically removed so that the original shape of the tissue is retained. Immediately after removal, the tissue may be loosely wrapped in aluminum foil and frozen in liquid nitrogen by gently lowering the tissue into the liquid nitrogen over a period of 30 – 60 seconds.⁵⁸ Immersing the tissue into the liquid nitrogen too quickly can lead to cracking and brittle edges. The foil acts to provide support for more malleable tissue and prevents adhesion of the tissue to the sides of the liquid nitrogen dewar. Freshly excised tissue that is placed into small plastic tubes may mold to the shape of the tube when frozen. Whole tissues may remain frozen in a freezer at -80°C for at least a year with little to no degradation of the sample.⁵⁸

Tissue Sectioning and Mounting

Frozen tissue samples are cut into thin sections in a cryostat, which allows for accurate sectioning to be accomplished at sub-freezing temperatures with minimal sample contamination. It is recommended that tissue samples be attached to the sample stage (Figure 1-5A) of the cryostat by freeze mounting with a few drops of deionized water at the interface between the tissue and the stage.⁵⁹ It is not advised to use an embedding medium such as agar or OCT (optimal cutting temperature polymer) to mount the tissue to the sample stage, because these compounds could suppress ion formation in MALDI-MS analysis.⁵⁸ Tissue samples, once mounted to the cryostat sample stage, are sliced with a stainless steel microtome blade. The sample stage temperature is typically maintained between -5 °C and -25 °C, depending on the tissue type. Tissues that have a higher fat content require lower temperatures to avoid tearing during sectioning. Although tissue thickness is not critical for most studies, 10 – 20 µm thick

tissue sections are optimal for handling. Analyte signal intensity has previously been shown to increase with increasing tissue section thickness; it was hypothesized that, during matrix application, matrix solvent may obtain access to the interior of the tissue to extract more analyte.³⁵

Sample Transfer

The tissue section can be transferred with a thin artist's brush and carefully positioned onto a cold MALDI target plate or glass microscope slide. Care should be taken during the transfer to avoid folding or tearing the thinly sliced tissue. Tears or rips distort the tissue section and create holes or gaps, which were not present in the native tissue. All equipment that will come into contact with the frozen tissue including the plate or glass slides should be kept in the cold box of the cryostat during sectioning. Once the tissue slice is positioned on the cold target plate or glass slide, they are removed from the cold box and quickly warmed, thus thaw-mounting the tissue onto the sample plate or slide (Figure 1-5B). Thaw-mounted tissue samples should be stored in a freezer at -80 °C until analyzed.

When tissue samples are ready to be analyzed, they are dehydrated in a vacuum desiccator at room temperature to remove moisture and avoid lateral migration of analytes before application of MALDI matrix. Traditional low pressure ($\sim 10^{-6}$ Torr) MALDI requires samples to be dried completely (~ 2 hours) before exposure to vacuum conditions. This prohibits the analysis of freshly cut tissue and reduces sample throughput. In addition, low pressure MALDI has been shown to produce in-source fragmentation of lipids in tissue, which makes low-level detection difficult (unpublished results). MALDI operated at an intermediate pressure (IP) of 0.17 Torr (100,000-times higher than traditional vacuum MALDI) has been shown to reduce the degree of source fragmentation by collisional cooling.⁶⁰ Tissue drying times with IP-MALDI

can be reduced to 30 minutes, which will increase sample throughput and allow for the analysis of tissue samples shortly after dissection.

MALDI Matrix

Matrix Selection

The success of MALDI-MSI for the analysis of drugs in tissue is dependent on the choice of matrix. The common UV-absorbing molecules used as matrices for MALDI analysis are benzoic acid-based components with low molecular weights (< 500 Da) such as sinapinic acid (SA, 3,5-dimethoxy-4-hydroxycinnamic acid), α -cyano-4-hydroxycinnamic acid (CHCA), and 2,5-dihydroxybenzoic acid (DHB). Various MALDI matrices, including organic, solid ionic, liquid, and liquid/solid two-phase matrices, have been reviewed.⁴⁸ Unfortunately, ions formed from most matrix compounds dominate the low-mass range background for a typical MALDI-MS spectrum, making MS/MS or high resolution MS critical for the analysis of small molecules.

One approach to circumvent matrix interference is to use a higher molecular weight matrix, which does not interfere in the low mass region. To this end, some porphyrins have been employed as MALDI matrices.⁶¹ Although the porphyrin matrices have been shown to be valuable for the detection of low-mass analytes with minimum mass interference from matrix signals,^{61,62} poor ion production yield for drug molecules in tissues was observed when these porphyrin matrices were employed.⁶³

Because of the nature of biological tissues, the growth of matrix crystals is more complicated on tissue than on an inert plate where a small volume of matrix is mixed with a neat drug solution. For example, on tissue, the matrix solvent not only plays a role in the co-crystallization of the matrix and analyte molecules, but the solvent composition also facilitates the extraction of analyte molecules to the surface of the tissue. Therefore, selecting a solvent composition that can readily dissolve the analyte is critical for crystal formation as well as

analyte extraction. Solvent composition can also play an active role in protonation of the analyte and result in higher ionization efficiency. Strong acids such as 0.1% trifluoroacetic acid (TFA) are normally added to the matrix solution to assist protonation of proteins, but have been found to have a marginal effect on the ionization efficiency for small molecules.³⁹ For small molecules, a higher matrix concentration (matrix-to-analyte ratio) can also produce better quality mass spectra.³⁹

Matrix Deposition

The analyte signal intensity, suppression of the matrix signal, and laser shot-to-shot reproducibility can be affected by the distribution of matrix and analyte during crystallization.⁶⁴ Crystal irregularities can occur when the matrix/analyte mixture partitions during the slow crystallization process;⁶⁵ thus, it is very important that the solubilities of all components are suitably matched. Many sample preparation procedures for improved co-crystallization of matrix and analyte have been reported and include electrospraying,⁶⁵ fast evaporation,⁶⁶ pneumatic spraying,⁶⁷ spray-droplet method,⁶⁸ sublimation,⁶⁹ inkjet printing,⁵⁷ acoustic drop ejection,⁷⁰ and solvent-free matrix dry-coating.⁷¹ By far the most common matrix deposition approach for MALDI-MSI of drugs in tissue is pneumatic spraying^{31, 32, 35-38, 41, 43, 44, 72, 73} with either CHCA, SA, or DHB matrix. Pneumatic spraying is an inexpensive and easy technique of applying MALDI matrix that is effective at depositing a homogeneous layer of small matrix crystals across the entire tissue sample. For the research conducted, MALDI matrix solution was applied to tissue by an artistic airbrush (Aztek A470, Testors; Rockford, IL, USA), Figure 1-5C. The application of MALDI matrix by airbrush has been previously published.⁶⁷

Tissue Washing

To optimize matrix crystallization, a washing step is sometimes performed before matrix deposition, which allows the majority of salts to be removed from the surface of the tissue.⁵⁸

Recent studies have shown that matrix crystallization and analyte incorporation are hampered by the presence of high concentrations of salt, which can result in an inhomogeneous sample surface and lead to high signal variability.⁷⁴ The removal of salt from tissue sections is typically performed by rinsing in 70-80% ethanol.⁵⁸ Improved peptide and protein signals were demonstrated with tissue-washing in organic solvents traditionally used for lipid extraction (i.e., methylene chloride, hexane, toluene, acetone, and xylene), especially from older or even archived tissue sections.⁷⁵ However, great care must be taken to prevent migration of analyte molecules or even the loss of analyte; thus, tissue washing is not recommended for small molecule applications such as cocaine analysis.

Quantitative MALDI-MS

Internal Standards

Although MALDI-MS is an established method for qualitative analysis, quantitative analysis is more difficult because MALDI exhibits irreproducible analyte signals as a result of inhomogeneous crystal formation, inconsistent sample preparation, and laser shot-to-shot variability.⁷⁶ Indeed, relative standard deviations can be higher than 50%.^{62, 77} The addition of an internal standard can compensate for several of these experimental factors that seriously complicate quantitative MALDI-MS.⁷⁷⁻⁸¹

An appropriate internal standard for MALDI must compensate not only for any crystallization irregularities but also for subsequent desorption and gas-phase effects. In choosing an internal standard, the relative polarities of the analytes and internal standard as well as their solvent solubilities should be considered.⁷⁷ Structural similarities should reflect the gas-phase behavior of the involved molecules, and extend to solubility. Naturally, an isotope-labeled standard is the ideal choice, since its chemical behavior is nearly identical to its unlabeled counterpart.⁸² Such a standard guarantees identical crystallization and gas-phase behavior of the

analyte and internal standard.⁸³ Traditional MALDI experiments demonstrate that using the ratio of the analyte peak intensities to those of a deuterated internal standard can improve signal reproducibility.⁸²

Tandem Mass Spectrometry

Another challenge for quantitative MALDI-MS, particularly for the analysis of small molecules such as drugs of abuse, is the strong interferences for $m/z < 500$ due to MALDI matrix ions.⁸⁴ In addition, interferences can originate from a multitude of ions produced from endogenous compounds (e.g., lipids) found in tissue sections during tissue analysis. The high molecular specificity of tandem mass spectrometry (MSⁿ) eliminates the problem of interfering ions by fragmenting the desorbed ions in the mass spectrometer and matching the fragment masses with the molecular structure of the analyte. The analytical advantage of the linear ion trap mass spectrometer is the ability to perform multiple stages of MS, which provides an increase in molecular specificity with each stage of mass analysis. For this reason, all the research conducted was performed on the linear ion trap mass spectrometer and thus the background is a focus on this instrumentation.

MALDI-MSI Instrumentation

All MSI experiments reported in this dissertation were performed on a Thermo Scientific LTQ XL linear ion trap (LIT) mass spectrometer (Thermo Scientific; San Jose, CA, USA) with an intermediate pressure MALDI source, as shown in Figure 1-6 and described in detail in elsewhere.^{67, 85} The MALDI source uses a nitrogen gas laser that fires pulses at 337.7 nm with a frequency of 60 Hz and energy of 250 μ J per pulse at 100% laser power. An iris attenuator is used to vary the laser power. The laser energy is directed to the MALDI source by a fiber optic cable. It is then focused using a series of mirrors and lenses to a spot size of approximately 100 μ m at an incident angle of 32°.⁶⁷ The LTQ XL MALDI source uses nitrogen gas to maintain a

pressure of 75 mTorr (170 mTorr for LTQ MALDI), which is considerably higher than a standard high vacuum MALDI source ($\sim 10^{-6}$ Torr), but substantially below that of an atmospheric pressure MALDI source.

The sample plate consists of a bottom support plate, which attaches to either a 96- or 384-well microtiter plate (12.7 cm x 8.6 cm) for general MALDI applications, or a microscope slide holder (2.5 cm x 7.5 cm, 0.1 cm thick) that is designed to hold four standard microscope slides for tissue imaging applications. Microscope slides are affixed to the slide holder with double-sided tape (Scotch 1.27 cm wide, 3M; Minneapolis, MN, USA). The MALDI control software automatically identifies which plate configuration is being used and calibrates the position of the sample plate. The sample plate mounts onto an XY stage by means of spring tension clamps, and two precision vacuum-rated stepper motors control the two-dimensional movement. These actuators position the XY stage with an accuracy of better than $\pm 3 \mu\text{m}$. The precision in going back to a specific location is $\pm 1 \mu\text{m}$ without taking the plate out and approximately $\pm 7 \mu\text{m}$ after taking the plate out of the vacuum and putting it back in.

A modified set of quadrupole rods, which can accommodate the entrance of the laser beam and access for camera viewing, is added to the front of the LTQ multipole arrangement behind the MALDI sample plate, Figure 1-6. Ions produced from the MALDI process are directed into the LIT mass analyzer through the ion optics consisting of a series of quadrupoles, lenses, and octopole.

Linear Ion Trap Mass Spectrometry

The LIT is a two-dimensional (2D) quadrupole ion trap (QIT), which is related to the three-dimensional (3D) QIT that was first introduced and described as a mass storage device in 1953 by Wolfgang Paul and Helmut Steinwedel.⁸⁶ The LIT operates in a fashion analogous to the QIT. However, unlike the 3D QIT which contains two end cap electrodes and a ring

electrode, the LIT is composed of a segmented hyperbolic quadrupole mass analyzer with three sets of hyperbolic rods⁸⁷ of lengths 12 mm (front), 37 mm (center), and 12 mm (back) shown in Figure 1-7.

Ions are trapped axially by applying separate direct current (DC) voltages (± 100 V) to all three sections while radial trapping is accomplished by applying an oscillating radio-frequency (RF) voltage (± 5 kV rod to ground, 1 MHz) in two phases to the X and Y rod pairs shown in Figure 1-8. A two-phase supplemental alternating current (AC) voltage (± 80 V, 5-500 kHz) is applied across the X rods for isolation, activation, and ejection of ions. Ions are ejected radially from the trap through opposing 30-mm long slits in the center section of X rods by mass-selective instability scanning.⁸⁷

Mass-Selective Instability

Mass-selective instability scanning⁸⁸ is accomplished by setting the DC component of the center section rods to zero while the amplitude of the RF resonance excitation voltage applied to the X rods is increased. As the amplitude of the RF voltage is increased, the magnitude of the oscillations of the trapped ions also increases so that the ions eventually develop unstable trajectories along the X axis, and are subsequently ejected from the trap in order of increasing mass-to-charge (m/z) value. Ions are ejected through the slits in the center X rods and strike a set of detectors consisting of a conversion dynode and an electron multiplier situated at each slit to catch the ejected ions.

Ions trapped inside the LIT follow trajectories described by the second-order Mathieu differential equation.⁸⁹ Solutions to the differential equation are in terms of two reduced parameters, a and q , which can be used to determine whether an ion will have a stable or unstable trajectory in the trap under the defined conditions of the electric field. The values of a

and q depend on the dimensions of the trap and the potentials applied according to Equations 1-1 and 1-2.⁸⁹

$$a_x = -a_y = \frac{8eU}{mr_o^2\Omega^2} \quad (1-1)$$

$$q_x = -q_y = \frac{4eV}{mr_o^2\Omega^2} \quad (1-2)$$

U is the applied DC amplitude (and is zero in the LIT), V is the applied RF potential, e is the charge on an ion (1.602×10^{-19} C), m is the mass of an ion, r_o is the radius of the hyperbolic rod profiles ($r_o = 4$ mm), and Ω is the angular drive frequency.

Ion Storage

From the known solutions to the Mathieu equation one can generate a stability diagram (Figure 1-9) that shows the common region in (a, q) space for which the X and Y components of the ion trajectory are stable simultaneously such that the ion can be confined in the trap.⁹⁰ The parameters β_x and β_y at any given coordinate of a and q relate to the secular frequency ω of the ion in the X and Y directions, respectively (Equation 1-3).

$$\omega_u = 0.5\beta_u\Omega \quad (1-3)$$

As the value of β approaches zero, the ion's secular frequency approaches zero, and the ion is not contained. When the value of β equals one, the ion's secular frequency equals half the frequency of the RF field, and the magnitude of its oscillation increases so that the ion escapes the trap or collides with one of the electrode surfaces. When β has a value between zero and unity, the ion can be trapped by the oscillating fields and will oscillate in a periodic mode at its secular frequency in x and y .

Automatic Gain Control

The LIT has a storage capacity of approximately 10^7 ions,⁸⁷ however, the ion trap can trap or hold only a certain number of ions before repulsive forces (space-charge) cause distortions in the applied trapping field, causing a degradation in resolution, a reduction in peak height, and a shift in mass assignments.⁹¹ At severe space-charge conditions, the mass peaks are further broadened and reduced in peak height to the point where they disappear into the baseline. Beyond the extreme limit of space-charge, the ion density becomes so large that additional ions injected into the quadrupole field may not be trapped at all, or previously trapped ions may be displaced.⁹² In order to control the number of ions that accumulate in the trap, a method was developed by Finnigan MAT⁹³ called automatic gain control (AGC). AGC quantitatively assesses the ion generation rate by use of a prescan (Figure 1-10), and then inversely applies a period of ionization (ion injection time) during each operational cycle of the ion trap to ensure that the number of ions in the trap never reaches an adverse level of space-charge.

The AGC feature assists in maintaining the quality of the MALDI spectra by adjusting the number of laser shots per laser spot to produce a similar number of ions for each scan.⁹⁴ If the number of ions produced per shot is low, more laser shots are fired. If the number of ions produced per shot is high, fewer laser shots are fired. The spectra are normalized so that the displayed signal reflects the actual signal level.

Helium Buffer Gas

During the ion injection time, ions transmitted from the ion optics are directed into the LIT where they accumulate before they are scanned out and detected. The ions enter the trap with a range of kinetic energies. Unless the ions enter the trap at the correct phase angle of the RF drive potential, they will not have the correct combination of velocity and displacement to remain in stable orbits and be trapped.⁹⁵ Even if they meet these conditions, they still enter the

trap with too much kinetic energy to be trapped forever. To remove some of this kinetic energy, a helium buffer gas is introduced into the trap. The flow of gas (1 mL/min) into and out of the trap is matched so that the partial pressure of helium in the mass analyzer cavity is maintained at approximately 1 mTorr. The ions are kinetically cooled to the center of the trap (over a period of a few milliseconds) through collisions with the low-molecular-weight helium atoms. As a result, mass resolution is improved, because the ions are ejected from the LIT in dense ion packets.

Resonance Ejection

One of the inherent features of the ion trap during the mass selective instability scan is that while the ions of lower m/z are being scanned out of the ion trap to the detectors, the higher m/z ions are still in the trap, and the space-charge that they contribute causes a broadening of the peaks formed as the lower m/z ions are being ejected.⁹⁶ This deleterious effect on peak shape can be reduced dramatically through a technique called resonance ejection. This is performed on the LTQ by applying a supplementary AC voltage to the X rods in dipolar fashion at a frequency of just less than half of the RF drive frequency (500 kHz, $\beta_x = 0.843$) and amplitude at a resonant ejection q_x of 0.88. As ions are scanned along the $a_x = 0$ line by ramping the RF voltage on the X rods, ions of increasing m/z consecutively come into resonance with the resonance ejection amplitude at $q_x = 0.88$. As the ions come in resonance with the supplementary RF field, the ions gain kinetic energy and are quickly ejected in a tight pack from the ion trap along the X axis. The RF voltage at which an ion is ejected from the mass analyzer is defined as its resonance ejection RF voltage. Without resonance ejection, or with ejection at a $q > 0.88$, ion motion may grow in the Y direction, resulting in reduced ejection efficiency through the 0.25 mm-thick slot. This use of resonance ejection greatly improves mass resolution, and enables the trapping of a larger number of ions in the ion trap without sacrificing resolution and peak shape, since resonant ejection is more tolerant of space-charge effects.

Mass Analysis

After ions have been successfully stored in the LIT, a number of different mass analyses can be performed. The analyses that were used in this research project include single-stage full scan (MS), and multi-stage full scan (MS^n , n = number of stages from 2 to 10). With MS, the ions formed in the ion source are stored in the mass analyzer, and then are sequentially scanned out of the mass analyzer to produce a full mass spectrum.

Isolation

MS^2 includes two stages of mass analysis. In the first stage, the ions formed in the ion source are stored in the mass analyzer. The RF voltage is then increased to move the stored ions towards higher q values until the ion of the m/z of interest (parent ion) is at a q of 0.83 (Figure 1-10). The parent ion is then selectively isolated and all other ions are ejected from the mass analyzer. This isolation occurs with the use of a sum-of-sines waveform consisting of many discrete sine components (5-500 kHz) spaced every 0.5 kHz. Sine components are removed from the isolation waveform at the secular frequency of the ions to be stored. This isolation waveform is applied to the X rods of the center section of the LIT in dipolar fashion to isolate a narrow m/z window (isolation window).⁹⁶ The isolation waveform applies a resonance ejection RF voltage at all frequencies corresponding to the secular frequency of the unwanted m/z ions. The isolation waveform is applied for a period of 16 ms at an amplitude adjusted to assure all other ions throughout the mass range are resonantly ejected from the trap. Resonance ejection of an ion occurs when an auxiliary RF field is applied that matches its secular frequency in the X-direction. The ion absorbs kinetic energy to the point that its magnitude of oscillation increases along the X axis so that it escapes the trap or collides with one of the center rod surfaces. The isolation waveform leaves a “frequency notch” around the frequencies corresponding to the m/z of the parent ion, thus isolating the parent ion in the trap.

Activation

After isolation, the RF amplitude is decreased to move the parent ion to a q of 0.25-0.35 (Figure 1-10). This allows all the product ions formed during collision induced dissociation (CID) of the parent ion to be trapped. The parent ion is then activated with a resonance excitation RF voltage, which is applied across the X rods in dipolar fashion (Figure 1-8) for 30 ms at a single frequency corresponding to the secular frequency of the ion to be excited, which is placed at a q of 0.25-0.35. The resonance excitation RF voltage has lower amplitude than the resonance ejection RF voltage, and thus is not strong enough to eject an ion from the mass analyzer. However, with sufficient voltage, the ion gains kinetic energy by resonant absorption, which results in more translational motion and increased collisions with the helium buffer gas present in the mass analyzer. After many collisions, the ion gains enough internal energy to cause it to dissociate into product ions. These fragment ions are then confined within the ion trap, because of the quadrupolar field except for those fragments that fall below the low mass cutoff (right edge of the Mathieu stability diagram in Figure 1-9) or those that do not retain a charge. This process is called collision-induced dissociation (CID).

The amount of energy imparted in the CID process significantly influences the type of fragmentation induced; it can be increased by either increasing the resonance excitation amplitude or the time of resonance excitation.⁹⁶ Within compound classes, the amount of energy required to fragment an ion is generally proportional to the m/z of the ion. Ions of higher m/z generally require a greater resonance excitation amplitude or a longer period of time.⁹⁷ The CID process can be used to obtain structurally characteristic fragmentation patterns that can be used to identify selected analytes in complex mixtures. In the second stage of mass analysis, the product ions are stored in the mass analyzer. They are then sequentially scanned out of the mass analyzer to produce a full product ion mass spectrum.

MSⁿ on the LTQ can have two to ten stages of mass analysis. For MS³ and higher, the first two stages are similar to MS² except that the product ions are not scanned out. Instead, product ions of one *m/z* are selected and all other ions are resonantly ejected from the mass analyzer. The selected product ions now become the new parent ions for the next stage of mass analysis. With each stage of analysis, the selected parent ions undergo CID to produce product ions. In the nth stage of mass analysis, the final product ions are stored in the mass analyzer, and are then sequentially scanned out to produce a full final product ion mass spectrum.

Overview of Dissertation

Quantitative imaging of drugs of abuse and their metabolites in brain tissue using MALDI-MS could prove to be an invaluable tool in the field of postmortem forensic toxicology. The purpose of this research was to design a quantitative mass spectrometric imaging method for determining the regional composition of drugs and their metabolites in postmortem brain tissue. A MALDI-MS imaging method that combined the use of internal standards for minimizing signal variability with the high molecular specificity of MSⁿ could provide a visual snapshot for the forensic toxicologist that reflects the distribution and concentration of drugs of abuse near the time of death. This information could be used to substantiate fatal overdoses as well as provide supportive data for neurotoxicity studies.

Current LTQ software allows for only one isolation window in MSⁿ experiments, isolating one parent mass (or range of masses) for collision-induced dissociation. This means that MSⁿ of the target ions of the analyte and internal standard would typically be performed with two separate MSⁿ experiments. This would increase the response variability and could counteract the signal normalizing effects of using an internal standard. Chapter 2 describes a MALDI-MSⁿ method developed that allows for a single MS³ experiment that uses a wide isolation window to isolate both analyte and internal standard target ions. This method is shown to provide improved

precision (~10-20 times reduction in percent relative standard deviation) for quantitative analysis compared to using two alternating MS³ experiments that separately isolate the target analyte and internal standard ions. The wide isolation method was used to quantify cocaine in brain tissue of a human cocaine user.

The wide isolation method is capable of improving precision of MALDI-MSⁿ quantitation by isolating the analyte and internal standard ions within a single MSⁿ experiment, but it also isolates other ions that are not of interest that fill up the ion trap and can interfere with detection of the target ions. Chapter 3 describes another strategy for isolating both the analyte and internal standard ions within a single MSⁿ experiment without storing unwanted background ions. This method employs a multi-notch stored waveform inverse Fourier transform (SWIFT) waveform that is applied to the linear ion trap mass spectrometer for selectively isolating multiple pairs of analyte and internal standard ions during a single MSⁿ scan. The precision of the multi-notch SWIFT isolation method for the MALDI-MS² analysis of cocaine was compared to the alternating MS² scan method and the wide isolation method.

Chapter 4 further develops the SWIFT isolation method by incorporating a high mass filter (HMF) SWIFT excitation waveform to eject high m/z background ions present from endogenous brain tissue compounds. This two-stage SWIFT isolation method (i.e. HMF and multi-notch SWIFT) was compared with the wide isolation method for quantification of cocaine and its metabolites in brain tissue. Quantitative results were then compared with a more conventional method for the quantification of cocaine in brain tissue that involves homogenate preparation, followed by solid-phase extraction, and MALDI-MS² analysis. Chapter 5 offers a conclusion to the areas examined and provides ideas for future studies. Appendix A illustrates how beta is calculated, which is used to determine the desired frequency notches of the SWIFT waveforms.

Appendix B contains the C⁺⁺ program used to calculate the SWIFT waveforms. Appendix C describes the modifications made to the LTQ instrument, which allow for the application of SWIFT.

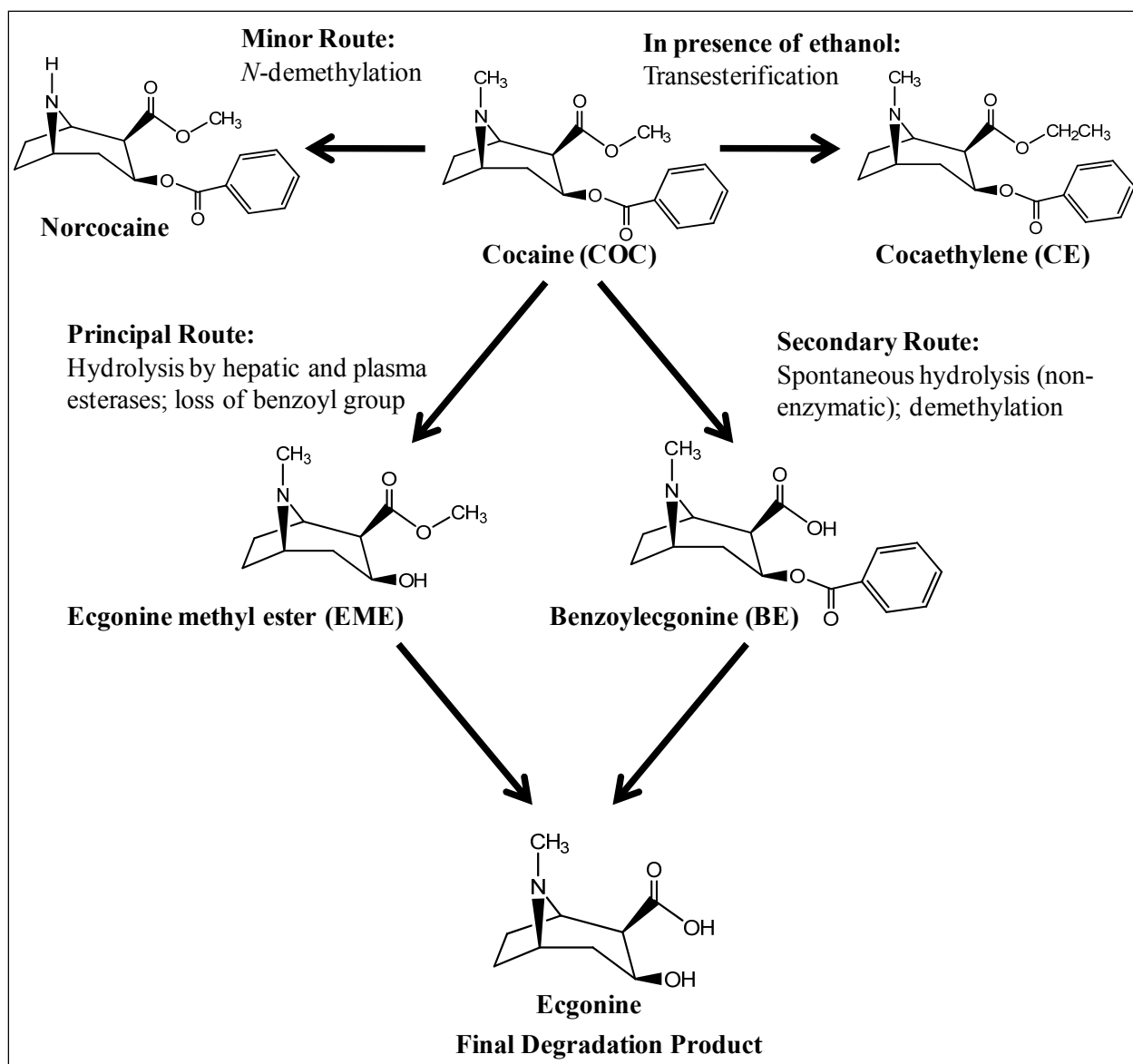


Figure 1-1. Metabolism of cocaine (adapted from Goldfrank's Toxicologic Emergencies, 8th Ed., New York: McGraw-Hill, 2006). The major route of metabolism is hydrolysis of cocaine by hepatic and plasma esterases, with loss of a benzoyl group to give ecgonine methyl ester. The secondary route is spontaneous hydrolysis, probably non-enzymatic, which leads to benzoylecgonine by demethylation. The final degradation of cocaine, which is a sequel to both the principal and secondary routes of metabolism, leads to ecgonine. N-demethylation of cocaine is a minor route leading to norcocaine.

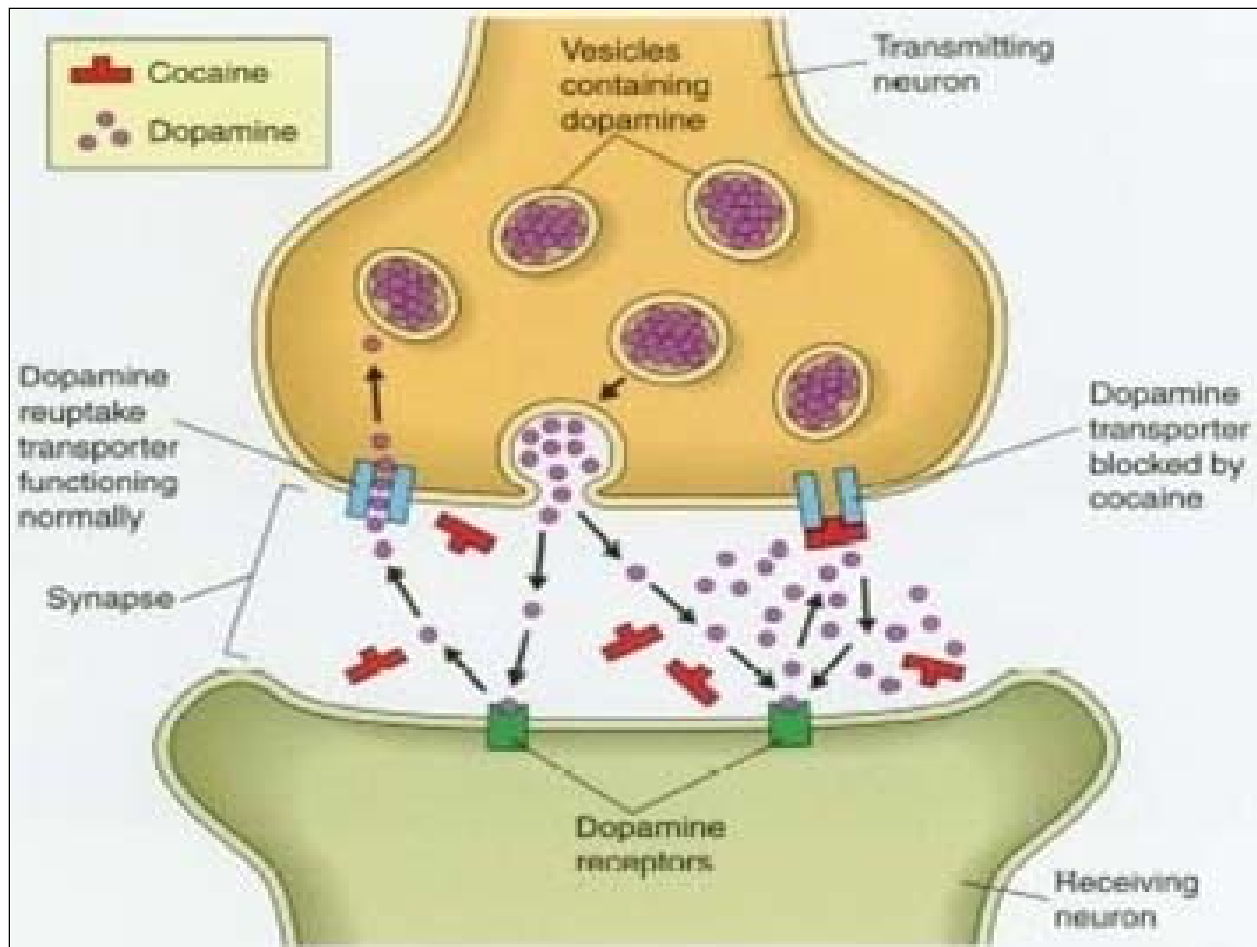


Figure 1-2. Cocaine's mechanism of action (*Human Illnesses and Behavioral Health*, <www.humanillnesses.com>, web accessed on 30 June 2008). Under normal conditions, dopamine is released by a neuron into the synapse, where it can bind with dopamine receptors on neighboring neurons. Normally dopamine is then recycled back into the transmitting neuron by a specialized protein called the dopamine transporter. If cocaine is present, it attaches to the dopamine transporter and blocks the normal recycling process, resulting in a build-up of dopamine in the synapse which contributes to the pleasurable effects of cocaine.

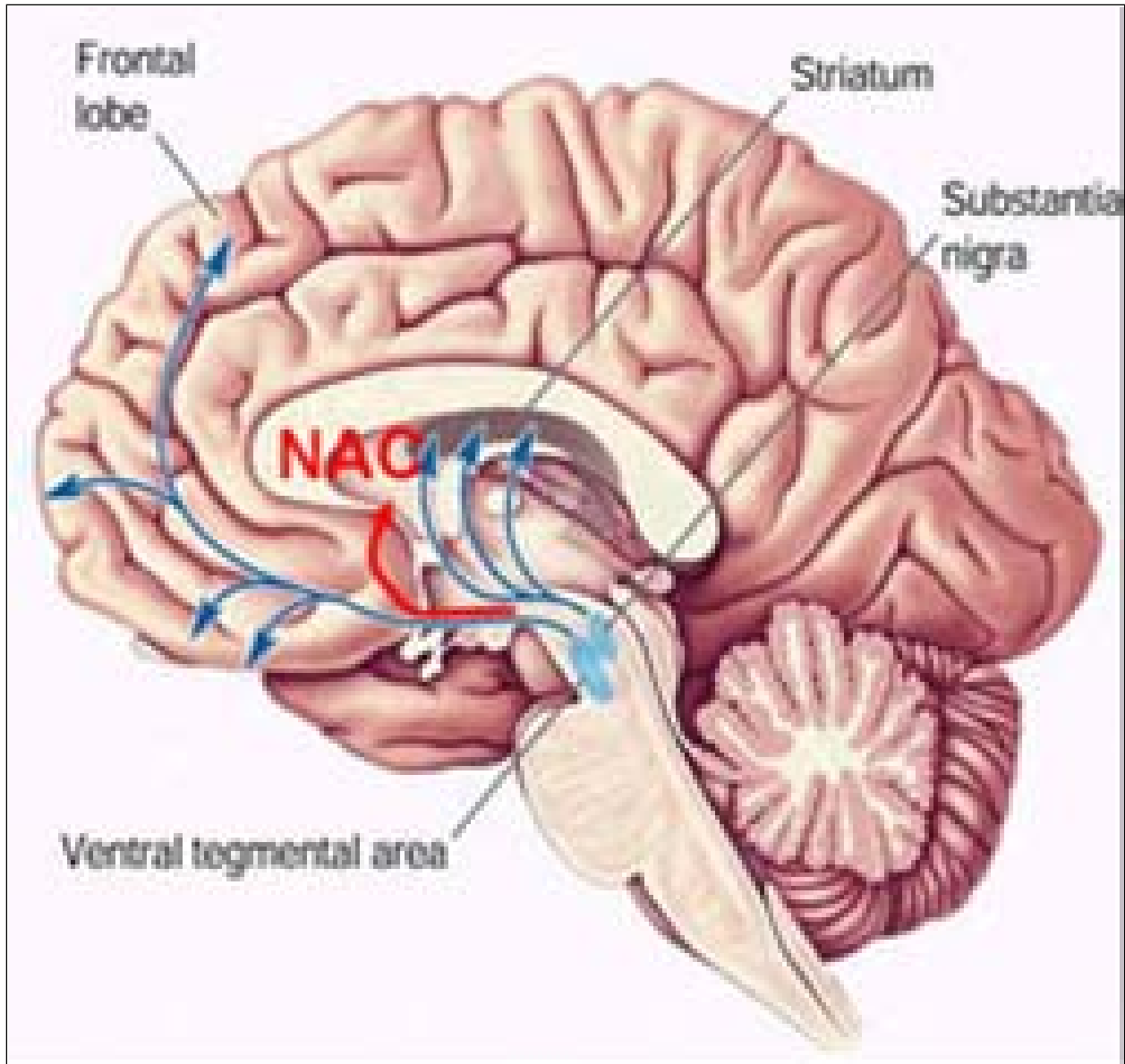
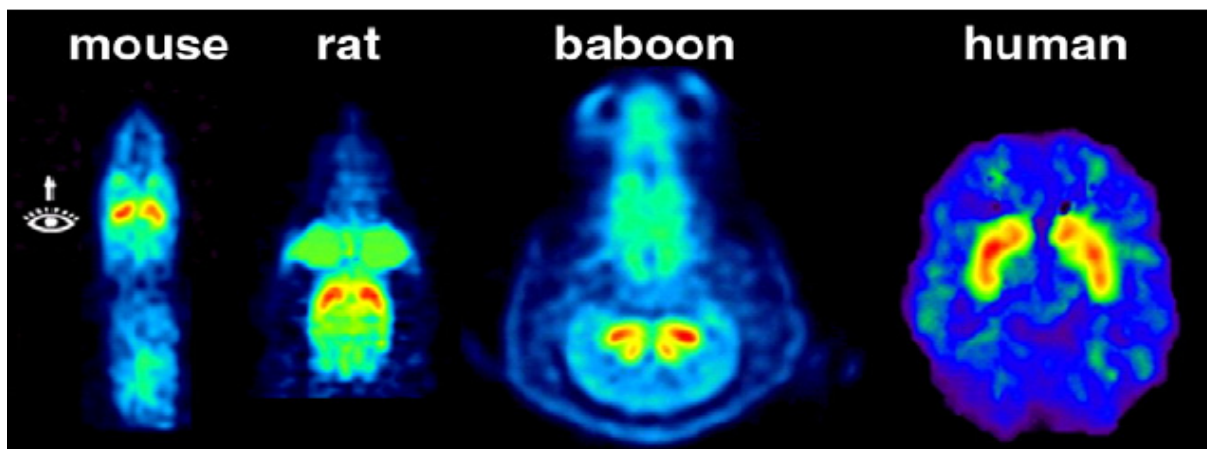


Figure 1-3. Dopaminergic pathway (www.humanillnesses.com, Web. Accessed on June 30, 2008.). Dopaminergic pathways are neural pathways in the brain which transmit the neurotransmitter dopamine from one region of the brain to another (e.g., from the ventral tegmental area to the nucleus accumbens (NAC)).

(a)



(b)

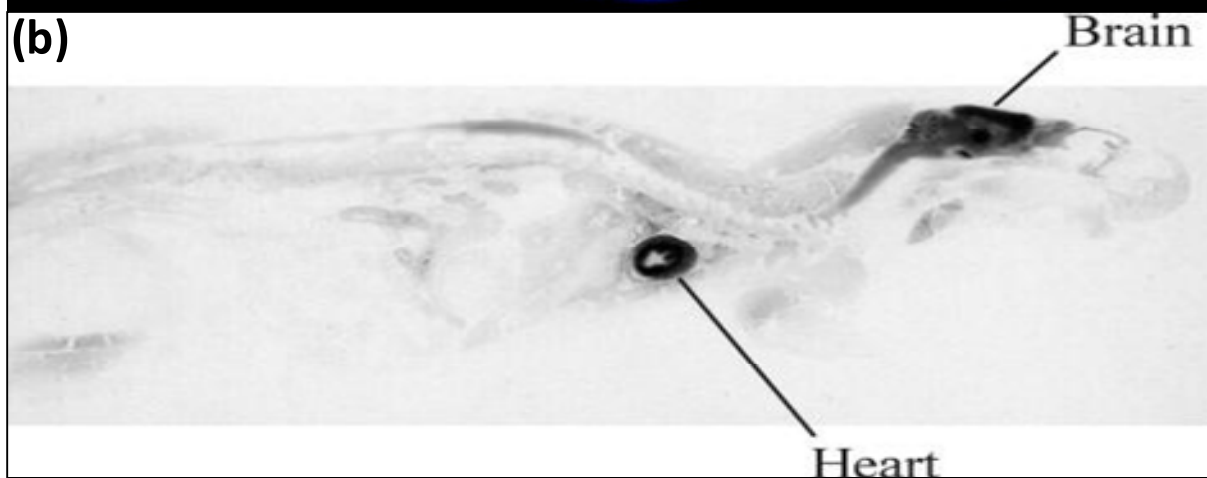


Figure 1-4. Cocaine imaging in tissue (www.invivopharm.com, web accessed on 30 June 2008). (a) Positron emission tomography (PET) image of [¹¹C]cocaine binding across species. (b) Whole body autoradiography (WBA) image of rat injected with [³H]cocaine.

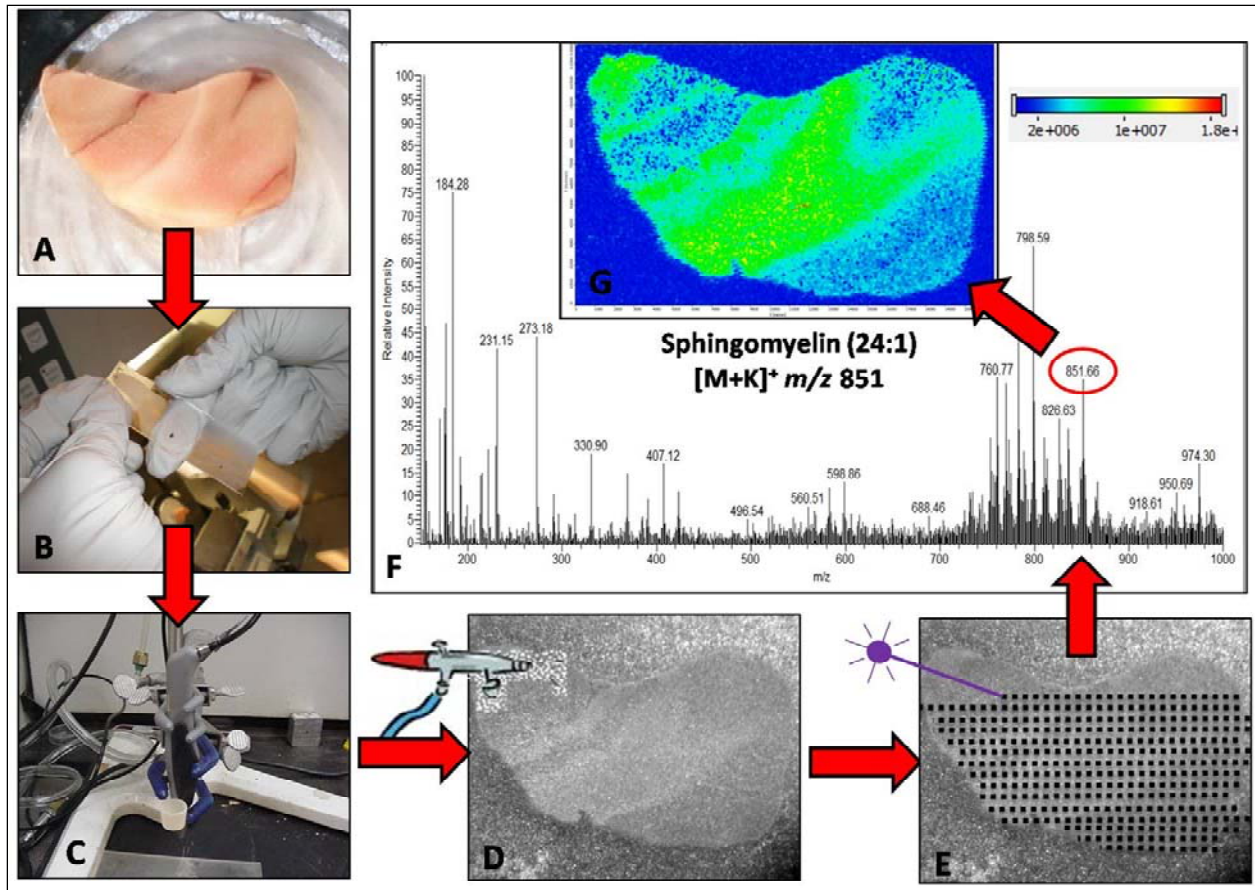


Figure 1-5. Tissue preparation and MALDI-MS imaging protocol. (A) Tissue sample is freeze-mounted onto the cryostat stage with deionized water and then cut into 20- μ m thick slices. (B) Tissue slices are thaw-mounted onto glass microscope slide. (C) Airbrush is used to apply a homogeneous layer of MALDI matrix (D) to the sample. (E) Sample is then analyzed by moving it step-wise beneath a pulsed laser beam. (F) A position-specific mass spectrum is produced from every laser spot. (G) Specific ions are extracted from the mass spectrum using software to generate an image.

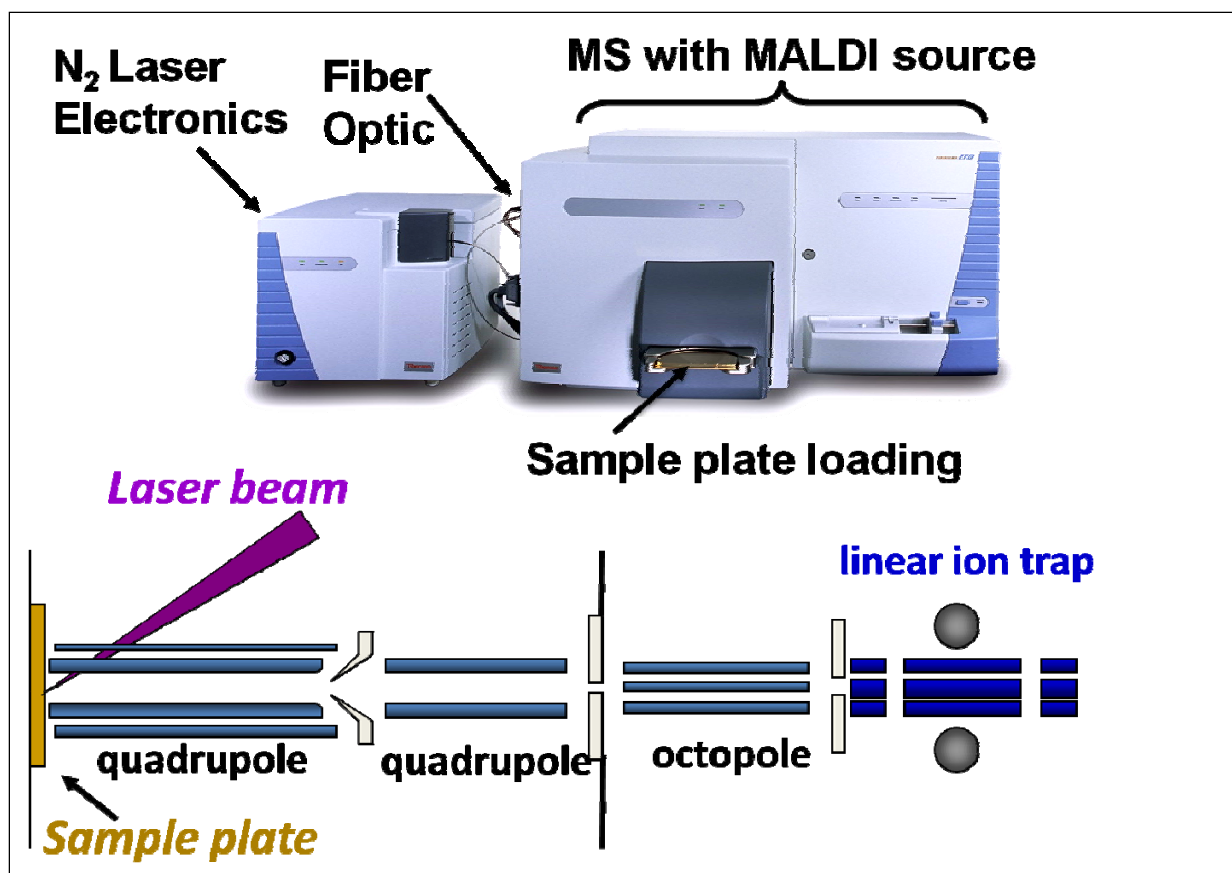


Figure 1-6. Schematic of the LTQ with MALDI source.⁶⁷

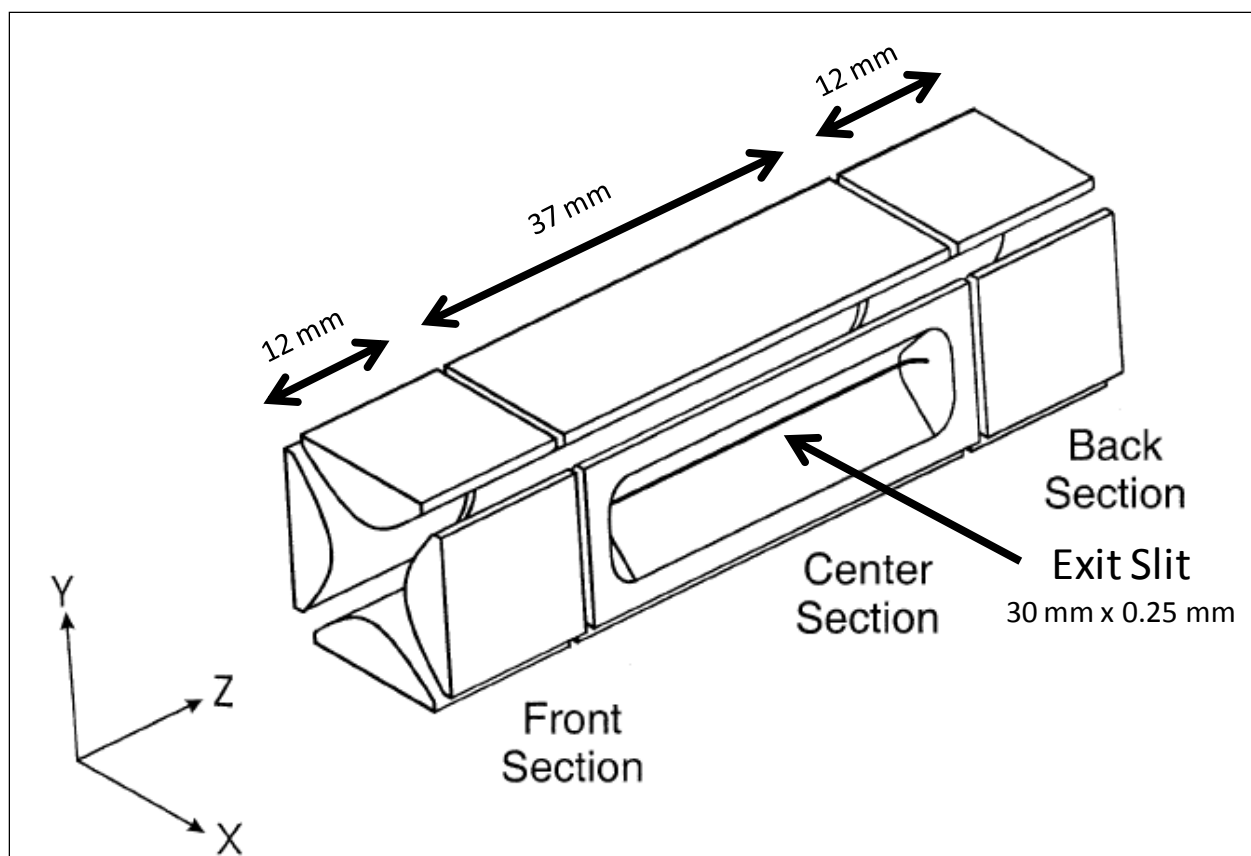


Figure 1-7. Basic design of the two-dimensional linear ion trap.⁸⁷

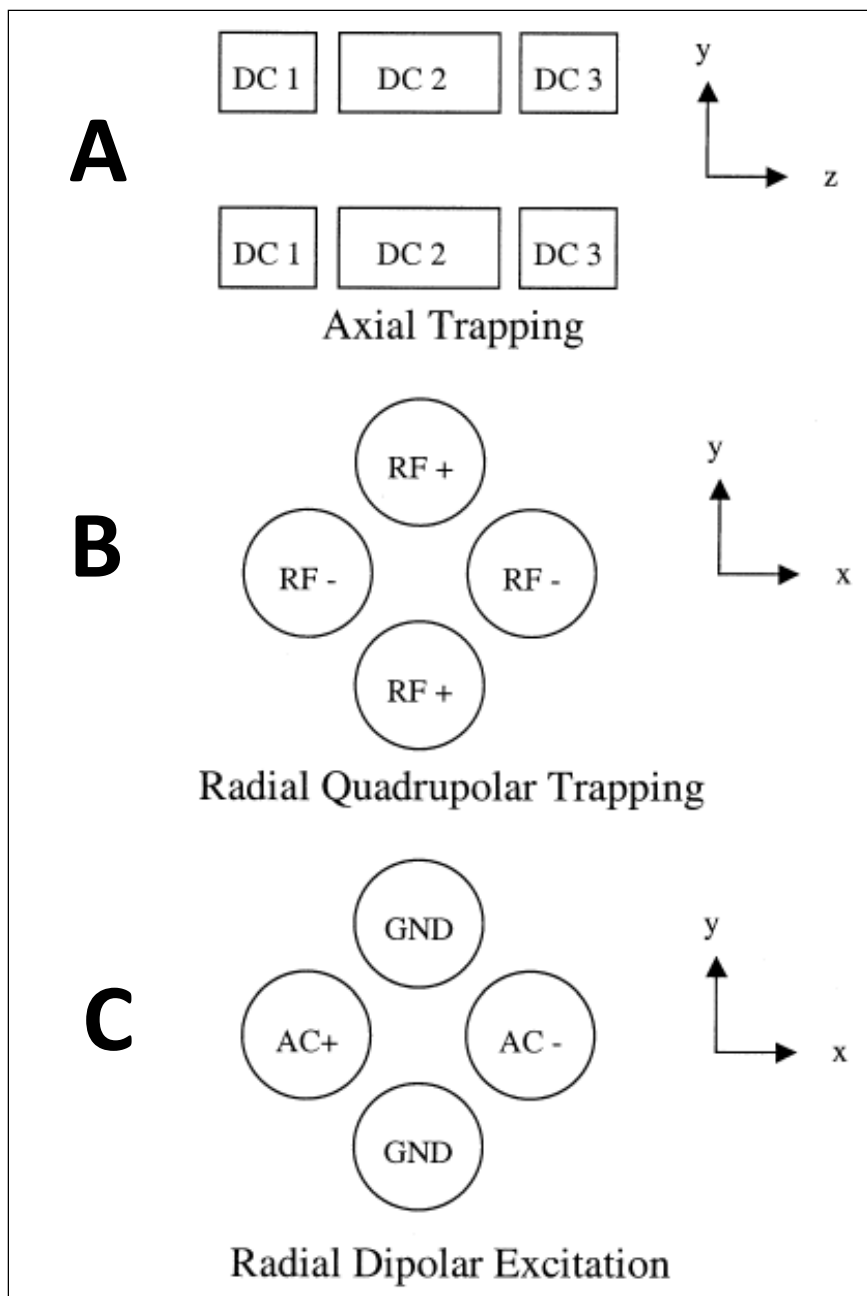


Figure 1-8. Scheme for application of DC, RF trapping, and AC excitation voltages necessary for operation of the 2D ion trap. (A) Separate DC voltages (± 100 V) applied to the separate sections of each rod produce an axial trapping field. (B) Two phases of the primary RF voltage (± 5 kV rod to ground, 1 MHz) are applied to all the electrodes of the ion trap to form the quadrupolar field. (C) Two phases of supplemental AC voltage (± 80 V, 5-500 kHz) are applied to only the X rods for isolation, activation, and ejection of ions.⁸⁷

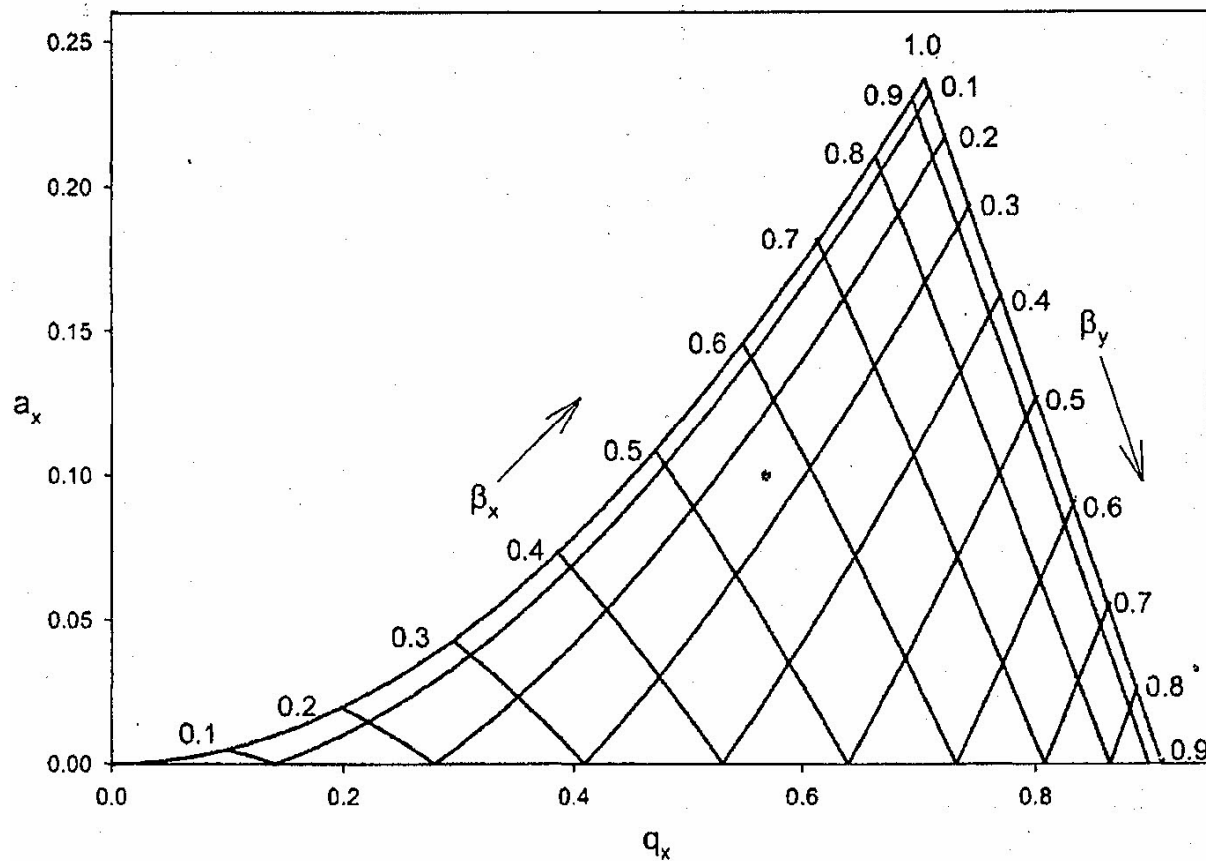


Figure 1-9. Mathieu stability diagram for the linear ion trap. The lines labeled β_x and β_y describe the oscillatory characteristics of ion motion. Solutions to Equations 1-1 and 1-2 give coordinates in a_x and q_x space that can be mapped onto the above diagram.⁹⁰

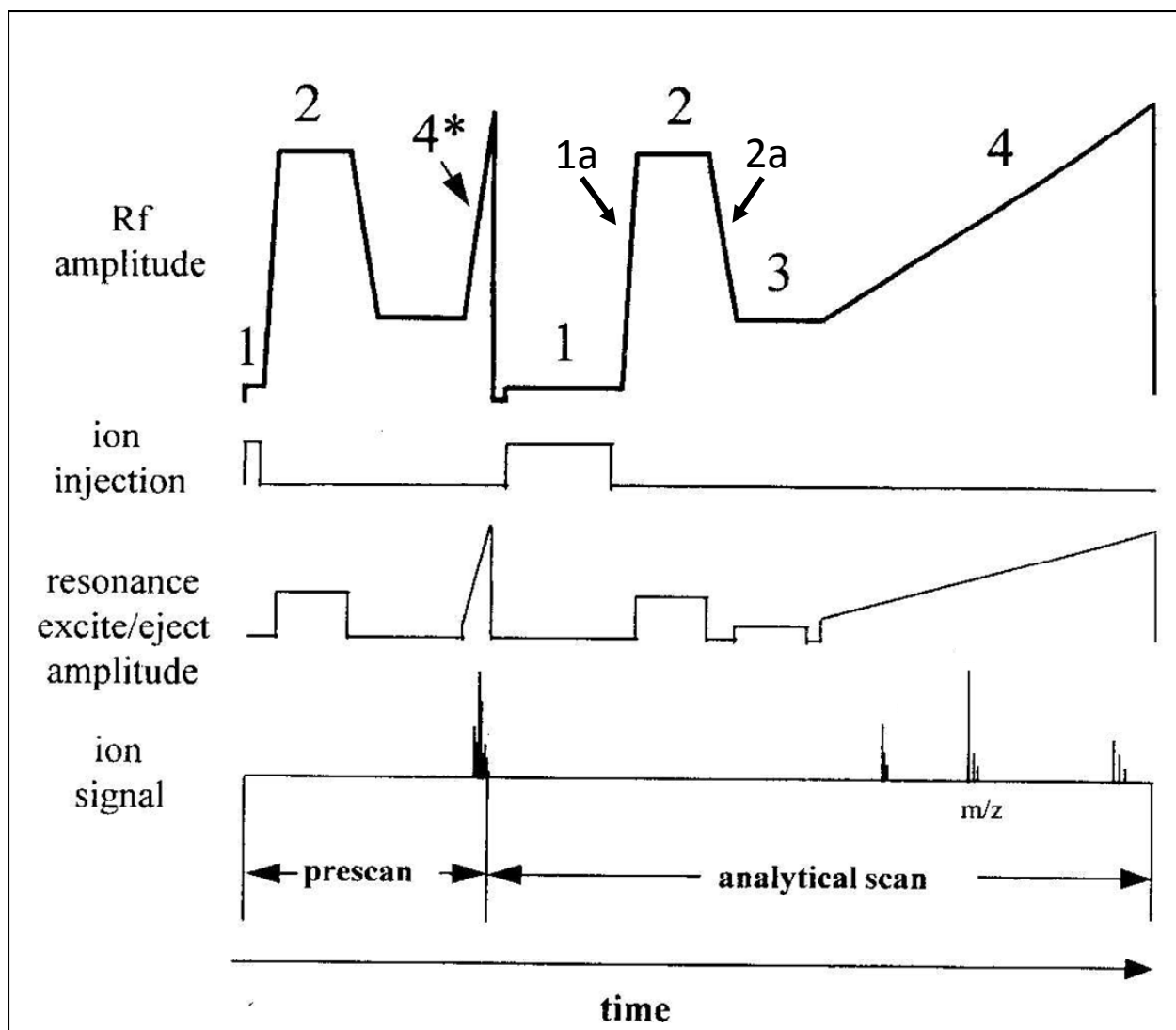


Figure 1-10. A simplified scan function for the quadrupole ion trap showing the prescan and the analytical scan which makes up one microscan. The four steps of the QIT operation: ion injection (1), isolation (2), excitation (3), and mass analysis (4) are shown in the scan function. The prescan mass analysis step (4*) is rapid, because only an ion-current measurement is required. At step 1a, the RF amplitude is increased to move the ions of interest to a q of 0.83 for isolation. At step 2a, the RF amplitude is decreased to move the isolated ions to a q of 0.25-0.35 for activation.⁹²

CHAPTER 2 WIDE ISOLATION

Introduction

Concentrations of drugs of abuse found in brain tissue better reflect drug concentrations at their site of action at the time of death than any other type of specimen used for postmortem forensic toxicology.⁵ Conventional quantification of cocaine in brain tissue involves homogenate preparation, followed by extraction and/or derivatization.⁹⁸ The extracts are then usually analyzed by gas chromatography/mass spectrometry (GC/MS), liquid chromatography/mass spectrometry (LC/MS), GC, or LC. Lengthy extraction procedures are required to remove large concentrations of lipids and other endogenous materials present in the brain, which may interfere with analysis.⁹⁹ Multiple sample pretreatment steps also allow opportunity for loss of analyte,³³ and tissue homogenization eliminates spatial information, which could provide histologically-specific drug distribution. Attempts have been made to determine the regional distribution of cocaine in postmortem brain of chronic human cocaine users.^{8, 12, 98} These analyses were performed on sections of ~ 100-200 mg of tissue from different regions of the brain, which were assumed to be homogeneous and accurately representative of the drug concentration in that excised region.

Direct MALDI-MS analysis of intact tissue can provide quantitative information about the distribution of cocaine in human brain more rapidly, with higher spatial resolution, and with less sample loss than drug analysis methods that involve tissue homogenization. Furthermore, the distribution of cocaine in brain tissue acquired by MALDI-MS can be directly related to the histology. The majority of MALDI-MS instruments use a time-of-flight (TOF) mass analyzer, which has benefits of high mass range and high throughput. Quantitative MALDI-MS is challenging, however, because MALDI exhibits irreproducible signal intensities due to

inhomogeneous crystal formation, inconsistent sample preparation, and laser shot-to-shot variability. A typical MALDI-TOF experiment will obtain 200-1000 consecutive mass spectra at each sample spot (one laser shot per spectrum), which are averaged to improve the reproducibility of the MALDI signal.²⁷ Similarly, MALDI-MS instruments that utilize a linear ion trap (LIT) mass analyzer can obtain multiple mass spectra at each spot and average them to improve reproducibility.⁸⁵ Here we obtain a single mass spectrum at each spot, with typically 10 laser shots used to fill the ion trap for each spectrum. Note that any ion trap has a finite ion storage capacity before space-charge reduces resolution and causes peak shifts.⁹⁶ MALDI-LIT instruments can minimize space-charge effects by utilizing automatic gain control (AGC),⁹⁶ which automatically controls the number of laser shots used to fill the trap (typically 1-20 shots) to optimally fill the ion trap for maximum signal without loss of mass resolution. Laser power can also be optimized along with choice of matrix compound to maximize analyte signal while avoiding space-charge effects. The use of internal standards for quantitative MALDI-MS has been shown to improve signal stability, if the solution-phase properties are carefully matched as in an isotopic standard.⁷⁷

Quantification of small drug molecules like cocaine using MALDI-MS is further complicated by the presence of interfering matrix peaks in the low mass range along with ions that may be produced from endogenous compounds present in the brain tissue.³³ One of the strengths of a linear ion trap mass spectrometer is its ability to perform multiple stages of mass analysis (MS^n) to significantly increase the selectivity for the analyte of interest. A MALDI- MS^n method could be developed to remove interferences from both MALDI matrix and the complex sample environment of brain tissue; however, a problem arises when trying to combine the use of MS^n with the use of internal standards. Instrument software allows for only one isolation

window (IW) in MSⁿ experiments, isolating one parent mass (or range of masses) for collision-induced dissociation (CID). This means that MSⁿ of the target ions of the analyte and internal standard would typically be performed with two separate MSⁿ experiments. This would increase the response variability and could counteract the signal normalizing effects of using an internal standard. In contrast, using a 6-Dalton (Da)-wide IW centered at a mass-to-charge (*m/z*) between the [M+H]⁺ ions of cocaine and its trideuterated analog allows for isolation and CID of both ions during a single MSⁿ experiment. This single isolation method reduces the signal variability inherent with MALDI compared to isolating each ion individually with a 1-Da IW (in two alternating MSⁿ experiments). This method is used here to detect and quantitatively image cocaine in postmortem human brain tissue.

This study demonstrates that MSⁿ increases selectivity, which is critical for differentiating analyte ions from matrix ions and endogenous compounds found in brain tissue. It is also shown that the use of internal standards corrects for signal variability in quantitative MALDI arising from inhomogeneous crystal formation, inconsistent sample preparation, and laser shot-to-shot variability. Using a single MSⁿ experiment with a wide IW to isolate both analyte and internal standard target ions provides improved precision (10-20 times reduction in %RSD) for quantitative imaging studies compared to using two alternating MSⁿ experiments that isolate the analyte and internal standard target ions separately.

Experimental

Chemicals

Cocaine (COC; MW 303.4 Da) and COC-d₃ (MW 306.4 Da, 0.29% d₃) were purchased from Cerilliant (Round Rock, TX, USA) at concentrations of 1 mg/mL and 100 µg/mL, respectively, in acetonitrile. High-performance liquid chromatography (HPLC)-grade acetonitrile, methanol, and water were purchased from Fisher Scientific (Pittsburgh, PA, USA).

Working standards of COC and COC-d₃ were diluted with acetonitrile and then stored at 4 °C. COC calibration standards were prepared in acetonitrile at concentrations of 5.0, 2.5, 1.25, 0.625, 0.312, 0.156, 0.078, 0.039, 0.020, 0.010, and 0.005 µg/mL with the COC-d₃ internal standard at a concentration of 2.0 µg/mL. Sinapinic acid (SA; MW 224.2 Da), 2,5-dihydroxybenzoic acid (DHB; MW 154.1 Da), and α -cyano-4-hydroxycinnamic acid (CHCA; MW 189.2 Da) were purchased from Acros Organics (Geel, Belgium). Saturated matrix solutions (40 mg/mL DHB, 10 mg/mL SA, and 10 mg/mL CHCA) were prepared in methanol/water (70:30, vol/vol) on the day of use.

Tissue Collection

Human brain tissue samples were provided by the El Paso County Coroner's Office in Colorado Springs, CO. Postmortem brain material was excised from the nucleus accumbens (NAc) from case number 07A-369, whose toxicological analysis indicated the presence of cocaine in blood at 69 ng/mL (COC concentration in the brain tissue was not quantified). The NAc is a dopamine-rich area of the striatum, which may contain an accumulation of COC due to its affinity to bind with the dopamine transporter.¹⁰⁰ At autopsy, the excised tissue was immediately snap-frozen in liquid nitrogen and then stored in a -80 °C freezer until analyzed.

Tissue Sectioning and Sample Preparation

Frozen brain tissue was cut into thin sections (20 µm thickness) in a cryostat (HM 505E; Microm International GmbH, Waldorf, Germany) at -25 °C. The tissue samples were frozen to the cryostat sample stage using distilled water. Serial brain sections were collected onto microscope slides where they were thaw mounted and then stored at -80 °C. Before mass spectrometric analysis, the tissue sections were removed from the freezer and placed in a vacuum dessicator for 30 min before spiking standards (1-µL droplets by micropipet) and applying MALDI matrix. The matrix was applied to the tissue sections using an artistic airbrush (Aztek

A470; Testors, Rockford, IL, USA). The application of MALDI matrix by airbrush has been previously published.⁶⁷ Matrix was applied using the dried-droplet method for experiments performed on MALDI plate.

Mass Spectrometry

Mass spectra were acquired using an LTQ linear ion trap with a vMALDI ion source (Thermo Finnigan, San Jose, CA, USA), equipped with a nitrogen laser (337 nm) at a frequency of 20 Hz and 100- μ m spot size. A more detailed description of this instrument has been published.⁶⁷ An average of 10 laser shots per scan was used to produce mass spectra, except for experiments that used AGC, in which the number of laser shots was automatically varied to optimally fill the trap with ions, thus avoiding space charge-related peak broadening and mass shifts. AGC assess the ion generation rate by use of a prescan, and then adjusts the number of laser shots per scan to produce a similar number of ions for each scan. The spectra are normalized to the number of laser shots for each scan.

Resonance excitation is used for isolation, activation, and mass analysis. For MSⁿ experiments, unwanted ions are resonantly ejected from the ion trap by applying a 5-500 kHz multi-frequency isolation waveform consisting of sine components spaced every 0.5 kHz. The ions of interest are isolated by removing sine components from the isolation waveform that correspond to the secular frequency of the desired ion(s). Ions are selected for isolation in the LTQ software by entering the m/z with its IW. The mass range for the ion is defined as $(m/z - IW/2)$ to $(m/z + IW/2)$. The IW should be narrow enough to minimize including interfering peaks, but wide enough to avoid loss of sensitivity for the desired ion(s). However, it is important to note that the activation width for resonance excitation (CID) has the same value as the IW. Therefore, the collision energy applied during MSⁿ is spread over the activation width. Thus, increasing the IW decreases the true collision energy for each ion.

The tissue-mounted microscope slides were affixed to a slide holder plate with double-sided tape. The plate was then inserted into the LTQ, and the plate was rastered beneath the laser spot at 100- μm steps to produce position-specific mass spectra. Specific ions and the total ion current (TIC) signal were extracted from the raw data files using ImageQuest version 1.0 (Thermo Fisher Scientific, San Jose, CA, USA), which was used to generate an image.

Results and Discussion

MS² and MS³ Mass Spectra of COC and COC-d₃

DHB was selected as the MALDI matrix in this study, as preliminary investigations showed that it produces more efficient ionization for COC at low concentrations than SA or CHCA. DHB was also preferred as the matrix for COC analysis due to its lack of interference with the $[\text{M}+\text{H}]^+$ ion of COC (m/z 304) and COC-d₃ (m/z 307). The COC standards in acetonitrile were characterized by MSⁿ. The MS² spectrum of m/z 304 and 307 (IW = 1.0 Da, CID = 20) each show one major product ion, corresponding to a neutral loss (NL) of benzoic acid (NL 122) at m/z 182 and 185, respectively. MS³ was performed on the product ion signal at m/z 182 of COC (IW = 1.0 Da; CID = 30), resulting in product ions at m/z 150 (NL of 32; CH₃OH), m/z 122 (NL of 60; CH₃OH + CO), m/z 119 (NL of 63; CH₃OH + CH₃NH₂), m/z 108 (NL of 74; CH₃OH + CH₂CO), m/z 91 (NL of 91; CH₃OH + CH₃NH₂ + CO), and m/z 82 (NL of 100; CH₃OH + C₄H₄O via a 6-electron Alder ene rearrangement). The structures of the fragment ions of the $[\text{M}+\text{H}]^+$ ion of COC and its proposed fragmentation pathway (Figure 2-1) have been previously published.¹⁰¹ MS³ was performed on the product ion signal at m/z 185 of COC-d₃ (IW = 1.0 Da; CID = 30) resulting in product ions at m/z 153 (NL of 32; CH₃OH), m/z 125 (NL of 60; CH₃OH + CO), m/z 119 (NL of 63; CH₃OH + CH₃NH₂), m/z 111 (NL of 74; CH₃OH + CH₂CO), m/z 91 (NL of 91; CH₃OH + CH₃NH₂ + CO), and m/z 85 (NL of 100; CH₃OH + C₄H₄O). The m/z values of the fragment ions of COC-d₃ at m/z 91 and 119 are the same as those

for COC because these ions have lost the trideuterated tag that was originally located on the *N*-methyl group.

Improving Signal Reproducibility with Internal Standards

Quantitative analysis by MALDI is challenging, because of signal irreproducibility due to variation in sample preparation, inhomogeneous co-crystallization of analyte and MALDI matrix, and laser shot-to-shot variability. Figure 2-2a shows the m/z 304 signal of the $[M+H]^+$ ion of COC detected from COC/COC- d_3 standard solutions spotted 1 μ L each in triplicate onto a MALDI plate with 1 μ L of DHB matrix pipetted on top. The COC/COC- d_3 solutions were composed of different concentrations of COC (5.0, 2.5, 1.2, and 0.63 μ g/mL) mixed with 1.0 μ g/mL of COC- d_3 . The histogram shows the high variability in signal for each concentration with %RSD ranging from 29 to 67%, making it difficult to distinguish signal from one concentration to another. Figure 2-2b shows the m/z 304 signal of COC normalized to the $[M+H]^+$ ion signal of COC- d_3 at m/z 307. Signal variability was reduced dramatically (%RSD ranged from 0.26 to 1.33%) by normalizing the analyte signal to that of the internal standard making quantification by MALDI possible.

Increasing Analyte Selectivity with MSⁿ

Figure 2-3a shows a full-scan MS spectrum of a 1.25:1 mixture (by mass) of COC and COC- d_3 standards spiked (1 μ L of 1.25 μ g/mL and 1.0 μ g/mL, respectively) onto a MALDI plate with DHB matrix. Peaks at m/z 304 and 307 represent the $[M+H]^+$ ions of COC and COC- d_3 , respectively. A number of cluster ions, fragment ions, and a molecular ion of DHB are also present, including m/z 137 $[DHB+H-H_2O]^+$, m/z 154 $[DHB]^+$, m/z 177 $[DHB+Na]^+$, m/z 199 $[2DHB+Na]^+$, m/z 221 $[DHB-2H+3Na]^+$, m/z 273 $[2DHB+H-2H_2O]^+$, m/z 291 $[2DHB+H-H_2O]^+$, and m/z 331 $[2DHB+Na]^+$. Figure 2-3b shows a full-scan MS spectrum of a 1:1 mixture (by

mass) of COC and COC-d₃ standards spiked (1 μL of 1.0 μg/mL each) onto a 20-μm thick human brain tissue slice with DHB airbrushed. The [M+H]⁺ ions of COC and COC-d₃ are observed at *m/z* 304 and 307, respectively. The same cluster ions, fragment ions, and molecular ion of DHB are present, in addition to numerous ions of endogenous compounds from the brain tissue, including the phosphocholine head group of phosphatidyl choline at *m/z* 184 [(CH₃)₃NCH₂CH₂PO₄H]⁺. Identification of COC and COC-d₃ on the MALDI plate and brain tissue was confirmed by characteristic MS² product ions at *m/z* 182 and 185, respectively.

MS² spectra of *m/z* 304 with COC spiked at concentrations below 5 ng/mL on plate and on tissue revealed an isobaric compound that has product ions at *m/z* 212 and 91. The isobaric ion likely originates from the surfactant, benzyldimethyldodecylammonium chloride (C₁₂BAC).¹⁰² The widespread use of C₁₂BAC and other BACs as disinfectants makes it a likely trace contaminant in the laboratory. The ion at *m/z* 212 results from fragmentation of the carbon-nitrogen bond between the toluyl substituent and the quaternary amine (Figure 2-4). The *m/z* 91 ion is a stable tropylium ion formed by fragmentation in which the toluyl substituent retains the positive charge (Figure 2-4). MS² of *m/z* 304 with COC spiked at concentrations below 5 ng/mL also results in the detection of product ions of isobaric compounds at *m/z* 256 and 286. These ions have not yet been identified, but are not present when DHB has been characterized on MALDI plate alone.

The presence of isobaric ions in samples increases with sample complexity and may interfere with quantification at low analyte concentrations. MSⁿ can improve analyte selectivity and produce higher signal-to-noise ratios, resulting in lower detection and quantification limits for the analyte. Combining the use of MSⁿ with internal standards is commonly performed by alternating MSⁿ scans of the analyte and the internal standard ions, and then ratioing the resulting

product ion signals. This method is effective for use with ionization techniques such as electrospray and atmospheric pressure chemical ionization; however, due to the shot-to-shot variability of MALDI, acquiring analyte and internal standard signals in alternating MSⁿ experiments may counteract the signal normalizing effects gained by using an internal standard.

Combining Internal Standards with MSⁿ using a Wide Isolation Window

One method for combining the use of internal standards with MSⁿ is to perform MS² on the analyte and internal standard ions separately during alternate MSⁿ experiments illustrated in Figure 2-5a. The [M+H]⁺ ion of COC (*m/z* 304) is isolated with a 1 Da window and then collisionally activated to produce the product ion at *m/z* 182 shown in the MS² spectrum in Figure 2-5b. In a separate MS² scan, the [M+H]⁺ ion of COC-d₃ (*m/z* 307) is isolated with a 1 Da window and CID is applied, resulting in the product ion at *m/z* 185 shown in the MS² spectrum in Figure 2-5c. The analyte ion signal at *m/z* 182 can then be normalized to the internal standard ion signal at *m/z* 185. An alternative approach to using two separate MSⁿ experiments is to use a single wide isolation window (e.g., 6-Da) centered at *m/z* 305.8, shown in Figure 2-5d, allowing the simultaneous isolation and CID of the [M+H]⁺ ion of COC (*m/z* 304) and COC-d₃ (*m/z* 307). The resulting MS² spectrum, shown in Figure 2-5e, contains the product ions of COC and COC-d₃ at *m/z* 182 and 185, respectively.

The performance of the MSⁿ experiment using a single wide isolation window was compared with that using two alternating MSⁿ experiments by detecting COC and COC-d₃ spiked on top of human brain tissue. Figure 2-6a shows a microscope image of a 20- μ m thick human brain tissue slice with COC/COC-d₃ solutions spotted 1 μ L each in triplicate (A, B, and C) on the surface of the tissue and then airbrushed with DHB. The five COC/COC-d₃ solutions spotted all contained 2.0 μ g/mL of COC-d₃ in addition to 0.31, 0.62, 1.2, and 5.0 μ g/mL of COC,

respectively. The compositions of the solutions spotted (1-5) are shown in the table below the image. The average dried spot size was 0.25 cm in diameter. Figure 2-6b shows the MS² product ion image of *m/z* 305.8 (IW = 6 Da, CID = 20) of the entire tissue slice generated from signal extracted from the mass range *m/z* 182-186 and normalized to the TIC. Higher signal intensity correlates with the darker shade of gray, illustrating how the COC and COC-d₃ co-crystallize along with the DHB towards the edge of each spot. The LTQ software was used to outline each spot to be analyzed. Each spot was analyzed twice: first by performing MS² of *m/z* 304 (IW = 1 Da, CID = 20) followed by MS² of *m/z* 307 (IW = 1 Da, CID = 20), and then by MS² of *m/z* 305.8 (IW = 6 Da, CID = 20). For each analysis, all of the spectra (~500 scans) were averaged for each spot, and the *m/z* 182 signal for COC was normalized to the *m/z* 185 signal for COC-d₃ and plotted against the concentration of COC spiked to produce two different calibration curves shown in Figure 2-7. Figure 2-7a shows the average ratio of peak intensities *m/z* 182 to *m/z* 185 as a function of the spiked COC concentration for alternating MS² experiment (i.e., MS² of *m/z* 304 in one scan and then MS² of *m/z* 307 the following scan). The line of best fit was $y = 0.68(\pm 0.07)x + 0.2(\pm 0.2)$ over the range 0.31-5.0 µg/mL with a standard error of the estimate (SEE) = 0.2833; the %RSD ranged from 12% to 30%. The 95% confidence intervals for the slope and y-intercept were 0.44 to 0.91 and -0.4 to 0.9, respectively. Figure 2-7b shows the average ratio of peak intensities *m/z* 182 to 185 as a function of the spiked COC concentration for a single MS² experiment with a wide 6-Da isolation window centered at *m/z* 305.8 (i.e., MS² of *m/z* 304 and *m/z* 307 in one scan). The line of best fit was $y = 0.492(\pm 0.001)x + 0.023(\pm 0.003)$ over the range 0.31 to 5.0 µg/mL with an SEE = 0.0052; the %RSD ranged from 0.50% to 5.1%. The 95% confidence intervals for the slope and y-intercept were 0.488 to 0.496 and 0.011 to 0.034, respectively. Precision was dramatically improved by using the single MS²

experiment with 6-Da wide isolation window compared with isolating each ion individually with a 1-Da window (two alternating MS² experiments). There was a 10-20 times reduction in %RSD and a 50 times reduction in SEE by using the wide isolation method.

Isolation Window Width and Automatic Gain Control

Usually the smallest isolation width is desired for MSⁿ experiments performed with an ion trap mass spectrometer to avoid isolating unwanted background ions and reducing analytical specificity. The minimum acceptable ion isolation width is defined as the lowest range providing no appreciable signal attenuation of the analyte and internal standard ions when compared to a wider setting. Signal attenuation can result either from losses during the resonance ejection step which is used to remove masses below and above the selected *m/z* range, or from decreased CID efficiency of the analyte and internal standard ions.

The effect of isolation width on the intensity of the product ions of the [M+H]⁺ ions of COC (*m/z* 304) and COC-d₃ (*m/z* 307) together in a single MS² scan was investigated. Five solutions of COC and COC-d₃ were prepared at equal concentrations and diluted with acetonitrile (0.12, 0.25, 0.50, 1.0, and 2.0 µg/mL). All five solutions were spotted in triplicate 1 µL each onto a MALDI plate followed by 1 µL of DHB matrix. For all MS² experiments, the parent ion was set to *m/z* 305.8, the center of the mass range between *m/z* 304.3 and *m/z* 307.3, and the CID was set to 20. The size of the isolation window width centered at *m/z* 305.8 was varied (4 Da, 6 Da, and 8 Da), and the ratio of the intensities of the products ions at *m/z* 182 and *m/z* 185 for COC and COC-d₃, respectively, were observed. It is important to note that MS² of *m/z* 304 (IW = 1.5 Da) produced a negligible amount of *m/z* 185 (<0.0005%), the product ion of *m/z* 307. Also, MS² of *m/z* 307 (IW = 1.5 Da) produced a negligible amount of *m/z* 182 (<0.002%), the product ion of *m/z* 304. The expected signal ratio of COC to COC-d₃ is 1.02 for

equal masses based on a calculated molar ratio of 1.01 corrected for the isotopic purity of COC-d₃ (0.29% COC-d₀). The measured signal ratio of *m/z* 182 to 185 was approximately equal to 1 for concentrations below 0.50 µg/mL, but the ratio increased at concentrations above 0.50 µg/mL (i.e., the *m/z* 185 signal decreased with respect to *m/z* 182). It was also observed that the signal ratio of *m/z* 182 to 185 was higher for a 4 Da isolation window (2.07 at 1.0 µg/mL and 3.50 at 2.0 µg/mL) compared with the 6 Da (1.18 at 1.0 µg/mL and 1.68 at 2.0 µg/mL) and 8 Da (1.05 at 1.0 µg/mL and 1.81 at 2.0 µg/mL) isolation windows widths. This suggests that either some of the *m/z* 307 ion is being lost during isolation or that the *m/z* 307 ion is being less efficiently excited during the CID step when narrower IWs are used.

An effort was made to separate the isolation step from the CID step of the MS² experiment to better understand the effect of isolation window width on the signal intensities of the MS² product ions of the [M+H]⁺ ions of COC and COC-d₃. The above experiment was repeated on the five COC/COC-d₃ solutions, except that no CID voltage was applied so that the ions at *m/z* 304 and 307 were isolated but not fragmented. The ratio of intensities of *m/z* 304 and *m/z* 307 were then monitored for different isolation window widths (4, 6, and 8 Da). Results showed that the signal ratio of *m/z* 304 and 307 remained approximately equal to 1 for concentrations 0.12 - 2.0 µg/mL for isolation widths of 6 and 8 Da; however, the signal ratio steadily increased for a 4 Da isolation window at concentrations above 0.50 µg/mL. The increase in the signal ratio of *m/z* 304 to 307 (i.e., *m/z* 307 signal decreased with respect to *m/z* 304) at higher concentration is presumably due to a mass shift of *m/z* 307 outside the isolation window, resulting in resonance ejection of some of the *m/z* 307 ions. This mass shift could be caused by space-charge effects at higher ion populations in the ion trap, and may be corrected by using AGC. The experiment was repeated again, comparing the signal ratio of *m/z* 304 to 307

with and without AGC with a 4 Da isolation window and no CID applied. Results showed that when AGC was used, the signal ratio of m/z 304 to 307 remained approximately equal to 1 for all concentrations analyzed (0.12 – 2.0 $\mu\text{g/mL}$), indicating that AGC can minimize space-charge effects, which may lead to ejection of the higher m/z ion when a narrower isolation width is employed.

Quantification of Cocaine in Postmortem Human Brain Tissue

The MS³ wide isolation method developed for COC was applied to human brain tissue from a subject whose toxicology report showed the presence of COC. The MS² product ion of the $[\text{M}+\text{H}]^+$ ion of COC at m/z 182 was not distinguishable from the background signal; therefore, an MS³ wide isolation method was developed to increase selectivity. The MS³ wide isolation method was evaluated by spotting 1 μL of a 4.0 $\mu\text{g/mL}$ solution of COC and COC-d₃ onto a MALDI plate followed by 1 μL of DHB matrix. The method involves centering a 6-Da isolation window at m/z 305.8 and applying a CID of 20 followed by a 6-Da isolation window centered at m/z 183.5 (between COC and COC-d₃ product ions at m/z 182 and 185) with a CID of 30. The resulting MS³ product ion spectrum revealed characteristic fragment ions of COC at m/z 150, 82, 108, 122, 119, and 91 and for COC-d₃ ions at m/z 153, 85, 111, 125, 119, and 91. The MS³ wide isolation method was applied to unspiked brain tissue from a cocaine user, and COC was detected and confirmed by matching all six of these MS³ ions. The relative intensities of the five most intense fragment ions (all but m/z 91) were within 12% of the standard fragment ion intensities.

Figure 2-8 shows the MS³ product ion image of m/z 305.8 (IW = 6 Da, CID = 20) of the entire tissue slice generated from signal extracted from the mass range m/z 150 – 151 and normalized by the TIC. The image shows no localization of COC in the section of the nucleus

accumbens analyzed. Browne et al.⁹⁸ analyzed 1 g samples from different regions of 3 human brains by solid-phase extraction (SPE) and LC. From these studies, cocaine and benzoylecgonine were found to be distributed throughout the different regions of the brain. However, significant differences in the concentration of cocaine were apparent in different regions of the brain (e.g., cocaine concentration was higher in the basal ganglia than the section of the cerebellum analyzed). These findings were consistent with other brain cocaine distribution studies, which reported that concentrations of cocaine and of its metabolites showed little regional heterogeneity in postmortem brain of chronic users of cocaine.^{8, 12} The homogeneous distribution of cocaine and its metabolites in specific regions of the brain may be a result of the high concentrations typical of behavioral usage.

Before quantifying unspiked COC in human brain tissue with the MS³ method, it was necessary to show that the response factors for COC and COC-d₃ were equal, so that the calibration curve of COC-d₃ could be used. A series of 1:1 solutions of COC and COC-d₃ at various concentrations (0.03, 0.06, 0.13, 0.25, 5.0, 1.0, and 2.0 µg/mL) were prepared and spiked in triplicate, 1 µL each, on top of serial tissue sections, and then DHB matrix was airbrushed over the tissue slices. Each spot was analyzed using the MS³ wide isolation method, and the *m/z* 150 signal from COC was plotted versus the *m/z* 153 signal from COC-d₃. The slope of the plot was 1.062 ± 0.002 with a correlation coefficient $r^2 = 0.99,998$ over the concentration range 0.03 to 2.0 µg/mL. The 95% confidence interval for the slope was 1.057 to 1.066. The expected slope based on a molar ratio of 1.01 and an isotopic purity for COC-d₃ of 0.29% d₀ is 1.02, which means that COC has a 4% higher response factor than COC-d₃ over the concentration range measured.

The MS³ wide isolation method was used to quantify the unspiked COC that was detected in the postmortem human brain tissue. The calibration curve used for quantification (Figure 2-8) was created by imaging three different concentrations of COC-d₃ (0.06, 0.13, and 0.25 µg/mL) were spiked (1 µL) onto a glass slide before thaw mounting a 20 µm-thick brain tissue slice on top and airbrushing DHB matrix. All three spots were then analyzed using the MS³ wide isolation method. Approximately 2000 scans were acquired to image the entire area of each of the spots (average area = 0.17 cm²). The *m/z* 153 signal from each spot was used to develop a calibration curve that resulted in a line of best fit of $y = 399(\pm 27)x - 17(\pm 4)$ (Figure 2-8). COC-d₃ was shown to have a linear response with increasing concentrations spiked underneath tissue. Since the MS³ wide isolation method analyzes both COC and COC-d₃ simultaneously, unspiked COC was detected from each spot analyzed at *m/z* 150, and the corresponding signal was plotted (◇) alongside each corresponding COC-d₃ signal (□) in Figure 2-9. An area of the tissue (500 MS scans) that was not spiked with COC-d₃ was analyzed using the MS³ wide isolation method and the acquired *m/z* 150 signal was averaged with the *m/z* 150 signals from the spiked COC-d₃ spots, resulting in a very trace signal of 29 ± 1 counts (highlighted as dashed line on Figure 2-8). Assuming that the amount of unspiked COC extracted from the tissue has a 1:1 response with the COC-d₃ spiked on top of tissue, the calibration curve for COC-d₃ can be used to quantify the amount of COC present in the analyzed tissue. From the equation of the line, it was determined that COC was present at a level equivalent to 0.12 ± 0.01 µg/mL.

Using the 1 µL volume of COC-d₃ spiked underneath tissue, it is calculated that the mass of COC present is 1.2×10^{-4} µg. Given that the area of an analyzed spot on tissue was 0.17 cm² and that the tissue thickness was 20 µm (2.0×10^{-3} cm), the volume of tissue from which COC was extracted was 3.4×10^{-4} cm³. The mass of the tissue is 3.4×10^{-4} g (density of wet tissue

$\sim 1.0 \text{ g/cm}^3$), resulting in an absolute concentration of COC detected in this area of the postmortem brain tissue of $0.35 \text{ }\mu\text{g/g}$ (350 ppb).

The MALDI-MS method has a smaller sample requirement ($\sim 100 \text{ }\mu\text{g}$ tissue) and less sample preparation than conventional GC/MS techniques, which require 1000 to 10,000 times more sample (0.1 to 1.0 g of brain tissue) to be homogenized before solid-phase extraction and GC/MS analysis.^{8,12} The GC/MS method developed by Kalasinsky et al.¹² reported a limit of detection of 0.1 ng/mL for the analysis of COC in brain tissue. COC was detectable at 30 ng/mL with the MALDI-MS³ wide isolation method developed here. Although the MALDI-MS³ wide isolation method is not as sensitive as the GC/MS method (primarily because it uses a 1000 times smaller sample), it readily detects cocaine at a level an order of magnitude below the lowest level (300 ng/mL) reported for COC detected by GC/MS analysis of 15 autopsied brain regions of 14 human chronic cocaine users.¹²

Conclusions

It has been demonstrated that MS² and MS³ increase selectivity, which is critical for differentiating analyte and internal standard ions from matrix ions and endogenous compounds found in brain tissue. It has also been shown that the use of internal standards corrects for signal variability during quantitative MALDI. A method was developed that allows for a single MS² experiment that uses a wide isolation window to isolate both analyte and internal standard ions. This method was shown to provide improved precision ($\sim 10\text{-}20$ times reduction in %RSD) for quantitative analysis of COC in postmortem brain tissue compared with using two alternating MS² experiments that isolate the analyte and internal standard target ions separately. When COC concentration is too low to distinguish the MS² product ion at m/z 182 from the background, the MS³ wide isolation method can be applied to increase selectivity.

The wide isolation window developed for the analysis of COC could be applied to quantitative MALDI-MSⁿ imaging of other drugs of abuse and their metabolites in brain tissue, which could prove to be an invaluable tool in the field of postmortem forensic toxicology. A MALDI-MS imaging method that combined the use of internal standards for minimizing signal variability with the high molecular specificity of MSⁿ could provide a visual snapshot for the forensic toxicologist that reflects the true distribution and concentration of drugs of abuse at the time of death. This information could be used to substantiate fatal overdoses as well as provide supportive data for neurotoxicity studies.

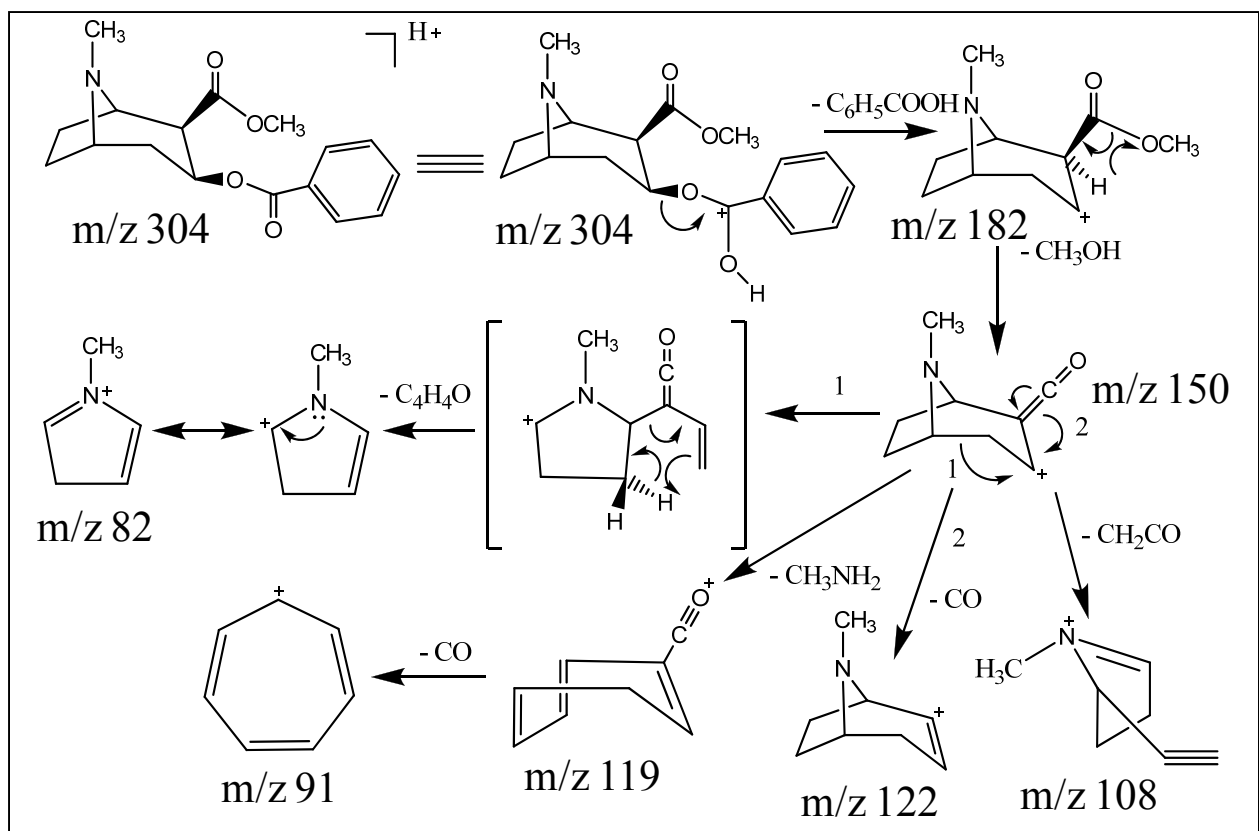


Figure 2-1. Cocaine dissociation pathway.¹⁰¹

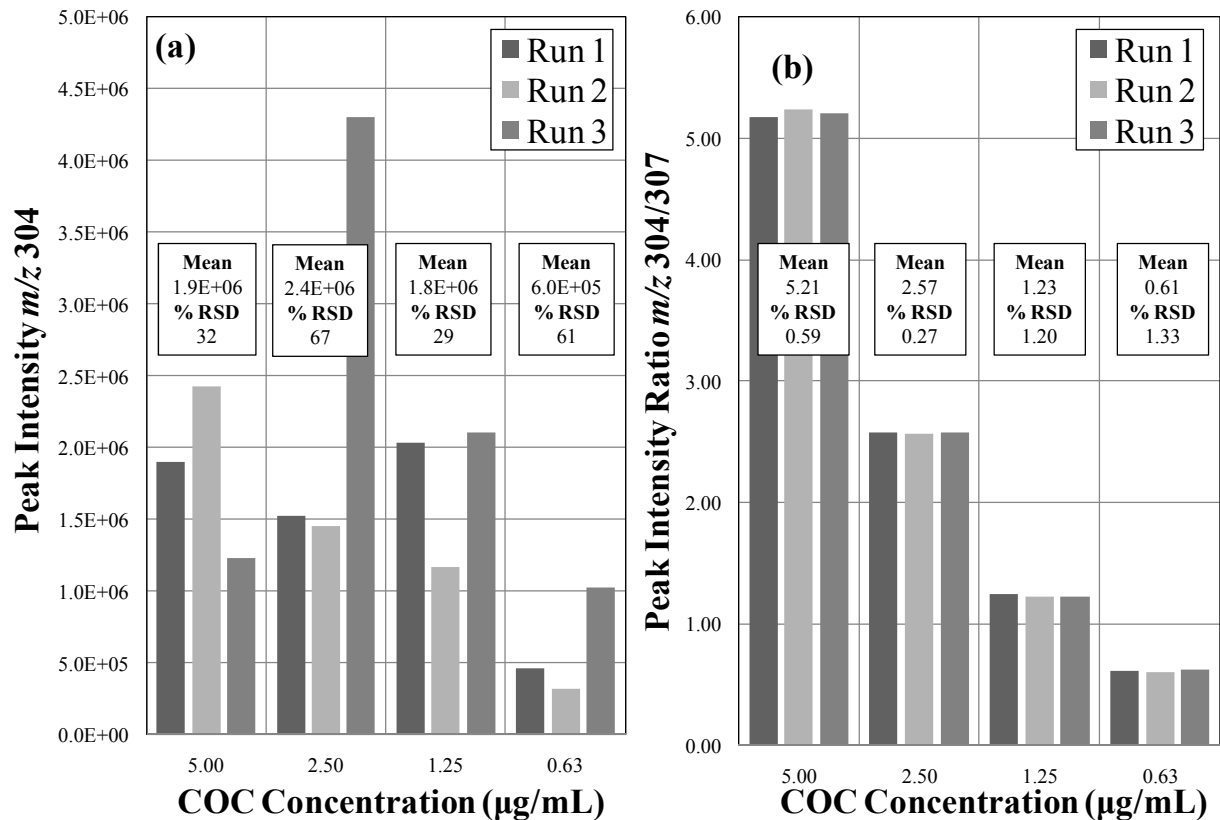


Figure 2-2. MALDI-MS signal variability with and without internal standards. Signal of m/z 304, $[\text{M}+\text{H}]^+$ of COC (a) and m/z 304 signal ratioed to m/z 307 signal, $[\text{M}+\text{H}]^+$ of COC- d_3 (b). All solutions spotted $1 \mu\text{L}$ in triplicate on MALDI plate with DHB matrix. The internal standard (COC- d_3) was maintained at $1 \mu\text{g/mL}$ for all solutions.

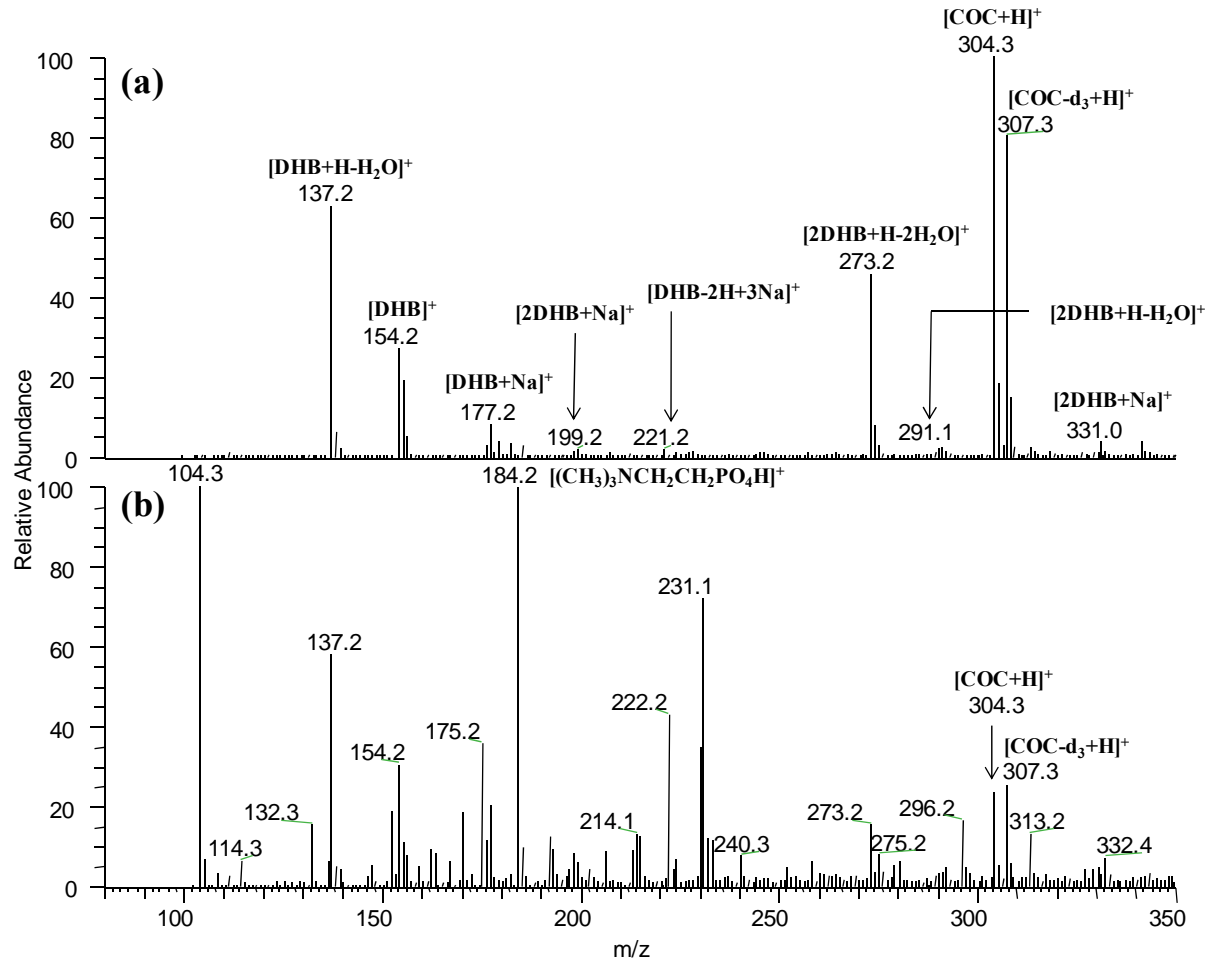


Figure 2-3. Comparing mass spectra of COC and COC-d₃ on MALDI plate and on brain tissue. MALDI mass spectrum of (a) a solution of COC (1.25 μg/mL) and COC-d₃ (1.0 μg/mL) spotted (1 μL) with DHB matrix on MALDI plate (run 1 from Figure 1) and (b) a solution of COC and COC-d₃ (1.0 μg/mL each) spiked (1 μL) on postmortem human brain tissue with DHB matrix airbrushed.

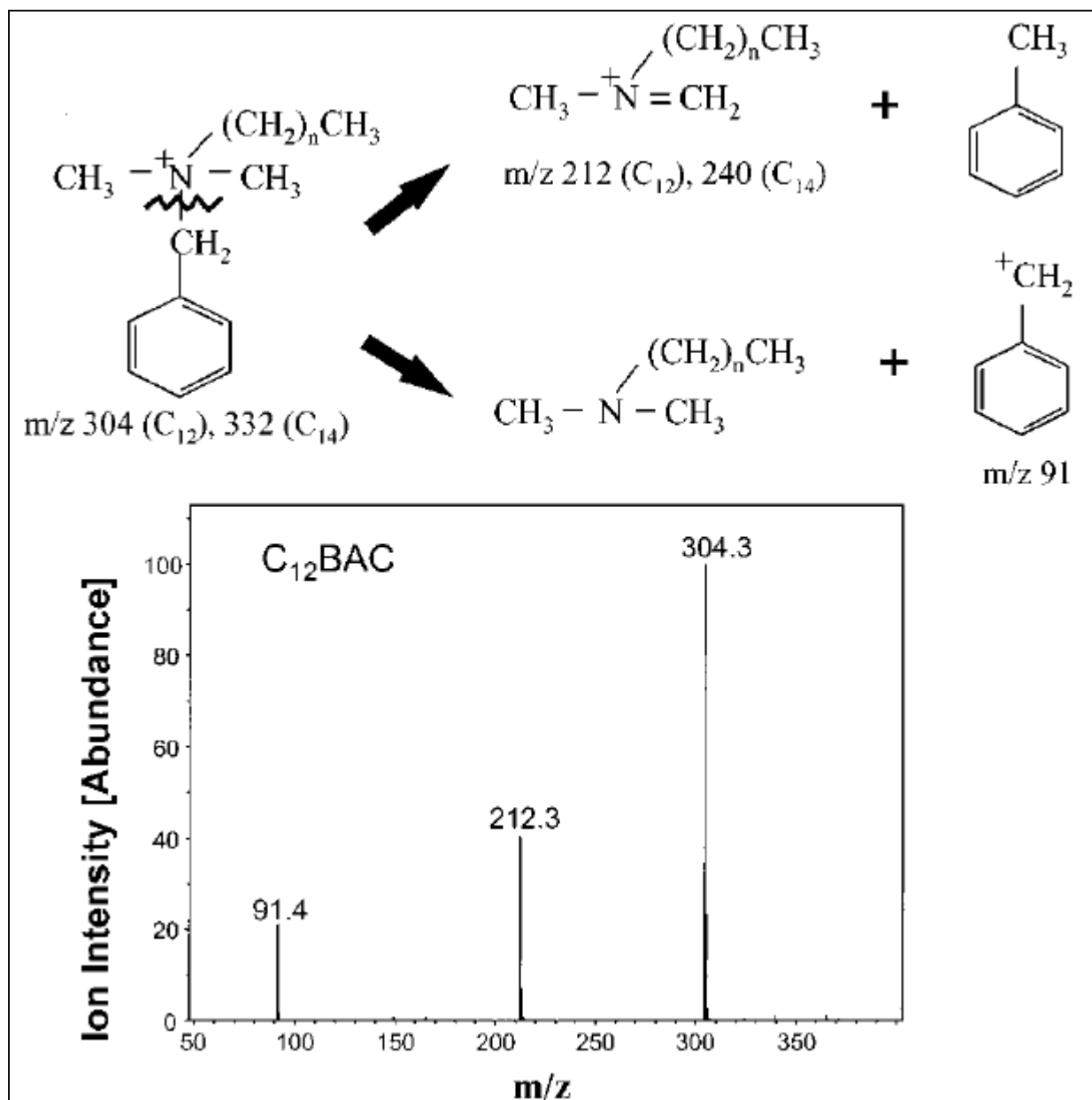


Figure 2-4. Fragmentation of the benzyldimethyldodecylammonium ion.¹⁰²

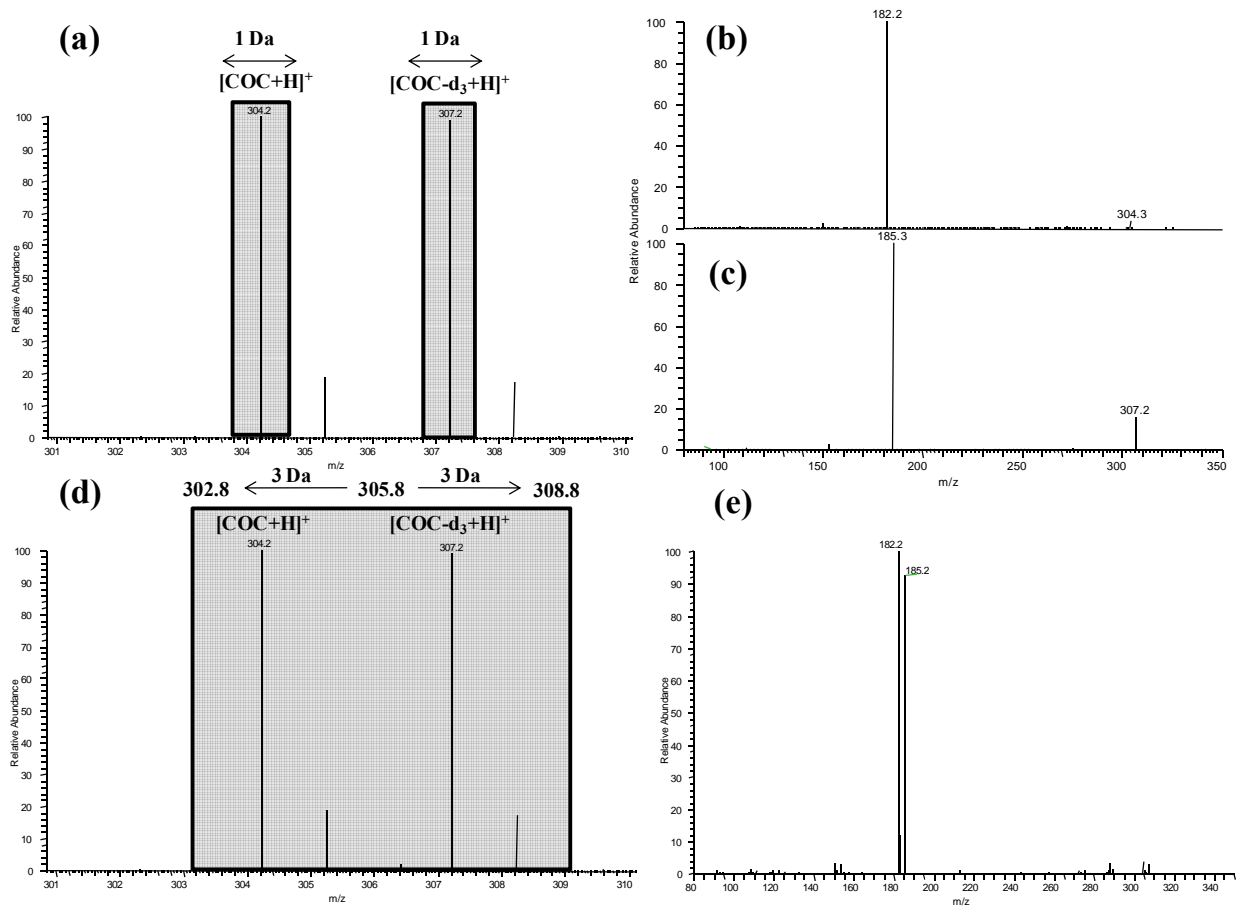


Figure 2-5. Wide isolation MALDI-MS². COC (1.0 $\mu\text{g/mL}$) and COC-d₃ (1.0 $\mu\text{g/mL}$) spotted (1 μL) with DHB matrix on MALDI plate. (a) Individual isolation (1 Da) and collisional activation of m/z 304 and m/z 307 with resulting MS² spectra of the $[M+H]^+$ ions of (b) COC at m/z 304 and (c) COC-d₃ at m/z 307. (d) Simultaneous isolation and CID activation of m/z 304 and m/z 307 with a 6-Da window centered at m/z 305.8 and (e) the resulting MS² spectra containing both COC and COC-d₃ fragment ions at m/z 182 and m/z 185, respectively.

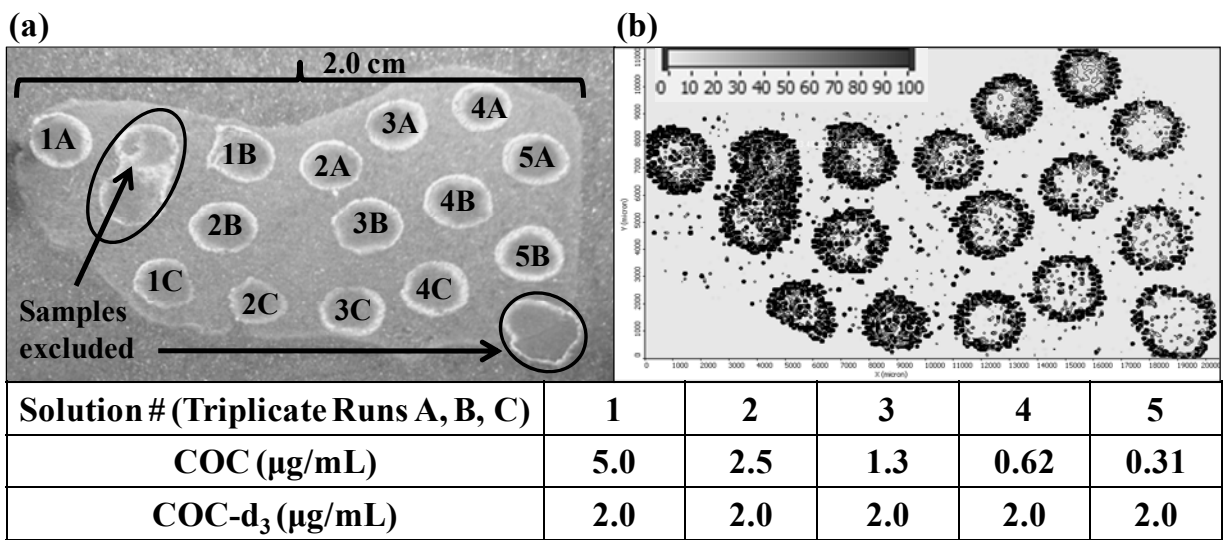


Figure 2-6. Images of standards spiked on brain tissue. (a) Photomicrograph of 20 μm thick human brain tissue mounted on slide with COC/COC-d₃ solutions spiked (1 μL) in triplicate (A, B, and C) on top of tissue and then airbrushed with DHB matrix. (b) MS² product ion image generated from signal selected from mass range *m/z* 182-186 and normalized by the TIC.

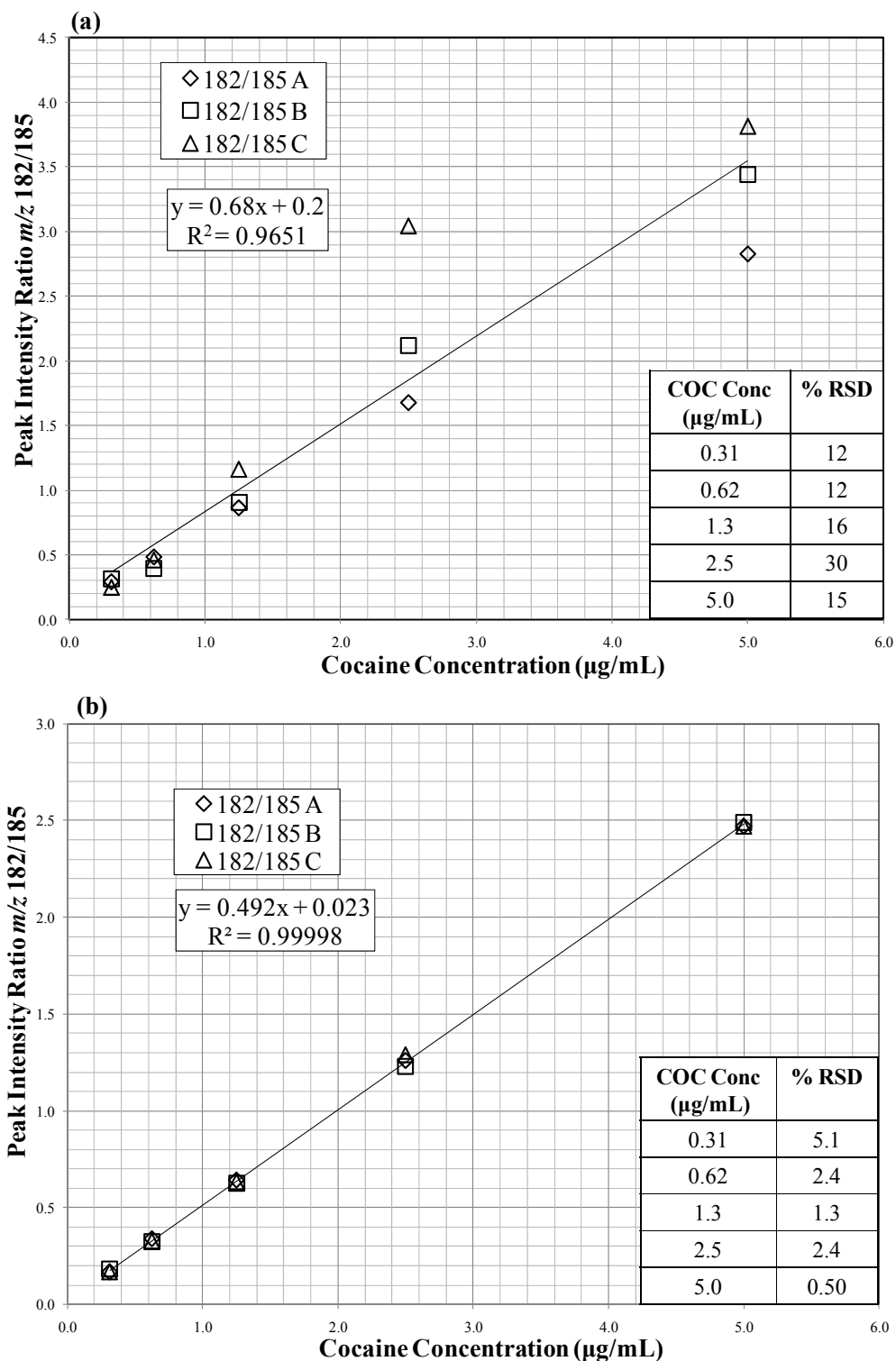


Figure 2-7. Calibration curves for alternating scans MS^2 and wide isolation MS^2 . Peak intensity ratio of m/z 182 to m/z 185 versus COC concentration for two alternating MS^2 experiments (a) and for a single MS^2 experiment using a 6-Da isolation and activation window.

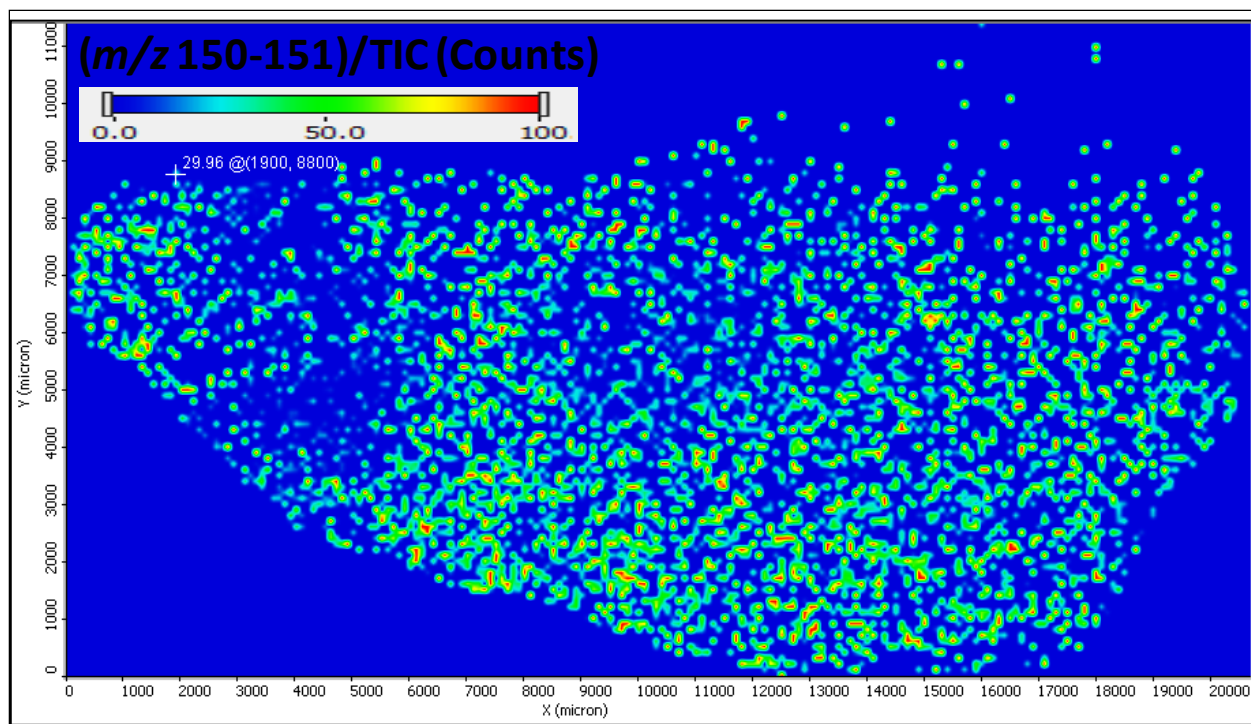


Figure 2-8. Mass spectrometric image of cocaine in brain tissue. The MS³ product ion image of $m/z\ 305.8$ (IW = 6 Da, CID = 20) of the entire tissue slice generated from signal extracted from the mass range $m/z\ 150 - 151$ and normalized by the TIC.

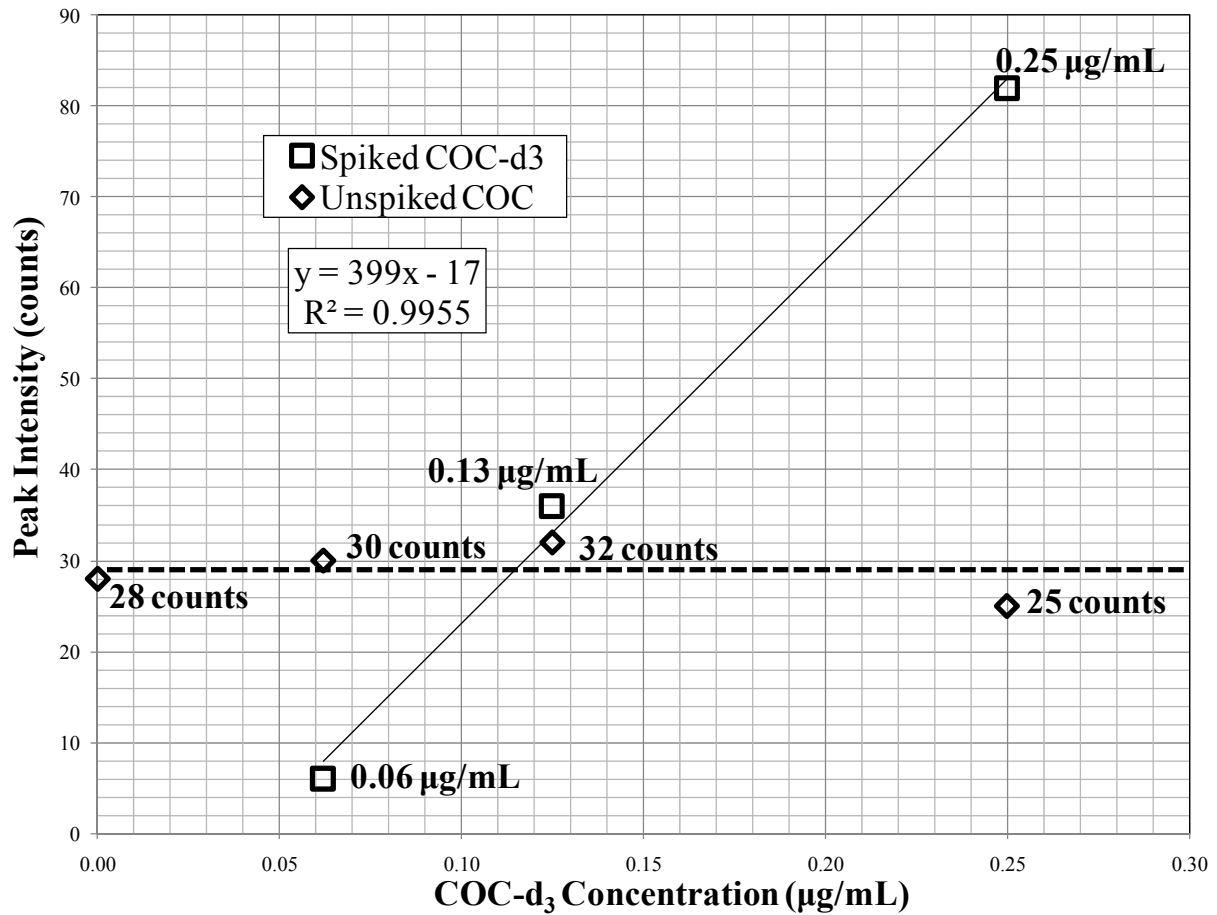


Figure 2-9. Cocaine quantification. Calibration curve created from plotting signal of MS³ fragment ion of COC-d₃ at *m/z* 153 versus COC-d₃ concentration spiked beneath 20 µm tissue from cocaine user. Unspiked COC was detected by the MS³ fragment ion of COC at *m/z* 150 and plotted against the calibration curve of COC-d₃ to quantify the amount of COC present in tissue.

CHAPTER 3 SWIFT ISOLATION

Introduction

Direct MALDI-MS analysis of intact tissue can provide information about the distribution of cocaine in human brain more rapidly, with higher spatial resolution, and with less sample loss than drug analysis methods that involve tissue homogenization. Furthermore, the distribution of cocaine in brain tissue acquired by MALDI-MS can be directly related to the histology. Quantitative analysis by MALDI-MS is challenging, however, because MALDI exhibits irreproducible signal intensities due to inhomogeneous crystal formation, inconsistent sample preparation, and laser shot-to-shot variability. The use of internal standards for quantitative MALDI-MS has been shown to improve signal stability, if the solution-phase properties are carefully matched as in an isotopic standard.⁷⁷

Quantification of small drug molecules such as COC using MALDI-MS is further complicated by the presence of interfering matrix peaks in the low-mass range along with ions that may be produced from endogenous compounds present in the brain tissue. One of the strengths of a linear ion trap mass spectrometer is its ability to perform multiple stages of mass analysis (MS^n) to significantly increase the selectivity for the analyte of interest. A MALDI- MS^n method could be developed to remove interferences from both MALDI matrix and the complex sample environment of brain tissue; however, a problem arises when trying to combine the use of MS^n with the use of internal standards. Current instruments allow for only one isolation window (IW) in MS^n experiments, isolating a single parent mass (or range of masses) for collision-induced dissociation (CID). This means that MS^n of the target ions of the analyte and internal standard typically requires two separate MS^n experiments. This increases the response variability and can counteract the signal normalizing effects of using an internal standard.

It was previously reported that using a wide IW (e.g., 6 Daltons (Da)) that simultaneously isolates the analyte and internal standards ions in a single MS² experiment provided improved precision for quantitative MALDI-MSⁿ of COC in tissue, when compared to using alternate MS² experiments that separately isolate the target analyte and internal standard ions.¹⁰³ Isolating both analyte and internal standard with a wide IW reduces signal variability when the analyte and internal standard signals are ratioed. However, the wide IW not only isolates the analyte and internal standard ions, but also ions in between that are not of interest. These ions may fill up the ion trap and may also interfere with detection of the target ions. This chapter reports a multi-notch isolation waveform that selectively isolates the analyte and internal standard ions, reducing the effects of background interferences and boosting the sensitivity for analyte ions. SWIFT (stored waveform inverse Fourier transform) is a broadband excitation technique that is capable of selectively isolating multiple ions and has the potential for improving precision of quantitative MALDI-MSⁿ.

SWIFT was first introduced to the field of mass spectrometry by Marshall et al. in 1985 for use with the Fourier transform ion cyclotron resonance mass spectrometer (FT/ICR).¹⁰⁴ SWIFT was later applied successfully to the quadrupole ion trap (QIT)^{105, 106} due to the similar principles of operation between the FT/ICR and the QIT. In 1994, Cooks and coworkers¹⁰⁷ made improvements on the application of SWIFT to the QIT for selective isolation by employing a two-stage coarse/fine procedure for isolating ions from a population of trapped ions. The advantage of the procedure was that the coarse step removes most of the ions that contribute to space-charging, and thereafter the frequencies of the analyte ions remain relatively constant.

Ions trapped in a linear ion trap (LIT) are stored radially in the center section of quadrupole rods by a two-dimensional radio frequency (RF) field, and stored axially by stopping

potentials applied to the end sections of quadrupole rods. The quadrupolar field within the mass analyzer has a voltage of constant angular frequency (e.g., $\Omega = 1188$ kHz for the LIT used here) and variable amplitude (0 to 5 kV_{0-p}), which drives ionic motion in both the axial and radial directions. Ionic motion must be stable in both directions for an ion to remain trapped. Trapped ions oscillate in the quadrupolar field with characteristic frequencies known as secular frequencies (ω_n). For a given set of trapping conditions, these frequencies are characteristic of ion mass-to-charge (m/z). By subjecting ions to a signal of frequency equal to a characteristic ion frequency, they can be radially excited and ejected from the ion trap. Secular frequencies (ω_n) are given by Equation 3-1,

$$\omega_n = (2n + \beta) \frac{\Omega}{2} \quad (0 \leq \beta \leq 1) \quad (3-1)$$

where $n = 0, 1, 2, \dots$ etc., Ω is the RF drive frequency, and β is a complex function of the Mathieu parameters a and q , whose solutions classify an ion as stable or unstable.¹⁰⁸ Since DC voltage is not applied to the LIT quadrupole electrodes, $a = 0$ resulting in Equation 3-2.

(3-2)

$$\beta^2 = \frac{q^2}{(2+\beta)^2 - \frac{q^2}{(4+\beta)^2 - \frac{q^2}{(6+\beta)^2 - \frac{q^2}{(8+\beta)^2 - \frac{q^2}{(10+\beta)^2 - \frac{q^2}{(12+\beta)^2}}}} + \frac{q^2}{(\beta-2)^2 - \frac{q^2}{(\beta-4)^2 - \frac{q^2}{(\beta-6)^2 - \frac{q^2}{(\beta-8)^2 - \frac{q^2}{(\beta-10)^2 - \frac{q^2}{(\beta-12)^2}}}}$$

In order to solve for β in Equation 3-2, it is first necessary to solve for the q value for the ion to be isolated. This q value is calculated using Equation 3-3, in which $(m/z)_{\text{center}}$ is the ion placed at the q of isolation (0.83).

$$q = \frac{(m/z)_{\text{center}}(0.83)}{m/z} \quad (3-3)$$

β is then calculated through an iterative process starting with an initial β value given by the Dehmelt's approximation given in Equation 3-4 for q values less than 0.4.

$$\beta \approx \sqrt{\frac{q^2}{2}} \quad (3-4)$$

This chapter introduces the use of a multi-notch SWIFT applied to the linear ion trap mass spectrometer for selectively isolating multiple pairs of analyte and internal standard ions during a single MSⁿ scan to improve precision during MALDI-MSⁿ quantification. A dual-notch SWIFT waveform was optimized for the isolation of cocaine and its metabolite benzoylecgonine along with their corresponding trideuterated analogs.

Experimental

Chemicals

Cocaine (COC; MW 303.4 Da), benzoylecgonine (BE; MW 289.3 Da) were purchased from Cerilliant (Round Rock, TX, USA) at concentrations of 1 mg/mL in acetonitrile. COC-d₃ (MW 306.4 Da, 0.17% d₀) and BE-d₃ (MW 292.3 Da, 0.08% d₀) were also purchased from Cerilliant at concentrations of 100 µg/mL in acetonitrile. High-performance liquid chromatography (HPLC)-grade acetonitrile, methanol, and water were purchased from Fisher Scientific (Pittsburgh, PA, USA). Working standards of COC, COC-d₃, BE, and BE-d₃ were diluted with acetonitrile and then stored at 4 °C. MALDI matrix, 2,5-dihydroxybenzoic acid (DHB; MW 154.1 Da), was purchased from ACROS Organics (Geel, Belgium). Saturated DHB matrix solutions (40 mg/mL DHB) were prepared in methanol/water (70:30, vol/vol) on the day of use.

Tissue Collection

Human brain tissue samples were provided by the El Paso County Coroner's Office in Colorado Springs, CO. Postmortem brain material was excised from the nucleus accumbens

(NAc) from case number 07A-369, whose toxicologic analysis indicated the presence of cocaine in blood at 69 ng/mL (COC concentration in the brain tissue was not quantified). The NAc is a dopamine-rich area of the striatum, which may contain an accumulation of COC due to its affinity to bind with the dopamine transporter.¹⁰⁰ At autopsy, the excised tissue was immediately snap-frozen in liquid nitrogen and then stored in a -80 °C freezer until analyzed.

Tissue Sectioning and Sample Preparation

Frozen brain tissue was cut into thin sections (20 µm thickness) in a cryostat (HM 505E; Microm International GmbH, Waldorf, Germany) at -25 °C. The tissue samples were frozen to the cryostat sample stage using distilled water. Serial brain sections were collected onto microscope slides where they were thaw mounted and then stored at -80 °C. Before mass spectrometric analysis, the tissue sections were removed from the freezer and placed in a vacuum desiccator for 30 min before spiking standards (1-µL droplets by micropipette) and applying MALDI matrix. The matrix was applied to the tissue sections using an artistic airbrush (Aztek A470; Testors, Rockford, IL, USA). The application of MALDI matrix by airbrush has been previously published.⁶⁷

Mass Spectrometry

All experiments were performed using an LTQ linear ion trap with a vMALDI ion source (Thermo Finnigan, San Jose, CA, USA), equipped with nitrogen laser (337 nm) at a frequency of 20 Hz and 100-µm spot size. A more detailed description of this instrument has been published.⁶⁷ The number of laser shots was automatically varied (between 1 and 17 shots) using automatic gain control (AGC) to optimally fill the trap with ions, thus avoiding space charge-related peak broadening and mass shifts. AGC assesses the ion generation rate by use of a

prescan, and then adjusts the number of laser shots per scan to produce an optimal number of ions for each scan. The spectra are normalized to the number of laser shots for each scan.

Resonance excitation is used for isolation, activation and mass analysis. For MSⁿ experiments, unwanted ions are resonantly ejected from the ion trap by applying a 5-500 kHz multi-frequency isolation waveform consisting of sine components spaced every 0.5 kHz. The ions of interest are isolated in the ion trap by removing sine components from the isolation waveform that correspond to the secular frequency of the desired ions. Ions to be isolated are selected in the LTQ software by entering the m/z with its IW. The mass range for the ion is defined as $(m/z - IW/2)$ to $(m/z + IW/2)$. The IW should be narrow enough to eliminate interfering peaks, but wide enough to avoid loss of sensitivity for the desired ions. However, it is important to note that the activation width for resonance excitation (CID) has the same value as the IW. Therefore, the collision energy applied during MSⁿ is spread over the activation width. Thus, increasing the IW decreases the collision energy for each ion.

SWIFT Calculation

Inverse Fourier Transform

A computer program written in C⁺⁺ was used to calculate the SWIFT waveform based on a process previously described.¹⁰⁶ Notches in the desired broadband magnitude spectrum, from frequency 0 to 500 kHz, were calculated to have centers corresponding to the secular frequencies of the ions to be isolated. The frequency spectrum was then transformed to the time domain using the inverse Fourier transform (IFT), which was performed using an adaptation of the Cooley-Tukey fast Fourier transform (FFT) algorithm.¹⁰⁹ The algorithm generates output, which must be midpoint reflected about the N/2 axis, where N equals the total number of points in the SWIFT waveform. This step is similar to a time shift and therefore affects the phase, but not the magnitude of the corresponding frequency-domain spectrum. The advantage of midpoint

reflection is that it avoids sudden voltage transients at the beginning and end of the excitation period.

Quadratic Phase Modulation

Phase modulation of the frequency spectrum is necessary in order to reduce the dynamic range of the time-domain waveform. The large dynamic range is caused by all of the specified frequency components starting with the same phase at time zero. A nonlinear phase modulation varies the phase continuously at a nonconstant rate with frequency, and results in a broader time-domain waveform after IFT that requires less amplitude to achieve the same power. The real, R_i , and imaginary, I_i , components are created from the magnitude data, Mag_i , using the following relationship:

$$\begin{aligned} R_i &= Mag_i \cos \varphi_i \\ I_i &= Mag_i \sin \varphi_i \end{aligned} \quad (3-5)$$

Where the phase, φ_i , varies quadratically with frequency:

$$\varphi_i = \varphi_0 + Ji + (K/2)i^2 \quad (3-6)$$

Here φ_0 is the initial phase (zero), i is the frequency index, and $J = 0.5\pi$ and $K = -\pi/N$ are the quadratic terms, where N is the number of nonzero data points in the frequency spectrum.

Values of J and K are chosen to satisfy the Nyquist criterion, such that the rate of phase change per frequency-domain data point is kept at half the Nyquist limit (π) or below, which removes nonuniformity of the magnitude in the frequency-domain.¹¹⁰

Temporal Spectral Inhomogeneity

It has been shown previously that quadratic phase modulation is effective at obtaining a more uniform excitation power spectrum.¹¹¹ However, an undesirable consequence of phase modulation is temporal spectral inhomogeneity. This means that SWIFT is essentially a frequency scan in which the frequency content is localized in time and varies systematically with

time. Figure 3-1a shows the time domain of a dual-notch SWIFT waveform with frequency notches corresponding to the secular frequencies of the $[M+H]^+$ ions of COC (m/z 304.25) and COC-d₃ (m/z 307.25). Figure 3-1b is the resulting frequency domain waveform after performing fast Fourier transform (FFT) of the time-domain waveform in Figure 3-1a. The two frequency notches are 1.6-Da wide at 431.88477 – 436.27930 kHz and 439.69727 – 444.33594 kHz. FFT of the first half (0 to 2047 μ s) of the time-domain waveform in Figure 3-1a is shown in Figure 3-1c and the FFT of the second half (2048 to 4096 μ s) of the waveform is shown in Figure 3-1d. The resulting frequency-domain spectra shown in Figures 3-1c and 3-1d illustrate that the SWIFT waveform scans from high to low frequency and that the frequency content is localized in time. Thus, ions of different m/z are excited at different times during the SWIFT waveform. This may not be such a critical issue for the FT-ICR, for which SWIFT was originally designed, but it is undesirable for LIT experiments, since many collisions with helium buffer gas (\sim 1 mTorr) occur during the excitation event. For the LIT, it is therefore desirable to excite ions of all desired m/z values simultaneously.

Three solutions were previously published¹¹² for correcting or minimizing the temporal spectral inhomogeneity of SWIFT. One solution involves using a short-duration (lower-resolution) SWIFT waveform that is repeated many times during the excitation event, which serves to increase the number of times a specific frequency is represented in the time domain during the excitation event; however, this leads to lower mass selectivity due to the lower-resolution SWIFT waveform. A second approach (multiple foldovers) involves overmodulation of the phase in which the quadratic term in the phase vs. frequency spectrum corresponds to a bandwidth multiple times (number of foldovers) higher than the Nyquist limit. If the foldover number is sufficiently high, then the SWIFT waveform effectively excites all frequency

components simultaneously. A third approach is to distribute the excitation frequency components randomly throughout the time-domain excitation period, which has been previously termed “filtered noise field” excitation.¹¹³

Apodization

The time-domain SWIFT waveform was multiplied by an apodization (smoothing) function to force the time-domain signal smoothly to zero at the beginning and end of the time-domain period. The apodization function consists of a quarter-wave sinusoid matched to the first one-fourth of the time-domain period, followed by unit weighting for the middle half period, followed by a quarter-wave sinusoid for the final one-fourth of the period.

It was previously shown¹¹⁴ that apodization can cause frequency notch distortion, which may lead to partial ejection of ions selected to be isolated. Multiplication of the apodizing function with the time-domain waveform corresponds to convolution of the Fourier transforms in the frequency domain. The process of convolution widens the bases of the spectral components, which may lead to power leakage into adjacent spectral components and loss of frequency resolution. Notched waveforms ideally represent discontinuities in the waveform; however, the process of apodization transforms these discontinuities or sharp edges of the notch into continuous transitions. Thus, the edges of a narrow notch may fuse into each other, thereby bridging the notch to some extent.

Figure 3-2a compares the time domain of a dual-notch SWIFT waveform that has been apodized (blue) with one that has not been apodized (red). It is shown that the apodization function only reduces the magnitude of the Gibb’s oscillations (spurious oscillations that occur when using a truncated Fourier series)¹¹⁵ for the first 700 μ s of the time-domain waveform, and only the magnitude of the first 200 μ s have been significantly smoothed to nearly zero. Figure 3-

2b compares the frequency domain of the dual-notch SWIFT waveform that has been apodized (blue) with one that has not been apodized (red). Apodization of the time domain results in convolution of the edges of the frequency notches in the frequency domain, which could lead to ejection of ions that are intended to be isolated.

SWIFT Application to LTQ

The non-apodized, time-domain, dual-notch SWIFT waveform was downloaded to the memory of an arbitrary waveform generator (AWG) (Stanford Research Systems Model DS345, Sunnyvale, CA, USA). The AWG has a maximum sampling rate of 40 MHz, time resolution of 16,300 data points, and a 12-bit DAC output. The LTQ has a programmable trigger that can be used to send a TTL pulse to the AWG at a specific time during the experimental sequence (e.g., isolation or activation). For experiments in which the AWG was triggered during isolation, the LTQ isolation waveform was turned off to avoid interference. Once triggered, the AWG applies the SWIFT waveform to the LTQ analog board, where it is summed with the other waveforms before being amplified and applied to the linear ion trap x-rods. The amplitude of the SWIFT waveform and the number of bursts were modified manually on the AWG. A two-channel digitizing oscilloscope (Tektronix Model TDS 540, Tektronix Inc., Beaverton, OR) was used to observe the SWIFT waveform.

Results and Discussion

Optimization of a Dual-Notch SWIFT

Frequency optimization

A 4096-point (4k) dual-notch SWIFT was calculated from frequency 0 to 500 kHz with a sampling frequency of 1000 kHz corresponding to a 0.244 kHz frequency step. Frequency notches (1.6-Da wide) are centered at the secular frequencies of the $[M+H]^+$ ion of COC (m/z 304.25) and COC-d₃ (m/z 307.25). The theoretical secular frequencies (ω) were calculated by

first calculating the q values for the ions using Equation 3-3 and the β values using Equation 3-2. Both q and β were then used to calculate the corresponding secular frequencies using Equation 3-1.

Experimental secular frequencies can shift from the theoretical secular frequencies calculated due to space-charge (shift to lower frequencies), higher-order fields, and resonance excitation amplitude (shift to higher frequencies).^{114, 116} A 1:1 solution of 1 $\mu\text{g/mL}$ of COC and COC- d_3 were spotted (1 μL each) onto a MALDI plate and airbrushed with DHB matrix for analysis. A dual-notch SWIFT waveform with 1.6-Da wide frequency notches centered at the theoretically calculated secular frequencies of m/z 304 and m/z 307 was applied to the LTQ with a SWIFT amplitude of $0.4 V_{p-p}$, and a burst count of 3 set by the AWG. The center m/z 305.8 was placed at a $q = 0.83$. The LTQ isolation waveform was turned off and the SWIFT waveform was triggered at isolation. The frequency notches for m/z 304 and m/z 307 were optimized separately for maximum peak intensity by shifting the 1.6-Da window to higher frequencies a number of frequency steps (0.244 kHz) from the starting position at a frequency lower than the theoretically calculated secular frequency (Figure 3-3). The frequency notches were shifted by recalculating the SWIFT waveform after each change of frequencies. The optimal frequency notches for m/z 304 and m/z 307 was 439.69727 – 444.33594 kHz and 431.88477 – 436.27930 kHz, respectively. This corresponds to a shift to higher frequencies for m/z 304 (+ 0.488 kHz) and m/z 307 (+ 0.732 kHz), which may be due to the amplitude of the SWIFT waveform applied.¹¹⁶

Burst count optimization

Increasing the number of SWIFT frequency-domain points lengthens the duration of the time-domain SWIFT waveform. However, the duration of the SWIFT pulse is limited by the

size of the stored-waveform data set. The AWG used for the experiments in this paper has a data point storage limit of 16,300 points. It would be ideal to apply the SWIFT waveform during the entire isolation event in order to maximize the opportunity for selective ejection of unwanted ions that are in resonance with the frequencies of the SWIFT pulse. The problem with a short SWIFT pulse duration can be overcome by applying multiple pulses (or bursts) of the same stored waveform in a series (or train). This allows the specific frequencies of the SWIFT waveform to be present for longer periods of time, which can lead to more efficient ejection of selected ions. The number of SWIFT waveform bursts in a train that are applied to the LTQ can be controlled by the AWG.

Figure 4a shows the digital scope image of a 1-burst (4.096 ms), 2-burst (8.192 ms), 3-burst (12.288 ms), 4-burst (16.384 ms), and 5-burst (20.480 ms) train of pulses shown above the digital scope image of the square-wave trigger during isolation (15.5 ms). Each SWIFT pulse in a train is the same dual-notch SWIFT waveform (frequency optimized to isolate ions at m/z 304 and m/z 307) that has been merely repeated. Each train of SWIFT bursts were applied five times individually to a 1:1 solution of COC and COC- d_3 (1 $\mu\text{g/mL}$ each) pipetted onto a MALDI plate and airbrushed with DHB matrix. Figure 3-4b shows the changes in absolute peak intensities for m/z 304 and m/z 307 with varying number of SWIFT bursts. Not shown, but also monitored, were the absolute peak intensities of the background ions at m/z 305, 306, and 308. From 1 to 3 bursts, there was a 12% and 14% decrease in signal for m/z 304 and 307, respectively. The signals for the background ions at m/z 305, 306, and 308 decreased by 69%, 59%, and 87%, respectively, from 1 to 3 bursts. At 4 bursts, the intensities of the ions at m/z 304 and 307 decreased by 39% and 49%, respectively. This significant decrease in ion signal may be attributed to the longer duration of the 4-burst train (16.384 ms) compared to the duration of the

isolation event (15.5 ms). The ions may not have enough time to relax towards the center of the LIT before they are moved from the q of isolation (0.83) to a lower q of activation (0.25). There is ~ 2 ms pause after the isolation event before the RF voltage is decreased to move the ions towards the lower q of activation. At 5 bursts (20.480 ms), all ions were ejected. The optimal number of SWIFT bursts was determined to be 3, since there was not a significant decrease in the signal intensity of m/z 304 and 307, and signal intensities of the background ions at m/z 305, 306, and 308 were reduced to below 3% intensity relative to the m/z 304 and 307 at 3 bursts.

Amplitude optimization

Another SWIFT parameter besides the duration of the SWIFT pulse that can affect the ejections of ions is the amplitude. Increasing the amplitude of the SWIFT waveform in turn increases the magnitude of the oscillations of the ions that are in resonance with the frequencies. It has also been reported that large amplitudes distort the frequency-domain cutoffs, causing the pulse to have an even wider frequency range, which can interfere with ions close in mass.¹⁰⁶ The secular frequencies of ions can shift to higher values with increased excitation amplitude, resulting in ions absorbing energy in a range near their secular frequency and being unintentionally ejected from the ion trap.

The amplitude of a dual-notch SWIFT waveform with a 3-burst train was optimized by varying the amplitude on the AWG from 0 to 1.0 V_{p-p} and monitoring the peak intensity of m/z 304 and m/z 307. A 1:1 solution of COC and COC- d_3 (1 $\mu\text{g/mL}$ each) was pipetted (1 μL) onto a MALDI plate and airbrushed with DHB matrix. Figure 3-5 shows the absolute peak intensities of the $[M+H]^+$ ions of COC (m/z 304) and COC- d_3 (m/z 307) along with the ^{13}C isotope ions at m/z 305 and 308. The optimal SWIFT amplitude (0.40 V_{p-p}) was determined to be the lowest potential needed to maintain a 1:1 signal of COC and COC- d_3 , while decreasing the background

ions below 3% relative intensity, and the maximum signal for the m/z 304 and 307 ions. Notice that at higher amplitudes above $0.50 V_{p-p}$, more m/z 304 ions are ejected than m/z 307 ions. This may be attributed to m/z 304 being at higher q , closer to the right-hand edge of the stability diagram.

Selective Ion Isolation of Standards on MALDI Plate

The optimized dual-notch SWIFT was applied to COC and COC- d_3 at 1 $\mu\text{g/mL}$ each pipetted onto a MALDI plate and airbrushed with DHB matrix. The amplitude on the AWG was set to $0.4 V_{p-p}$ with a burst count of 3. Figure 3-6a compares the full scan mass spectrum (top), a mass spectrum of a 5-Da wide isolation window centered at m/z 305.8 (middle), and the mass spectrum from the application of the optimized dual-notch SWIFT (bottom). The 5-Da wide isolation window is effective at eliminating the background ions outside the window, but retains ions at m/z 305 and 306. The dual-notch SWIFT (bottom) is able to eliminate the same background ions as well as reduce the ion intensities for m/z 305 and 306 without reducing the signal for the desired ions at m/z 304 and 307. Figure 3-6b shows the MS^2 scans resulting from applying a 5-Da wide broadband excitation waveform ($CID = 55$) to the isolated ions from the 5-Da wide isolation (top) and the dual-notch SWIFT isolation (bottom). The MS^2 scan of the isolated SWIFT ions (bottom) resulted in no background fragment ions in the product spectrum. The only ions present are the fragment ions of m/z 304 and 307 at m/z 182 and 185, respectively, both formed from the neutral loss of benzoic acid. In comparison, the product spectrum of the ions isolated with the 5-Da wide isolation window (top), shows the presence of fragment ions from the background as well as those from m/z 304 and 307.

Improving MALDI Precision with SWIFT

It was previously shown that isolating the analyte and internal standard ions in a single MS^n scan using a wide isolation window can improve precision for MALDI quantification

compared to isolating the analyte and internal standard ions separately during alternate MSⁿ scans.¹⁰³ In order to compare the ability of a dual-notch SWIFT waveform to also improve precision for MALDI quantification, five solutions (31, 62, 125, 250, and 500 ng/mL COC with 250 ng/mL COC-d₃) were pipetted onto a MALDI plate and airbrushed with DHB matrix. The peak intensity of *m/z* 182 and *m/z* 185 were ratioed from three different MS² experiments (CID = 55): alternating scans (MS² of *m/z* 304 and *m/z* 307 during separate scans), MS² of *m/z* 304 and *m/z* 307 during a single scan isolated by a dual-notch SWIFT, and during a single MS² scan isolated by a 5-Da window. The 5-Da wide isolation experiment had the best precision (% RSD = 1 to 9%) for isotopic ratios, followed by dual-notch SWIFT (% RSD = 5 to 23%), and then alternating MS² scans (% RSD = 44 to 56%). This reinforces the conclusion¹⁰³ that isolating the analyte and internal standard ions during a single MSⁿ scan improves precision over isolating the analyte and internal standard ions during separate scans. The dual-notch SWIFT isolation may be less precise than wide-isolation due to irreproducible shifts in the secular frequencies of the analyte and internal standard ions, which leads to their ejection.

Although SWIFT isolation may be less precise of a method for MALDI quantification than wide isolation, the major advantage of SWIFT is that it can selectively isolate multiple ions or *m/z* ranges. This is done simply by removing the appropriate frequencies from the SWIFT waveform corresponding to the secular frequencies of the desired ions. A quad-notch SWIFT was calculated with frequency notches (1.5-Da wide) corresponding to the secular frequencies of the [M+H]⁺ ions of BE (*m/z* 290.25), BE-d₃ (*m/z* 293.25), COC (*m/z* 304.25), and COC-d₃ (*m/z* 307.25). The quad-notch SWIFT was applied to a solution of BE, BE-d₃, COC, and COC-d₃ at 1 µg/mL each that was pipette (1 µL) onto a MALDI plate and then airbrushed with DHB matrix. Figure 3-8a compares the full scan mass spectrum (top), the mass spectrum from a 20-Da wide

isolation window centered at m/z 298.75 (middle), and the mass spectrum from applying a quad-notch SWIFT (bottom). The 20-Da wide isolation (middle) was effective at eliminating background ions outside the isolation window, but because of the large width of the isolation window necessary to isolate all of the analyte and internal standard ions present, many undesired background ions were isolated as well. The intensities of the ions isolated by the quad-notch SWIFT (bottom) were lower than the intensities of the same ions isolated by a 20-Da wide isolation window centered at m/z 298.75, but the quad-notch SWIFT was able to significantly reduce the intensities of the background ions, which should help to simplify the product spectra from MS² analysis.

Figure 3-8b shows the MS² scans from applying a 20-Da broadband excitation (CID = 55) to the ions isolated from the 20-Da wide isolation (top) and a quad-notch SWIFT (bottom). The product ion spectrum of the quad-notch SWIFT isolation (bottom) shows the presence of the product ions of m/z 290, 293, 304, and 307 at m/z 168, 171, 182, and 185, respectively, formed from the neutral loss of benzoic acid. Also present is the common fragment ion of both m/z 290 and 304 at m/z 150 (neutral loss of benzoic acid and methanol) and the common fragment ion of m/z 293 and 307 at m/z 153 (neutral loss of benzoic acid and methanol). The quad-notch SWIFT was able to reduce background ions during isolation, which resulted in the elimination of ¹³C peaks and MALDI matrix ions (e.g., m/z 137, [DHB-H₂O+H]⁺) from the product ion spectrum that are present in the product ion spectrum from the 20-Da wide isolation (top).

Selective Ion Isolation of Standards on Tissue

The quad-notch SWIFT was applied to 20- μ m thick human brain tissue that was spiked (1 μ L on top of tissue) with BE, BE-d₃, COC, and COC-d₃ at 1 μ g/mL each and then airbrushed with DHB matrix. Figure 3-9a shows that the full mass spectrum is dominated by lipid and DHB

matrix ions and it is difficult to see the target ions at m/z 290, 293, 304, and 307. Figure 3-9b shows an expanded view of the mass range from m/z 250 to 350 with the full scan mass spectrum (top), mass spectrum from a 20-Da wide isolation centered at m/z 298.75 (middle), and the mass spectrum resulting from the application of a the quad-notch SWIFT (bottom). The 20-Da wide isolation window (middle) isolates the $[M+H]^+$ ions of BE, BE-d₃, COC, and COC-d₃ at m/z 290, 293, 304, and 307, respectively, as well as a number of background ions. The quad-notch SWIFT (bottom) was successful in eliminating or reducing the background ions during isolation of the analyte and internal standard ions.

Conclusions

It was previously shown that isolating the analyte and internal standard ions during a single MS² scan using a wide isolation window can provide improved precision for the quantitative analysis of COC in postmortem brain tissue compared to using two alternating MS² scans that isolate the analyte and internal standard ions separately.¹⁰³ Here, multi-notch SWIFT waveforms were investigated as an alternative isolation technique to wide isolation for isolating the analyte and internal standard ions during a single MS² scan for improved MALDI-MS² precision. It was determined that multi-notch SWIFT isolation can provide improved precision when compared to using two alternating MS² scans; however, it is not as precise as the wide isolation method.

Nevertheless, SWIFT isolation offers the advantage of higher selectivity and is better able to reduce background ions that may complicate or interfere with MS² analysis (e.g., isobaric product ions). Also, analysis times can be reduced as more frequency notches are added to the SWIFT waveform. This can become very important when quantitatively imaging several analytes from a large tissue sample.

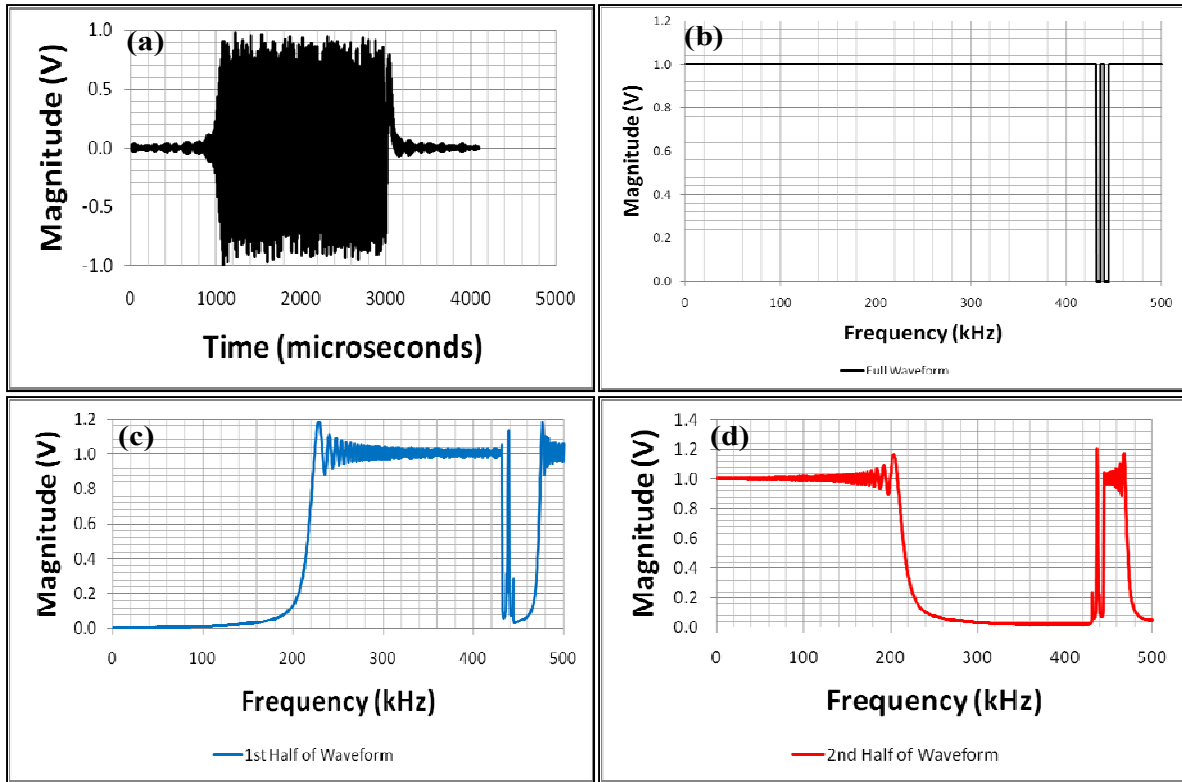


Figure 3-1. Temporal spectral inhomogeneity of SWIFT. (a) Time domain of dual-notch SWIFT waveform calculated by inverse Fourier transform (IFT) of the frequency domain. (b) Fast Fourier transform (FFT) of the full (0 to 4096 μs) time-domain SWIFT waveform. (c) FFT of the first half (0 to 2047 μs) of the time-domain SWIFT waveform. (d) FFT of the second half (2048 to 4096 μs) of the time-domain SWIFT waveform.

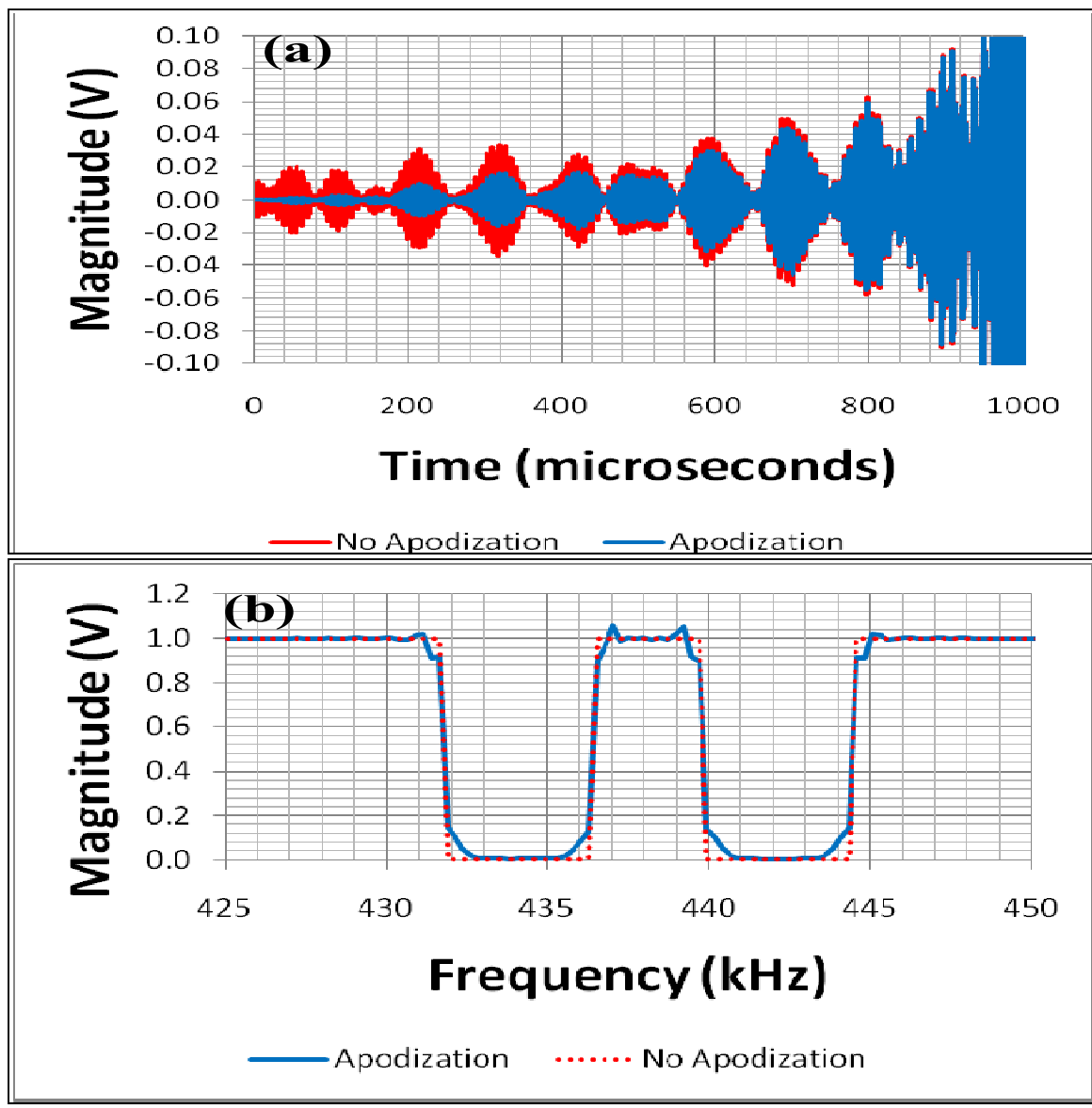


Figure 3-2. Effects of apodization on SWIFT. (a) Time domain of dual-notch SWIFT waveform that has been apodized (blue) overlapped with the time domain of the same dual-notch SWIFT waveform without apodization (red). (b) Comparing the frequency domain of a dual-notch SWIFT waveform with apodization (blue) and without apodization (red).

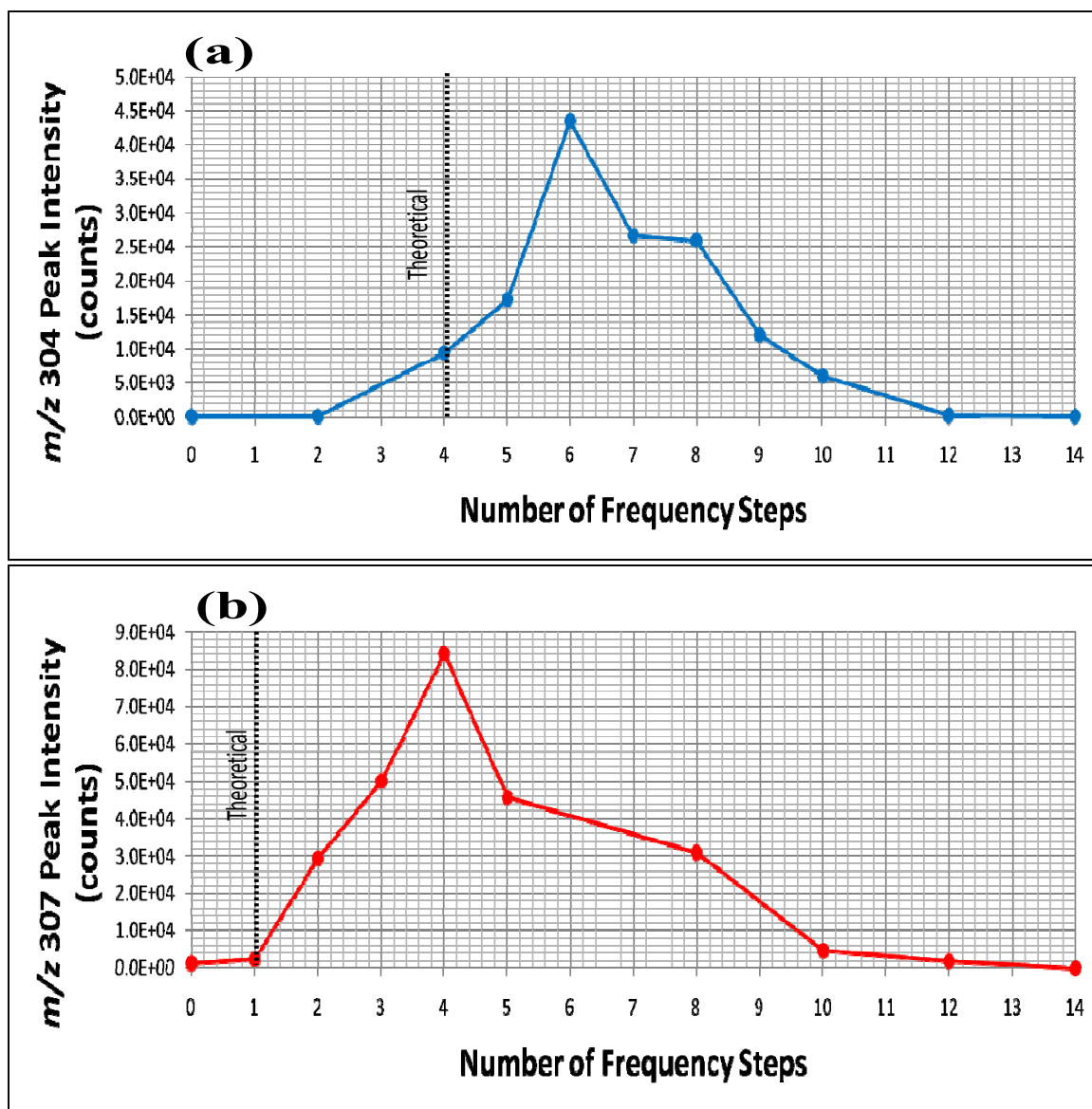


Figure 3-3. Optimization of frequency notches (1.6-Da) for (a) m/z 304 and (b) m/z 307. Frequency notches were shifted to higher frequencies a number of frequency steps (0.244 kHz) from the starting position to maximize the peak intensities of m/z 304 and m/z 307. The optimal frequency notches for m/z 304 and m/z 307 were 439.69727 – 444.33594 kHz and 431.88477 – 436.27930 kHz, respectively.

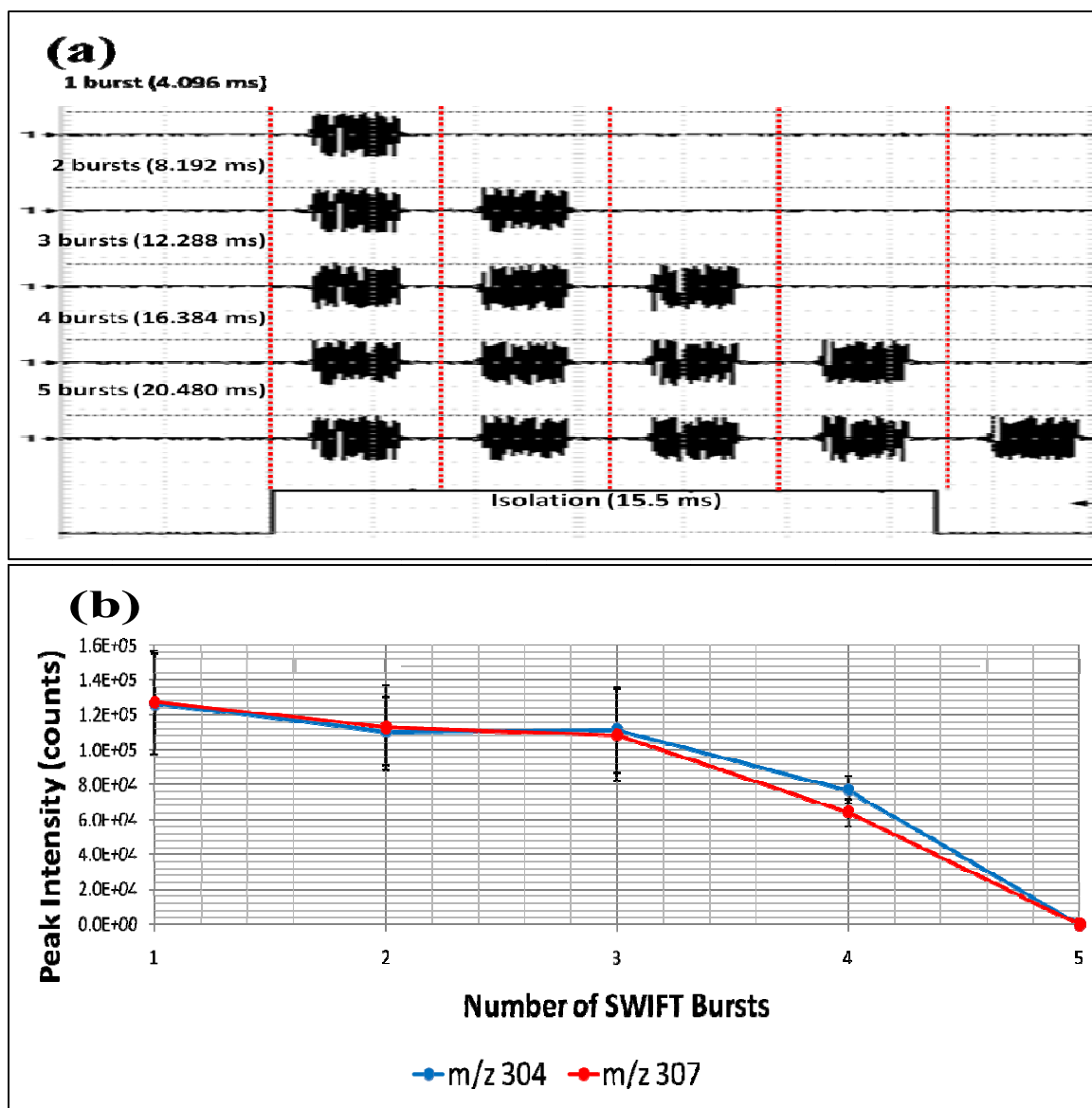


Figure 3-4. Optimization of burst counts for a dual-notch SWIFT waveform. (a) Digital scope images of a 1 burst (4.096 ms), 2 burst (8.192 ms), 3 burst (12.288 ms), 4 burst (16.384 ms), and 5 burst (20.480 ms) train of pulses shown above the digital scope image of the square-wave trigger during isolation (15.5 ms). (b) The average absolute peak intensities of the $[M+H]^+$ ion of COC (m/z 304) and COC- d_3 (m/z 307) plotted versus the number of SWIFT bursts of a dual-notch SWIFT applied during isolation. The error bars correspond to \pm the standard error (5 replicates).

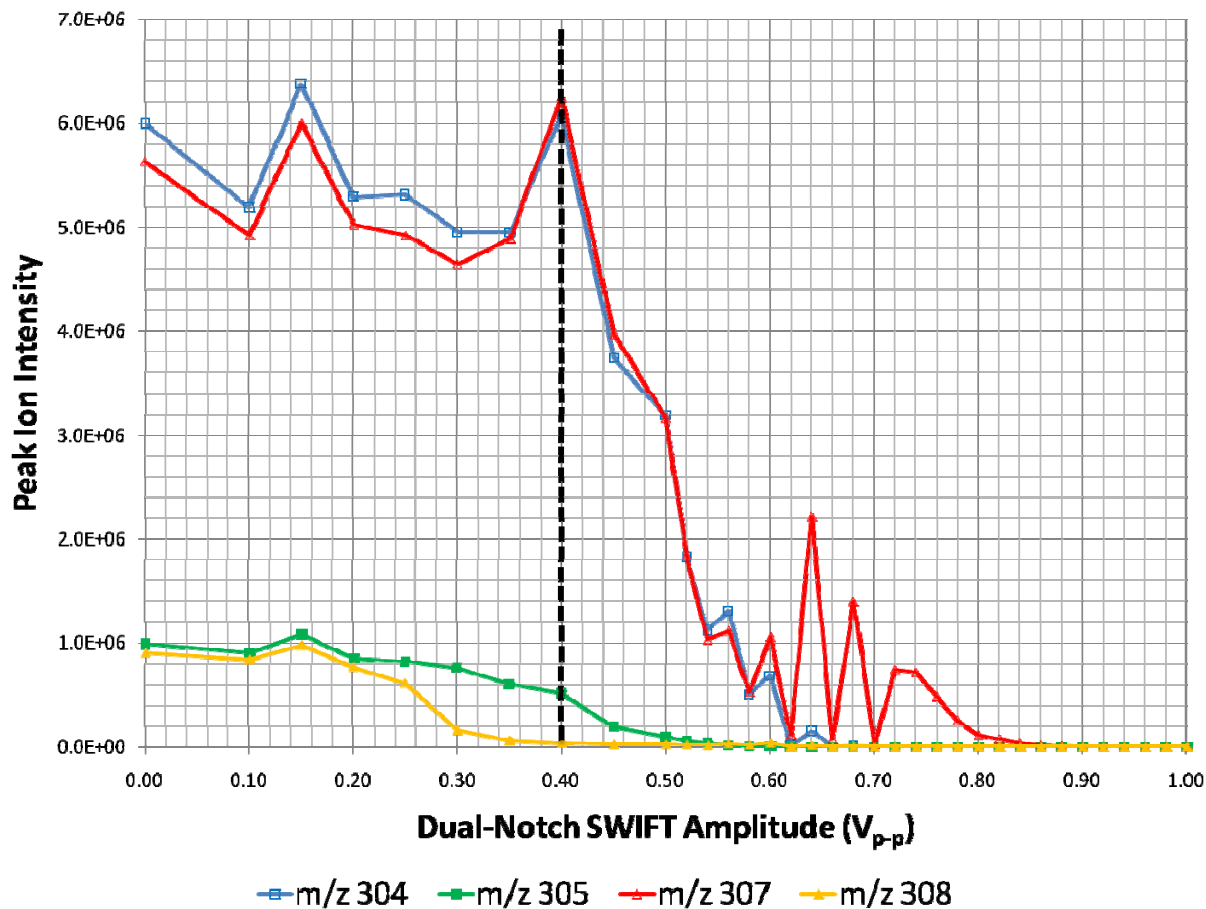


Figure 3-5. Optimization of SWIFT amplitude for a dual-notch SWIFT waveform. SWIFT amplitude was optimized by varying the potential from 0 to 1.0 V_{p-p} and monitoring the absolute peak intensities of the [M+H]⁺ ions of COC (*m/z* 304) and COC-d₃ (*m/z* 307) along with the ions of their corresponding ¹³C isotopic peaks at *m/z* 305 and *m/z* 308. The optimal SWIFT amplitude (0.40 V_{p-p}) was the lowest potential needed to maintain a 1:1 signal of COC and COC-d₃ (1 μg/mL each) that were pipetted (1 μL) onto a MALDI plate and airbrushed with DHB matrix.

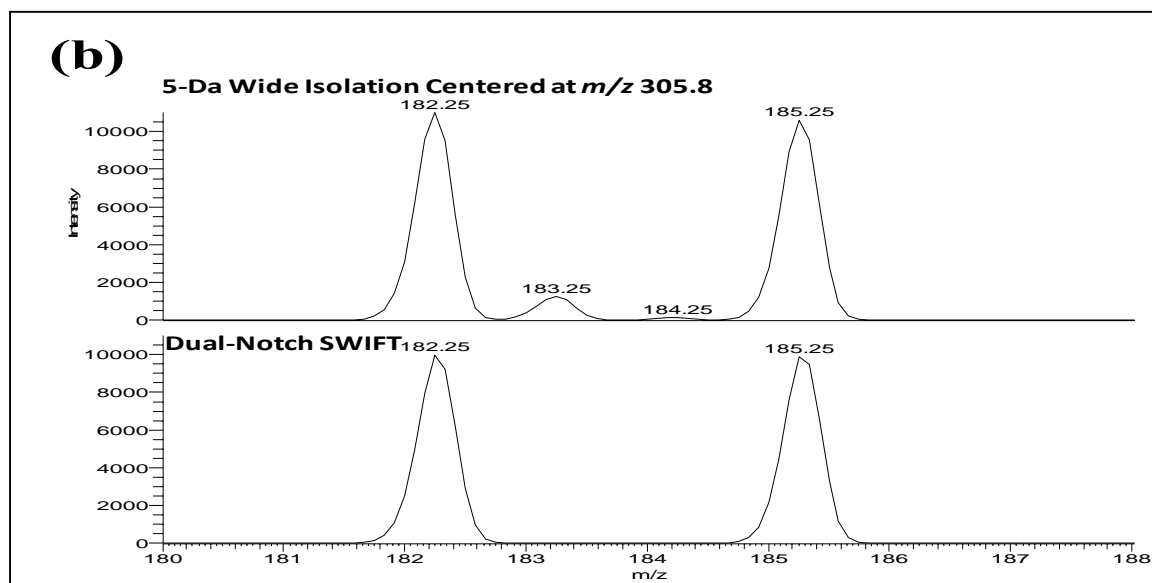
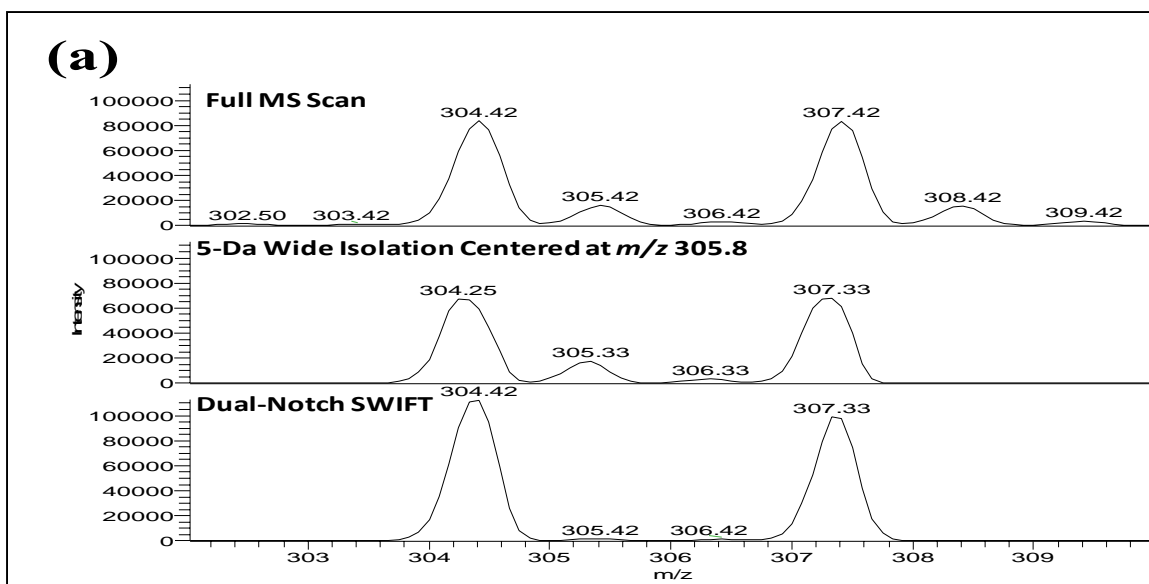


Figure 3-6. SWIFT isolation and wide isolation comparison. (a) Comparing full scan (top), 5-Da wide isolation window centered at m/z 305.8 (middle), and dual-notch SWIFT (bottom) of a 1:1 solution of COC and COC- d_3 (1 $\mu\text{g}/\text{mL}$ each) that was pipetted onto a MALDI plate (1 μL) and airbrushed with DHB matrix. (b) Comparing the MS² scan of ions fragmented with a 5-Da broadband excitation waveform (CID = 55) applied to ions isolated with a 5-Da wide isolation window centered at m/z 305.8 (top) and ions isolated with a dual-notch SWIFT waveform (bottom).

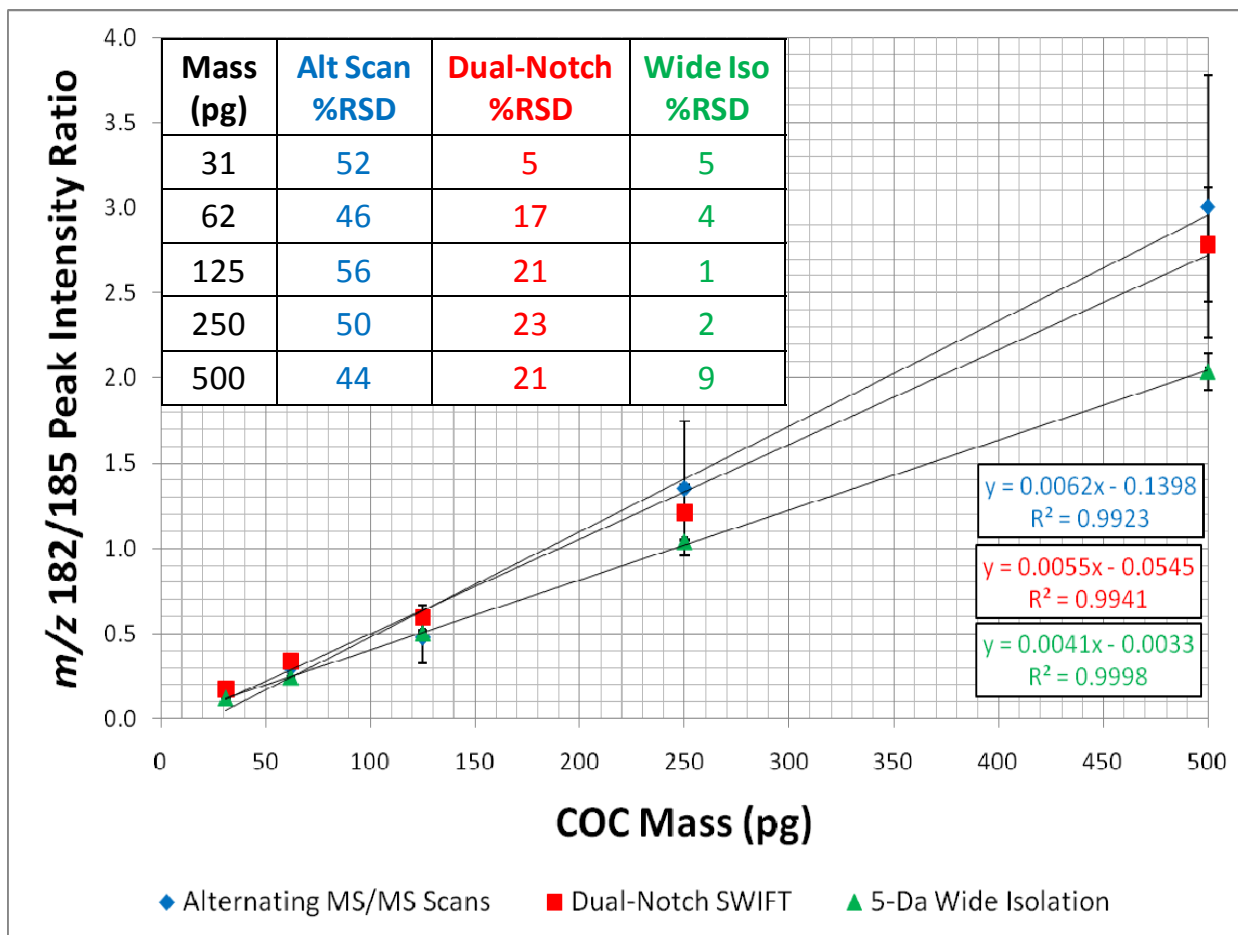


Figure 3-7. SWIFT isolation and wide isolation calibration curves. Five solutions (31, 62, 125, 250, and 500 ng/mL COC with 250 ng/mL COC-d₃) were pipetted onto a MALDI plate (1 μ L each) and airbrushed with DHB matrix. The peak intensity of *m/z* 182 and *m/z* 185 were ratioed from three different MS² experiments (CID = 55): alternating scans (MS² of *m/z* 304 and *m/z* 307 during separate scans), MS² of *m/z* 304 and *m/z* 307 during a single scan isolated by a dual-notch SWIFT and during a single MS² scan isolated by a 5-Da window. The error bars correspond to \pm the standard error (3 replicates).

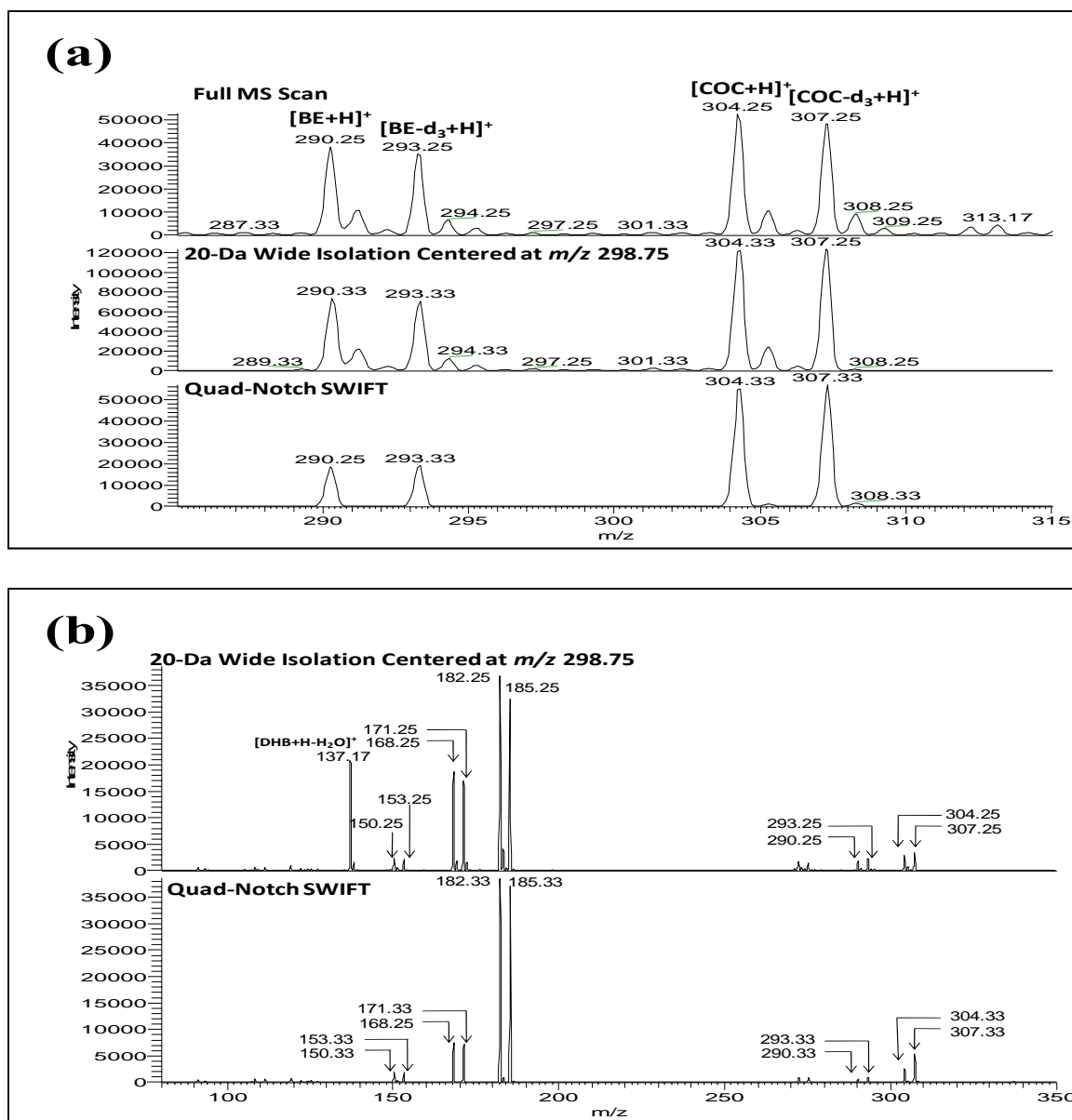


Figure 3-8. Quad-notch SWIFT isolation of standards on MALDI plate. (a) Comparing full scan (top), 20-Da wide isolation window centered at m/z 298.75 (middle), and quad-notch SWIFT (bottom) of a solution of BE, BE-d₃, COC, and COC-d₃ at 1 $\mu\text{g}/\text{mL}$ each that was pipetted (1 μL) onto a MALDI plate and then airbrushed with DHB matrix. (b) Comparing the MS² scan of ions fragmented with a 20-Da broadband excitation waveform (CID = 55) applied to ions isolated with a 20-Da wide isolation window centered at m/z 298.75 (top) and ions isolated with a quad-notch SWIFT waveform (bottom).

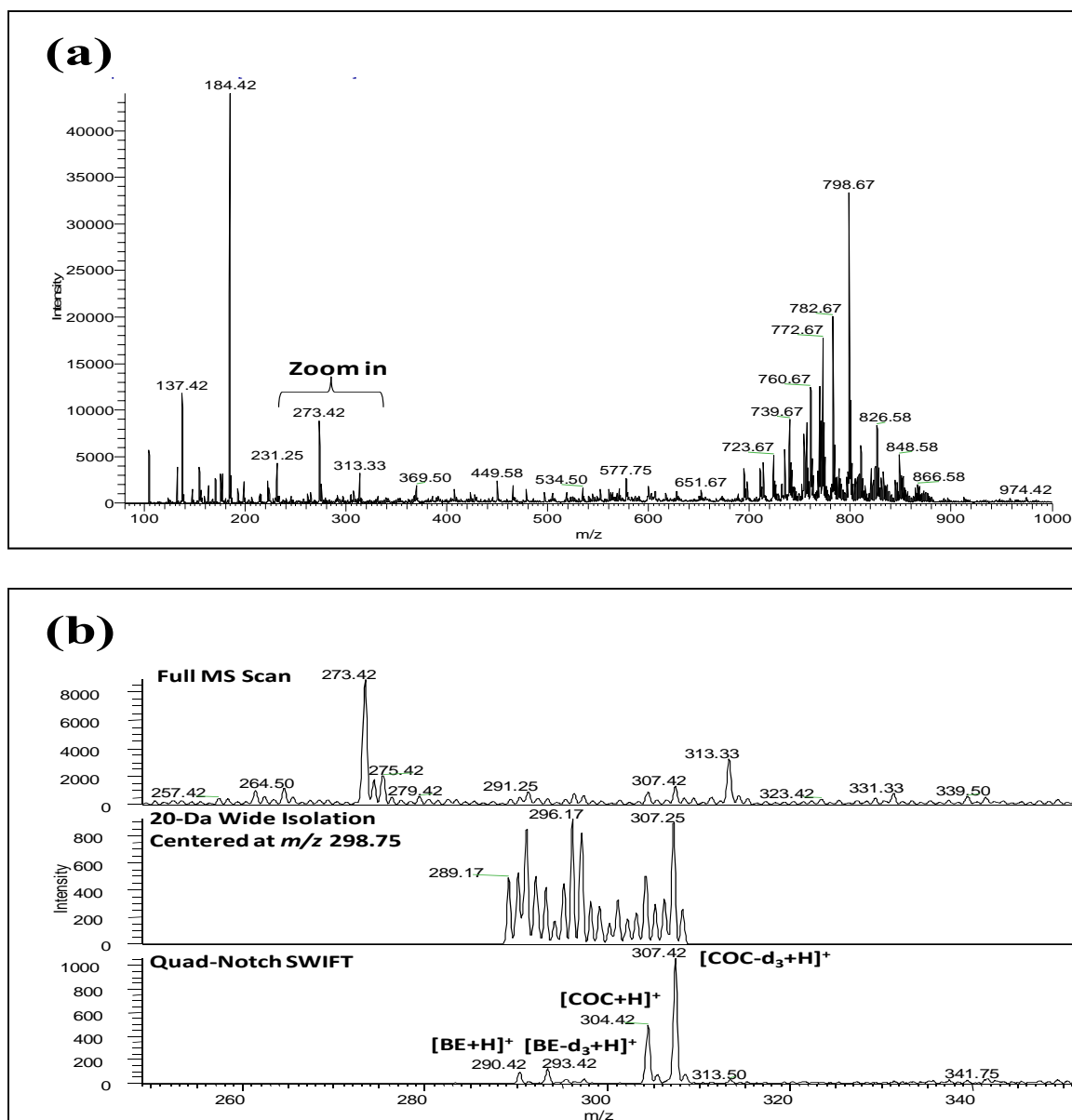


Figure 3-9. Quad-notch SWIFT isolation of standards on brain tissue. (a) Mass spectrum of 20- μ m thick brain tissue slice that was spiked (1 μ L) with a solution of BE, BE- d_3 , COC, and COC- d_3 at 1 μ g/mL each and airbrushed with DHB matrix. (b) Expanded region (m/z 250 – 350) comparing full scan (top), 20-Da wide isolation window centered at m/z 298.75 (middle), and quad-notch SWIFT (bottom).

CHAPTER 4 QUANTITATIVE ANALYSIS OF DRUGS IN BRAIN TISSUE

Introduction

A large variety of specimens are collected in the field of postmortem forensic toxicology including blood, liver, brain, and urine.⁴ For the analysis of drugs of abuse, brain samples show several advantages over all other specimens in postmortem forensic toxicology.⁵ One advantage is due to the brain being an isolated compartment, which delays putrefaction after death.⁶ Also, the metabolic activity is lower in the brain than in other tissues or in blood, resulting in slower decomposition.⁷ Finally, drugs of abuse establish their effects through the central nervous system. Therefore, it can be assumed that concentrations of drugs of abuse found in the brain better reflect drug concentrations at their site of action at the time of death.⁸

Analysis of drugs of abuse in the brain has applications in forensic and postmortem toxicology. Drug concentrations in the brain may be needed to substantiate fatal overdoses⁹ and support neurotoxicity studies.¹⁰ Direct measurement of drug and metabolite concentrations in discrete brain regions can also be used to study the mechanisms of drug action,¹¹ regional distribution,¹² and preferential accumulation of drugs.¹³

Conventional drug analysis in tissue involves tissue homogenization of the tissue prior to subsequent chromatographic analysis.¹⁴ Such sample pretreatments are known to introduce variation in detection due to inhomogeneity of the analyte within the sample matrix.¹⁵ Also, homogenization of tissue eliminates the opportunity to acquire detailed anatomical and histological information for *in situ* drug distribution. Imaging techniques that include mass spectrometric imaging can help provide this information.

Experimental

Chemicals

Cocaine (COC; MW 303.4 Da), benzoylecgonine (BE; MW 289.3 Da), and cocaethylene (CE; MW 317.4 Da) were purchased from Cerilliant (Round Rock, TX, USA) at concentrations of 1 mg/mL in acetonitrile. COC-d₃ (MW 306.4 Da, 0.17% d₀), BE-d₃ (MW 292.3 Da, 0.08% d₀), and CE-d₃ (MW 320.4 Da 0.15% d₀) were also purchased from Cerilliant at concentrations of 100 µg/mL in acetonitrile. High-performance liquid chromatography (HPLC)-grade acetonitrile, methanol, and water were purchased from Fisher Scientific (Pittsburgh, PA, USA). Working standards of COC, COC-d₃, BE, BE-d₃, CE, and CE-d₃ were diluted with acetonitrile and then stored at 4 °C. MALDI matrix, 2,5-dihydroxybenzoic acid (DHB; MW 154.1 Da), was purchased from ACROS Organics (Geel, Belgium). Saturated DHB matrix solutions (40 mg/mL DHB) were prepared in methanol/water (70:30, vol/vol) on the day of use.

Tissue Collection

Human brain tissue samples were provided by the El Paso County Coroner's Office in Colorado Springs, CO. Postmortem brain material was excised from the nucleus accumbens (NAc) from case number 07A-369, whose toxicologic analysis indicated the presence of cocaine in blood at 69 ng/mL (COC concentration in the brain tissue was not quantified). The NAc is a dopamine-rich area of the striatum, which may contain an accumulation of COC due to its affinity to bind with the dopamine transporter.¹⁰⁰ At autopsy, the excised tissue was immediately snap-frozen in liquid nitrogen and then stored in a -80 °C freezer until analyzed.

Tissue Sectioning and Sample Preparation

Frozen brain tissue was cut into thin sections (20 µm thickness) in a cryostat (HM 505E; Microm International GmbH, Waldorf, Germany) at -25 °C. The tissue samples were frozen to the cryostat sample stage using distilled water. Serial brain sections were collected onto

microscope slides where they were thaw mounted and then stored at -80 °C. Before mass spectrometric analysis, the tissue sections were removed from the freezer and placed in a vacuum desiccator for 30 min before spiking standards (1- μ L droplets by micropipette) and applying MALDI matrix. The matrix was applied to the tissue sections using an artistic airbrush (Aztek A470; Testors, Rockford, IL, USA). The application of MALDI matrix by airbrush has been previously published.⁶⁷

Tissue Homogenization

One gram of blank human brain tissue (i.e., tissue for which toxicological analysis did not indicate the presence of the analyte drug) was cut and weighed, and then finely minced with a scalpel. The minced tissue was then placed into a glass tissue grinder (Duall 21; Kontes Glass Inc., Vineland, New Jersey, USA), where it was homogenized into a liquid. The reservoir and pestle shaft of the tissue grinder were rinsed with 3 mL of 60 μ M sodium fluoride (NaF), which serves as an inhibitor for esterases to prevent COC hydrolysis.⁹⁹ The volume of NaF added was measured to be approximately twice the mass of the corresponding tissue sample. The homogenized tissue was then transferred to an 8-mL glass vial and placed in a sonicator for 1 min.

Preparation of Standard Solutions

Five standard solutions were prepared for spiking into tissue homogenate for generation of calibration curves. The concentrations of these 1-mL solutions was 62, 125, 250, 500, and 1000 ng/mL each of BE, COC, and CE, as well as a mixture of their corresponding internal standards (BE-d₃, COC-d₃, and CE-d₃; 200 ng/mL each). The five standard solutions were dried with nitrogen gas and then reconstituted with a 400- μ L aliquot of the sonicated homogenate. The solutions were immediately vortex-mixed (1 min) and centrifuged at 10,000 rpm for 30 min. The supernatants were then used for solid-phase extraction.

Preparation of Unknown Sample Solution

One gram of human brain tissue from case number 07A-369, for which toxicological analysis indicated the presence of cocaine in blood at 69 ng/mL (COC concentration in the brain tissue was not quantified) was cut and weighed, and then finely minced with a scalpel. The minced tissue was then placed into a glass tissue grinder, where it was homogenized into a liquid. The reservoir and pestle shaft of the tissue grinder were rinsed with 3 mL of 60 μ M sodium fluoride (NaF). The homogenized tissue was then transferred to an 8-mL glass vial and placed in a sonicator for 1 min.

A 1-mL solution of the internal standards (BE-d₃, COC-d₃, and CE-d₃; 200 ng/mL each) was prepared, dried with nitrogen gas and then reconstituted with a 400- μ L aliquot of the sonicated homogenate from case number 07A-369. The solution was immediately vortex-mixed (1 min) and centrifuged at 10,000 rpm for 30 min. The supernatant was then used for solid-phase extraction.

Solid-Phase Extraction

The extraction of cocaine and its metabolites was performed using underivatized silica (50 μ m average particle size; 60 Å pore size) solid-phase extraction (SPE) cartridges (HyperSep SI; 3-mL reservoir, 500-mg bed; Thermo Scientific, Bellafonte, PA, USA). The analytes in the homogenate were separated from impurities using a selective elution scheme shown in Figure 4-1, in which the adsorbed compounds of interest were eluted in a solvent that left the strongly retained impurities behind on the cartridge. The SPE cartridge was first conditioned using 2 mL of methanol followed by 2 mL of deionized water. Then a 100- μ L aliquot of the supernatant from the centrifuged homogenate was loaded and drawn through the cartridge using low vacuum (~ 5 in. Hg; 1 in. Hg = 388.638 Pa) in a vacuum manifold (PrepSep 12-Port Vacuum Manifold;

Fisher Scientific, Pittsburgh, PA, USA). After discarding the eluent, analytes in the cartridge were eluted using 3 mL of 5% ammonia in methanol solution. A washing step is typically performed to remove interferences in the biological matrices that may affect the assay; however, this step was not performed to avoid loss in recoveries of the highly polar metabolite ecgonine methyl ester. The high selectivity of MSⁿ makes the lack of this washing step less of a concern. The eluents from the extraction cartridge were then dried using nitrogen gas. The residue was reconstituted in 500 µL of water/methanol (90:10, vol/vol), spotted onto a MALDI plate (1 µL) and airbrushed with DHB matrix.

Mass Spectrometry

All experiments were performed using an LTQ linear ion trap with a vMALDI ion source (Thermo Finnigan, San Jose, CA, USA), equipped with nitrogen laser (337 nm) at a frequency of 20 Hz and 100-µm spot size. A more detailed description of this instrument has been published.⁶⁷ The number of laser shots was automatically varied (between 1 and 17 shots) using automatic gain control (AGC) to optimally fill the trap with ions, thus avoiding space charge-related peak broadening and mass shifts. AGC assesses the ion generation rate by use of a prescan, and then adjusts the number of laser shots per scan to produce an optimal number of ions for each scan. The spectra are normalized to the number of laser shots for each scan.

Resonance excitation is used for isolation, activation and mass analysis. For MSⁿ experiments, unwanted ions are resonantly ejected from the ion trap by applying a 5-500 kHz multi-frequency isolation waveform consisting of sine components spaced every 0.5 kHz. The ions of interest are isolated in the ion trap by removing sine components from the isolation waveform that correspond to the secular frequency of the desired ions. Ions to be isolated are selected in the LTQ software by entering the *m/z* with its IW. The mass range for the ion is

defined as $(m/z - IW/2)$ to $(m/z + IW/2)$. The IW should be narrow enough to eliminate including interfering peaks, but wide enough to avoid loss of sensitivity for the desired ions. However, it is important to note that the activation width for resonance excitation (CID) has the same value as the IW. Therefore, the collision energy applied during MS^n is spread over the activation width. Thus, increasing the IW decreases the collision energy for each ion.

SWIFT Calculation

A computer program written in C++ was used to calculate the SWIFT waveform based on a process previously described.¹⁰⁶ The same procedure was used here except that the final time-domain signal was left unapodized. Notches in the desired broadband magnitude spectrum, from frequency 0 to 500 kHz, were calculated to have centers corresponding to the secular frequencies of the ions to be isolated. The frequency spectrum was then transformed to the time domain using the inverse Fourier transform (IFT), which was performed using an adaptation of the Cooley-Tukey fast Fourier transform (FFT) algorithm.¹⁰⁹ The algorithm generates output, which must be midpoint reflected about the $N/2$ axis, where N equals the total number of points in the SWIFT waveform. This step is similar to a time shift and therefore affects the phase, but not the magnitude of the corresponding frequency-domain spectrum. The advantage of midpoint reflection is that it avoids sudden voltage transients at the beginning and end of the excitation period.

The frequency spectrum was then quadratically modulated in order to reduce the dynamic range of the time-domain waveform. The real, R_i , and imaginary, I_i , components are created from the magnitude data, Mag_i , using the following relationship:

$$\begin{aligned} R_i &= Mag_i \cos \varphi_i \\ I_i &= Mag_i \sin \varphi_i \end{aligned} \tag{4-1}$$

Where the phase, φ_i , varies quadratically with frequency:

$$\phi_i = \phi_0 + Ji + (K/2)i^2 \quad (4-2)$$

Here ϕ_0 is the initial phase (zero), i is the frequency index, and $J = 0.5\pi$ and $K = -\pi/N$ are the quadratic terms, where N is the number of nonzero data points in the frequency spectrum.

Values of J and K are chosen to satisfy the Nyquist criteria, such that the rate of phase change per frequency-domain data point is kept at half the Nyquist limit (π) or below, which removes nonuniformity of the magnitude in the frequency-domain.¹¹⁰

SWIFT Application to LTQ

The resulting digitized waveform was downloaded to the memory of an arbitrary waveform generator (AWG) (Stanford Research Systems Model DS345, Sunnyvale, CA, USA). The AWG has a maximum sampling rate of 40 MHz, time resolution of 16,300 data points, and a 12-bit DAC output. The LTQ has a programmable trigger that can be used to send a TTL pulse to the AWG at a specific time during the experimental sequence (e.g., isolation or activation). For experiments in which the AWG was triggered during isolation, the LTQ isolation waveform was turned off to avoid interference. Once triggered, the AWG applies the SWIFT waveform to the LTQ analog board, where it is summed with the other waveforms before being amplified and applied to the linear ion trap x-rods. The amplitude of the SWIFT waveform and the number of bursts were modified manually on the AWG. A two-channel digitizing oscilloscope (Tektronix Model TDS 540, Tektronix Inc., Beaverton, OR) was used to observe the SWIFT waveform.

Results and Discussion

Hexa-Notch SWIFT Isolation

One of the greatest strengths of SWIFT isolation is the ability to isolate multiple mass-to-charge (m/z) ranges simultaneously, which allows for the selective ejection of ions that may interfere with analysis. Multi-notch SWIFT isolation becomes a huge advantage when applied to

MALDI mass spectrometric imaging (MSI) when performing MSⁿ. Typically for an MSⁿ experiment, only one parent ion is isolated and then activated with collision-induced dissociation (CID) to produce product ions. MALDI MSI of a 2.0 cm by 1.0 cm tissue sample with 100- μ m laser steps (a total of 20,000 spectra) would take 5-6 hours to image, and this would have to be repeated for every analyte analyzed by MSⁿ. In addition, the analyte ion would normally be analyzed separately from its internal standard ion, which has been shown to have increased signal variability when compared to analyzing both the analyte and internal standard ions simultaneously with a wide isolation window (Chapter 2) or by dual-notch SWIFT isolation (Chapter 3). Multi-notch SWIFT isolation when applied to MALDI MSI can save considerable analysis time as well as conserve laser shots, since fewer analyses will need to be performed.

A hexa-notch SWIFT isolation waveform was calculated for the [M+H]⁺ ions of BE (m/z 290.2), BE-d₃ (m/z 293.2), COC (m/z 304.2), COC-d₃ (m/z 307.2), CE (m/z 318.2), and CE-d₃ (m/z 321.2). The center m/z of these ions (m/z 305.8) was placed at the q of isolation at $q = 0.830$. The frequencies of the 1.5-Da notches centered about each of the six ions to be isolated were calculated using a LabView program described in Appendix A. The frequencies of the notches calculated are listed in Table 4-1. Figure 4-2 shows the calculated hexa-notch SWIFT isolation waveform in the frequency domain. Although the width of all six notches is maintained at 1.5 Da, the width of the notches in the frequency domain becomes wider at higher frequencies. This is due to the nonlinearity of frequencies in relation to q at values greater than $q = 0.4$ (Figure 4-3). Isolation with the LTQ typically occurs at $q = 0.83$, because at this high q value, frequencies are dispersed enough in q -space to allow for selective isolation. Below $q = 0.4$, frequencies are too tightly spaced to allow for selective isolation (e.g., 1 kHz = 0.002 q ; given an RF drive frequency $\Omega = 1188$ kHz).

SWIFT Isolation on Tissue

The hexa-notch SWIFT isolation waveform was used to analyze BE, BE-d₃, COC, COC-d₃, CE, and CE-d₃ standards that were spiked (1 μL each) onto blank human brain tissue at 1 μg/mL each, and then airbrushed with DHB matrix. Figure 4-4 shows the peak ion intensities of the [M+H]⁺ ions of BE (*m/z* 290.2), BE-d₃ (*m/z* 293.2), COC (*m/z* 304.2), COC-d₃ (*m/z* 307.2), CE (*m/z* 318.2), and CE-d₃ (*m/z* 321.2) that were isolated at various hexa-notch SWIFT amplitudes (V_{p-p}). There was approximately a 50% decrease in signal across the monitored ions when the SWIFT amplitude was increased from 0.0 V_{p-p} to 0.1 V_{p-p} . There was a steady decrease in peak ion intensities with increasing SWIFT amplitude, with *m/z* 290.2 decreasing most rapidly followed by *m/z* 293.2. Figure 4-5a shows the mass spectrum of the spiked brain tissue with a SWIFT amplitude of 0.0 V_{p-p} . The mass spectrum is dominated by endogenous lipid ions from the brain tissue and it is difficult to distinguish the presence of any analyte ions. The most intense ion in the mass spectrum at *m/z* 313 was determined to be a phthalate contaminant from a plastic bottle that was used to store the DHB matrix solution. MSⁿ analysis revealed product ions at *m/z* 177, 149, and 121, which confirmed the phthalate contaminant. Figure 4-5b shows the mass spectrum with a SWIFT amplitude of 0.4 V_{p-p} . Notice that by increasing the SWIFT amplitude, the lower *m/z* background ions (< *m/z* 500) are ejected more efficiently than the higher *m/z* ions (*m/z* 500-2000). The higher *m/z* background ions (i.e., endogenous lipid region *m/z* 700 – 900) are not ejected until the SWIFT amplitude is at 0.8 V_{p-p} (Figure 4-5c). Figure 4-6 shows a more detailed view of the mass spectra that ranges from *m/z* 280 to *m/z* 330. Before SWIFT is applied (0.0 V_{p-p}), *m/z* 313 dominates the spectrum (Figure 4-6a) and the analyte ions are buried in the background. At a SWIFT amplitude of 0.4 V_{p-p} (Figure 4-6b), the *m/z* 313 peak has been reduced along with other low *m/z* background ions, revealing the presence of the

analyte ions at m/z 290, 293, 304, 307, 318, and 321. However, notice that the intensity of m/z 290, which should be relatively at the same intensity as its trideuterated analog at m/z 293, has decreased. At a SWIFT amplitude of $0.8 V_{p-p}$, which is sufficient enough to eject all background ions including high m/z ions, the high SWIFT amplitude has also ejected ions at m/z 290, 293, and 304 and reduced intensity of the analyte ions at m/z 307, 318, and 321 (Figure 4-6c).

Ion Ejection

To understand how ions can be ejected from the ion trap that were intended to be isolated by a multi-notch SWIFT waveform, it is helpful to look at a diagram of the pseudopotential well depth of the linear ion trap (Figure 4-7). Each ion confined within the ion trap is associated with a q value, which lies on the q_x -axis on the Mathieu stability diagram (Chapter 1). Ions of relatively high m/z have q values near the left side of the stability diagram ($\beta_x = 0$, $q_x = 0$) while ions of lower m/z have q values which extend towards the $\beta_x = 1$ stability boundary, as shown using colored circles of various sizes in Figure 4-7. At the intersection of the $\beta_x = 1$ stability boundary and the q_x -axis, where $q_x = 0.908$, the trajectories of trapped ions become unstable along the X-axis such that ions of m/z less than the low mass cutoff (LMCO) are not stored. This method of ion ejection, which can occur only at a boundary of the stability diagram, is referred to as mass-selective instability.⁹⁶

One other method for ions to be ejected from the ion trap is called resonant ejection,¹⁰⁸ which is the method of ejection used by SWIFT. The advantage of resonant ejection is that it can be carried out at any frequency. Ions are resonantly ejected from the ion trap when a frequency is applied that is in resonance with the secular frequency (ω) of the ion and has sufficient amplitude (depth of pseudopotential well) to increase the oscillation of the excited ions until they exit through the slits in the center X-rods of the linear ion trap.

In Figure 4-6b, it makes sense that the intensity of m/z 290 ($q = 0.875$) would decrease with increasing SWIFT amplitude, before ions at m/z 293 ($q = 0.866$), 304 ($q = 0.835$), 307 ($q = 0.827$), 318 ($q = 0.798$), and 321 ($q = 0.791$), because m/z 290 lies the closest to the LMCO (m/z 280, $\omega = 500$ kHz) at the mass-selective instability boundary ($q = 0.908$). It also has a shallower pseudopotential well depth (Figure 4-7) than the other ions, meaning that it takes a lower SWIFT amplitude to eject it from the ion trap. One way to correct for the instability of m/z 290 at higher SWIFT amplitudes would be to decrease its q value and move it away from the mass-selective instability boundary ($q = 0.908$). This can be accomplished by changing the m/z at the q of isolation ($q = 0.830$) from the center m/z of the analytes (m/z 305.8) to the lowest m/z analyte (m/z 290). The new q values and notch frequencies for the calculated hexa-notch SWIFT based on m/z 290.2 at $q = 0.830$ are listed in Table 4-2.

One issue with not placing the center m/z ion at the q of isolation is that the LTQ software couples the isolation window width with the activation window width. This means that in order to perform resonance excitation (CID) on the ions at m/z 290.2, 293.2, 304.2, 307.2, 318.2, and 321.2, with m/z 290.2 placed at the q of isolation ($q = 0.830$), at minimum, a 62-Da wide isolation window (m/z 259.2 – m/z 321.2) centered at m/z 290.2 is required to include these ions in activation. A 70-Da wide isolation window (m/z 255.2 – m/z 325.2) centered at m/z 290.2 would be wide enough to ensure complete activation of the ion at m/z 321.2. However, in the LTQ software, isolation windows and consequentially, activation windows that are wider than 47 Da, are assigned a q of isolation that is lower than $q = 0.830$ (Figure 4-8). In the LTQ software, the q of isolation is decreased linearly with increasing isolation window width to ensure that ions to be isolated are above the LMCO. The maximum isolation window width allowed by the LTQ software is 100 Da. The q of isolation for a 70-Da wide isolation window centered at m/z 290.2

is $q = 0.791$. The q values and notch frequencies for the calculated hexa-notch SWIFT based on m/z 290.2 at $q = 0.791$ are listed in Table 4-3.

Figure 4-9 compares the hexa-notch SWIFT isolation of m/z 290, 293, 304, 307, 318, and 321 at a SWIFT amplitude of $0.6 V_{p-p}$ with the m/z at q of isolation set to m/z 305.8 ($q = 0.830$) (Figure 4-9a), m/z 290.2 ($q = 0.830$) (Figure 4-9b), and m/z 290.2 ($q = 0.791$) (Figure 4-9c). Figure 4-9a shows a large decrease in signal for m/z 290 ($q = 0.875$) and m/z 293 ($q = 0.866$) compared to Figure 4-9b when m/z 290 ($q = 0.830$) and m/z 293 ($q = 0.822$) are placed at lower q values further away from the mass-selective instability boundary ($q = 0.908$). At the lower q values, m/z 290 and m/z 293 are deeper in the pseudopotential well of the ion trap and therefore can tolerate a higher SWIFT amplitude before they are resonantly ejected from the trap. The analyte ions at m/z 290 ($q = 0.791$), 293 ($q = 0.783$), 304 ($q = 0.755$), 307 ($q = 0.747$), 318 ($q = 0.721$), and 321 ($q = 0.715$) are even deeper in the pseudopotential well and show an overall increase in signal at lower q values (Figure 4-9c).

Figure 4-10 shows the peak ion intensities of the $[M+H]^+$ ions of BE (m/z 290.2), BE- d_3 (m/z 293.2), COC (m/z 304.2), COC- d_3 (m/z 307.2), CE (m/z 318.2), and CE- d_3 (m/z 321.2) when the hexa-notch SWIFT described in Table 4-3 based on m/z 290.2 at $q = 0.791$ was applied at various SWIFT amplitudes. The results shown in Figure 4-10 are very different than the results shown in Figure 4-4 from the hexa-notch SWIFT described in Table 4-1 based on m/z 305.8 at $q = 0.830$. Figure 4-4 showed approximately a 50% decrease in signal across the monitored ions when the SWIFT amplitude was increased from $0.0 V_{p-p}$ to $0.1 V_{p-p}$ followed by a steady decrease in peak ion intensities with increasing SWIFT amplitude. In contrast, when the amplitude of the hexa-notch SWIFT (Table 4-3) is increased, the analyte ion intensities steadily increase as well until the amplitude reaches $0.6 V_{p-p}$. When the SWIFT amplitude is increased

from $0.6 V_{p-p}$ to $1.0 V_{p-p}$, all of the analyte ion intensities decrease, but not in the order of low to high m/z (e.g., m/z 304 decreases faster than m/z 293 and m/z 318 decreases faster than m/z 321), as would be expected based on the pseudopotential well depth (Figure 4-7). This behavior may be explained due to the fact that the energy absorption profile for ions subjected to resonance excitation broadens with the amplitude of ion oscillation and shifts to higher frequencies.¹¹⁶ If the ions to be isolated shift to higher frequencies, they will be outside the frequency notches of the SWIFT isolation waveform and will come into resonance with the excitation frequencies thus ejecting them from the trap. Therefore, it is beneficial to use the lowest SWIFT amplitude possible to isolate the desired ions to avoid causing frequency shifts and sequential resonant ejection (Figure 4-11). However, at lower SWIFT amplitudes (Figure 4-12), higher m/z background ions will not be ejected and will remain trapped .

Two-Stage Isolation

One strategy for ejecting high m/z background ions while avoiding frequency shifts caused from higher SWIFT amplitudes, is to perform two-stage isolation. The first stage would be a coarse isolation that would coarsely isolate the ions of interest, while ejecting background ions. The frequency notches during this stage would be wide enough so that if any frequency shifts did occur, the ions of interest would not be ejected. This coarse isolation stage would be followed by a fine isolation stage, which would utilize a higher degree of mass discrimination to eject background ions close to the ions of interest.

This two-stage coarse/fine SWIFT isolation was first proposed by Soni and Cooks¹⁰⁷ for isolating ions having a single m/z value from a population of trapped ions. The coarse/fine isolation technique used a doubly notched SWIFT pulse to perform the isolation in two steps at two different q values. The coarse isolation step used a single notch centered at $q = 0.0778$ to coarsely isolate the ion of interest. Then the RF amplitude was increased to move the trapped

ions to a higher q value in which a second narrower notch centered at $q = 0.4035$ was used to finely isolate ions of a single m/z value only. The resonance frequencies of ions are more spread out at higher q values (Figure 4-3), which allows for higher mass discrimination. The advantage of this two-stage isolation is that the coarse step removes most of the ions that contribute to space charging, and thereafter the frequencies of the analyte ions remain relatively constant. However, although frequency shifts were minimized with the two-stage strategy, Soni and Cooks still reported a 20% loss of target ion population as a result of the sharp mass discrimination of the second fine isolation notch.¹⁰⁷

High Mass Filter (HMF)

In order to minimize frequency shifts, a SWIFT excitation waveform was calculated that ejects background ions higher in m/z than the highest m/z analyte (m/z 321). This SWIFT excitation waveform was termed high mass filter (HMF), because it serves to filter out or eject ions above a certain m/z . Figure 4-13 shows the frequency domain of a HMF that was calculated to excite at frequencies 0 to 338 kHz. The right-hand edge of the HMF at 338 kHz corresponds to a m/z cutoff at m/z 325.8 based on m/z 290.2 placed at a q of isolation ($q = 0.791$). This HMF is designed to eject/excite ions from m/z 325.8 to greater than m/z 2000 (LTQ upper m/z limit; 48 kHz).

The HMF SWIFT excitation waveform was applied to the analysis of BE, BE-d₃, COC, COC-d₃, CE, and CE-d₃ standards that were spiked (1 μ L each) onto blank human brain tissue at 1 μ g/mL each, and then airbrushed with DHB matrix. Figure 4-14 shows the peak ion intensities of the $[M+H]^+$ ions of BE (m/z 290.2), BE-d₃ (m/z 293.2), COC (m/z 304.2), COC-d₃ (m/z 307.2), CE (m/z 318.2), and CE-d₃ (m/z 321.2) while the HMF was applied at various SWIFT amplitudes (V_{p-p}). When the HMF amplitude is increased from 0.0 V_{p-p} to 0.2 V_{p-p} there is a 19 to 43%

increase in signal for the analyte ions as the high m/z background signal begins to decrease. The signal for the analyte ions then shows a decrease when the HMF amplitude is increased from 0.2 V_{p-p} to 0.4 V_{p-p} . At a HMF amplitude of 0.5 V_{p-p} , all of the high m/z background ions are removed, resulting in a 14 to 22% increase in analyte signal from 0.4 V_{p-p} to 0.5 V_{p-p} . The analyte signals then begin to steadily decrease as the HMF amplitude is increased from 0.5 V_{p-p} to 1.0 V_{p-p} . At a HMF amplitude of 1.0 V_{p-p} the analyte signals have decreased 36 to 47% from the amplitude of 0.5 V_{p-p} with the analyte ions at m/z 290.2 and 293.2 decreasing the most (47%).

Figure 4-15 shows the mass spectra of the spiked brain tissue with the HMF amplitude at 0.0 V_{p-p} (Figure 4-15a), 0.4 V_{p-p} (Figure 4-15b), and 0.5 V_{p-p} (Figure 4-15c). Notice the dramatic change in the high m/z background when the HMF amplitude is increased from 0.4 V_{p-p} (Figure 4-15b) to 0.5 V_{p-p} (Figure 4-15c). Figure 4-16 shows a more detailed view of the mass spectra from m/z 280 to m/z 330. Although the HMF SWIFT excitation waveform should only affect ions from m/z 325.8 to m/z 2000, the signal intensities of the analyte ions steadily increase when the HMF amplitude is changed from 0.0 V_{p-p} (Figure 4-16a) to 0.4 V_{p-p} (Figure 4-16b) and then to 0.5 V_{p-p} (Figure 4-16c). This increase in analyte signal may be attributed to the reduction in high m/z background ions, which dominate the mass spectrum. By ejecting the high m/z background ions, space-charge effects are reduced that would normally cause frequency shifts of the analyte ions outside the notches of the SWIFT isolation waveform resulting in some ejection of analyte ions.

Combining HMF with Hexa-Notch SWIFT

Two-stage isolation was performed by combining the HMF SWIFT excitation waveform to eject ions above m/z 325.8 with a hexa-notch SWIFT isolation waveform to selectively isolate ions at m/z 290.2, 293.2, 304.2, 307.2, 318.2, and 321.2 (Figure 4-17). The frequency domain of the two-stage isolation is shown in Figure 4-17 with the HMF waveform shown in red and the

hexa-notch waveform shown in blue. The time domain of the two-stage isolation is shown in Figure 4-18. The HMF SWIFT excitation waveform (red) occurs from 0 to 4,096 μs and the hexa-notch SWIFT isolation waveform (blue) occurs from 4,097 to 8,192 μs . A single burst of the two-stage isolation pulse (8,192 μs) is triggered during the LTQ isolation event (15,500 μs) with the LTQ isolation waveform turned off.

The two-stage isolation was used to analyze BE, BE- d_3 , COC, COC- d_3 , CE, and CE- d_3 standards that were spiked (1 μL each) onto blank human brain tissue at 1 $\mu\text{g}/\text{mL}$ each, and then airbrushed with DHB matrix. Figure 4-19 shows the peak ion intensities of the $[\text{M}+\text{H}]^+$ ions of BE (m/z 290.2), BE- d_3 (m/z 293.2), COC (m/z 304.2), COC- d_3 (m/z 307.2), CE (m/z 318.2), and CE- d_3 (m/z 321.2) that were isolated at various two-stage isolation amplitudes ($V_{\text{p-p}}$). Both the HMF SWIFT excitation waveform and the hexanotch SWIFT isolation waveform were set to the same amplitude using the function generator. The analyte ion intensities decreased steadily as the amplitude was increased from 0.1 $V_{\text{p-p}}$ to 0.4 $V_{\text{p-p}}$. The analyte ion intensities then remained relatively constant between 0.4 $V_{\text{p-p}}$ and 0.6 $V_{\text{p-p}}$. When the amplitude was increased from 0.6 $V_{\text{p-p}}$ to 1.0 $V_{\text{p-p}}$, the analyte ion intensities quickly decreased with the m/z 290.2 ion decreasing the fastest. The instability of m/z 290.2 at SWIFT amplitudes greater than 0.6 $V_{\text{p-p}}$ is probably due to the shallow position of this ion in the pseudopotential well. One strategy for correcting this would be to move the analyte ions to lower q values further away from the LMCO during isolation.

Figure 4-20 shows the mass spectra of the spiked blank brain tissue with the two-stage isolation amplitude at 0.0 $V_{\text{p-p}}$ (Figure 4-20a), 0.5 $V_{\text{p-p}}$ (Figure 4-20b), and 0.6 $V_{\text{p-p}}$ (Figure 4-20c). When the HMF SWIFT excitation waveform was used alone without the hexa-notch SWIFT isolation waveform, the high m/z background ions were ejected efficiently at a SWIFT

amplitude of $0.5 V_{p-p}$ (Figure 4-15c); however, when the HMF SWIFT excitation waveform is combined with the hexa-notch SWIFT isolation waveform in the two-stage isolation, the high m/z background ions are not ejected at $0.5 V_{p-p}$ (Figure 4-20b), but requires an amplitude of $0.6 V_{p-p}$ (Figure 4-20c) for the high m/z ion background to be removed. Increasing the amplitude from $0.5 V_{p-p}$ to $0.6 V_{p-p}$ actually results in a slight increase in the analyte ion intensities (3% to 18%), which could be due to the removal of the high m/z background ions that cause frequency shifts of the analyte ions. Figure 4-21 shows a more detailed view of the mass spectra from m/z 280 to m/z 330. Notice how the background ion signals have been reduced around the analyte ions.

The overall difference in the analyte ion intensities with the application of the two-stage isolation at $0.6 V_{p-p}$ compared to no two-stage isolation ($0.0 V_{p-p}$) is 54% decrease for m/z 290.2, 37% decrease for m/z 293.2, 19% decrease for m/z 304.2, 12% decrease for m/z 307.2, 9% decrease for m/z 318.2, and 22% decrease for m/z 321.2. The high decreases in signal for m/z 290.2 (54%) and m/z 293.2 (37%) are probably due to their proximity to the LMCO, which could be remedied by lowering the q values of the ions during isolation. The high decrease in signal for m/z 321.2 (22%) could be due to its proximity to the m/z cutoff (m/z 325.8) of the HMF applied. This can be fixed by applying a different HMF that allows for more space between the m/z 321.2 ion and the m/z cutoff, but still allows removal of the majority of the high m/z background ions.

MS/MS with Two-Stage Isolation

The overall goal of the two-stage isolation was to provide an isolation strategy that would allow for the isolation of the analyte and internal standard ions during a single MS/MS scan. The MS/MS provides higher mass selectivity which is essential for distinguishing the analyte from MALDI matrix and endogenous species (e.g., lipids) present in the brain tissue, and isolating the

analyte and internal standard ions in the same MS/MS scan has shown to improve the precision of MALDI-MS/MS (Chapters 2 and 3).¹⁰³ Figure 4-22a shows the mass spectrum of spiked brain tissue with the two-stage SWIFT isolation waveform applied at 0.6 V_{p-p} . A 70-Da wide isolation window was centered at the lowest m/z analyte ion at m/z 290.2, which placed the q of isolation at $q = 0.791$. Since the LTQ software couples the isolation width with the activation width, CID will be applied across the 70-Da wide activation window centered at m/z 290.2. This means that ions in the mass range m/z 255.2 to 325.2 will all be activated by CID and fragmented. It is also important to note that the collision energy applied during MS/MS is spread over the entire activation width. Thus, increasing the isolation width decreases the collision energy for each ion. It was determined that the CID value necessary to dissociate the analyte ions during MS/MS and reduce the parent ions to a relative intensity of 10%, needed to be increased with the wider activation window. It was determined that a CID of 55 was optimal for the analytes with a 5-Da wide activation window, but the CID was increased to 90 for the 70-Da wide activation window.

Figure 4-22b shows the MS/MS product ion spectrum of ions isolated by a two-stage SWIFT isolation. Since the most intense fragment ion of the $[M+H]^+$ ion of BE (m/z 290.2), BE- d_3 (m/z 293.2), COC (m/z 304.2), COC- d_3 (m/z 307.2), CE (m/z 318.2), and CE- d_3 (m/z 321.2) all result from the neutral loss (NL) of benzoic acid (122 Da), it is easy to distinguish the origins of each product ion. BE produces the product ion at m/z 168.2, BE- d_3 produces the product ion at m/z 171.2, COC produces the product ion at m/z 182.2, COC- d_3 produces the product ion at m/z 185.2, CE produces the product ion at m/z 196.2, and CE- d_3 produces the product ion at m/z 199.2. A common product ion of BE, COC, and CE is m/z 150.2 and a common product ion of BE- d_3 , COC- d_3 , and CE- d_3 is m/z 153.2, both of which are due to the NL of benzoic acid

(C₆H₅COOH) and methanol (CH₃OH). Common product ions were not used for quantification due to the difficulty in determining the signal attributable to each parent ion.

Figure 4-23a shows the MS/MS product ion spectrum of ions isolated with a 40-Da wide isolation window with CID = 55. Notice that this product ion spectrum contains the same product ions from the MS/MS of ions isolated with a two-stage SWIFT isolation (Figure 4-23b) with some additional ions (e.g., *m/z* 137 and *m/z* 147) produced from the MS/MS of background ions. These background ions were isolated along with the analyte ions in the 40-Da wide isolation (Figure 4-24b). The intense product ion at *m/z* 137 is [DHB+H-H₂O]⁺ caused by the NL of DHB from the DHB cluster matrix ion at *m/z* 291, [2DHB+H-H₂O]⁺. Background ions can complicate the product ion spectrum and might even interfere with the analyte product ion signals if the background ions produce fragment ions that are isobaric; therefore, removal of background ions during isolation before MS/MS is beneficial.

Comparing Wide Isolation and Two-Stage SWIFT Isolation

It was previously shown that isolating the analyte and internal standard ions in a single MS/MS scan using a wide isolation window can improve precision for MALDI quantification compared to isolating the analyte and internal standard ions separately during alternate MS/MS scans (Chapters 2 and 3).¹⁰³ In order to compare the ability of the two-stage SWIFT isolation waveform to also improve precision for MALDI quantification, five solutions (mixture of BE, COC, and CE at 62, 125, 250, 500, and 1000 ng/mL with a mixture of BE-d₃, COC-d₃, and CE-d₃ at 200 ng/mL) were pipetted in triplicate (1 μL each) onto blank human brain tissue and airbrushed with DHB matrix. The tissue was then analyzed using two different MS/MS experiments: two-stage SWIFT isolation (0.6 V_{p-p}; CID = 90) and 40-Da wide isolation (CID = 55). Figure 4-25 shows the calibration curves for BE for both experiments (two-stage SWIFT

isolation and wide isolation) produced by plotting the peak intensity ratio of m/z 168 and m/z 171 versus the mass of BE standard spiked on tissue. The two-stage SWIFT isolation has comparable precision (% RSD = 0 to 11%) for isotopic ratios compared to wide isolation (% RSD = 2 to 11%). Figure 4-26 shows the calibration curves for COC for both experiments (two-stage SWIFT isolation and wide isolation) produced by plotting the peak intensity ratio of m/z 182 and m/z 185 versus the mass of COC standard spiked on tissue. The two-stage SWIFT isolation has similar precision (% RSD = 1 to 6%) for isotopic ratios compared to wide isolation (% RSD = 3 to 5%). The precision of the two-stage SWIFT isolation for the MS/MS analysis of COC is better than what was reported for dual-notch SWIFT isolation of COC in Chapter 3 (% RSD = 5 to 23%). This improvement may be due to the addition of the HMF during the first stage of the two-stage isolation, which removes the space-charge effects of the high m/z background ions. Finally, Figure 4-27 shows the calibration curves for CE for both experiments (two-stage SWIFT isolation and wide isolation) produced by plotting the peak intensity ratio of m/z 196 and m/z 199 versus the mass of CE standard spiked on tissue. The two-stage SWIFT isolation % RSD ranged from 3 to 12% compared to the % RSD for wide isolation that ranged from 1 to 29%.

Although two-stage SWIFT isolation overall has comparable precision to that of wide isolation, the higher mass selectivity of the two-stage SWIFT isolation affords a significant loss in absolute signal intensity of the analyte ions when it is applied. BE and BE- d_3 showed an average percent loss in absolute signal intensity of 83% and 75%, respectively. COC and COC- d_3 showed an average percent loss in absolute signal intensity of 69% and 75%, respectively. CE and CE- d_3 showed an average percent loss in absolute signal intensity of 65% and 77%, respectively.

Two-Stage SWIFT MALDI-MS/MS Quantification

The MS/MS two-stage SWIFT isolation method and the MS/MS 40-Da wide isolation method were compared for the quantification of unspiked BE, COC, and CE from human brain tissue from a subject whose toxicology report showed the presence of COC. Three different concentrations of BE-d₃, COC-d₃, and CE-d₃ (31, 62, and 125 ng/mL) were spiked (1 μL) onto a glass slide before thaw mounting a 20 μm-thick brain tissue slice on top and airbrushing DHB matrix. All three spots were then analyzed using the MS/MS two-stage SWIFT isolation method and then the MS/MS 40-Da wide isolation method. Approximately 2000 scans were acquired to image the entire area of each of the spots (average area = 0.17 cm²). The *m/z* 171 signal from using the MS/MS two-stage SWIFT isolation for BE-d₃ from each spot was used to develop a calibration curve that resulted in a line of best fit of $y = 0.97(\pm 0.08)x + 6(\pm 7)$. BE-d₃ was shown to have a linear response with increasing concentrations spiked underneath tissue. Since the MS/MS two-stage SWIFT isolation method analyzes both BE and BE-d₃ simultaneously, unspiked BE was detected from each spot analyzed at *m/z* 168. An area of the tissue (500 MS/MS scans) that was not spiked with BE-d₃ was analyzed using the MS/MS two-stage SWIFT isolation method and the acquired *m/z* 168 signal was averaged with the *m/z* 168 signals from the spiked BE-d₃ spots, resulting in a very trace signal of 53 ± 6 counts. Assuming that the amount of unspiked BE extracted from the tissue has a 1:1 response with the BE-d₃ spiked on top of tissue, the calibration curve for BE-d₃ can be used to quantify the amount of BE present in the analyzed tissue. From the equation of the line, it was determined that BE was present at a level equivalent to 50 ng/mL.

Using the 1 μL volume of BE-d₃ spiked underneath tissue, it is calculated that the mass of BE present is 50 pg. Given that the area of an analyzed spot on tissue was 0.17 cm² and that the

tissue thickness was 20 μm (2.0×10^{-3} cm), the volume of tissue from which BE was extracted was 3.4×10^{-4} cm^3 . The mass of the tissue is 3.4×10^{-4} g (density of wet tissue ~ 1.0 g/cm^3), resulting in an absolute concentration of BE detected in this area of the postmortem brain tissue of 140 ng/g (140 ppb). Since the MS/MS two-stage SWIFT isolation method and the MS/MS 40-Da wide isolation method both acquire the analyte and internal standard ions for BE (m/z 168 and 171), COC (m/z 182 and 185), and CE (m/z 196 and 199) from each spot analyzed simultaneously, the amount of unspiked COC and unspiked CE were also quantified from the tissue using the same process described above. The results for the quantification of BE, COC, and CE using both the MS/MS two-stage SWIFT isolation method and the MS/MS 40-Da wide isolation method are summarized in Table 4-4.

SPE-MALDI-MS/MS Quantification

Drugs and their metabolites in tissue are typically quantified from tissue homogenate instead of from intact tissue. For this reason, tissue homogenates were prepared and extracted by solid-phase extraction (SPE) as described in the previous experimental section, and analyzed using MALDI-MS/MS to quantify the presence of BE, COC, and CE in unspiked tissue. One gram of blank human brain tissue (case number 07A-355) was cut, weighed (0.9830 g), and homogenized. Then 3 mL of 60 μM NaF was added and the homogenate was sonicated. Five 1-mL standard solutions (62, 125, 250, 500, and 1000 ng/mL each of BE, COC, and CE and 200 ng/mL each of BE- d_3 , COC- d_3 , and CE- d_3) were dried with nitrogen gas and then reconstituted with a 400- μL aliquot of the sonicated homogenate. The solutions were immediately vortex-mixed and centrifuged. Then a 100- μL aliquot of the supernatant from the centrifuged homogenate was loaded onto a preconditioned underivatized silica SPE cartridge. Analytes in the cartridge were then eluted using 3 mL of 5% ammonia in methanol solution. The eluents

from the extraction cartridge were then dried using nitrogen gas, and the residue was reconstituted in 500 μ L of water/methanol (90:10, vol/vol), spotted onto a MALDI plate (1 μ L) in triplicate, and airbrushed with DHB matrix.

Each spot on the MALDI plate was analyzed using a MS/MS 5-Da wide isolation method specific for each set of analyte and internal standard ions. The 5-Da wide isolation method was used, because it was shown to have better precision than using alternating MS/MS scans.¹⁰³ The $[M+H]^+$ ions of BE (m/z 290.2) and BE- d_3 (m/z 293.2) were isolated with a 5-Da wide isolation window centered at m/z 291.8 with CID = 55 to produce the product ions at m/z 168.2 and m/z 171.2 for BE and BE- d_3 , respectively. The $[M+H]^+$ ions of COC (m/z 304.2) and COC- d_3 (m/z 307.2) were isolated with a 5-Da wide isolation window centered at m/z 305.8 with CID = 55 to produce the product ions at m/z 182.2 and m/z 185.2 for COC and COC- d_3 , respectively. The $[M+H]^+$ ions of CE (m/z 318.2) and CE- d_3 (m/z 321.2) were isolated with a 5-Da wide isolation window centered at m/z 319.8 with CID = 55 to produce the product ions at m/z 196.2 and m/z 199.2 for CE and CE- d_3 , respectively. Figure 4-28 shows the calibration curve for BE with the peak intensity ratio of m/z 168.2 and m/z 171.2 versus the mass of BE spotted on the MALDI plate from the tissue homogenate. The 5-Da wide isolation method was fairly precise with % RSD ranging from 3 to 8%. The BE calibration curve has a line of best fit of $y = 0.00543(\pm 0.00005)x - 0.0007(\pm 0.02)$. Figure 4-29 shows the calibration curve for COC with the peak intensity ratio of m/z 182.2 and m/z 185.2 versus the mass of COC spotted on the MALDI plate from the tissue homogenate. % RSD ranged from 4 to 12%. The COC calibration curve showed a linear response with a line of best fit of $y = 0.00633(\pm 0.00005)x + 0.02(\pm 0.02)$. The calibration curve for CE is shown in Figure 4-30 with the peak intensity ratio of m/z 196.2 and m/z 199.2 versus the mass of CE spotted on the MALDI plate from the tissue homogenate. %

RSD ranged from 3 to 6%. The CE calibration curve showed a linear response with a line of $y = 0.00581(\pm 0.00003)x - 0.02(\pm 0.02)$.

The equations of the calibration curves developed were used to quantify the amount of unspiked BE, COC, and CE present in unspiked tissue homogenate from human brain tissue (case number 07A-369), for which toxicological analysis indicated the presence of cocaine in blood (69 ng/mL). One gram of this tissue was cut, weighed (0.9862 g), and homogenized. Then 3 mL of 60 μ M NaF was added and the homogenate was sonicated. A 1-mL solution of the internal standards (BE-d₃, COC-d₃, and CE-d₃; 200 ng/mL each) was prepared, dried with nitrogen gas, and then reconstituted with a 400- μ L aliquot of the sonicated homogenate from case number 07A-369. The solution was immediately vortex-mixed and centrifuged. Then a 100- μ L aliquot of the supernatant from the centrifuged homogenate was loaded onto a preconditioned underivatized silica SPE cartridge. Analytes in the cartridge were then eluted using 3 mL of 5% ammonia in methanol solution. The eluents from the extraction cartridge were then dried using nitrogen gas, and the residue was reconstituted in 500 μ L of water/methanol (90:10, vol/vol), spotted onto a MALDI plate (1 μ L) in triplicate, and airbrushed with DHB matrix. Each spot on the MALDI plate was analyzed using the MS/MS 5-Da wide isolation method specific for each set of analyte and internal standard ions described previously. Using the calibration curves it was determined that there was 270 ± 14 ng BE/g of tissue, 380 ± 11 ng COC/g of tissue, and 430 ± 16 ng CE/g of tissue.

The concentrations for BE, COC, and CE are not comparable to the concentrations determined by analyzing the tissue directly by the MS/MS two-stage SWIFT isolation method and the MS/MS 40-Da wide isolation method (Table 4-4). One reason for this difference might be in the sample size for the different methods. The tissue homogenate method analyzes a larger

tissue sample (~ 1 g) for quantification, which averages the signal for the analytes over the entire tissue. The intact tissue MALDI methods analyze much smaller samples (3.4×10^{-4} g) across different regions of the tissue to develop a calibration curve for quantification. This analytical strategy assumes that the internal standard spotted underneath the tissue will have a similar response across the different regions of the tissue. It also assumes that the internal standard will have similar extraction efficiencies through the tissue for all regions analyzed. In addition, since it is difficult to spot different concentrations of the internal standard in triplicate underneath the tissue, precision of the quantitative analysis for the intact tissue methods was not determined.

Conclusions

In Chapter 3, multi-notch SWIFT isolation waveforms were explored as a strategy for isolating the analyte and internal standard ions during a single MS/MS scan, which has been shown to provide improved precision for MALDI-MS compared to using two alternating MS/MS scans that isolate the analyte and internal standard ions separately. However, it was determined that multi-notch SWIFT isolation was not as precise as the wide isolation method. This might have been due to frequency shifts of the analyte and internal standard ions from space-charge effects caused by high m/z background ions.

A two-stage SWIFT isolation method was developed that utilizes a high mass filter (HMF) SWIFT excitation waveform to remove high m/z background ions during the first stage of isolation. This has been shown to increase isolated ion signals and improve the precision of SWIFT when compared to the application of SWIFT without the HMF. This may suggest that the HMF reduces the irreproducible frequency shifts of the analyte and internal standard ions by preventing them from moving outside the notches of the multi-notch SWIFT isolation waveform and being ejected. A hexa-notch SWIFT isolation waveform was used during the second stage of the two-stage SWIFT isolation to mass selectively isolate the $[M+H]^+$ ions of BE (m/z 168.2),

BE-d₃ (*m/z* 171.2), COC (*m/z* 304.2), COC-d₃ (*m/z* 307.2), CE (*m/z* 318.2), and CE-d₃ (*m/z* 321.2). The hexa-notch SWIFT isolation waveform was able to effectively remove background ions around the analyte and internal standard ions that may have interfered with MS/MS analysis. The two-stage SWIFT isolation overall showed similar precision to that of wide isolation when performing MS/MS on the analyte and internal standards spiked on blank brain tissue. However, the higher mass selectivity of the two-stage SWIFT isolation affords a significant loss in absolute signal intensity of the analyte and internal standard ions when it is applied.

Two-stage SWIFT isolation was compared to wide isolation of intact tissue and SPE extracted homogenized tissue for the MALDI-MS/MS quantification of BE, COC, and CE from unspiked human brain tissue, whose toxicological analysis indicated the presence of cocaine in blood. The two-stage SWIFT isolation method showed a lower analyte signal per gram of tissue than the wide isolation method for BE, COC, and CE present in tissue. The quantification results for the two-stage SWIFT isolation and the wide isolation of intact tissue was not comparable to the wide isolation analysis of tissue homogenate (Table 4-4). However, the intact tissue methods required considerably less sample preparation and smaller sample sizes than the tissue homogenate method. There was no analysis time saved when comparing the two-stage SWIFT isolation and wide isolation since the [M+H]⁺ ions of BE, BE-d₃, COC, COC-d₃, CE, and CE-d₃ were all isolated simultaneously during the same MS/MS scan. In conclusion, a wide isolation method may still be a better choice over SWIFT isolation for improving MALDI-MS/MS precision for quantification and reducing analysis time, despite the inclusion of unwanted background ions during isolation.

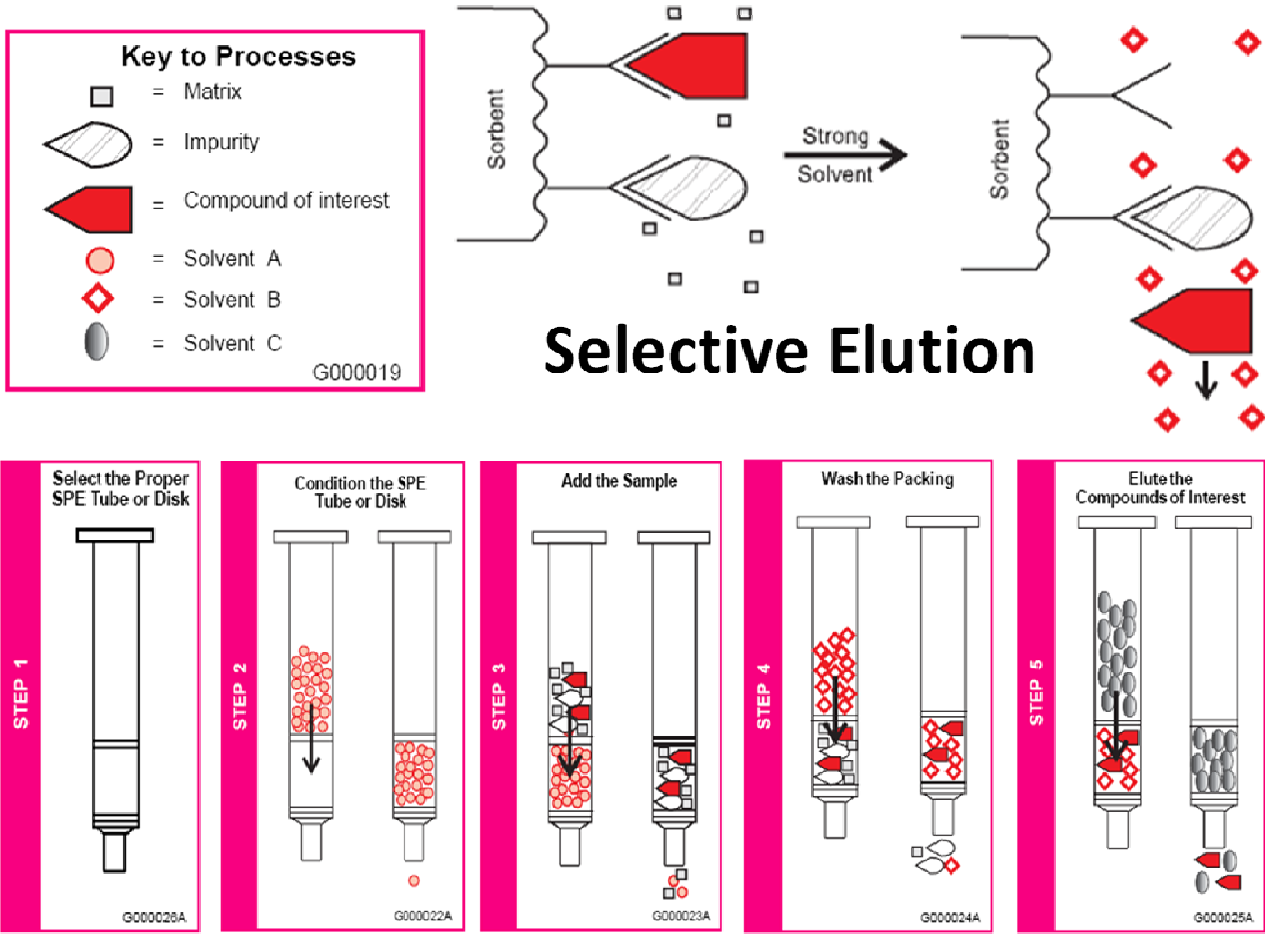


Figure 4-1. Solid-phase extraction scheme. Selective elution is the solid-phase extraction (SPE) scheme used. Adsorbed compounds of interest are eluted in a solvent (3 mL 5% NH₃ in MeOH) that leaves the strongly retained impurities behind. The SPE process typically involves 5 steps: (1) select the proper SPE tube (HyperSep SI), (2) condition the SPE tube (2 mL of methanol followed by 2 mL of deionized water), (3) add the sample (100- μ L of homogenate), (4) wash the packing (not performed), and (5) elute the compounds of interest (3 mL 5% NH₃ in MeOH). Adapted from Supelco Bulletin 910: Guide to Solid-Phase Extraction, 1998.

Table 4-1. Hexa-notch SWIFT properties based on m/z 305.8 at $q = 0.830$

Analyte	$[M+H]^+$ (m/z)	q value	Notch Width (Da)	Notch Frequencies (kHz)
BE	290.2	0.875	1.5	488.037109 to 494.873047
BE-d ₃	293.2	0.866	1.5	475.341797 to 481.445312
COC	304.2	0.835	1.5	439.208984 to 443.603516
COC-d ₃	307.2	0.827	1.5	431.152344 to 435.058594
CE	318.2	0.798	1.5	405.029297 to 408.203125
CE-d ₃	321.2	0.791	1.5	398.681641 to 401.855469

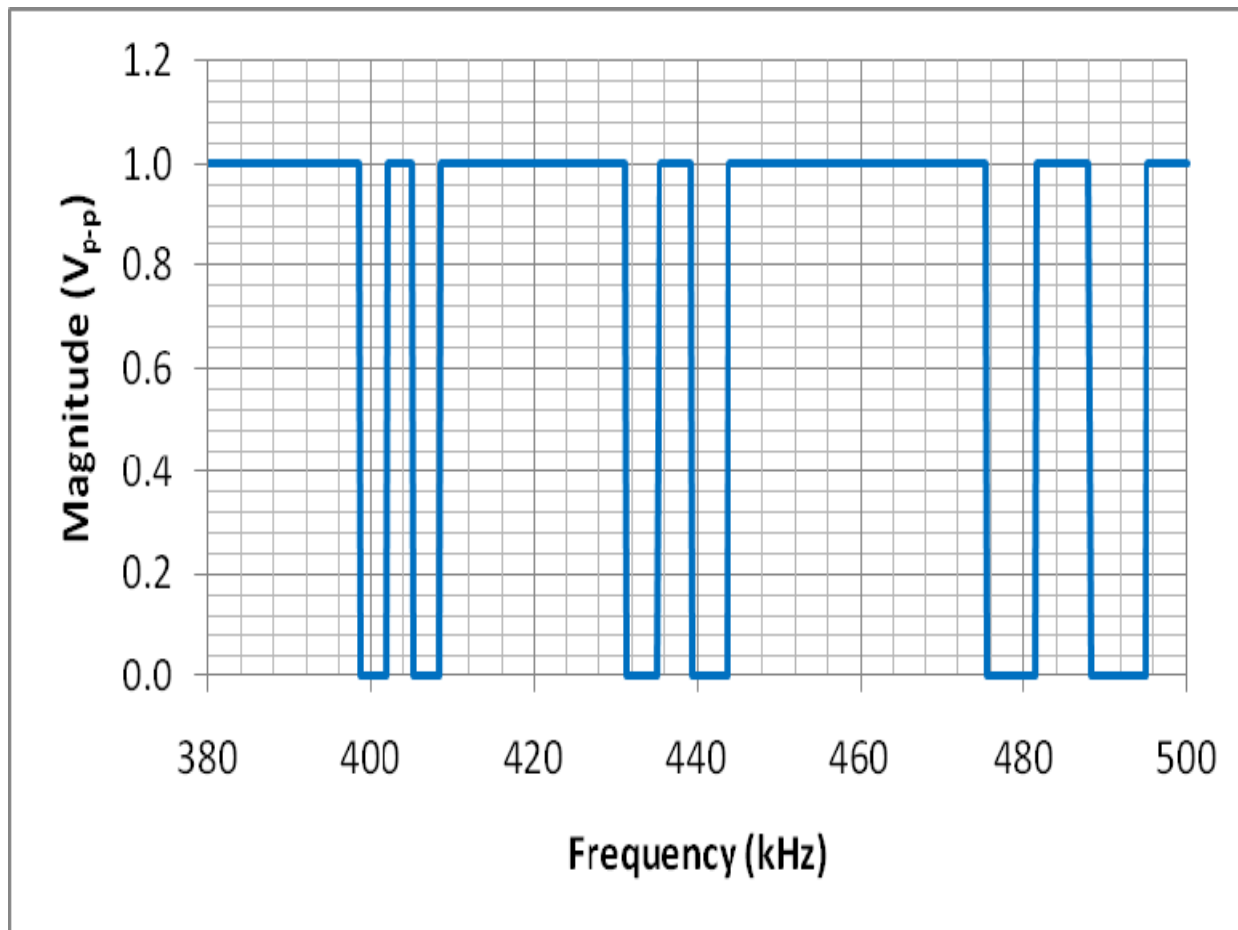


Figure 4-2. Frequency domain of hexa-notch SWIFT isolation waveform. Frequency notches correspond to the secular frequencies of the $[M+H]^+$ ion of BE (m/z 290.2), BE- d_3 (m/z 293.2), COC (m/z 304.2), COC- d_3 (m/z 307.2), CE (m/z 318.2), and CE- d_3 (m/z 321.2) with the center m/z 305.8 placed at the q of isolation at $q = 0.83$.

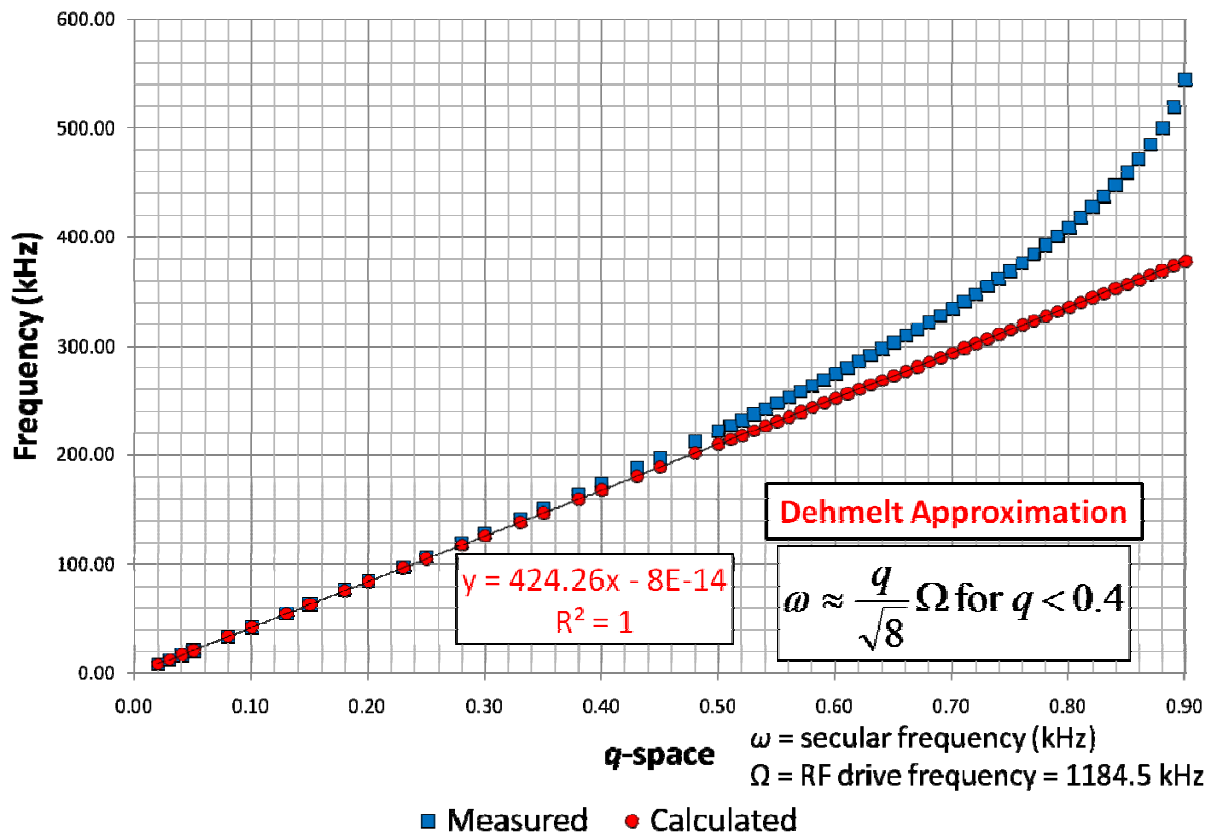


Figure 4-3. Relationship between secular frequency (ω) and q -space. The Dehmelt approximation (red trace) states that ω varies linearly with q for values of q less than 0.4. Secular frequency (ω) diverts from linearity (blue trace) at q values higher than 0.4, which can be measured from the LTQ MSⁿ diagnostic settings and verified by calculations explained in Appendix A.

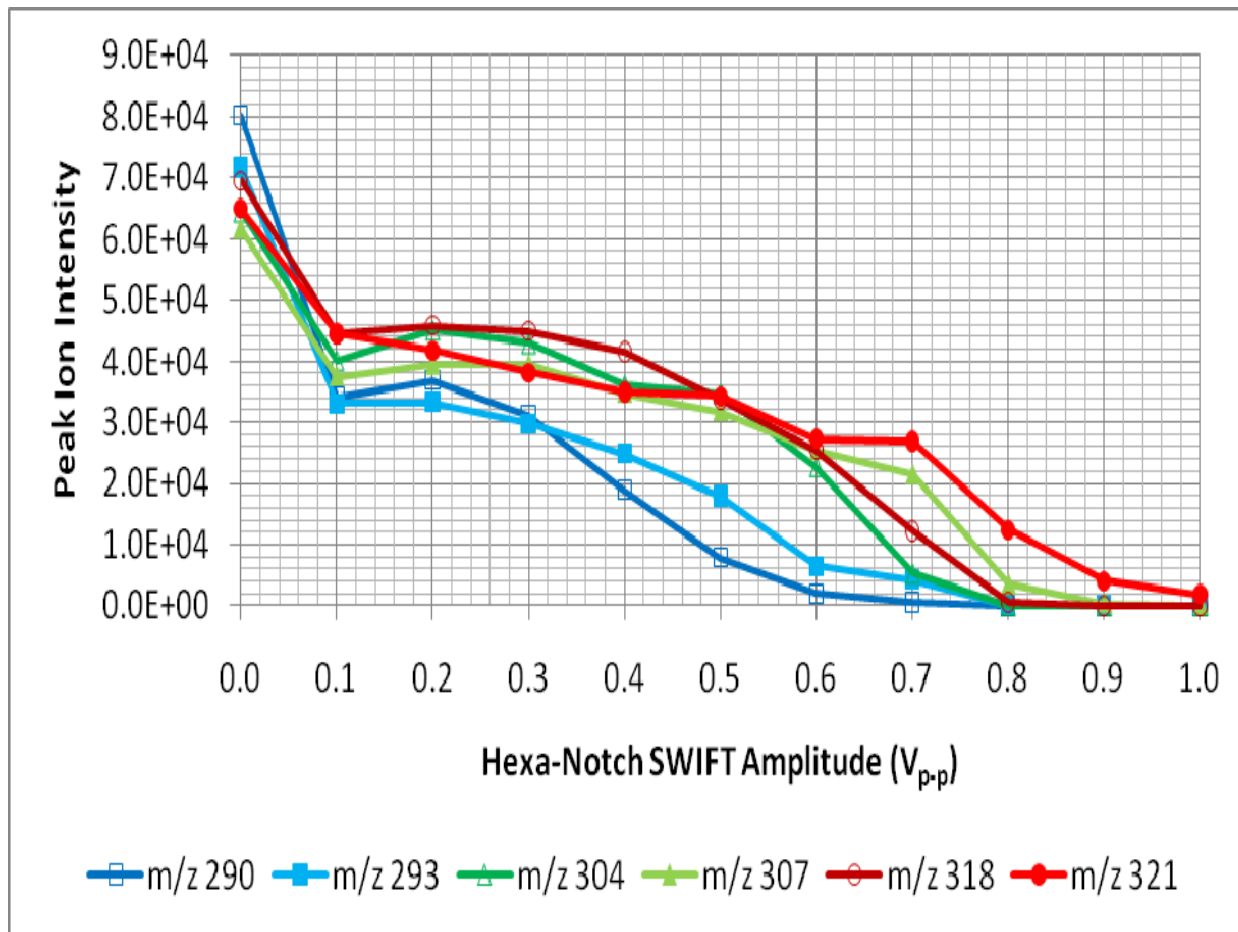


Figure 4-4. Variable hexa-notch SWIFT amplitude (m/z 305.8 at $q = 0.830$). Peak ion intensities of the $[M+H]^+$ ions of BE (m/z 290.2), BE- d_3 (m/z 293.2), COC (m/z 304.2), COC- d_3 (m/z 307.2), CE (m/z 318.2), and CE- d_3 (m/z 321.2) at different amplitudes (V_{p-p}) of a hexa-notch SWIFT isolation waveform applied to the analysis of brain tissue.

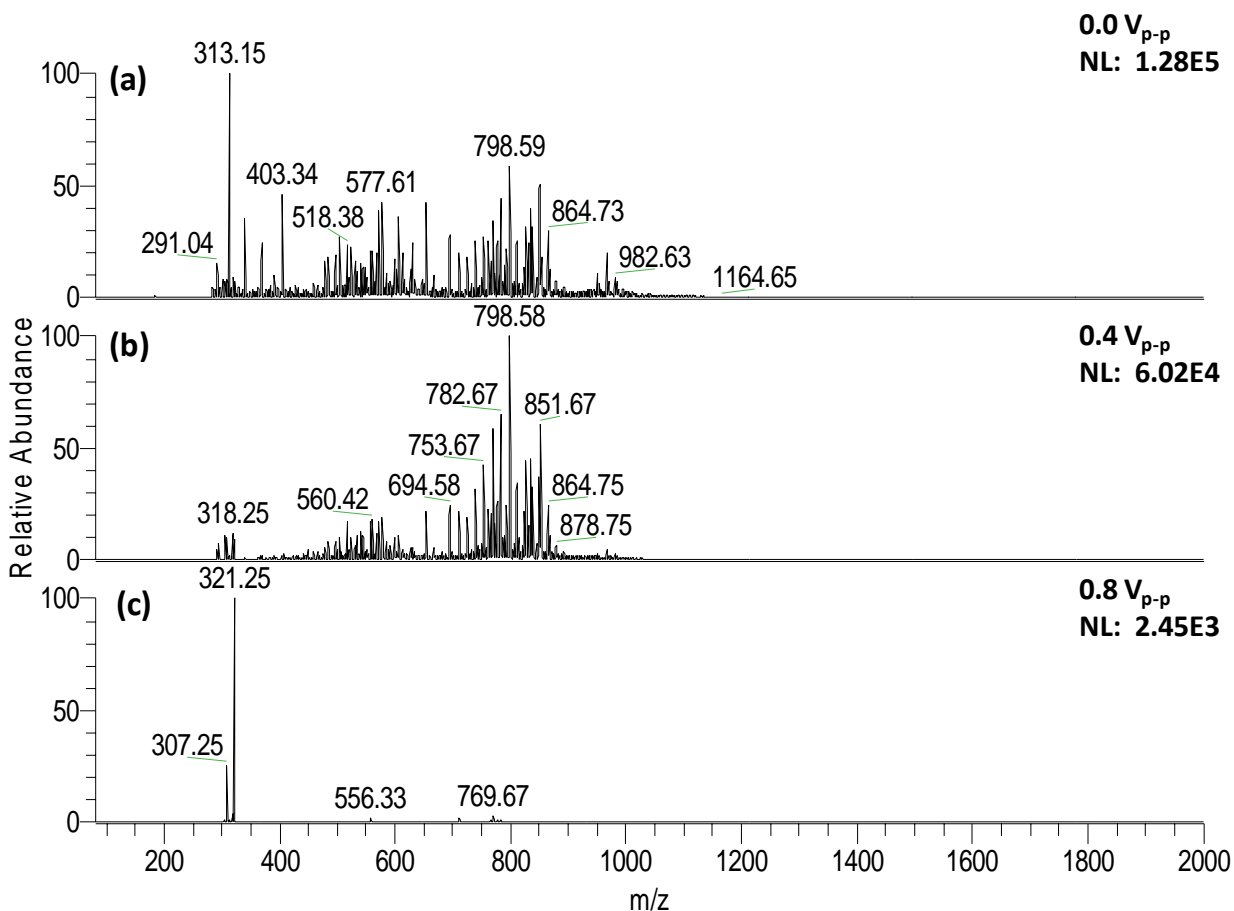


Figure 4-5. Mass spectra (m/z 80 to 2000) of hexa-notch SWIFT at different amplitudes. Hexa-notch SWIFT isolation waveform applied to BE, BE-d₃, COC, COC-d₃, CE, and CE-d₃ standards that were spiked (1 μ L; 1 μ g/mL each) onto blank brain tissue and airbrushed with DHB matrix with a SWIFT amplitude of (a) 0.0 V_{p-p} (b) 0.4 V_{p-p} , and (c) 0.8 V_{p-p} .

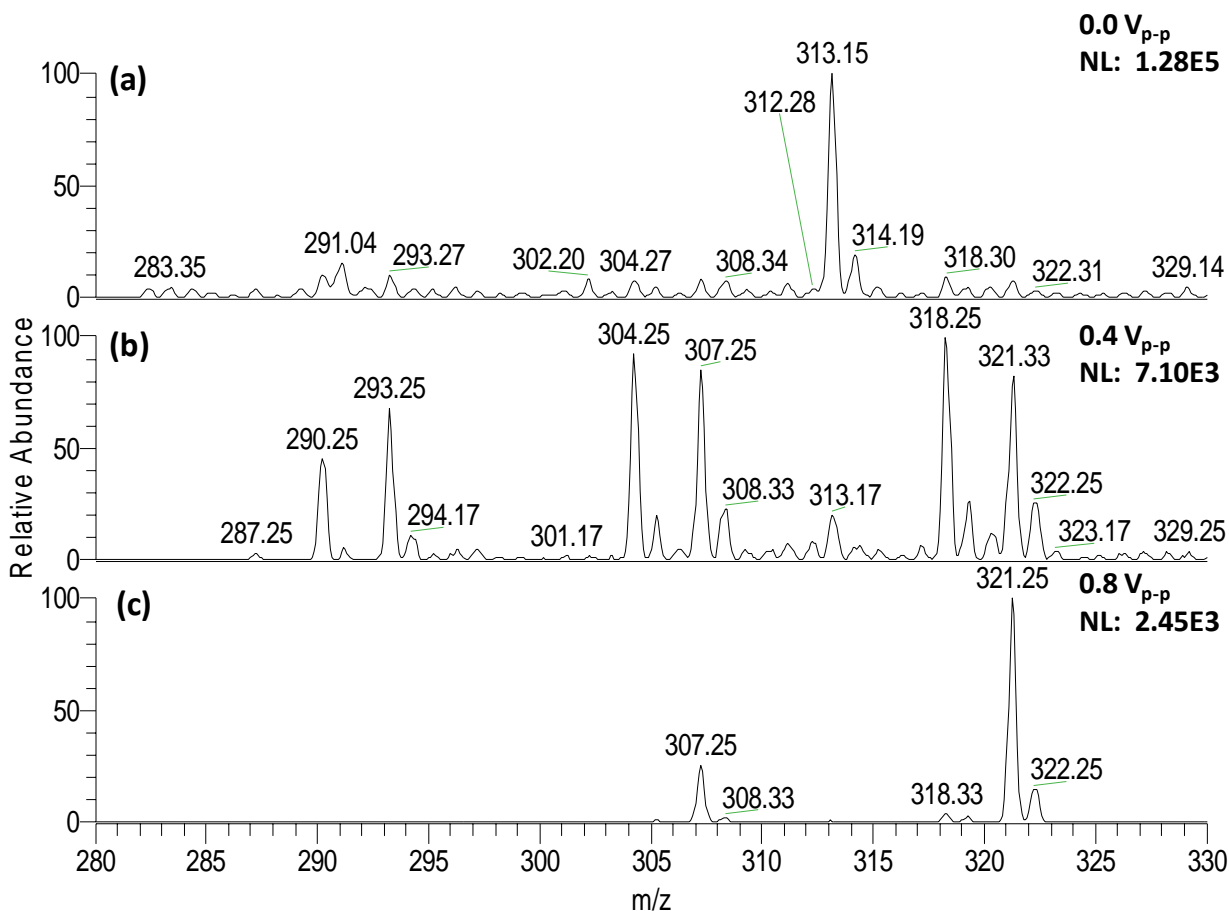


Figure 4-6. Mass spectra (m/z 280 to 330) of hexa-notch SWIFT at different amplitudes. Hexa-notch SWIFT isolation waveform applied to BE, BE-d₃, COC, COC-d₃, CE, and CE-d₃ standards that were spiked (1 μ L; 1 μ g/mL each) onto blank brain tissue and airbrushed with DHB matrix with a SWIFT amplitude of (a) 0.0 V_{p-p} (b) 0.4 V_{p-p} , and (c) 0.8 V_{p-p} .

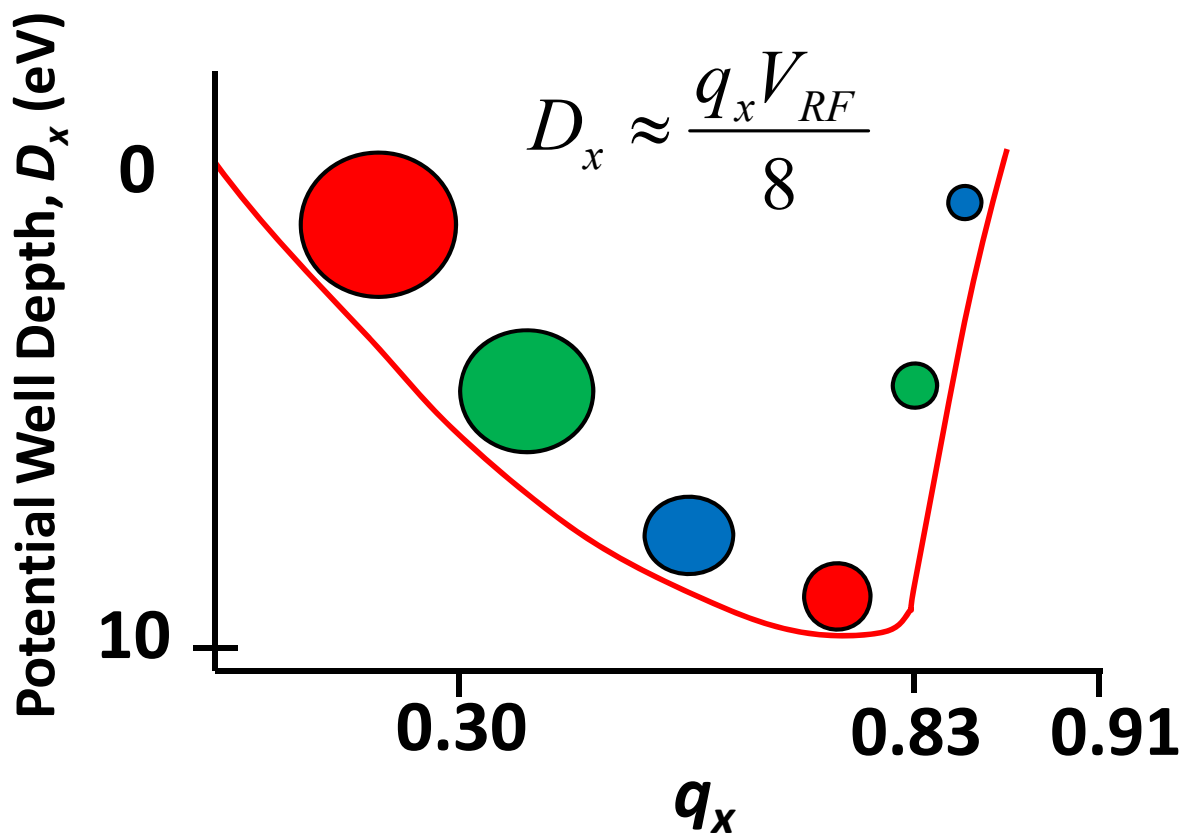


Figure 4-7. Pseudopotential well depth (D_x) of the ion trap. The deepest part of the pseudopotential well is near the q of isolation at $q_x = 0.83$. The sizes of the circles are proportional to the m/z of the ions. Adapted from March, R.E. *J. Mass Spectrom.* **1997**, 32, 351.

Table 4-2. Hexa-notch SWIFT properties based on m/z 290.2 at $q = 0.830$

Analyte	$[M+H]^+$ (m/z)	q value	Notch Width (Da)	Notch Frequencies (kHz)
BE	290.2	0.830	1.5	435.058594 to 439.453125
BE-d ₃	293.2	0.822	1.5	426.757812 to 430.664062
COC	304.2	0.792	1.5	400.146484 to 403.564453
COC-d ₃	307.2	0.784	1.5	393.798828 to 396.972656
CE	318.2	0.757	1.5	372.802734 to 375.488281
CE-d ₃	321.2	0.750	1.5	367.675781 to 370.117187

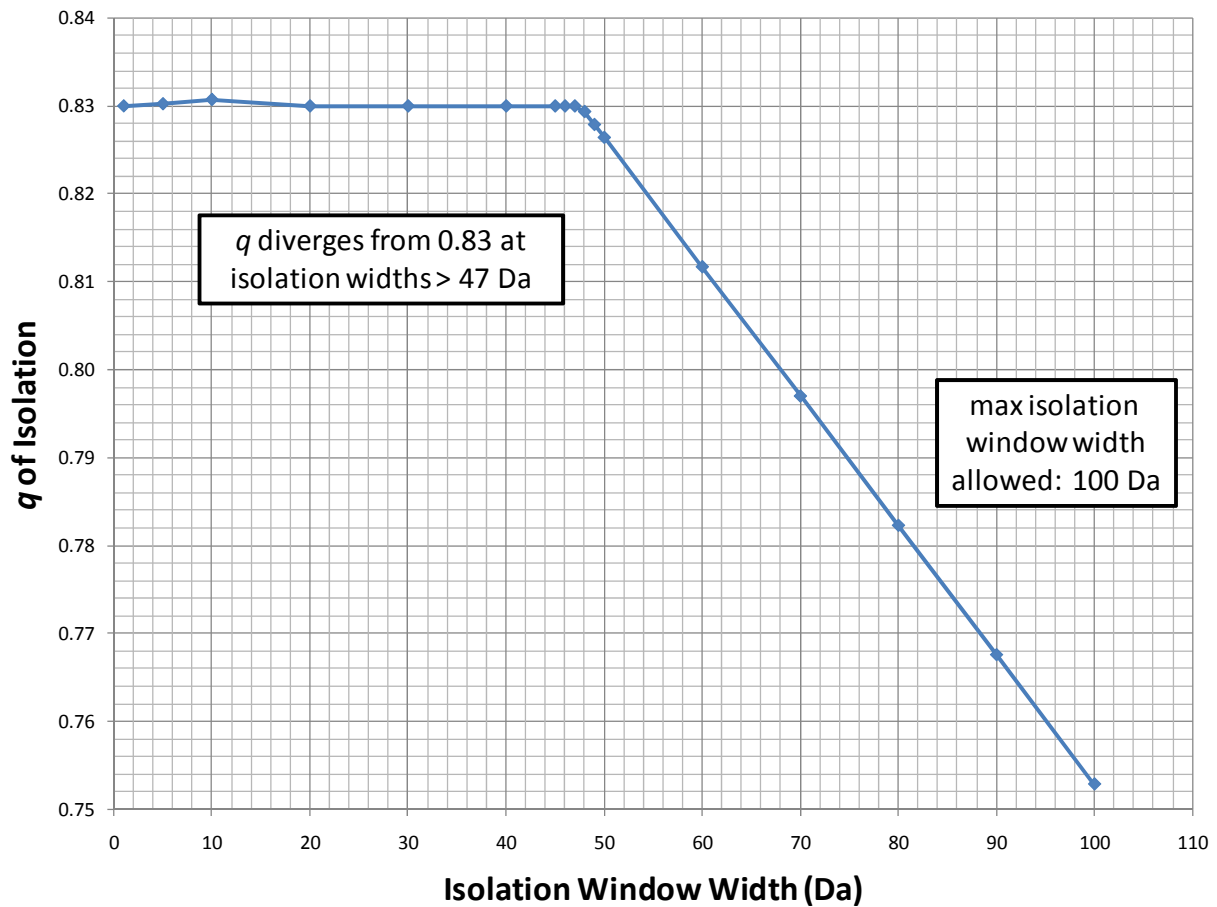


Figure 4-8. Isolation window width (Da) determined by the preset q of isolation. The q of isolation diverges from $q = 0.83$ at isolation widths greater than 47 Da to ensure that ions to be isolated are above the low mass cutoff (LMCO). The maximum isolation window width allowed by the LTQ software is 100 Da.

Table 4-3. Hexa-notch SWIFT properties based on m/z 290.2 at $q = 0.791$

Analyte	$[M+H]^+$ (m/z)	q value	Notch Width (Da)	Notch Frequencies (kHz)
BE	290.2	0.791	1.5	399.902344 to 403.320312
BE-d ₃	293.2	0.783	1.5	393.066406 to 396.484375
COC	304.2	0.755	1.5	371.337891 to 374.023437
COC-d ₃	307.2	0.747	1.5	365.966797 to 368.652344
CE	318.2	0.721	1.5	347.656250 to 350.097656
CE-d ₃	321.2	0.715	1.5	343.261719 to 345.458984

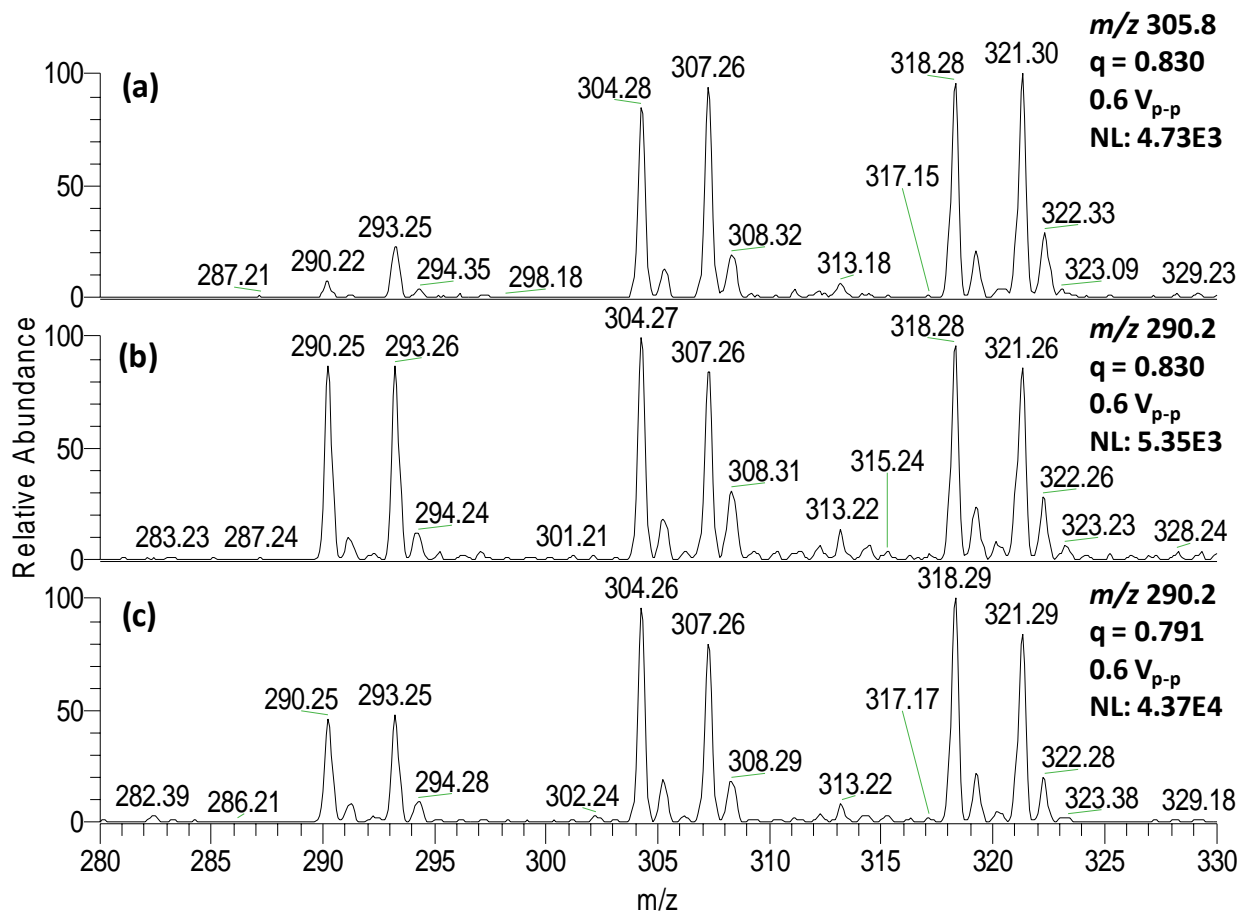


Figure 4-9. Hexa-notch SWIFT applied at variable q of isolation. Hexa-notch SWIFT isolation waveform applied to BE, BE-d₃, COC, COC-d₃, CE, and CE-d₃ standards that were spiked (1 μ L; 1 μ g/mL each) onto blank brain tissue and airbrushed with DHB matrix with a SWIFT amplitude of $0.6 V_{p-p}$ and the m/z at q of isolation set to (a) m/z 305.8 ($q = 0.830$), (b) m/z 290.2 ($q = 0.830$), and (c) m/z 290.2 ($q = 0.791$); m/z range 280 to 330.

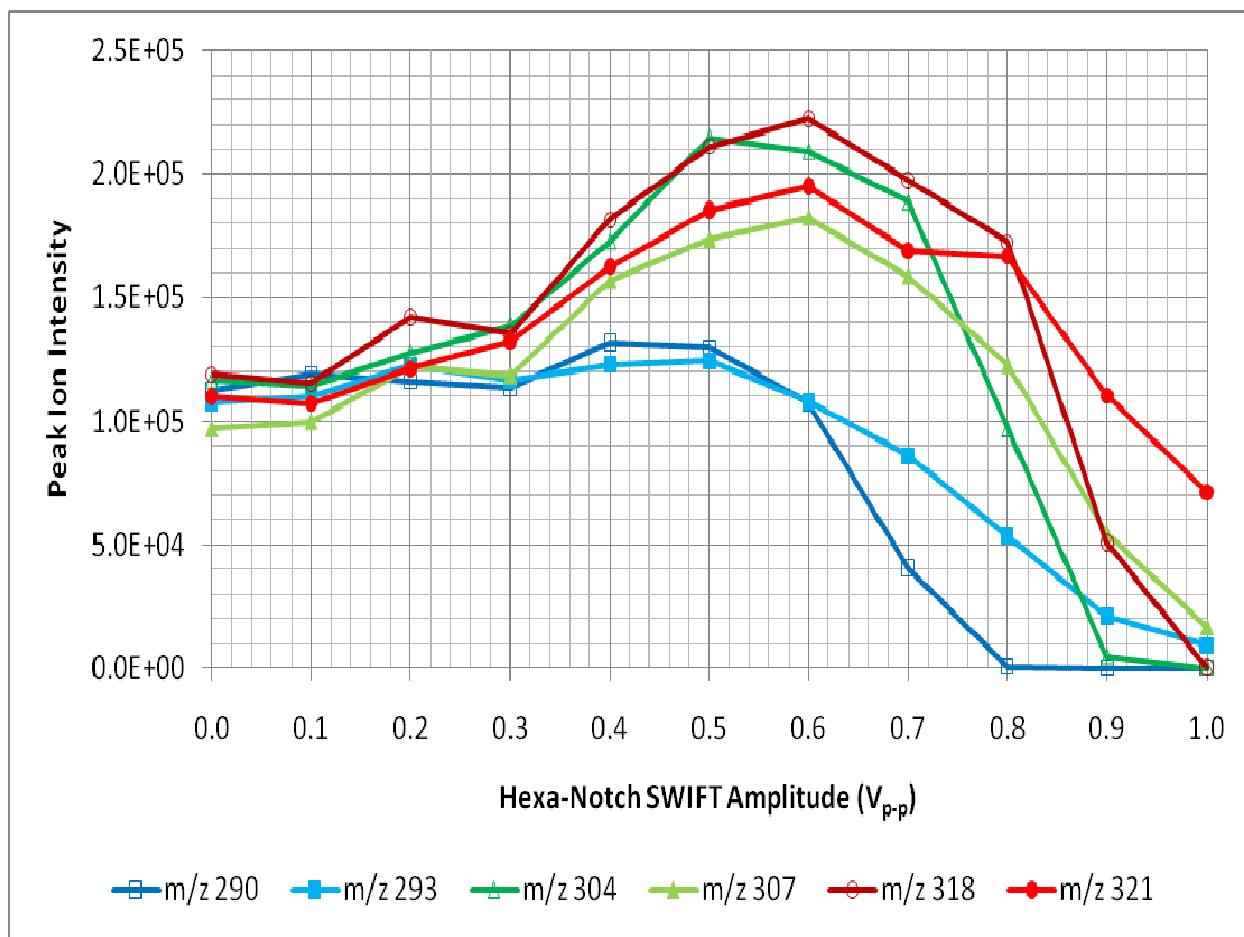


Figure 4-10. Variable hexa-notch SWIFT amplitude (m/z 290.2 at $q = 0.791$). Peak ion intensities of the $[M+H]^+$ ions of BE (m/z 290.2), BE- d_3 (m/z 293.2), COC (m/z 304.2), COC- d_3 (m/z 307.2), CE (m/z 318.2), and CE- d_3 (m/z 321.2) at different amplitudes (V_{p-p}) of a hexa-notch SWIFT isolation waveform based on m/z 290.2 at $q = 0.791$.

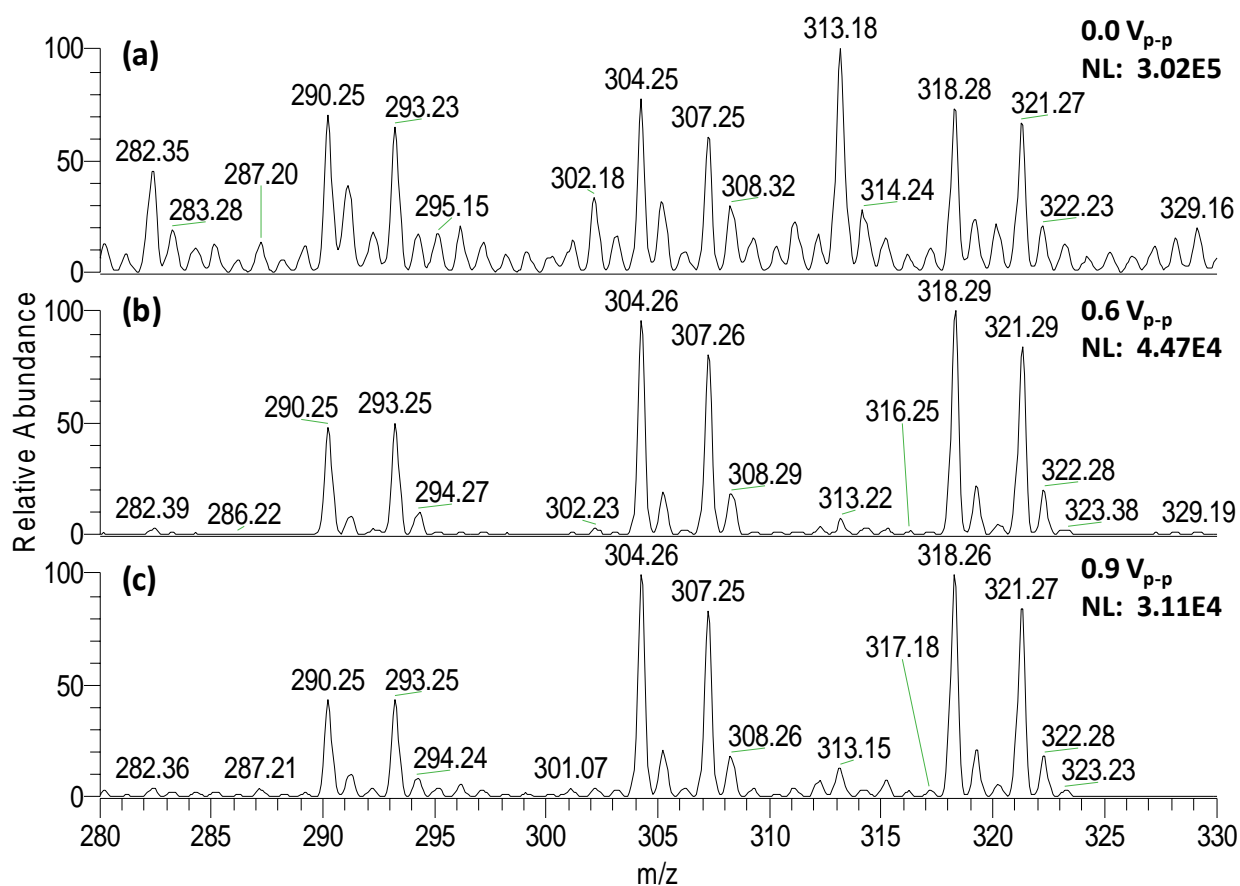


Figure 4-11. Mass spectra (m/z 280 to 330) of hexa-notch SWIFT at different amplitudes. Hexa-notch SWIFT isolation waveform based on m/z 290.2 at $q = 0.791$ applied to BE, BE- d_3 , COC, COC- d_3 , CE, and CE- d_3 standards that were spiked (1 μ L; 1 μ g/mL each) onto blank brain tissue and airbrushed with DHB matrix with a SWIFT amplitude of (a) $0.0 V_{p-p}$, (b) $0.6 V_{p-p}$, and (c) $0.9 V_{p-p}$

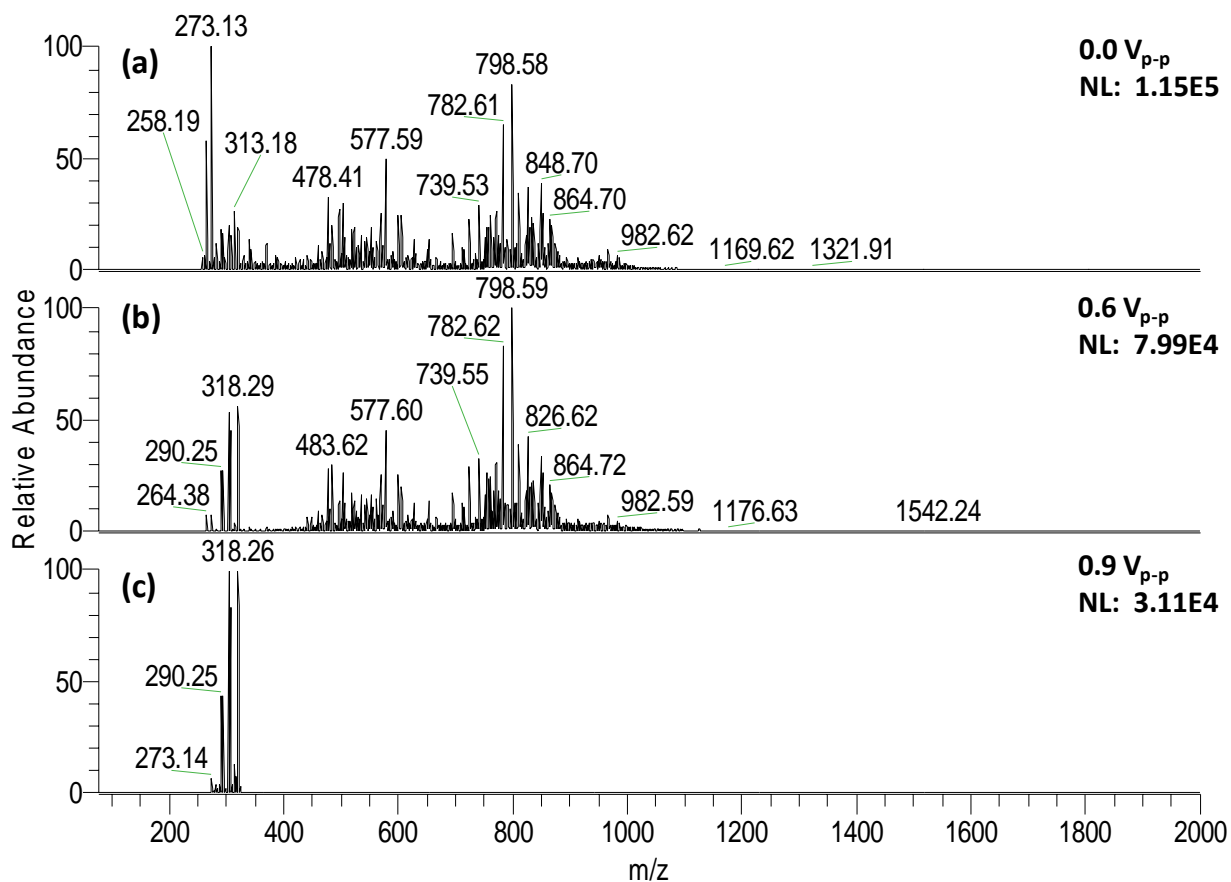


Figure 4-12. Mass spectra (m/z 80 to 2000) of hexa-notch SWIFT at different amplitudes. Hexa-notch SWIFT isolation waveform based on m/z 290.2 at $q = 0.791$ applied to BE, BE- d_3 , COC, COC- d_3 , CE, and CE- d_3 standards that were spiked (1 μ L; 1 μ g/mL each) onto blank brain tissue and airbrushed with DHB matrix with a SWIFT amplitude of (a) 0.0 V_{p-p} , (b) 0.6 V_{p-p} , and (c) 0.9 V_{p-p} .

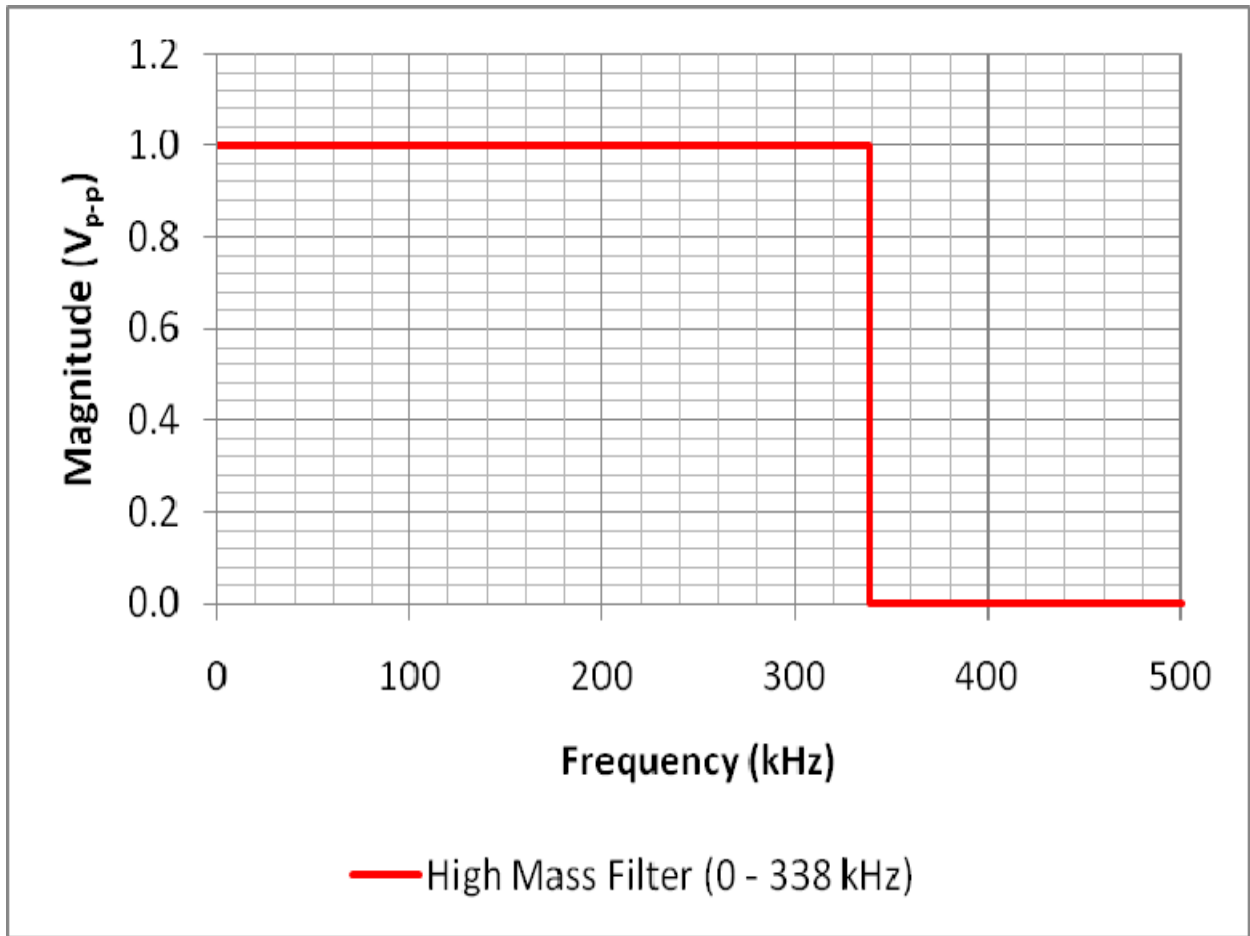


Figure 4-13. Frequency domain of high mass filter (HMF). HMF is calculated to excite at frequencies 0 to 338 kHz based on m/z 290.2 at a q of isolation ($q = 0.791$). This HMF is designed to eject/excite ions from m/z 325.8 to greater than m/z 2000 (LTQ upper m/z limit; 48 kHz).

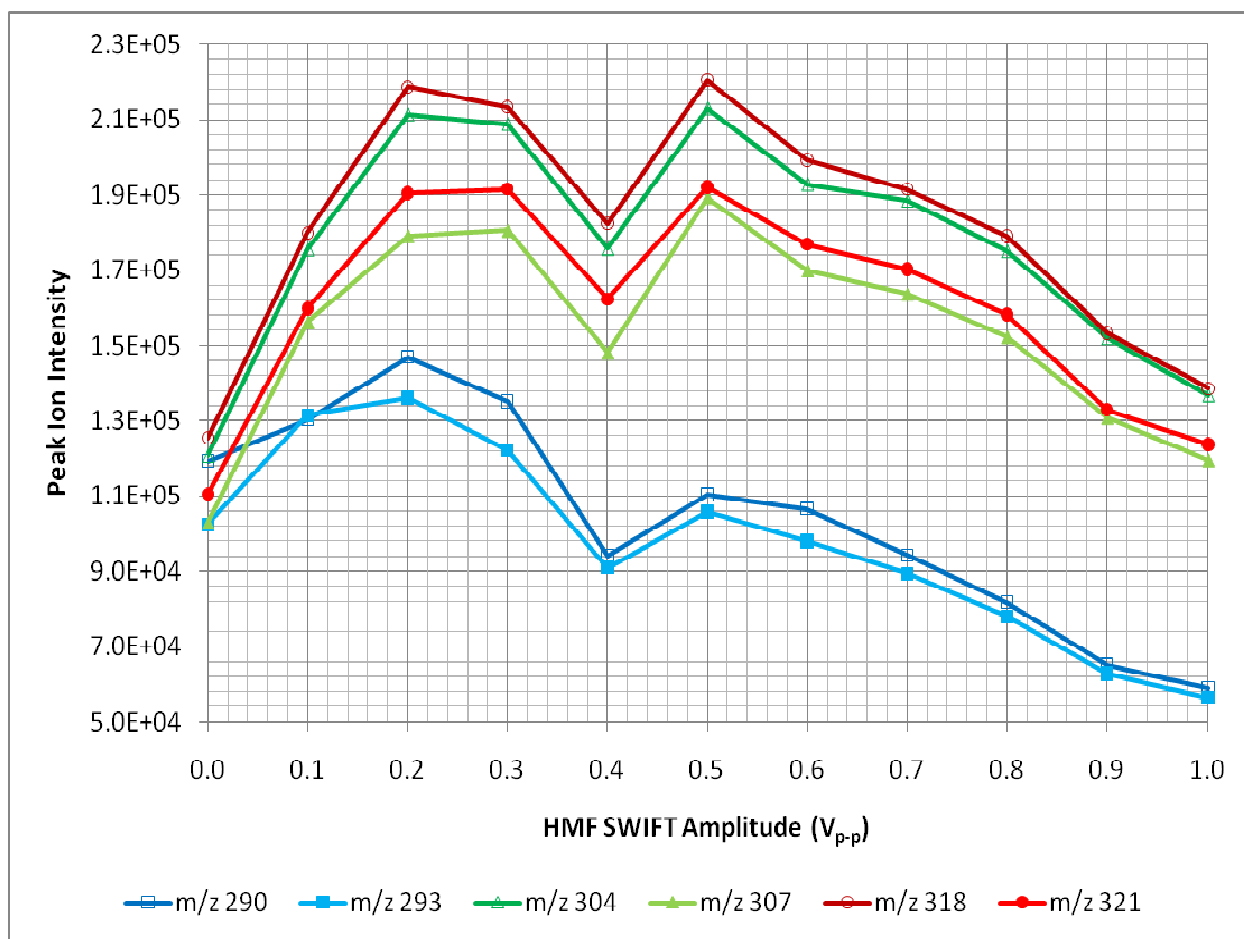


Figure 4-14. Variable amplitude of HMF. Peak ion intensities of the $[M+H]^+$ ions of BE (m/z 290.2), BE- d_3 (m/z 293.2), COC (m/z 304.2), COC- d_3 (m/z 307.2) CE (m/z 318.2), and CE- d_3 (m/z 321.2) at different amplitudes (V_{p-p}) of a high mass filter (HMF) with m/z cutoff at 325.8 applied to the analysis of brain tissue.

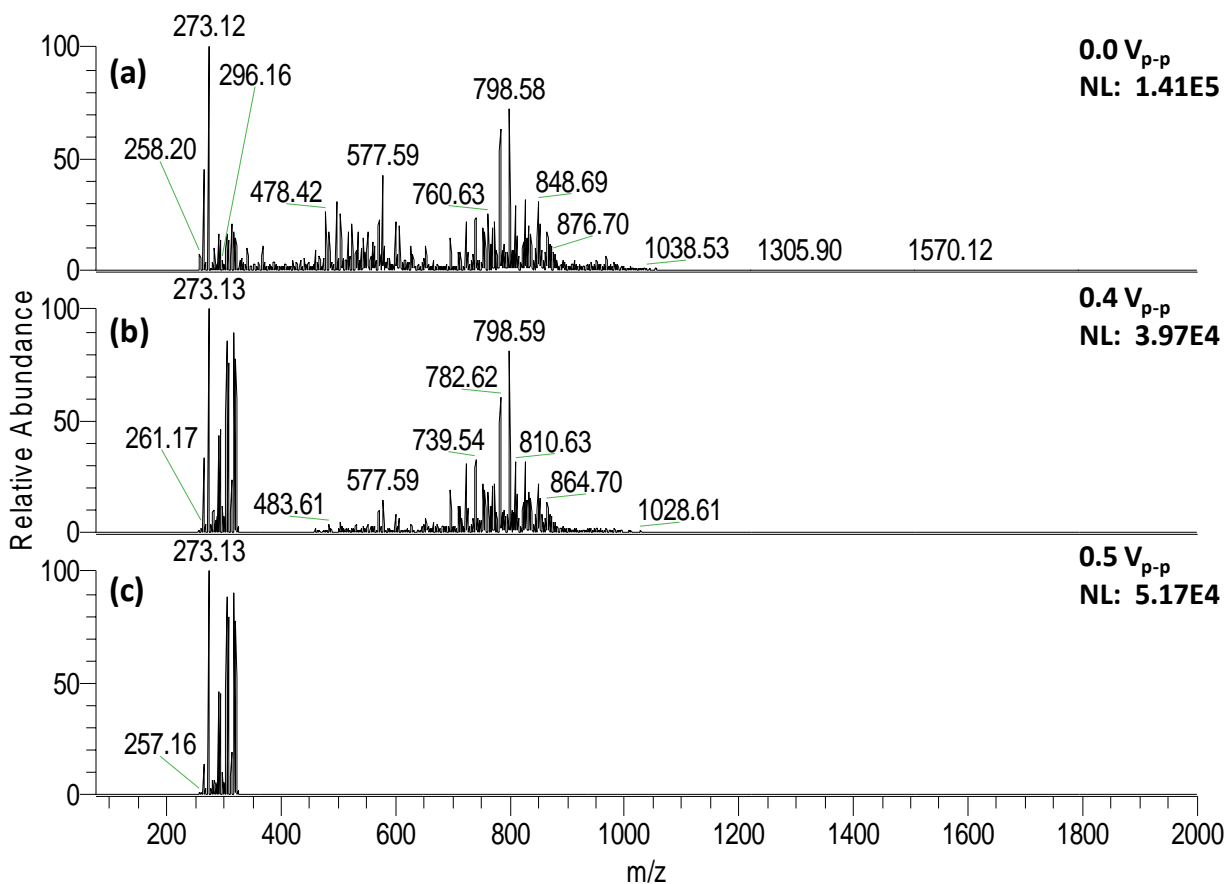


Figure 4-15. Mass spectra (m/z 80 to 2000) of HMF at different amplitudes. HMF SWIFT excitation waveform applied to BE, BE- d_3 , COC, COC- d_3 , CE, and CE- d_3 standards that were spiked (1 μ L; 1 μ g/mL each) onto blank brain tissue and airbrushed with DHB matrix with a SWIFT amplitude of (a) 0.0 V_{p-p} , (b) 0.4 V_{p-p} , and (c) 0.5 V_{p-p} .

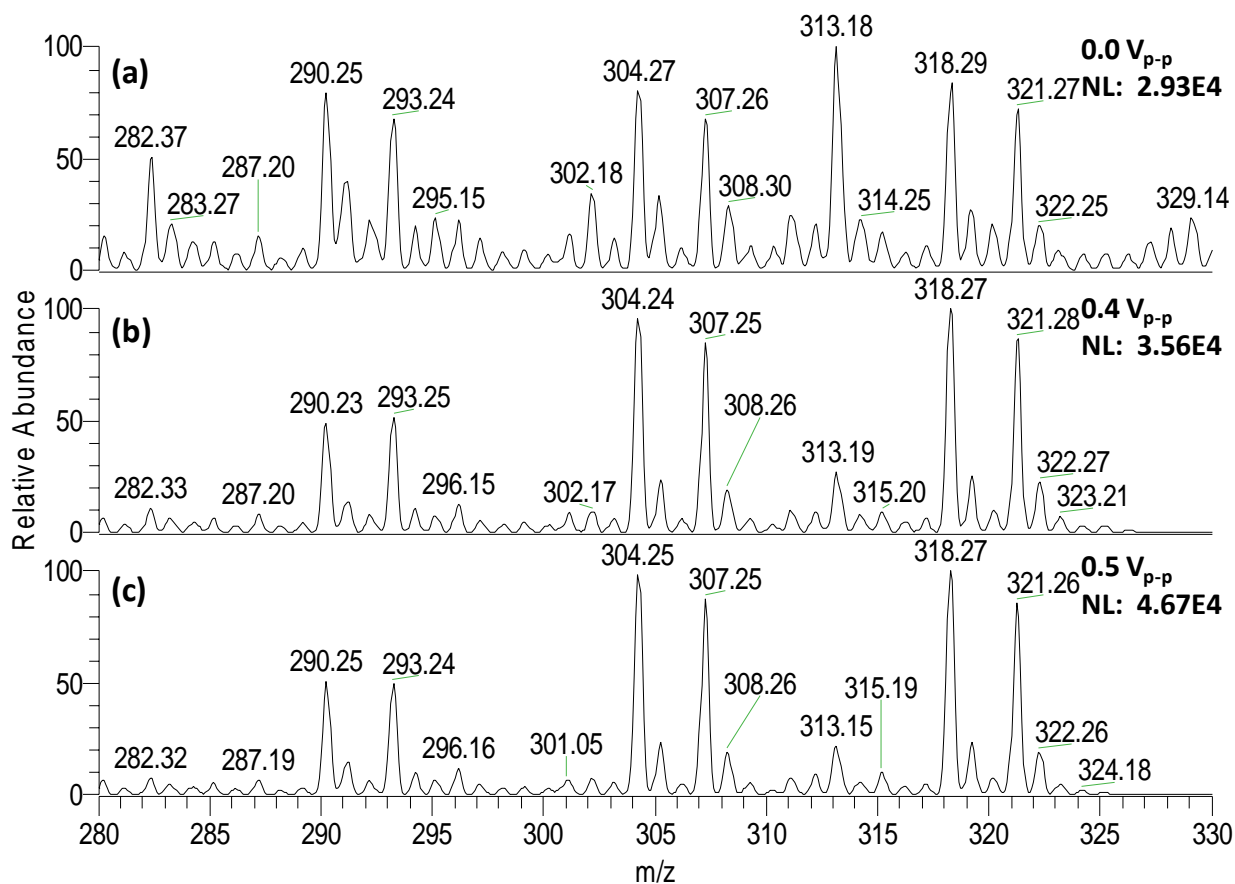


Figure 4-16. Mass spectra (m/z 280 to 330) of HMF at different amplitudes. HMF SWIFT excitation waveform applied to BE, BE- d_3 , COC, COC- d_3 , CE, and CE- d_3 standards that were spiked (1 μ L; 1 μ g/mL each) onto blank brain tissue and airbrushed with DHB matrix with a SWIFT amplitude of (a) $0.0 V_{p-p}$, (b) $0.4 V_{p-p}$, and (c) $0.5 V_{p-p}$.

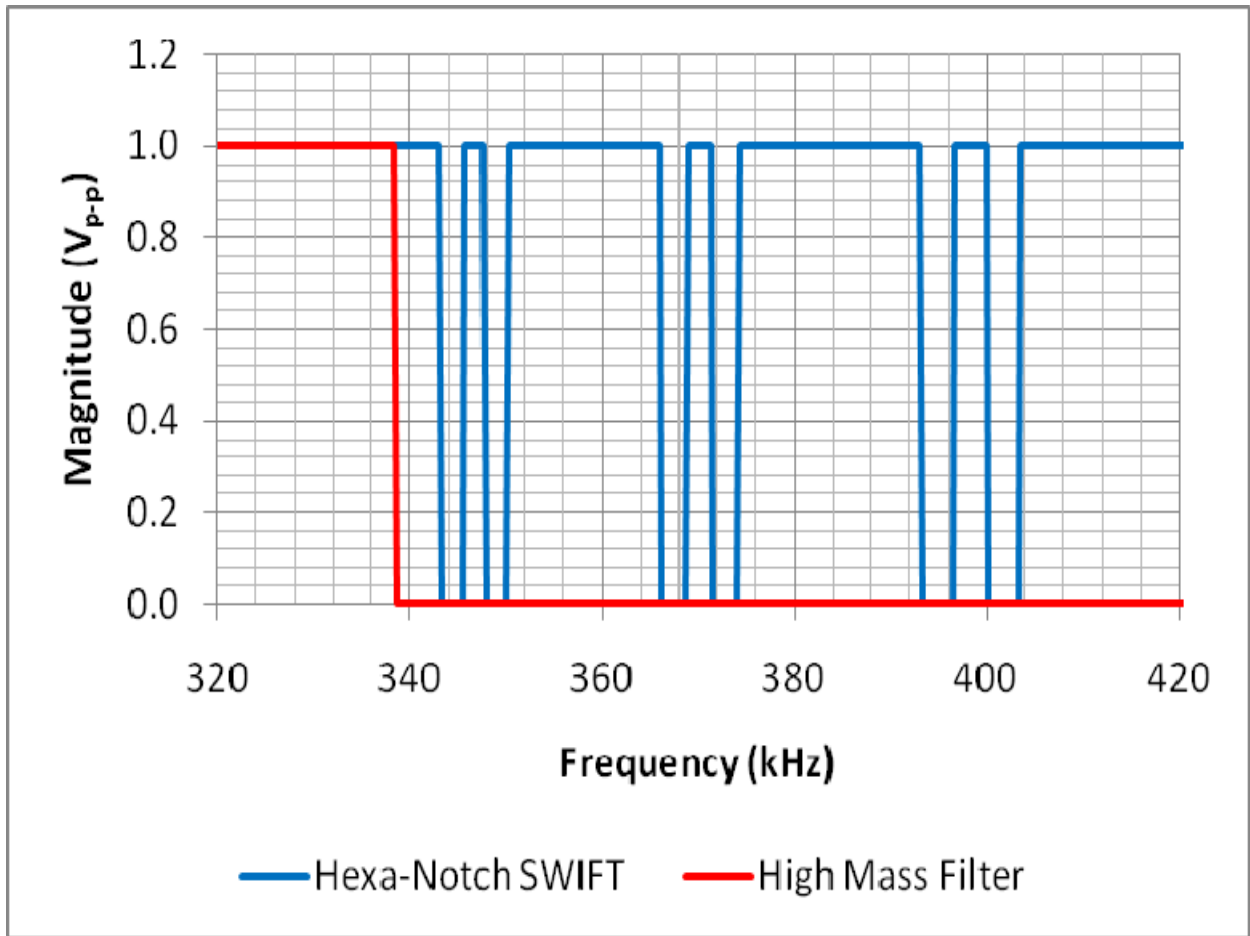


Figure 4-17. Frequency domain of two-stage SWIFT isolation. The frequency domain of the two-stage isolation performed by combining a HMF SWIFT excitation waveform (red) to eject ions heavier than m/z 325.8 with a hexa-notch SWIFT isolation waveform (blue) to selectively isolate ions at m/z 290.2, 293.2, 304.2, 307.2, 318.2, and 321.2.

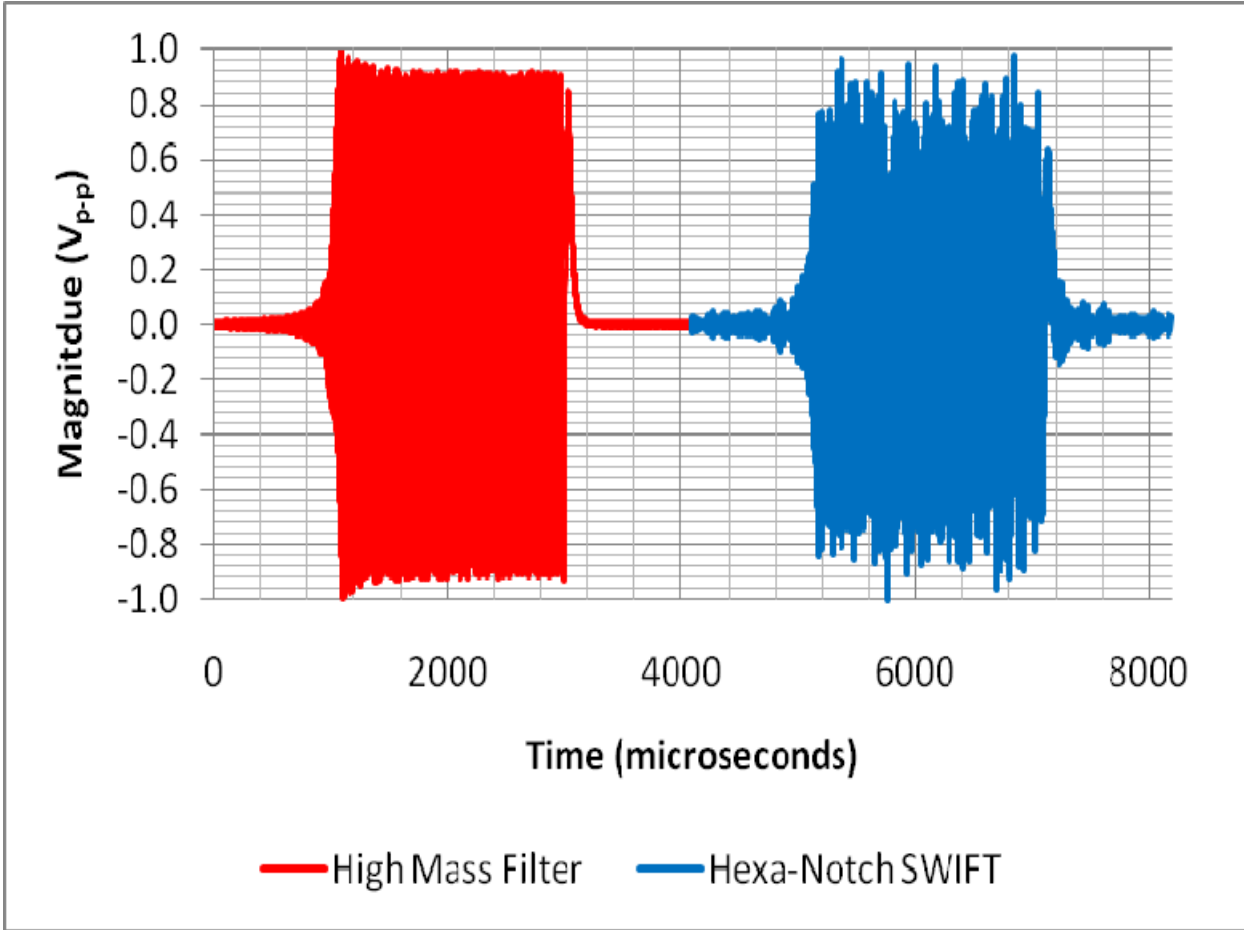


Figure 4-18. The time domain of the two-stage SWIFT isolation. The two-stage isolation is composed of a HMF SWIFT excitation waveform (red) occurring from 0 to 4,096 μs and the hexa-notch SWIFT isolation waveform (blue) occurring from 4,097 to 8,192 μs . A single burst of the two-stage isolation pulse (8,192 μs) is triggered during the LTQ isolation event (15,500 μs).

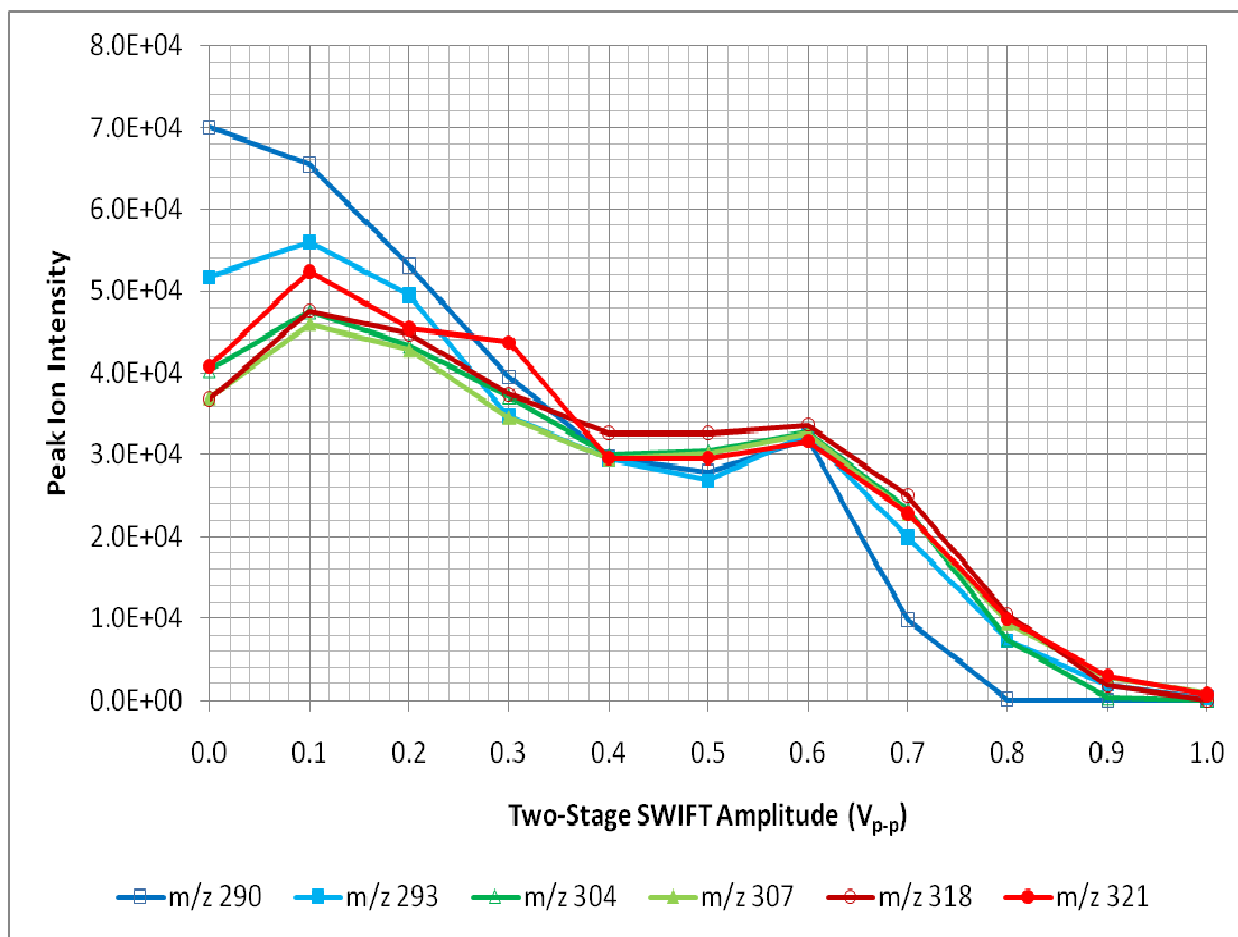


Figure 4-19. Variable amplitude of two-stage SWIFT isolation. Peak ion intensities of the $[M+H]^+$ ions of BE (m/z 290.2), BE- d_3 (m/z 293.2), COC (m/z 304.2), COC- d_3 (m/z 307.2) CE (m/z 318.2), and CE- d_3 (m/z 321.2) at different amplitudes (V_{p-p}) of a two-stage isolation composed of a HMF SWIFT excitation waveform and a hexa-notch SWIFT isolation waveform applied to the analysis of brain tissue.

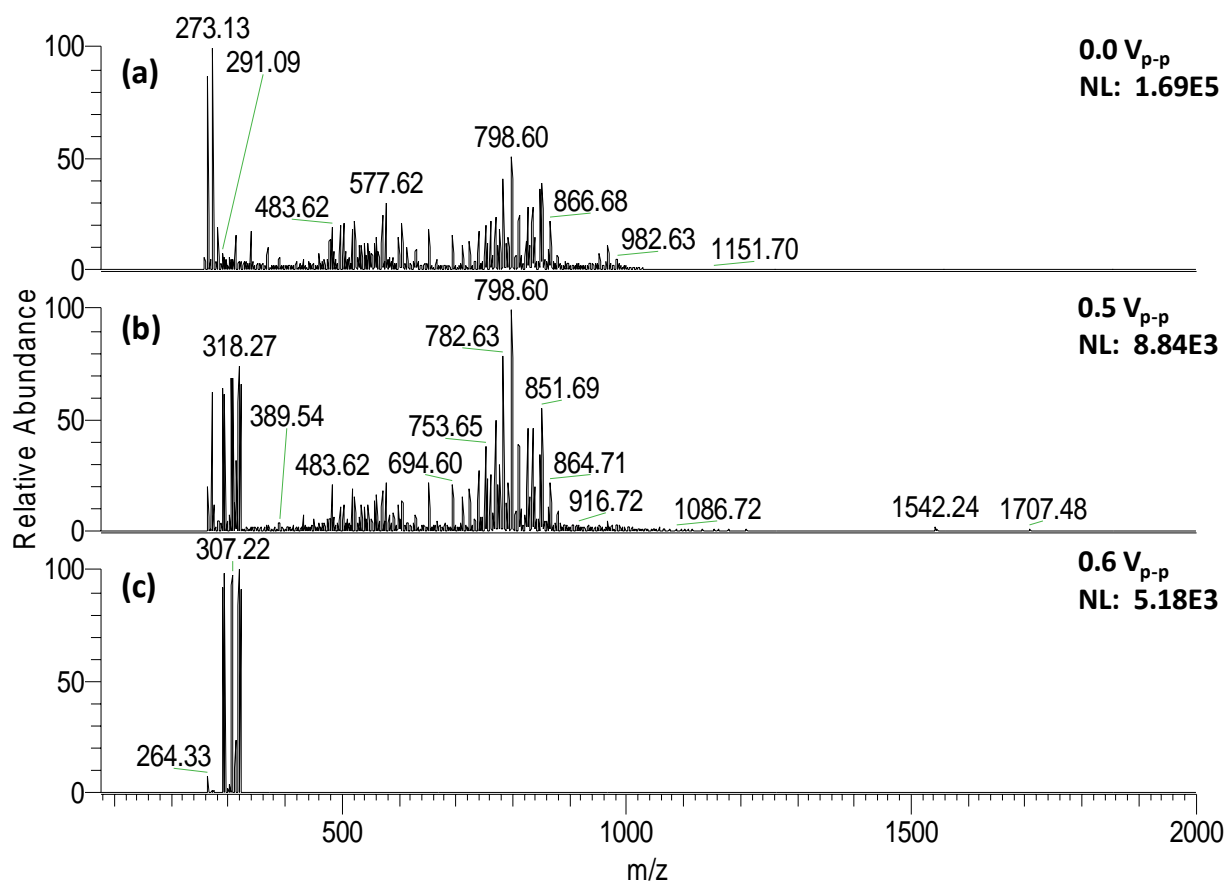


Figure 4-20. Mass spectra (m/z 80 to 2000) of two-stage SWIFT isolation at different amplitudes. Two-stage isolation composed of a HMF SWIFT excitation waveform and a hexa-notch SWIFT isolation waveform that was applied to BE, BE- d_3 , COC, COC- d_3 , CE, and CE- d_3 standards that were spiked ($1 \mu\text{L}$; $1 \mu\text{g/mL}$ each) onto blank brain tissue and airbrushed with DHB matrix with both SWIFT amplitudes at (a) $0.0 V_{p-p}$, (b) $0.5 V_{p-p}$, and (c) $0.6 V_{p-p}$.

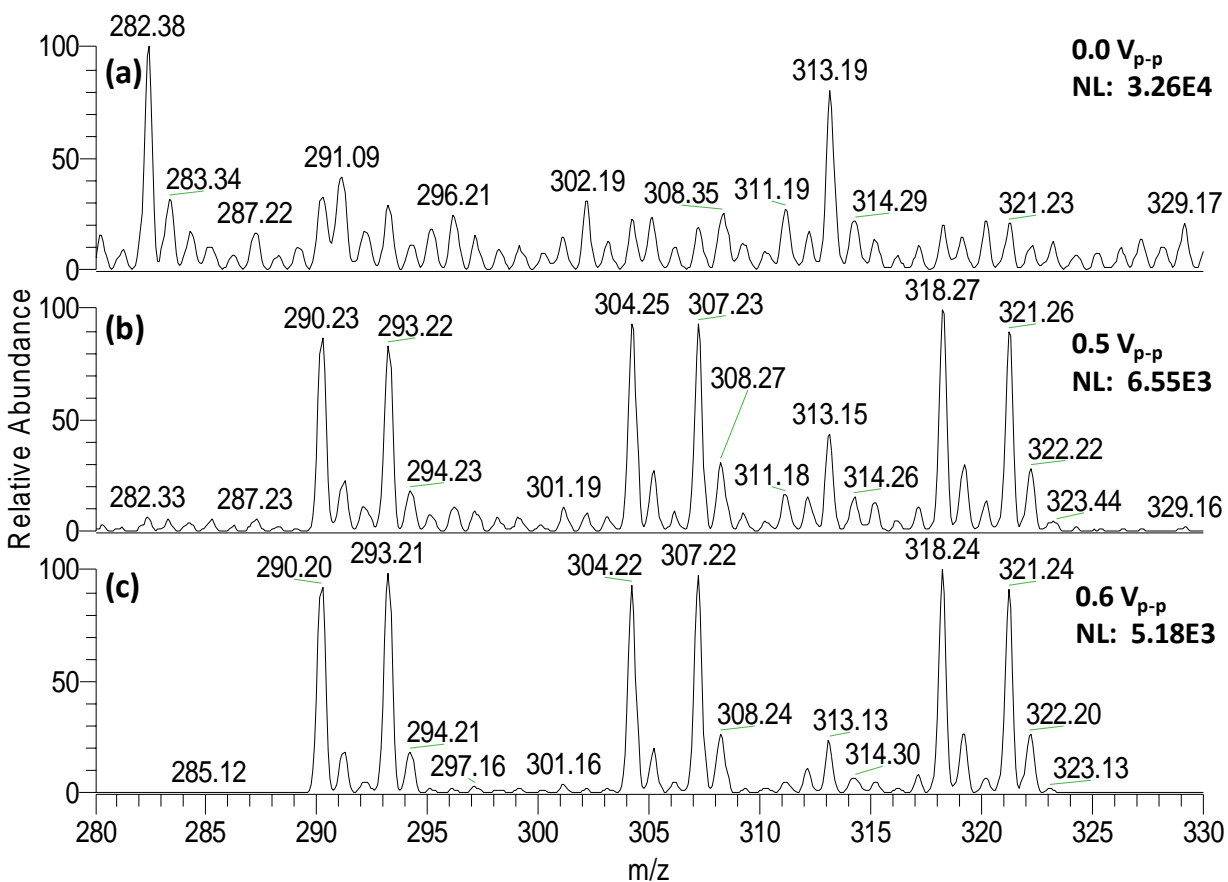


Figure 4-21. Mass spectra (m/z 280 to 330) of two-stage SWIFT isolation at different amplitudes. Two-stage isolation composed of a HMF SWIFT excitation waveform and a hexa-notch SWIFT isolation waveform that was applied to BE, BE- d_3 , COC, COC- d_3 , CE, and CE- d_3 standards that were spiked (1 μ L; 1 μ g/mL each) onto blank brain tissue and airbrushed with DHB matrix with both SWIFT amplitudes at (a) 0.0 V_{p-p} , (b) 0.5 V_{p-p} , and (c) 0.6 V_{p-p} .

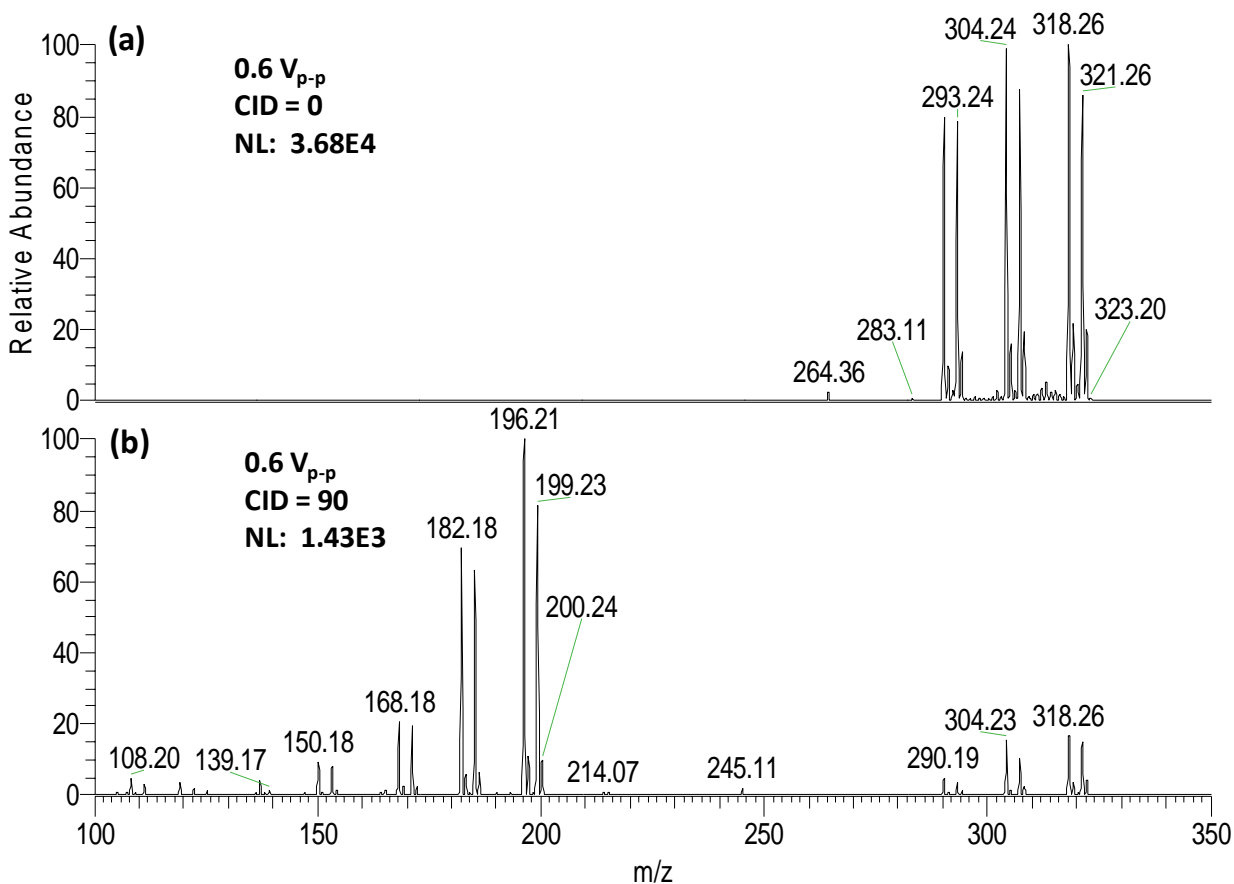


Figure 4-22. MS/MS product spectra from the application of a two-stage isolation. Two-stage SWIFT is composed of a HMF SWIFT excitation waveform and a hexa-notch SWIFT isolation waveform with both SWIFT amplitudes at 0.6 V_{p-p} and collision-induced dissociation (CID) set to (a) 0 and (b) 90.

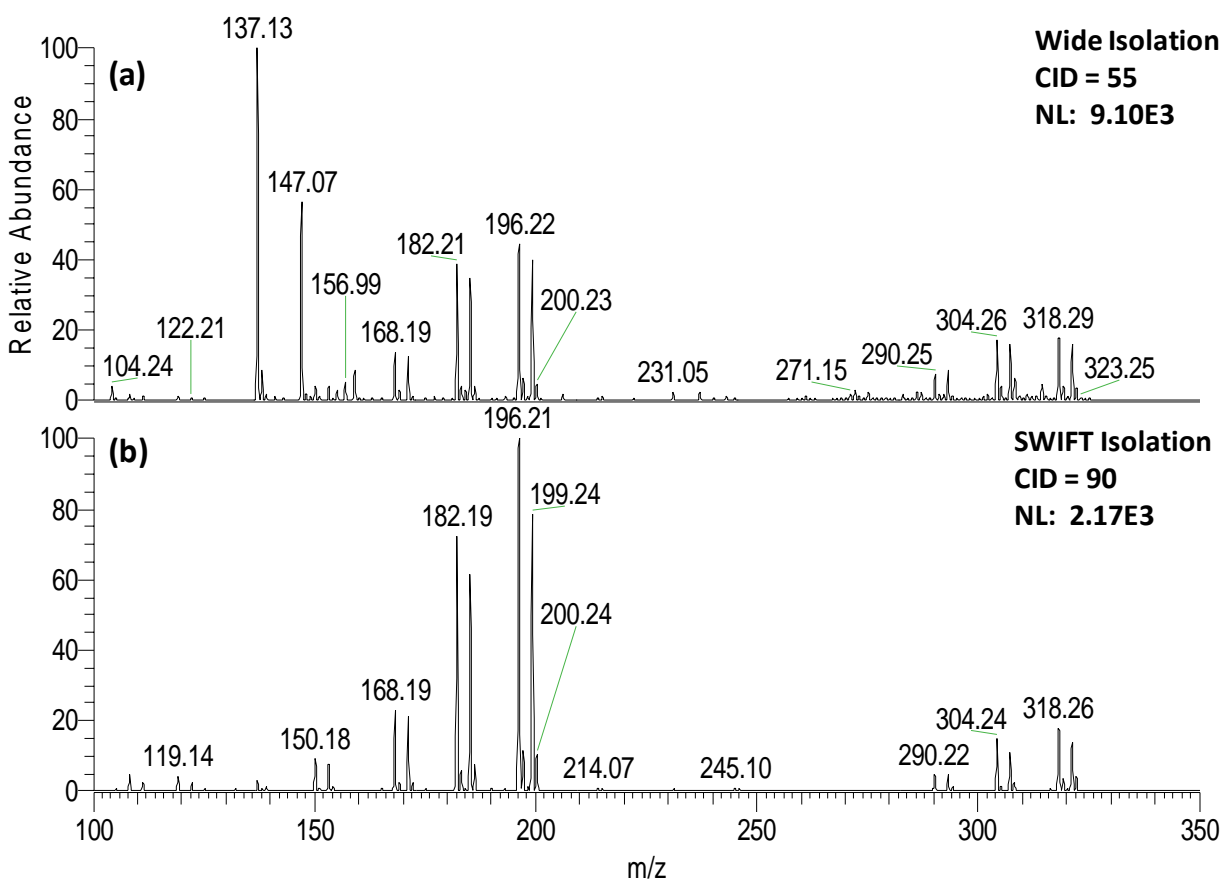


Figure 4-23. Comparison of MS/MS with wide isolation and two-stage SWIFT isolation. MS/MS product spectra from the application of a (a) 40-Da wide isolation with CID = 55 and a (b) two-stage isolation composed of a HMF SWIFT excitation waveform and a hexa-notch SWIFT isolation waveform with both SWIFT amplitudes at $0.6 V_{p-p}$ and CID = 90.

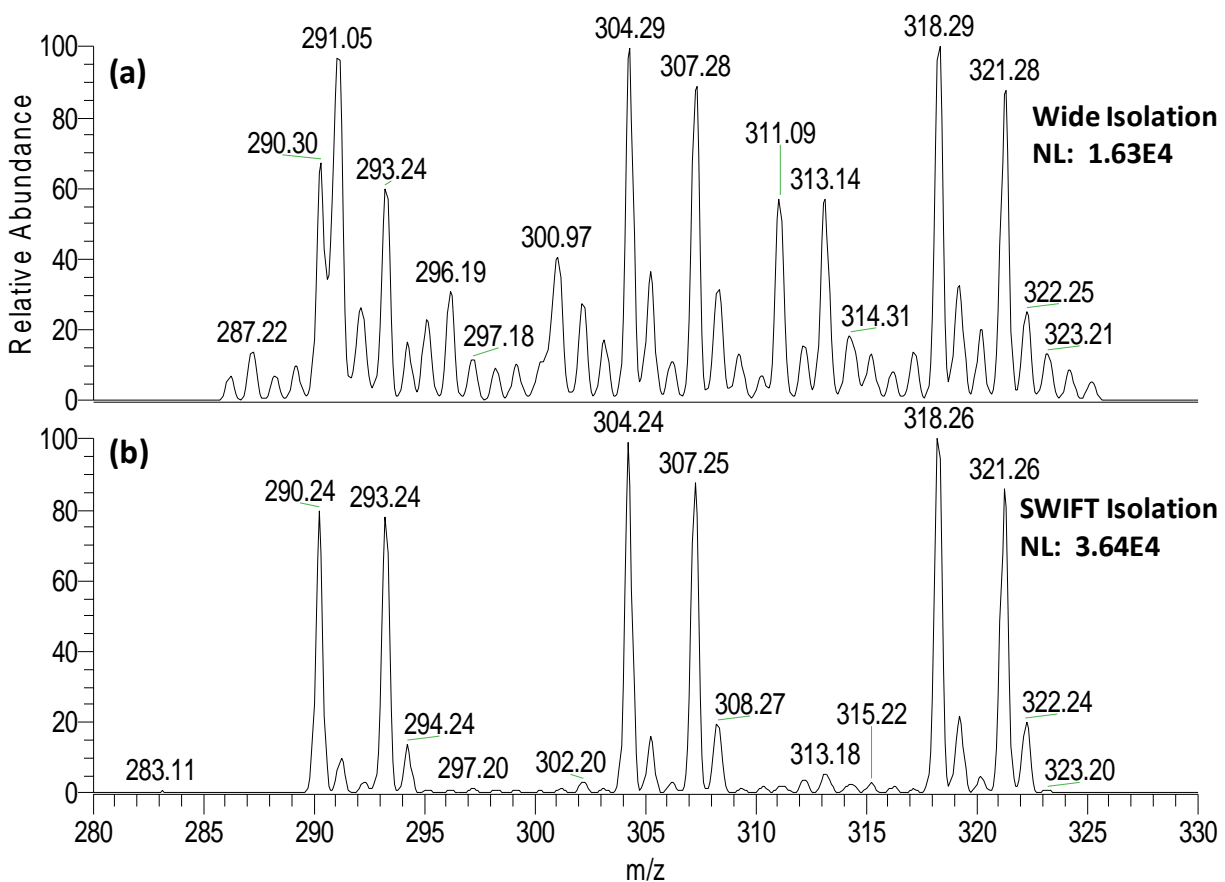


Figure 4-24. Mass spectra comparison of wide isolation and two-stage SWIFT isolation. Isolated ions from the application of a (a) 40-Da wide isolation and a (b) two-stage isolation composed of a HMF SWIFT excitation waveform and a hexa-notch SWIFT isolation waveform with both SWIFT amplitudes at $0.6 V_{p-p}$.

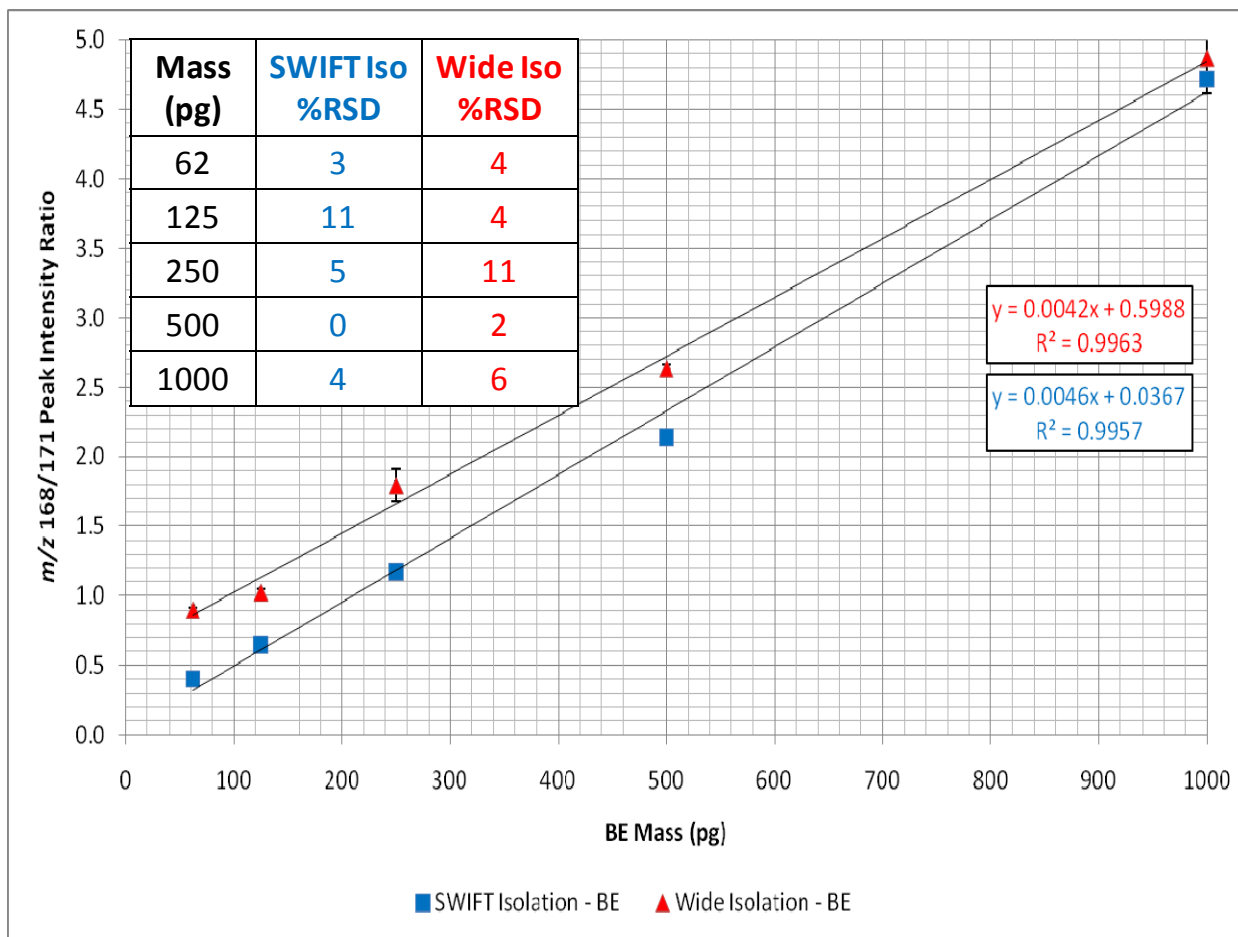


Figure 4-25. BE calibration curve for BE spiked on intact brain tissue. Five solutions (mixture of BE, COC, and CE at 62, 125, 250, 500, and 1000 ng/mL with a mixture of BE-d₃, COC-d₃, and CE-d₃ at 200 ng/mL) were pipetted in triplicate (1 μL each) onto blank human brain tissue and airbrushed with DHB matrix. The peak intensities of the product ions of BE and BE-d₃ at *m/z* 168 and *m/z* 171, respectively, were ratioed from two different MS/MS experiments: MS/MS of the ions isolated by a two-stage SWIFT isolation (CID = 90) and MS/MS of the ions isolated by a 40-Da wide isolation (CID = 55). The error bars correspond to ± the standard error (3 replicates).

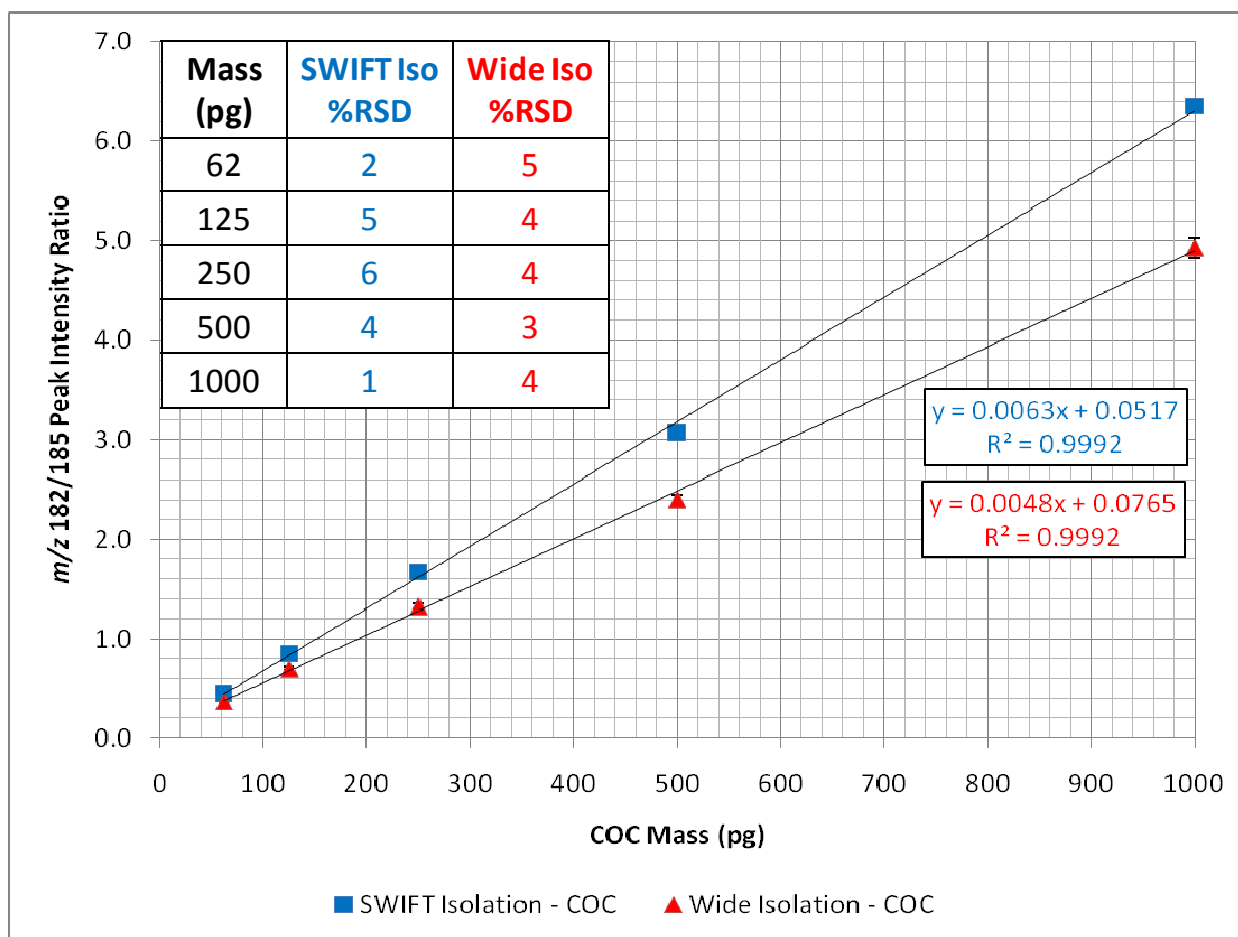


Figure 4-26. COC calibration curve for COC spiked on intact brain tissue. Five solutions (mixture of BE, COC, and CE at 62, 125, 250, 500, and 1000 ng/mL with a mixture of BE-d₃, COC-d₃, and CE-d₃ at 200 ng/mL) were pipetted in triplicate (1 μL each) onto blank human brain tissue and airbrushed with DHB matrix. The peak intensity of the product ions of COC and COC-d₃ at *m/z* 182 and *m/z* 185, respectively, were ratioed from two different MS/MS experiments: MS/MS of the ions isolated by a two-stage SWIFT isolation (CID = 90) and MS/MS of the ions isolated by a 40-Da wide isolation (CID = 55). The error bars correspond to ± the standard error (3 replicates).

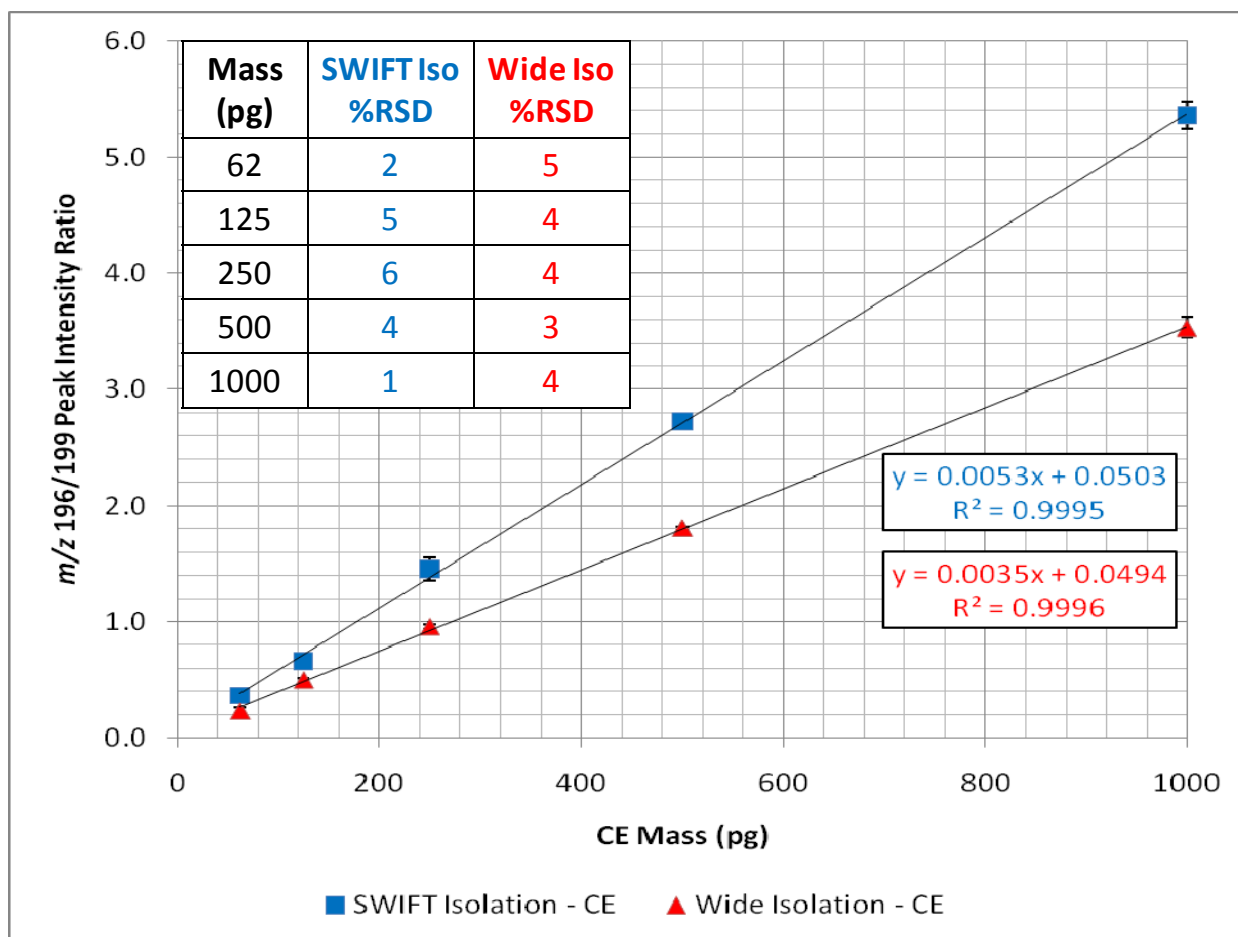


Figure 4-27. Five solutions (mixture of BE, COC, and CE at 62, 125, 250, 500, and 1000 ng/mL with a mixture of BE-d₃, COC-d₃, and CE-d₃ at 200 ng/mL) were pipetted in triplicate (1 μL each) onto blank human brain tissue and airbrushed with DHB matrix. The peak intensity of the product ions of CE and CE-d₃ at *m/z* 196 and *m/z* 199, respectively, were ratioed from two different MS/MS experiments: MS/MS of the ions isolated by a two-stage SWIFT isolation (CID = 90) and MS/MS of the ions isolated by a 40-Da wide isolation (CID = 55). The error bars correspond to ± the standard error (3 replicates).

Table 4-4. Quantification of BE, COC, and CE from Unspiked Human Brain Tissue

Analyte	MS/MS Ion (<i>m/z</i>)	Two-Stage SWIFT Intact Tissue (ng/g tissue)	40-Da Wide Isolation Intact Tissue (ng/g tissue)	5-Da Wide Isolation Tissue Homogenate (ng/g tissue)
BE	168.2	140	170	270±14
COC	182.2	230	60	380±11
CE	196.2	40	30	430±16

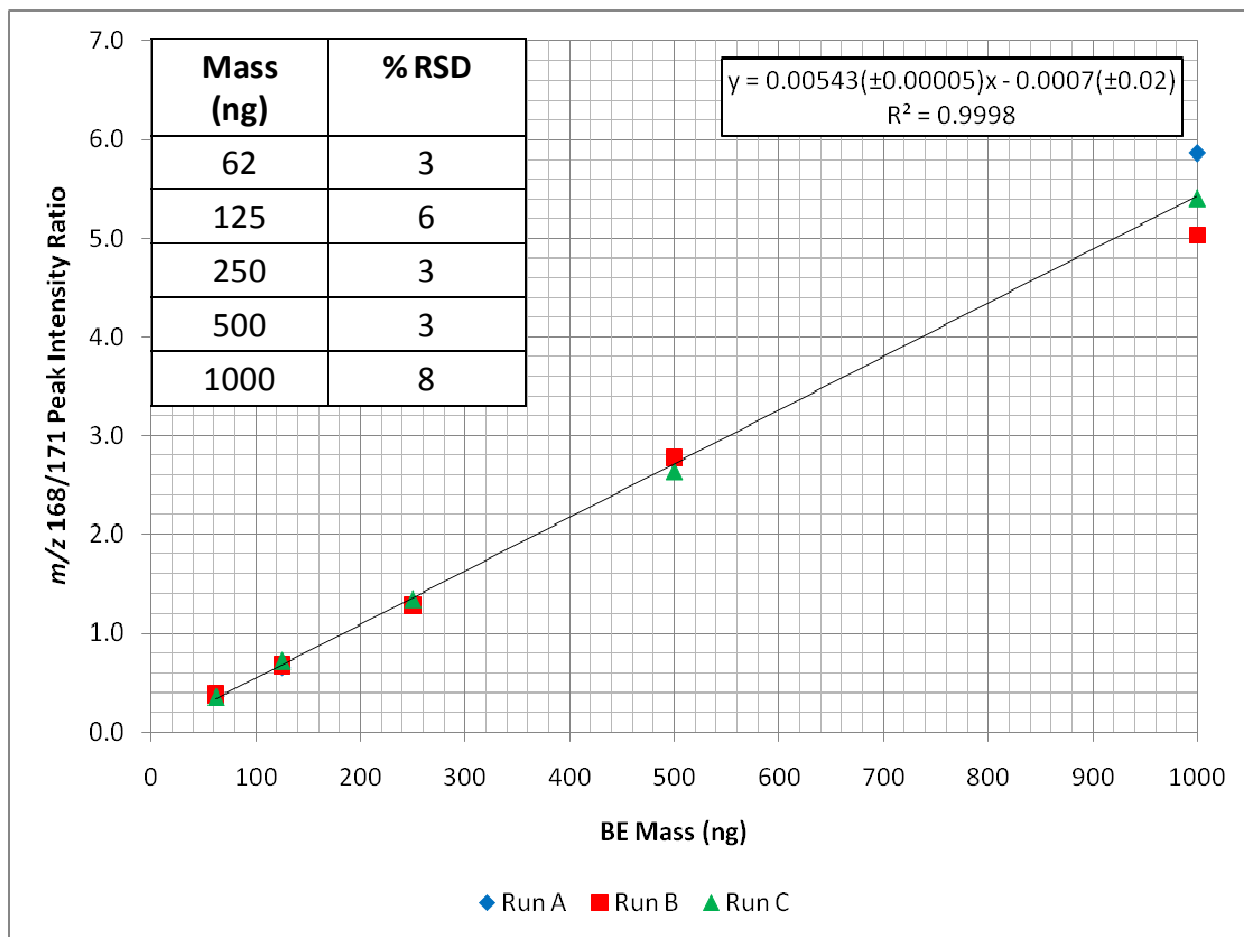


Figure 4-28. BE calibration curve for BE standards spiked in blank brain tissue homogenate.

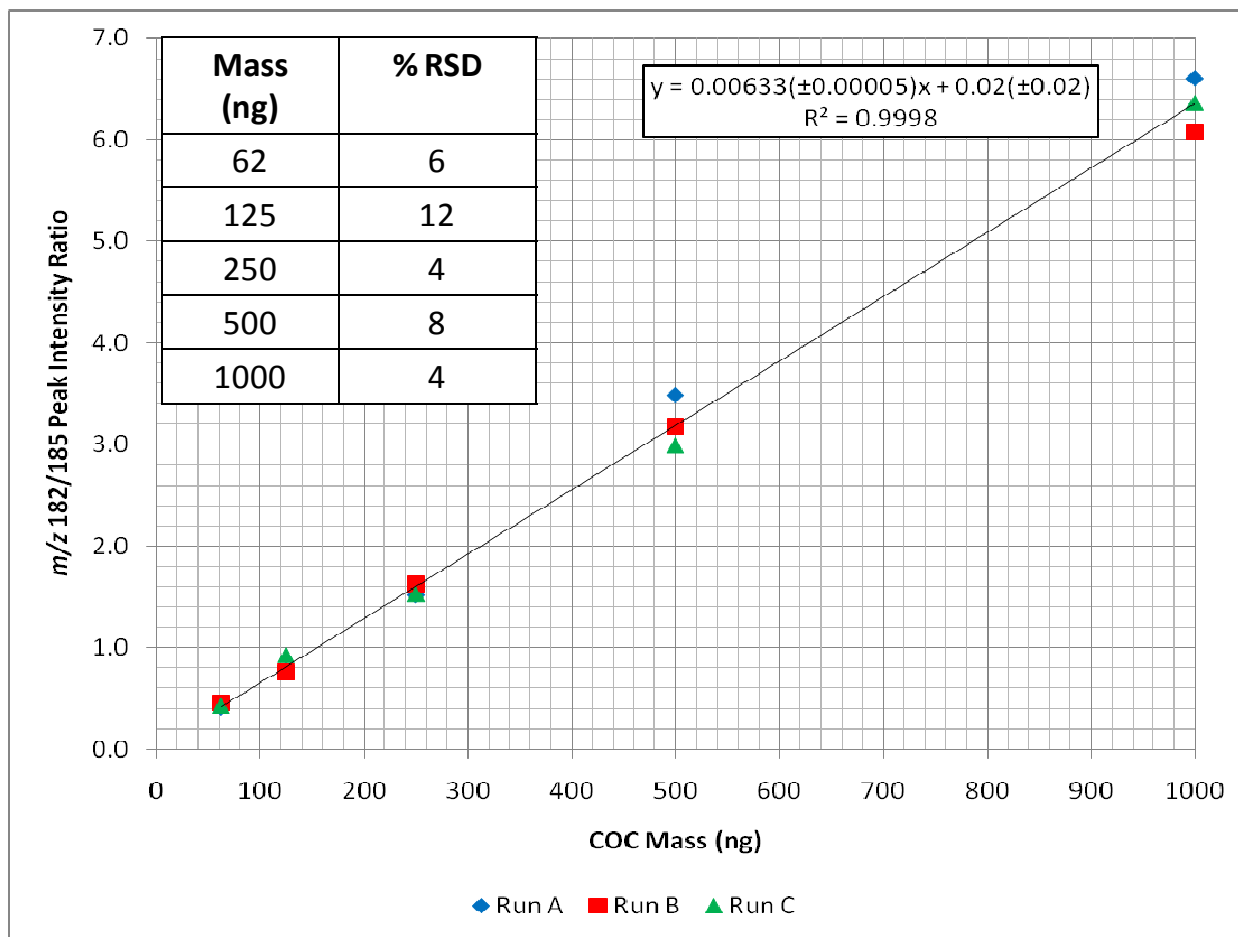


Figure 4-29. COC calibration curve for COC standards spiked into blank brain tissue homogenate.

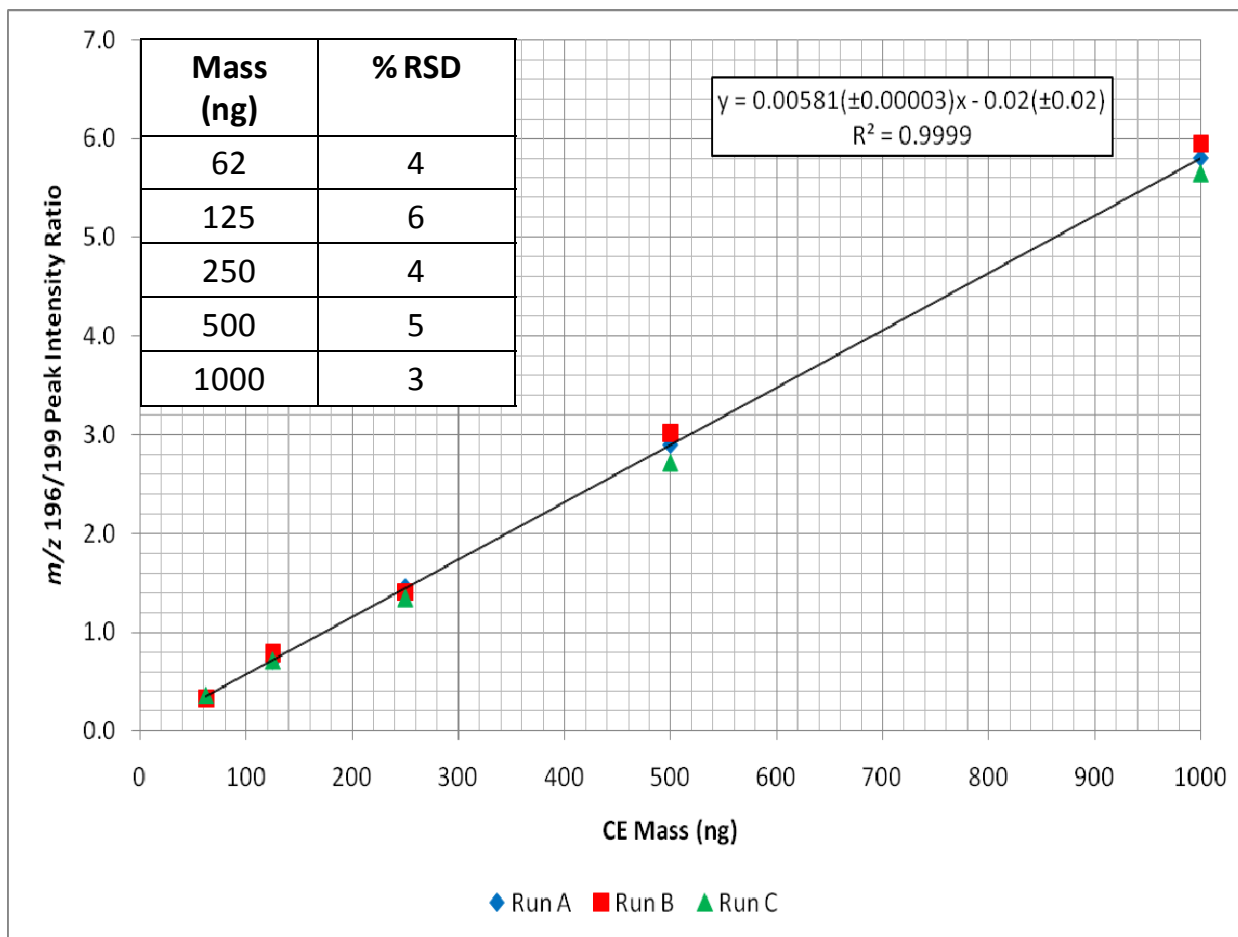


Figure 4-30. CE calibration curve for CE standards spiked into blank brain tissue homogenate.

CHAPTER 5 CONCLUSIONS AND FUTURE WORK

Conclusions

The goal of this research was to develop a quantitative mass spectrometric imaging (MSI) method for determining the regional composition of drugs and their metabolites in postmortem brain tissue. This research focused on the analysis of cocaine (COC) and two of its major metabolites, benzoylecgonine (BE) and cocaethylene (CE). COC is the most frequent cause of drug-related deaths in the United States, so it is of particular interest to the field of postmortem toxicology.

Conventional quantification of COC in brain tissue involves homogenate preparation, followed by extraction and/or derivatization. The extracts are then usually analyzed by gas chromatography/mass spectrometry (GC/MS), liquid chromatography/mass spectrometry (LC/MS), GC, or LC. Lengthy extraction procedures are required to remove large concentrations of lipids and other endogenous materials present in the brain, which may interfere with the analysis. Multiple sample pretreatment steps also allow opportunity for loss of analyte, and tissue homogenization eliminates spatial information, which could provide histologically-specific drug distribution.

MSI using matrix-assisted laser desorption/ionization (MALDI) mass spectrometry (MS) could provide quantitative information about the distribution of COC and its metabolites in brain tissue more rapidly, with higher spatial resolution, and with less sample loss than conventional drug analysis methods that involve tissue homogenization. Quantitative MALDI-MS is challenging, however, because MALDI exhibits irreproducible signal intensities due to inhomogeneous crystal formation, inconsistent sample preparation, and laser shot-to-shot variability. It has been shown though, that normalizing the analyte ion signal to that of a

structurally similar internal standard ion (e.g., $[M+H]^+$ ion of COC and COC-d₃) can dramatically reduce signal variability making quantification by MALDI-MS possible.

Mass spectrometry analysis of brain tissue can be very complicated, especially without the benefit of extraction and chromatography methods to clean up the sample and separate compounds. The presence of isobaric ions in samples increases with sample complexity and may interfere with quantification at low analyte concentrations. Tandem mass spectrometry (MSⁿ) can improve analyte selectivity and produce higher signal-to-noise ratios, resulting in lower detection and quantification limits for the analyte. Combining the use of MSⁿ with internal standards is commonly performed by alternating MSⁿ scans of the analyte and the internal standard ions, and then ratioing the resulting product ion signals. This method is effective for use with ionization techniques such as electrospray and atmospheric pressure chemical ionization; however, due to the shot-to-shot variability of MALDI, acquiring analyte and internal standard signals in alternating MSⁿ scans may counteract the signal normalizing effects gained by using an internal standard.

Strategies for isolating the analyte and internal standard ions during a single MSⁿ scan were investigated in order to improve the precision of MALDI-MSⁿ to allow for quantification of COC and its metabolites in brain tissue. One strategy was to use a single wide isolation window (e.g., 5 Da) centered at a mass-to-charge (m/z) between that of the analyte and internal standard ions. This allows for the simultaneous isolation and collision-induced dissociation (CID) of the analyte and internal standard ions. For example, for the analysis of COC, a 5-Da isolation window could be placed at m/z 305.8 to isolate the $[M+H]^+$ ion of COC at m/z 304.2 and the $[M+H]^+$ ion of its trideuterated analog, COC-d₃ at m/z 307.2. By applying CID across the isolation window, a MS² spectrum is produced containing the product ions of COC and COC-d₃

at m/z 182.2 and m/z 185.2, respectively. This method was shown to provide improved precision (~ 10 to 20 times reduction in %RSD) for quantitative analysis of COC in postmortem brain tissue compared with using two alternating MS^2 scans that isolate the analyte and internal standard ions separately. It was also shown that wide isolation can be used for multiple stages of mass analysis (e.g., MS^3) as long as the product ion derived from the deuterated internal standard maintains the deuterated tag allowing it to be distinguished from the product ion of the analyte. For MS^3 analysis of COC, the product ion at m/z 150 for COC was ratioed with the product ion at m/z 153 for COC- d_3 .

Multi-notch SWIFT isolation was investigated as an alternative isolation strategy to wide isolation for isolating the analyte and internal standard ions during a single MS^2 scan for improved MALDI- MS^2 precision. SWIFT isolation has higher mass selectivity than wide isolation and is able to reduce background ions that may complicate or interfere with MS^2 analysis (e.g., isobaric product ions). Also, analysis times and subsequently laser shots can be reduced as more frequency notches are added to the SWIFT isolation waveform. This can become very important when quantitatively imaging several analytes from a large tissue sample. It was determined that multi-notch SWIFT isolation can provide improved precision when compared to using two alternating MS^2 scans that isolate the analyte and internal standard ions separately. However, it was determined that multi-notch SWIFT isolation was not as precise as the wide isolation method. This might be due to frequency shifts of the analyte and internal standard ions from space-charge effects caused by high m/z background ions from the brain tissue (e.g., lipid region at m/z 700 to 900).

A two-stage SWIFT isolation method was developed that utilizes a high mass filter (HMF) SWIFT excitation waveform to remove high m/z background ions (e.g., m/z 325 to 2000) during

the first stage of isolation. This has been shown to reduce the frequency shifts of the analyte and internal standard ions by preventing them from moving outside the notches of the multi-notch SWIFT isolation waveform. This prevents the ions desired for isolation from being ejected by the SWIFT isolation waveform and resulted in an increased signal for the isolated ions compared to the application of a multi-notch SWIFT isolation waveform without the HMF. A hexa-notch SWIFT isolation waveform was used during the second stage of the two-stage SWIFT isolation to mass selectively isolate the $[M+H]^+$ ions of BE (m/z 168.2), BE- d_3 (m/z 171.2), COC (m/z 304.2), COC- d_3 (m/z 307.2), CE (m/z 318.2), and CE- d_3 (m/z 321.2). The hexa-notch SWIFT isolation waveform was able to effectively remove background ions around the analyte and internal standard ions that may have interfered with MS/MS analysis. The two-stage SWIFT isolation overall showed similar precision to that of wide isolation when performing MS/MS on the analyte and internal standards spiked on blank brain tissue. However, the higher mass selectivity of the two-stage SWIFT isolation affords a significant loss in absolute signal intensity of the analyte and internal standard ions when it is applied.

Two-stage SWIFT isolation was compared to wide isolation of intact tissue and SPE extracted homogenized tissue for the MALDI-MS/MS quantification of BE, COC, and CE from unspiked human brain tissue, whose toxicological analysis indicated the presence of cocaine in blood. The two-stage SWIFT isolation method showed lower analyte signal per gram of tissue than the wide isolation method for BE, COC, and CE. The quantification results for the two-stage SWIFT isolation and the wide isolation of intact tissue was not comparable to that for the wide isolation analysis of tissue homogenate (Table 4-4). However, the intact tissue methods required considerably less sample preparation and smaller sample sizes than the tissue homogenate method. There was no analysis time saved or fewer laser shots fired when

comparing the two-stage SWIFT isolation and wide isolation since the $[M+H]^+$ ions of BE, BE-d₃, COC, COC-d₃, CE, and CE-d₃ were all isolated simultaneously during the same MS/MS scan. In conclusion, a wide isolation method may still be a better choice over SWIFT isolation for improving MALDI-MS/MS precision for quantification and reducing analysis time, despite the inclusion of unwanted background ions during isolation.

Future Work

The linear ion trap has a limited ion storage capacity ($\sim 10^7$ ions) before coulombic interactions between stored ions degrade the mass resolution and reduce sensitivity (space-charge effects). Sensitivity is reduced when space-charge, created by unwanted matrix ions, limits the total number of analyte ions which may be trapped. Julian and Cooks first applied SWIFT to the quadrupole ion trap during injection to resonantly eject these matrix ions and to selectively accumulate and store analyte ions to increase sensitivity and avoid interference.¹⁰⁶ For this research, the application of SWIFT during different periods of the LTQ scan function was explored to include at the beginning of scan, injection period, isolation, activation, and scan out. All of these periods of the LTQ scan function are included in the programmable trigger provided by the LTQ software; however, application of SWIFT during the injection period was unsuccessful and requires further investigation to exploit the sensitivity gains promised by selective accumulation and storage of analyte ions.

Quantitative imaging of cocaine and its metabolites from brain tissue of a habitual cocaine user showed no localization of the analytes in the section of the nucleus accumbens analyzed. A controlled animal study involving lower doses of cocaine may show localization of cocaine and its metabolites within specific regions of the brain, and provide more information about the mechanisms of this drug.

APPENDIX A BETA CALCULATION

Beta (β) is defined precisely by a continued fraction (aqb_conf) expression in terms of a and q . Since $a = 0$, this expression simplifies to Equation A-1 (same as Equation 3-2):

$$aqb_conf = \frac{q^2}{(2+\beta)^2 - \frac{q^2}{(4+\beta)^2 - \frac{q^2}{(6+\beta)^2 - \frac{q^2}{(8+\beta)^2 - \frac{q^2}{(10+\beta)^2 - \frac{q^2}{(12+\beta)^2}}}}} + \frac{q^2}{(\beta-2)^2 - \frac{q^2}{(\beta-4)^2 - \frac{q^2}{(\beta-6)^2 - \frac{q^2}{(\beta-8)^2 - \frac{q^2}{(\beta-10)^2 - \frac{q^2}{(\beta-12)^2}}}}} - \beta^2 \quad (\text{A-1})$$

A LabView subprogram, or subVI (VI = virtual instrument), was written to calculate aqb_conf based on q and β inputs. Figure A-1 shows the block diagram of the aqb_conf sub VI, which is a graphical representation of Equation A-1.

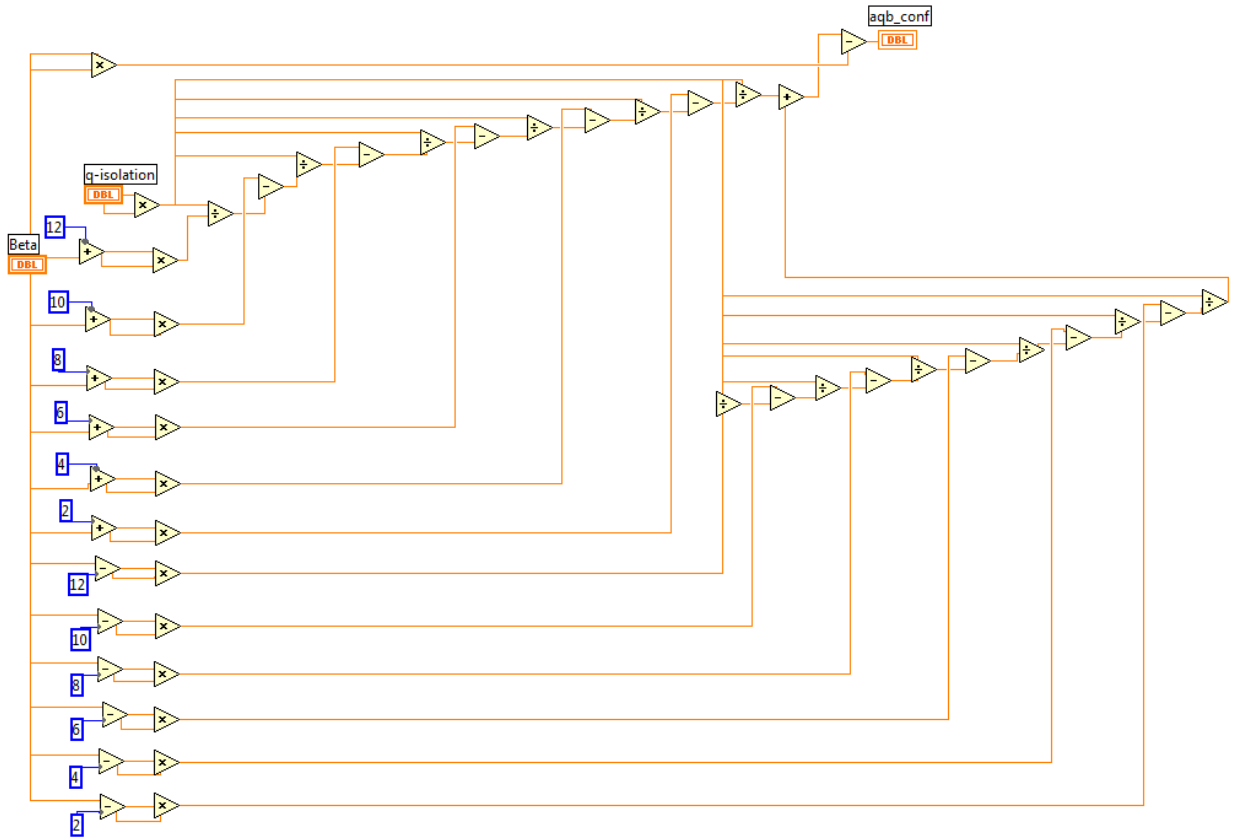


Figure A-1. LabView block diagram of subVI aqb_conf, which is used to calculate the continued fraction given q and β inputs.

A LabView program called Trap Calculator was written to calculate β through an iterative process given a specific q input, such as $q = 0.83$ for isolation. Trap Calculator makes a first guess at the value for β based on the Dehmelt approximation given in Equation A-2, same as Equation 3-4:

$$\beta \approx \sqrt{\left(a + \frac{q^2}{2}\right)} \quad (\text{A-2})$$

This approximation is assigned the variable $x1$. Ninety percent of the approximation is assigned the variable $x0$. Both $x0$ and $x1$ are applied as β inputs for the `aqb_conf` sub VI with the desired q as the q inputs resulting in the function outputs of $fx0$ and $fx1$. The variable $x2$ is used to store the next iterative approximation of β , in which $x2 = x1 - ((x0 - x1) / (fx0 / fx1 - 1))$. Then $x0$ is replaced with the value of $x1$ and $x1$ is replaced with the value of $x2$. This process is repeated until the absolute value of the difference between $x0$ and $x1$ is greater than 1×10^{-7} , and then the variable `beta` is assigned the value of $x1$. Figure A-2 shows the block diagram for the Trap Calculator LabView program, which is a graphical representation of the iterative process described to calculate β .

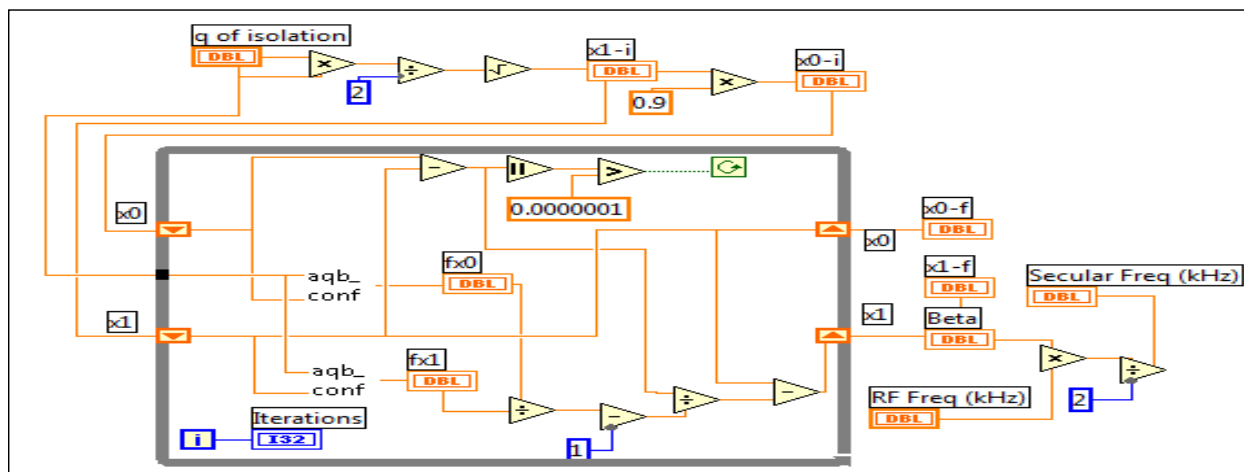


Figure A-2. Trap Calculator LabView program used to calculate β through an iterative process.

This process of calculating β is shown graphically in Figure A-3, where β was calculated after 5 iterations with $q = 0.830$. The value for β was plotted versus the number of iterations.

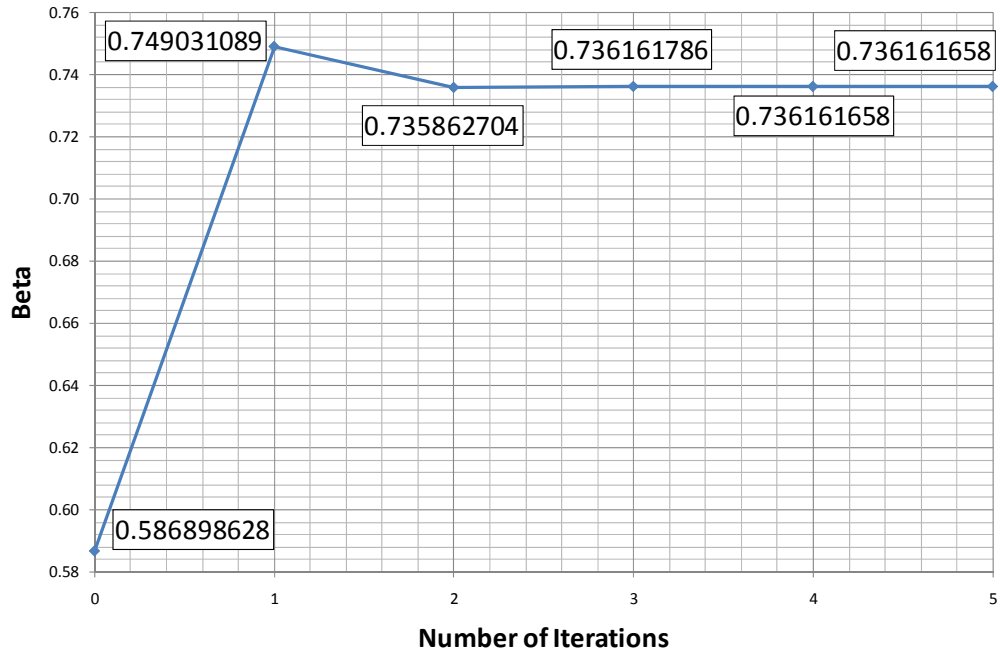


Figure A-3. Iterative calculation of β using the LabView program Trap Calculator.

APPENDIX B C++ SWIFT PROGRAM

```

/*=====
Name:          REICH-HexSWIFT.cpp

Author:        C++ version by Richard Reich (12 August 2009) using Microsoft Visual C++ 2008 Express Edition

Purpose:       This program calculates a hextuple-notch stored waveform inverse Fourier transform (SWIFT) pulse and
                downloads the data points to an arbitrary waveform generator (DS345) to be applied to the X-rods
                of the center section of a linear ion trap (LTQ) for isolation of 3 analytes and their corresponding
                internal standard ions in the linear ion trap for increased precision during MALDI-MS^n quantitation.

References:    This C++ program is adapted from the original C program written by P.T. Palmer (4 Sep 92). Palmer's
                program was based on the paper: Chen, L.; Wang, T.C.L.; Ricca, T.L.; Marshall, A.G. "Phase-Modulated
                Stored Waveform Inverse Fourier Transform Excitation for Trapped Ion Mass Spectrometry"; Anal. Chem.
                1987, 59, 449-454. The fast Fourier transform (FFT) algorithm and required data format are described
                in Vetterling, W.T.; Teukolsky, S.A.; Press, W.H.; Flannery, B.P. "Numerical Recipes in C: the Art of
                Scientific Computing", 2nd ed., New York: Cambridge University Press, 1992, pp. 399-413.

Modifications: The following modifications to Peter Palmer's original C SWIFT program were made when writing program
                in C++ to remove compiler warnings and errors:

                - Removed "huge" from float t[N]; f[N/2+1]; r[N/2+1]; p[N/2+1]; x[N/2+1]; and y[N/2+1], because term
                  caused several compiling errors. (fixed errors C2146, C4430, C2086, C2371)
                - Replaced "gets()" function with "gets_s()" function as recommended by compiler to avoid overrunning
                  buffer. "_s" suffix stands for secure. (fixed warning C4996)
                - Replaced "scanf()" function with "scanf_s()" function as recommended by compiler to avoid
                  overrunning buffer. (fixed warning C4996)
                - Replaced "strcpy()" function with "strcpy_s()" function as recommended by compiler to avoid
                  overrunning buffer. (fixed warning C4996)
                - Included "cstdlib" source file to identify "exit". (fixed error C3861)
                - Removed "ieeio.h" source file and "download" function for downloading time-domain waveform over an
                  IEEE-488 to the DS345 waveform generator through a GPIB. Will use RS232 instead.
                - Included "system("PAUSE");" at end of program before function definitions to prevent black window
                  from disappearing before user can read it. Requires user to hit any key to close window.

Operation:     1. Specify the following parameters:
                N:          number of points in time-domain SWIFT waveform
                freq:       sampling rate of function generator (kHz)
                lfreq:      lower limit of frequency pulse (kHz)
                rfreq:      upper limit of frequency pulse (kHz)
                mag:        normalization value for time-domain waveform

                2. Setup output file (ascii format) for time and frequency domain waveforms for plotting and inspection.

                3. Generate desired frequency-domain waveform. Compute magnitude and phase spectra. Use a quadratic
                  function for phase modulation. Convert waveform from polar (magnitude and phase) to a complex
                  array of real and imaginary numbers for Fourier transform.

                4. Perform inverse Fourier transform to convert SWIFT waveform from frequency domain to the time domain.

                5. Reflect the time-domain waveform about its time midpoint to reduce problems with large initial
                  signal transients.

                6. Generate the apodization or smoothing function. This is a quarter-wave sinusoid matched to one-
                  fourth of the time-domain period, followed by unit weighting for the next half period, followed by
                  a quarter-wave sinusoid for final one-fourth of the period. This function is designed to force the
                  time-domain signal smoothly to zero at the beginning and end of the time-domain period.

                7. Multiply the time-domain waveform by the apodization function and normalize.

```

Figure B-1. Program introductory comments. Briefly describes purpose, references, modifications, and operation of program.

8. Write waveform data to output file. This data includes:
 - frequency vs magnitude of specified waveform
 - frequency vs phase of specified waveform
 - time vs amplitude of computed waveform (reflected, apodized, and normalized)
9. Download the time-domain waveform over an RS232 serial port to the function generator.
10. Write waveform data to output file.

```

===== */
/* insert source files from standard C library using the preprocessor #include command */
#include <iostream> /*(standard input/output header); allows functions from C standard library to be used */
#include <string.h> /*(standard string header); allows use of string handling and various memory handling functions */
#include <math.h> /*(standard math header); allows basic mathematical operations */
#include <cstdlib> /* added in C++ version to identify function "exit". (fixed error C3861) */

/* define symbolic constants (conventionally name is capitalized) using the preprocessor #define command */
#define SWAP(a,b) tempr = (a); (a) = (b); (b) = tempr /* function swaps values of two variables (a & b) */
#define PI      3.141592654
#define N      4096      /* max # points in SWIFT waveform */
#define MAX    2047      /* max amplitude for SWIFT waveform */
#define LF1    398.681641 /* default value for lower limit of first frequency band (kHz) */
#define RF1    401.855469 /* default value for upper limit of first frequency band (kHz) */
#define LF2    405.029297 /* default value for lower limit of second frequency band (kHz) */
#define RF2    408.203125 /* default value for upper limit of second frequency band (kHz) */
#define LF3    431.152344 /* default value for lower limit of third frequency band (kHz) */
#define RF3    435.058594 /* default value for upper limit of third frequency band (kHz) */
#define LF4    439.208984 /* default value for lower limit of fourth frequency band (kHz) */
#define RF4    443.603516 /* default value for upper limit of fourth frequency band (kHz) */
#define LF5    475.341797 /* default value for lower limit of fifth frequency band (kHz) */
#define RF5    481.445312 /* default value for upper limit of fifth frequency band (kHz) */
#define LF6    488.037109 /* default value for lower limit of sixth frequency band (kHz) */
#define RF6    494.873047 /* default value for upper limit of sixth frequency band (kHz) */
#define SF     1000      /* default sampling frequency (kHz) for DS345 arbitrary waveform generator (AWG) */
#define V      1.0       /* default value for voltage of output waveform */

/* declaration of variables (property of variable and name); int=integer (whole #), float=floating point (# with fraction) */
unsigned int freq; /* DS345 sampling frequency (kHz); unsigned means no negative values */
float vpp; /* peak to peak voltage of SWIFT waveform */
float t[N]; /* time vector for plotting time domain axis in microseconds */
float f[N/2 + 1]; /* frequency vector for plotting freq domain axis in kHz */
float r[N/2 + 1]; /* magnitude spectrum of SWIFT waveform (polar coordinate) */
float p[N/2 + 1]; /* phase spectrum of SWIFT waveform (polar coordinate) */
float x[N/2 + 1]; /* real portion of SWIFT waveform (cartesian coordinate) */
float y[N/2 + 1]; /* imaginary portion of SWIFT waveform (cartesian coordinate) */
float data[2*N]; /* SWIFT waveform of N complex points (real, imag) */
float apod[N]; /* apodization or smoothing function */
int wave[N+1]; /* scaled, int format of SWIFT with checksum at end */

void fft(float data[], int n, int isign); /* void means that function doesn't return a value */

void main()
{

```

Figure B-2. Definition of constants and declaration of variables.

```

/*****
VARIABLE DEFINITIONS
*****/

int      sflag;      /* flag to indicate SWIFT waveform type */
float    tempr;      /* temporary variable for swap function */
char     inbuf[20];  /* input buffer array for character strings */
float    l1freq;     /* lower limit of first frequency pulse (kHz) */
float    r1freq;     /* upper limit of first frequency pulse (kHz) */
float    l2freq;     /* lower limit of second frequency pulse (kHz) */
float    r2freq;     /* upper limit of second frequency pulse (kHz) */
float    l3freq;     /* lower limit of third frequency pulse (kHz) */
float    r3freq;     /* upper limit of third frequency pulse (kHz) */
float    l4freq;     /* lower limit of fourth frequency pulse (kHz) */
float    r4freq;     /* upper limit of fourth frequency pulse (kHz) */
float    l5freq;     /* lower limit of fifth frequency pulse (kHz) */
float    r5freq;     /* upper limit of fifth frequency pulse (kHz) */
float    l6freq;     /* lower limit of sixth frequency pulse (kHz) */
float    r6freq;     /* upper limit of sixth frequency pulse (kHz) */
int      errflag;    /* flag to denote input errors */
float    freqmax;    /* Nyquist freq or maximum possible fast Fourier transform (FFT) freq (kHz) */
float    deltat;     /* time interval in microseconds */
float    deltaf;    /* frequency interval in kHz */
int      l1index;    /* lower index of first frequency band */
int      r1index;    /* upper index of first frequency band */
int      l2index;    /* lower index of second frequency band */
int      r2index;    /* upper index of second frequency band */
int      l3index;    /* lower index of third frequency band */
int      r3index;    /* upper index of third frequency band */
int      l4index;    /* lower index of fourth frequency band */
int      r4index;    /* upper index of fourth frequency band */
int      l5index;    /* lower index of fifth frequency band */
int      r5index;    /* upper index of fifth frequency band */
int      l6index;    /* lower index of sixth frequency band */
int      r6index;    /* upper index of sixth frequency band */
float    a;          /* coefficient of x term for quadratic phase modulation */
float    b;          /* coefficient of x^2 term for quadratic phase modulation */
int      i,j;        /* array indices */
char     fileflag;   /* flag to indicate output desired */
char     ascfile[20]; /* filename for ASCII file output of SWIFT waveform */
char     binfile[20]; /* filename for binary file output of SWIFT waveform */
FILE     *ascfp;     /* file pointer for ASCII file output */
FILE     *binfp;     /* file pointer for binary file output */
int      dlflag;     /* flag to denote downloading of SWIFT waveform */
float    max;        /* maximum amplitude (volts) in SWIFT waveform */
float    norm1,norm2; /* normalization factors computed from time-domain maximum */
int      checksum;   /* check sum value for downloading SWIFT to AWG (DS345) */

```

Figure B-3. Variable definitions.

```

/*****
INITIALIZE VARIABLES
*****/

printf("This program can generate SWIFT waveforms for excitation or isolation.\n");
printf("Would you like to generate a SWIFT waveform for excitation (default = Y)? ");

gets_s(inbuf, 20);
if ((strstr(inbuf,"N") != NULL) || (strstr(inbuf,"n") != NULL)) sflag = 1; /* set flag to 1 if input is N or n */
else sflag = 0; /* if input is other than N or n, set flag to 0 */

printf("Lower limit of first frequency notch in kHz (default = %i)? ", LF1);
gets_s(inbuf, 20); /* reads the input from the user and stores it in the character string "inbuf" */
i = strlen(inbuf); /* counts length of input string from user */
if (i == 0) l1freq = LF1; /* if no input from user (i.e, string length is equal to 0), then default LF1 value is used */
else sscanf_s(inbuf, "%f", &l1freq, 20); /* read input from user, format it, and store in variable l1freq */

printf("Upper limit of first frequency notch in kHz (default = %i)? ", RF1);
gets_s(inbuf, 20); /* reads the input from the user and stores it in the character string "inbuf" */
i = strlen(inbuf); /* counts length of input string from user */
if (i == 0) r1freq = RF1; /* if no input from user (i.e, string length is equal to 0), then default RF1 value is used */
else sscanf_s(inbuf, "%f", &r1freq, 20); /* read input from user, format it, and store in variable r1freq */

printf("Lower limit of second frequency notch in kHz (default = %i)? ", LF2);
gets_s(inbuf, 20); /* reads the input from the user and stores it in the character string "inbuf" */
i = strlen(inbuf); /* counts length of input string from user */
if (i == 0) l2freq = LF2; /* if no input from user (i.e, string length is equal to 0), then default LF2 value is used */
else sscanf_s(inbuf, "%f", &l2freq, 20); /* read input from user, format it, and store in variable l2freq */

printf("Upper limit of second frequency notch in kHz (default = %i)? ", RF2);
gets_s(inbuf, 20); /* reads the input from the user and stores it in the character string "inbuf" */
i = strlen(inbuf); /* counts length of input string from user */
if (i == 0) r2freq = RF2; /* if no input from user (i.e, string length is equal to 0), then default RF2 value is used */
else sscanf_s(inbuf, "%f", &r2freq, 20); /* read input from user, format it, and store in variable r2freq */

printf("Lower limit of third frequency notch in kHz (default = %i)? ", LF3);
gets_s(inbuf, 20); /* reads the input from the user and stores it in the character string "inbuf" */
i = strlen(inbuf); /* counts length of input string from user */
if (i == 0) l3freq = LF3; /* if no input from user (i.e, string length is equal to 0), then default LF3 value is used */
else sscanf_s(inbuf, "%f", &l3freq, 20); /* read input from user, format it, and store in variable l3freq */

printf("Upper limit of third frequency notch in kHz (default = %i)? ", RF3);
gets_s(inbuf, 20); /* reads the input from the user and stores it in the character string "inbuf" */
i = strlen(inbuf); /* counts length of input string from user */
if (i == 0) r3freq = RF3; /* if no input from user (i.e, string length is equal to 0), then default RF3 value is used */
else sscanf_s(inbuf, "%f", &r3freq, 20); /* read input from user, format it, and store in variable r3freq */

printf("Lower limit of fourth frequency notch in kHz (default = %i)? ", LF4);
gets_s(inbuf, 20); /* reads the input from the user and stores it in the character string "inbuf" */
i = strlen(inbuf); /* counts length of input string from user */
if (i == 0) l4freq = LF4; /* if no input from user (i.e, string length is equal to 0), then default LF4 value is used */
else sscanf_s(inbuf, "%f", &l4freq, 20); /* read input from user, format it, and store in variable l4freq */

```

Figure B-4. Initialize variables for notches 1 through 4.

```

printf("Upper limit of fourth frequency notch in kHz (default = %i)? ", RF4);
gets_s(inbuf, 20); /* reads the input from the user and stores it in the character string "inbuf" */
i = strlen(inbuf); /* counts length of input string from user */
if (i == 0) r4freq = RF4; /* if no input from user (i.e, string length is equal to 0), then default RF4 value is used */
else sscanf_s(inbuf, "%f", &r4freq, 20); /* read input from user, format it, and store in variable r4freq */

printf("Lower limit of fifth frequency notch in kHz (default = %i)? ", LF5);
gets_s(inbuf, 20); /* reads the input from the user and stores it in the character string "inbuf" */
i = strlen(inbuf); /* counts length of input string from user */
if (i == 0) l5freq = LF5; /* if no input from user (i.e, string length is equal to 0), then default LF5 value is used */
else sscanf_s(inbuf, "%f", &l5freq, 20); /* read input from user, format it, and store in variable l5freq */

printf("Upper limit of fifth frequency notch in kHz (default = %i)? ", RF5);
gets_s(inbuf, 20); /* reads the input from the user and stores it in the character string "inbuf" */
i = strlen(inbuf); /* counts length of input string from user */
if (i == 0) r5freq = RF5; /* if no input from user (i.e, string length is equal to 0), then default RF5 value is used */
else sscanf_s(inbuf, "%f", &r5freq, 20); /* read input from user, format it, and store in variable r5freq */

printf("Lower limit of sixth frequency notch in kHz (default = %i)? ", LF6);
gets_s(inbuf, 20); /* reads the input from the user and stores it in the character string "inbuf" */
i = strlen(inbuf); /* counts length of input string from user */
if (i == 0) l6freq = LF6; /* if no input from user (i.e, string length is equal to 0), then default LF6 value is used */
else sscanf_s(inbuf, "%f", &l6freq, 20); /* read input from user, format it, and store in variable l6freq */

printf("Upper limit of sixth frequency notch in kHz (default = %i)? ", RF6);
gets_s(inbuf, 20); /* reads the input from the user and stores it in the character string "inbuf" */
i = strlen(inbuf); /* counts length of input string from user */
if (i == 0) r6freq = RF6; /* if no input from user (i.e, string length is equal to 0), then default RF6 value is used */
else sscanf_s(inbuf, "%f", &r6freq, 20); /* read input from user, format it, and store in variable r6freq */

```

Figure B-5. Initialize variables for notches 5 and 6.

```

if(r1freq < l1freq || r2freq < l2freq || r3freq < l3freq || r4freq < l4freq || r5freq < l5freq || r6freq < l6freq) /* checks to make
sure that the upper limit is not less than the lower limit of freq notch */
{
    printf("Your upper limit of your frequency notch cannot be less than your lower limit.\n");
    printf("This program will now terminate,\n");
    exit(-1); /* causes normal program termination */
}

do
    /* Do-while loop for acquiring appropriate sampling frequency from user */
    {
        errflag = 0; /* presets errflag to zero */
        printf("Sampling frequency for DS345 in kHz (default = 1000)?", SF);
        gets_s(inbuf, 20); /* reads the input from the user and stores it in the character string "inbuf" */
        i = strlen(inbuf); /* counts length of input string from user */
        if (i == 0) freq = SF; /* if no input from user (i.e, string length is equal to 0), then default SF value is used */
        else
            {
                sscanf_s(inbuf, "%u", &freq, 20); /* read input from user, format it, & store in variable freq */
                if (freq & 1) /* assign to freq the address of 1 */
                    {
                        printf("Number must be a multiple of 2 - try again\n");
                        errflag = 1;
                    }
                else if (freq > 40000)
                    {
                        printf("Number must be less than or equal to 40,000 - try again\n");
                        errflag = 1;
                    }
            }
    }
while (errflag == 1);

printf("Peak-to-peak voltage of output waveform (default = %2.1f)? ", V);
gets_s(inbuf, 20); /* reads the input from the user and stores it in the character string "inbuf" */
i = strlen(inbuf); /* counts length of input string from user */
if (i == 0) vpp = V; /* if no input from user (i.e, string length is equal to 0), then default V value is used */
else sscanf_s(inbuf, "%f", &vpp, 20); /* read input from user, format it, and store in variable vpp */

freqmax = freq/2; /* in kHz */
deltat = 1000/freq; /* in microseconds */
deltaf = 2 * freqmax/N; /* in kHz */
l1index = floor(l1freq/deltaf); /* floor rounds down to nearest integer; sets lower index of 1st freq band */
r1index = ceil(r1freq/deltaf); /* ceil rounds up to nearest integer; sets upper index of 1st freq band */
l2index = floor(l2freq/deltaf); /* floor rounds down to nearest integer; sets lower index of 2nd freq band */
r2index = ceil(r2freq/deltaf); /* ceil rounds up to nearest integer; sets upper index of 2nd freq band */
l3index = floor(l3freq/deltaf); /* floor rounds down to nearest integer; sets lower index of 3rd freq band */
r3index = ceil(r3freq/deltaf); /* ceil rounds up to nearest integer; sets upper index of 3rd freq band */
l4index = floor(l4freq/deltaf); /* floor rounds down to nearest integer; sets lower index of 4th freq band */
r4index = ceil(r4freq/deltaf); /* ceil rounds up to nearest integer; sets upper index of 4th freq band */
l5index = floor(l5freq/deltaf); /* floor rounds down to nearest integer; sets lower index of 5th freq band */
r5index = ceil(r5freq/deltaf); /* ceil rounds up to nearest integer; sets upper index of 5th freq band */
l6index = floor(l6freq/deltaf); /* floor rounds down to nearest integer; sets lower index of 6th freq band */
r6index = ceil(r6freq/deltaf); /* ceil rounds up to nearest integer; sets upper index of 6th freq band */

```

Figure B-6. Test initialized variables.

```

/*****
                                SETUP OUTPUT FILES
*****/

fileflag = 0; /* fileflag stores the type of output files desired (1 = ASCII, 2 = binary) */

printf("Write SWIFT waveform data to an ASCII file (default = N)? ");
gets_s(inbuf, 20); /* reads the input from the user and stores it in the character string "inbuf" */
if ( (strstr(inbuf, "Y") != NULL) || (strstr(inbuf, "y") != NULL) )
    {
        fileflag = 1;

        do
            {
                printf("Filename for the ASCII data file (default = SWIFT.DAT)? ");
                gets_s(inbuf, 20); /* reads the input from the user & stores it in the character string "inbuf" */
                i = strlen(inbuf); /* counts length of input string from user */
                sscanf_s(inbuf, "%s", ascfile, 20);
                if (i == 0) /* if no input from user, then ascfile set to SWIFT.DAT */
                    strcpy_s(ascfile, "SWIFT.DAT");

                if (i > 16)
                    printf("Filename must be less than or equal to 16 characters - try again\n");
            }
        while (i > 16);

        if ( (strstr(ascfile, ".DAT") == NULL) && (strstr(ascfile, ".dat") == NULL) )
            strcat(ascfile, ".DAT");
        if ( (ascfp = fopen(ascfile, "wt")) == NULL )
            {
                printf("Error - could not open %s\n", ascfile);
                fileflag = 0;
            }
    }

printf("Write SWIFT waveform data to a binary file (default = N)? ");
gets_s(inbuf, 20); /* reads the input from the user and stores it in the character string "inbuf" */
if ( (strstr(inbuf, "Y") != NULL) || (strstr(inbuf, "y") != NULL) )
    {
        fileflag = fileflag + 2;

        do
            {
                printf("Filename for binary data file (default = SWIFT.ARB)? ");
                gets_s(inbuf, 20); /* reads the input from the user & stores it in the
                character string "inbuf" */
                i = strlen(inbuf); /* counts length of input string from user */
                sscanf_s(inbuf, "%s", binfile, 20);
                if (i == 0) /* if no input from user, then binfile set to SWIFT.ARB */
                    strcpy(binfile, "SWIFT.ARB");

                if (i > 16)
                    printf("Filename must be less than or equal to 16
                    characters - please try again\n");
            }
        while (i > 16);
    }

```

Figure B-7. Setup output files.

```

if ( (strstr(binfile, ".ARB") == NULL) && (strstr(binfile, ".arb") == NULL) )
    strcat(binfile, ".ARB");
if ( (binfp = fopen(binfile, "wb")) == NULL)
    {
        printf("      Error - could not open %s\n", binfile);
        fileflag = fileflag - 2;
    }
}

dflag = 0;
printf("Download SWIFT waveform to the DS345 waveform generator (default = N)? ");
gets_(inbuf, 20); /* reads the input from the user and stores it in the character string "inbuf" */
if ( (strstr(inbuf, "Y") != NULL) || (strstr(inbuf, "y") != NULL) ) dflag = 1;

/*****

GENERATE DESIRED FREQUENCY-DOMAIN WAVEFORM

*****/

printf("Generating hexa-notch SWIFT waveform ... \n");

for (i = 0; i < N; i++) /* increment i up to N (number of points in time-domain SWIFT waveform) */
    t[i] = i * deltat; /* initialize time axis array in microseconds */
if (sflag == 0) /* if SWIFT waveform type is excitation (sflag equal to 0) */
    {
        a = PI/2; /* component "a" of quadratic phase modulation equation */
/***** Building component 1, 3, 5, 7, 9, and 11 of excitation SWIFT waveform *****/

        for (i = 0; i <= N/2; i++)
            {
                f[i] = deltat * i; /* initialize frequency axis array in kHz */
                r[i] = 0; /* zero fill r (magnitude, polar coordinate) array */
                p[i] = 0; /* zero fill p (phase, polar coordinate) array */
                x[i] = 0; /* zero fill x (real, cartesian coordinate) array */
                y[i] = 0; /* zero fill y (imaginary, cartesian coordinate) array */
            }

/***** Building component 2 of excitation SWIFT waveform *****/
        b = -PI/(r1index - l1index); /* component "b" of quadratic phase modulation equation */
        for (i = l1index; i <= r1index; i++) /* increment i up to right-side of 1st freq notch */
            {
                j = i - l1index; /* increment j used in quadratic function */
                r[i] = 1; /* set magnitude array to unity - scale later */
                p[i] = (a * j) + (b/2 * j * j); /* set phase to quadratic function */
                x[i] = cos(p[i]); /* set real portion of complex number */
                y[i] = sin(p[i]); /* set imaginary portion of complex number */
            }

/***** Building component 4 of excitation SWIFT waveform *****/
        b = -PI/(r2index - l2index); /* component "b" of quadratic phase modulation equation */
        for (i = l2index; i <= r2index; i++) /* increment i up to right-side of 2nd freq notch */
            {
                j = i - l2index; /* increment j (shifted from i) used in quadratic function */
                r[i] = 1; /* set magnitude array to unity - scale later */
                p[i] = (a * j) + (b/2 * j * j); /* set phase to quadratic function */
                x[i] = cos(p[i]); /* set real portion of complex number */
                y[i] = sin(p[i]); /* set imaginary portion of complex number */
            }

```

Figure B-8. Build components 1, 2, 3, 4, 5, 7, 9 and 11 of excitation waveform.

```

/***** Building component 6 of excitation SWIFT waveform*****/
b = -PI/(r3index - l3index); /* component "b" of quadratic phase modulation equation */
for (i = l3index; i <= r3index; i++) /* increment i up to right-side of 3rd freq notch */
{
    j = i - l3index; /* increment j (shifted from i) used in quadratic function */
    r[i] = 1; /* set magnitude array to unity - scale later */
    p[i] = (a * j) + (b/2 * j * j); /* set phase to quadratic function */
    x[i] = cos(p[i]); /* set real portion of complex number */
    y[i] = sin(p[i]); /* set imaginary portion of complex number */
}

/***** Building component 8 of excitation SWIFT waveform*****/
b = -PI/(r4index - l4index); /* component "b" of quadratic phase modulation equation */
for (i = l4index; i <= r4index; i++) /* increment i up to right-side of 4th freq notch */
{
    j = i - l4index; /* increment j (shifted from i) used in quadratic function */
    r[i] = 1; /* set magnitude array to unity - scale later */
    p[i] = (a * j) + (b/2 * j * j); /* set phase to quadratic function */
    x[i] = cos(p[i]); /* set real portion of complex number */
    y[i] = sin(p[i]); /* set imaginary portion of complex number */
}

/***** Building component 10 of excitation SWIFT waveform*****/
b = -PI/(r5index - l5index); /* component "b" of quadratic phase modulation equation */
for (i = l5index; i <= r5index; i++) /* increment i up to right-side of 5th freq notch */
{
    j = i - l5index; /* increment j (shifted from i) used in quadratic function */
    r[i] = 1; /* set magnitude array to unity - scale later */
    p[i] = (a * j) + (b/2 * j * j); /* set phase to quadratic function */
    x[i] = cos(p[i]); /* set real portion of complex number */
    y[i] = sin(p[i]); /* set imaginary portion of complex number */
}

/***** Building component 12 of excitation SWIFT waveform*****/
b = -PI/(r6index - l6index); /* component "b" of quadratic phase modulation equation */
for (i = l6index; i <= r6index; i++) /* increment i up to right-side of 6th freq notch */
{
    j = i - l6index; /* increment j (shifted from i) used in quadratic function */
    r[i] = 1; /* set magnitude array to unity - scale later */
    p[i] = (a * j) + (b/2 * j * j); /* set phase to quadratic function */
    x[i] = cos(p[i]); /* set real portion of complex number */
    y[i] = sin(p[i]); /* set imaginary portion of complex number */
}
else
    /* for isolation SWIFT waveform */
    {

```

Figure B-9. Build components 6, 8, 10 and 12 of excitation waveform.

```

/***** Building component 1 of isolation SWIFT waveform*****/
a = Pi/2; /* component "a" of quadratic phase modulation */
b = -Pi/l1index; /* component "b" of quadratic phase modulation */
for (i = 0; i < l1index; i++) /* increment i up to left-side of 1st freq notch */
{
    f[i] = deltaf * i; /* initialize frequency axis array in kHz */
    r[i] = 1; /* scale magnitude array to unity - scale later */
    p[i] = (a * i) + (b/2 * i * i); /* set phase to quadratic function */
    x[i] = cos(p[i]); /* set real portion of complex number */
    y[i] = sin(p[i]); /* set imaginary portion of complex number */
}

/***** Building component 2 of isolation SWIFT waveform*****/
for (i = l1index; i <= r1index; i++) /* increment i from left-side to right-side of 1st freq notch */
{
    f[i] = deltaf * i; /* initialize frequency axis array in kHz */
    r[i] = 0; /* set magnitude to zero */
    p[i] = 0; /* set phase to zero */
    x[i] = 0; /* set real portion of complex number to zero */
    y[i] = 0; /* set imaginary portion of complex number to zero */
}

/***** Building component 3 of isolation SWIFT waveform*****/
b = -Pi/(l2index - r1index); /* component "b" of quadratic phase modulation */
for (i = r1index + 1; i <= l2index; i++) /* increment i from right of 1st freq notch to left of 2nd freq notch */
{
    j = i - r1index; /* increment j (shifted from i) used in quadratic function */
    f[i] = deltaf * i; /* initialize frequency axis array in kHz */
    r[i] = 1; /* set magnitude array to unity - scale later */
    p[i] = (a * j) + (b/2 * j * j); /* set phase to quadratic function */
    x[i] = cos(p[i]); /* set real portion of complex number */
    y[i] = sin(p[i]); /* set imaginary portion of complex number */
}

/***** Building component 4 of isolation SWIFT waveform*****/
for (i = l2index + 1; i <= r2index; i++) /* increment i from left-side to right-side of 2nd freq notch */
{
    f[i] = deltaf * i; /* initialize frequency axis array in kHz */
    r[i] = 0; /* set magnitude to zero */
    p[i] = 0; /* set phase to zero */
    x[i] = 0; /* set real portion of complex number to zero */
    y[i] = 0; /* set imaginary portion of complex number to zero */
}

/***** Building component 5 of isolation SWIFT waveform*****/
b = -Pi/(l3index - r2index); /* component "b" of quadratic phase modulation */
for (i = r2index + 1; i <= l3index; i++) /* increment i from right of 2nd freq notch to left of 3rd freq notch */
{
    j = i - r2index; /* increment j (shifted from i) used in quadratic function */
    f[i] = deltaf * i; /* initialize frequency axis array in kHz */
    r[i] = 1; /* set magnitude array to unity - scale later */
    p[i] = (a * j) + (b/2 * j * j); /* set phase to quadratic function */
    x[i] = cos(p[i]); /* set real portion of complex number */
    y[i] = sin(p[i]); /* set imaginary portion of complex number */
}

```

Figure B-10. Build components 1 through 5 of isolation waveform.

```

/***** Building component 6 of isolation SWIFT waveform*****/
for (i = l3index + 1; i <= r3index; i++)/* increment i from left-side to right-side of 3rd freq notch */
{
    f[i] = deltax * i; /* initialize frequency axis array in kHz */
    r[i] = 0; /* set magnitude to zero */
    p[i] = 0; /* set phase to zero */
    x[i] = 0; /* set real portion of complex number to zero */
    y[i] = 0; /* set imaginary portion of complex number to zero */
}

/***** Building component 7 of isolation SWIFT waveform*****/
b = -PI/(l4index - r3index); /* component "b" of quadratic phase modulation */
for (i = r3index + 1; i <= l4index; i++)/* increment i from right of 3rd freq notch to left of 4th freq notch */
{
    j = i - r3index; /* increment j (shifted from i) used in quadratic function */
    f[i] = deltax * i; /* initialize frequency axis array in kHz */
    r[i] = 1; /* set magnitude array to unity - scale later */
    p[i] = (a * j) + (b/2 * j * j); /* set phase to quadratic function */
    x[i] = cos(p[i]); /* set real portion of complex number */
    y[i] = sin(p[i]); /* set imaginary portion of complex number */
}

/***** Building component 8 of isolation SWIFT waveform*****/
for (i = l4index + 1; i <= r4index; i++)/* increment i from left-side to right-side of 4th freq notch */
{
    f[i] = deltax * i; /* initialize frequency axis array in kHz */
    r[i] = 0; /* set magnitude to zero */
    p[i] = 0; /* set phase to zero */
    x[i] = 0; /* set real portion of complex number to zero */
    y[i] = 0; /* set imaginary portion of complex number to zero */
}

/***** Building component 9 of isolation SWIFT waveform*****/
b = -PI/(l5index - r4index); /* component "b" of quadratic phase modulation */
for (i = r4index + 1; i <= l5index; i++)/* increment i from right of 4th freq notch to left of 5th freq notch */
{
    j = i - r4index; /* increment j (shifted from i) used in quadratic function */
    f[i] = deltax * i; /* initialize frequency axis array in kHz */
    r[i] = 1; /* set magnitude array to unity - scale later */
    p[i] = (a * j) + (b/2 * j * j); /* set phase to quadratic function */
    x[i] = cos(p[i]); /* set real portion of complex number */
    y[i] = sin(p[i]); /* set imaginary portion of complex number */
}

/***** Building component 10 of isolation SWIFT waveform*****/
for (i = l5index + 1; i <= r5index; i++)/* increment i from left-side to right-side of 5th freq notch */
{
    f[i] = deltax * i; /* initialize frequency axis array in kHz */
    r[i] = 0; /* set magnitude to zero */
    p[i] = 0; /* set phase to zero */
    x[i] = 0; /* set real portion of complex number to zero */
    y[i] = 0; /* set imaginary portion of complex number to zero */
}

```

Figure B-11. Build components 6 through 10 of isolation waveform.

```

/***** Building component 11 of isolation SWIFT waveform *****/
b = -PI/(l6index - r5index); /* component "b" of quadratic phase modulation */
for (i = r5index + 1; i <= l6index; i++) /* increment i from right of 5th freq notch to left of 6th freq notch */
{
    j = i - r5index; /* increment j (shifted from i) used in quadratic function */
    f[i] = delfaf * i; /* initialize frequency axis array in kHz */
    r[i] = 1; /* set magnitude array to unity - scale later */
    p[i] = (a * j) + (b/2 * j * j); /* set phase to quadratic function */
    x[i] = cos(p[i]); /* set real portion of complex number */
    y[i] = sin(p[i]); /* set imaginary portion of complex number */
}
/***** Building component 12 of isolation SWIFT waveform *****/
for (i = l6index + 1; i <= r6index; i++) /* increment i from left-side to right-side of 6th freq notch */
{
    f[i] = delfaf * i; /* initialize frequency axis array in kHz */
    r[i] = 0; /* set magnitude to zero */
    p[i] = 0; /* set phase to zero */
    x[i] = 0; /* set real portion of complex number to zero */
    y[i] = 0; /* set imaginary portion of complex number to zero */
}
/***** Building component 13 of isolation SWIFT waveform *****/
b = -PI/(N/2 - r6index); /* component "b" of quadratic phase modulation */
for (i = r6index + 1; i <= N/2; i++) /* increment i from right-side of 6th freq notch to N/2 */
{
    j = i - r6index; /* increment j (shifted from i) used in quadratic function */
    f[i] = delfaf * i; /* initialize frequency axis array in kHz */
    r[i] = 1; /* set magnitude array to 1 */
    p[i] = (a * j) + (b/2 * j * j); /* set phase to quadratic function */
    x[i] = cos(p[i]); /* set real portion of complex number */
    y[i] = sin(p[i]); /* set imaginary portion of complex number */
}
}

```

Figure B-12. Build components 11 through 13 of isolation waveform.

```

/*****
Create data array, which will be filled with frequency data.
The contents of this array are shown below for f = 100 and N = 8:

f          real data pts          imaginary data pts
-----
0          data[0] = x[0]          data[1] = y[0]
12.5      data[2] = x[1]          data[3] = y[1]
25        data[4] = x[2]          data[5] = y[2]
37.5      data[6] = x[3]          data[7] = y[3]
50        data[8] = x[4]          data[9] = y[4]
-37.5     data[10] = x[3]         data[11] = -y[3]
-25       data[12] = x[2]         data[13] = -y[2]
-12.5     data[14] = x[1]         data[15] = -y[1]

From this example, its obvious (hopefully) why the f, r, p, x, and y arrays
were dimensioned by N+1 (since we need values from f[0] = 0 to f[N/2 + 1] = freqmax).
However, we need only calculate values for the positive frequencies, since we can
compute the values for the negative frequencies, which are simply the complex
conjugate of the positive portion (complex conjugate of (x + yi) = (x - yi)).
*****/
i = 0;
for (j = 0; j <= N/2; j++)
{
    data[i++] = x[j];
    data[i++] = y[j];
}
for (j = N/2 - 1; j > 0; j--)
{
    data[i++] = x[j];
    data[i++] = -y[j];
}

```

Figure B-13. Create data array for frequency data.

```

/*****
PERFORM INVERSE FOURIER TRANSFORM TO COMPUTE TIME-DOMAIN WAVEFORM
*****/

fft(data-1,N,-1);
for (i = 0; i < 2*N; i++) /* normalize results */
    data[i] = data[i]/N;

/*****
REFLECT TIME-DOMAIN SIGNAL ABOUT MIDPOINT
*****/

/* enclose the SWAP statement in {} since it compiles to multiple statements */
for (i = 0; i < N; i++)
    {
        SWAP(data[i], data[N+i]);
    }

/*****
GENERATE APODIZATION FUNCTION AND SMOOTH TIME-DOMAIN WAVEFORM
*****/

for (i = 0; i < N; i++)
    {
        if (i < .25 * N) /* set 1st quarter = 1st quarter of sine wave */
            apod[i] = sin(2*P*i/N);
        else if (i < .75 * N) /* set next half = unit */
            apod[i] = 1;
        else
            /* set last quarter = last quarter of sine wave */
            apod[i] = apod[N-1-i]; /* compute from reflection of 1st quarter */
    }

for (i = j = 0; i < 2*N; i+=2, j++)
    {
        data[i] = data[i] * apod[j];
        data[i+1] = data[i+1] * apod[j];
    }

```

Figure B-14. Inverse Fourier transform, midpoint time reflection, and apodization.

```
/******  
  
NORMALIZE WAVEFORM AND DOWNLOAD TO FUNCTION GENERATOR  
  
*****/  
  
max = 0;  
for (i = 0; i < 2*N; i++)  
    if (fabs(data[i]) > max) max = fabs(data[i]);  
norm1 = MAX/max; /* calc scaling factor for wave (int data) */  
norm2 = vpp/max; /* calc scaling factor for data (real data) */  
checksum = 0;  
  
for (i = 0; i < N; i++) /* norm waveform to give max amp */  
    {  
        wave[i] = (int) (data[2*i] * norm1);  
        data[2*i] = data[2*i] * norm2;  
        checksum += wave[i]; /* and keep running checksum */  
    }  
wave[N] = checksum; /* tack checksum onto end of array */  
  
if (dlflag == 1)  
    {  
        printf("Still trying to figure out how to download using RS232 instead of GPIB - any suggestions? ...\\n");  
    }  
}
```

Figure B-15. Normalize waveform and download to function generator.

```

/*****
WRITE WAVEFORM DATA TO OUTPUT FILES
*****/

if (fileflag & 1)
{
printf("Outputting SWIFT data to ASCII file ...\n");

fprintf(ascfp, "\\ DATASET 1: frequency vs magnitude of SWIFT waveform\n");
fprintf(ascfp, "%i %i\n", N/2 + 1, 2); /* print number of rows and columns */
for (i = 0; i <= N/2; i++)
    fprintf(ascfp, "%f %f\n", f[i], r[i]);

fprintf(ascfp, "\\ DATASET 2: frequency vs phase of SWIFT waveform\n");
fprintf(ascfp, "%i %i\n", N/2 + 1, 2);
for (i = 0; i <= N/2; i++)
    fprintf(ascfp, "%f %f\n", f[i], p[i]);

fprintf(ascfp, "\\ DATASET 3: time-domain SWIFT waveform (apodized and normalized)\n");
fprintf(ascfp, "%i %i\n", N, 2);
for (i = 0; i < N; i++)
    fprintf(ascfp, "%f %f\n", t[i], data[2*i]);

for (i = 0; i < N; i++) /* normalize waveform to give original amplitude */
    data[2*i] = data[2*i]/norm2;
fft(data-1,N,1); /* perform forward Fourier transform */
for (i = 0; i <= N/2; i++) /* compute magnitude */
    r[i] = sqrt( pow(data[2*i],2) + pow(data[2*i+1],2) );

fprintf(ascfp, "\\ DATASET 4: frequency-domain SWIFT waveform (zero filled, mag mode)\n");
fprintf(ascfp, "%i %i\n", N/2 + 1, 2); /* print number rows and columns */
for (i = 0; i <= N/2; i++)
    fprintf(ascfp, "%f %f\n", f[i], r[i]);

fclose(ascfp);
}

if (fileflag & 2)
{
printf("Outputting SWIFT data to binary file ...\n");
fwrite(wave, sizeof(int), N+1, binfp);
fclose(binfp);
}

system("PAUSE");
}

```

Figure B-16. Write waveform data to output files.

```

/*=====
Function:      FFT

Purpose:      This function performs a discrete fast Fourier transform and is adapted fro the algorithm in "Numerical
               Recipes in C", pp. 411-412.  If isign is 1, it replaces data with a Fourier transform.  If isign is -1,
               it replaces data by nn times its inverse Fourier transform.  Data is a complex array of length nn input
               as a real array data[1..2*nn].  nn must be an integer power of 2 (this is not checked for).
=====*/
void fft(float data[], int nn, int isign)
{
    int          n,mmax,m,j,istep,i;
    double       wtemp,wr,wpr,wpi,wi,theta;
    float        tempr,tempi;

    n=nn<<1;
    j=1;
    for (i=1; i<n; i+=2) /* perform bit reversal */
        {
            if (j > i)
                {
                    SWAP(data[j],data[i]);
                    SWAP(data[j+1],data[i+1]);
                }

            m=n>>1;
            while (m >= 2 && j > m)
                {
                    j-=m;
                    m>>=1;
                }

            j+=m;
        }

    mmax=2;
    while (n > mmax) /* perform Danielson-Lanczos transform */
        {
            istep=2*mmax;
            theta=6.28318530717959/(isign*mmax);
            wtemp=sin(0.5*theta);
            wpr=-2.0*wtemp*wtemp;
            wpi=sin(theta);
            wr=1.0;
            wi=0.0;
            for (m=1; m<=mmax; m+=2)
                {
                    for (i=m; i<n; i+=istep)
                        {
                            j=i+mmax;
                            tempr=wr*data[j]-wi*data[j+1];
                            tempi=wr*data[j+1]+wi*data[j];
                            data[j]=data[i]-tempr;
                            data[j+1]=data[i+1]-tempi;
                            data[i] += tempr;
                            data[i+1] += tempi;
                        }

                    wr=(wtemp*wr)*wpr-wi*wpi+wr;
                    wi=wi*wpr+wtemp*wpi+wi;
                }

            mmax=istep;
        }
}

```

Figure B-17. Fast Fourier transform function.

APPENDIX C LTQ MODIFICATIONS

The SWIFT waveform is calculated from the C⁺⁺ program in Appendix B and stored in an arbitrary waveform generator (AWG) (Stanford Research Systems Model DS345, Sunnyvale, CA, USA). The SWIFT output of the AWG is then connected to the LTQ analog printed circuit board (PCB). The LTQ analog PCB contains a pair of AD734 multiplier/divider microchips shown in Figure C-1. Chip U46 multiplies the LTQ isolation waveform signal ($X_1 - X_2$) by the isolation waveform gain ($Y_1 - Y_2$). This product is then divided by the denominator interface ($U_1 - U_2$) and then the results of chip U64 ($Z_1 - Z_2$) are subtracted from this quotient. Chip U64 multiplies the resonant ejection/excitation (Res Ej/Ex) waveform ($X_1 - X_2$) by the Res Ej/Ex waveform gain ($Y_1 - Y_2$). This product is then divided by the denominator interface ($U_1 - U_2$). The resulting quotient is subtracted by ($Z_1 - Z_2$), which is usually set to ground. Z_2 corresponds to pin 10 of chip U64. The pin was lifted from the PCB and was wired to the center contact of the BNC (Bayonet Neill-Concelman) cable connected to the output of the AWG (Figure C-2). The grounding sheath of the AWG BNC cable was wired to a ground pin on the analog PCB. When SWIFT is not being applied to the LTQ, a BNC grounding cap is placed on the BNC connector wired to pin 10 of chip U64.

The LTQ software has a programmable trigger that allows an external waveform to be triggered during a designated location of the scan function. The location of the programmable trigger in the LTQ software is in the Diagnostics menu underneath the Tools list. By clicking on Triggers, the window shown in Figure C-3 appears, which allows the user to input two arguments (ARG1 and ARG2), which defines the ion trap control language (ITCL) trigger function, $\text{trig}(\text{ARG1}, \text{ARG2})$. ARG1 is the trigger location type (e.g., -1 = all triggers off, 0 = beginning of scan, 1 = injection period, 2 = isolation, 3 = activation, and 4 = scan out), and

ARG2 is the n^{th} position of that type. If no ARG1 or ARG2 is given, the trigger is set at the start of the analytical scan. If no ARG2 is given, it is set to 0 (the first position of that location type). The available values for ARG2 will depend on the mode and the trigger location type (Figure C-3). If ARG2 = -1, then triggers are on for all periods of that trigger location type. Figure C-4 shows a diagram of the mass spectrometer scan function with the different locations labeled with the corresponding trigger functions values.

The programmable trigger was accessed by connecting a wire to pin 14 of the J1 connector of the LTQ digital PCB (Figure C-5). The other end of the wire was connected to the center contact of the BNC cable leading to the trigger input on the back of the AWG. The grounding sheath of the AWG BNC cable was wired to a ground pin on the digital PCB.

The locations of the programmable trigger were tested by using a two-channel digitizing oscilloscope with screen capture capability (Model TDS 540, Tektronix Inc., Beaverton, OR, USA). The trigger pulse from the LTQ digital PCB was connected to channel 1 of the oscilloscope, and the waveform output after amplification was connected to channel 2 of the oscilloscope through an RCA (Radio Corporation of America) connector on the LTQ analog PCB. Figure C-6 shows the oscilloscope image of channels 1 and 2 with the trigger set to the beginning of the scan [trig(0,0)] with automatic gain control (AGC) on. Note that there are two different triggers shown for channel 1, one during the beginning of the prescan and the other one during the beginning of the analytical scan. The end of the prescan is indicated by the large AGC signal from channel 2, where the radiofrequency (RF) voltage is ramped up to scan out the trapped ions from the ion trap. Channel 2 also shows two signals, one for the prescan and one for the analytical scan, that correspond to the LTQ isolation (ISO) waveform.

Figure C-7 shows the oscilloscope image of channels 1 and 2 with the trigger set to the injection period [trig(1,0)] and AGC on. Channel 1 shows no visible trigger pulses, which indicate that the programmable trigger is not sending a measurable trigger pulse during the injection period highlighted in Figure C-4. Channel 2 however does indicate the presence of the prescan and analytical scan each containing an isolation waveform signal and a scan out signal.

Figure C-8 shows the oscilloscope image of channels 1 and 2 with the trigger set to the isolation period [trig(2,0)] and AGC on. Channel 1 shows visible trigger pulses that line up with the isolation waveform signals of the prescan and analytical scan shown from channel 2. Before the SWIFT isolation waveform can be triggered during the isolation period, it is important to turn off the LTQ isolation waveform to avoid interference. Under the Diagnostics Tools menu in the LTQ software, Toggles can be selected (Figure C-9). Then the Isolation waveform can be highlighted and the off or on radio buttons selected before the Set button is pressed. It is important to note that if the Define Scan window is opened in the LTQ software, the toggles return to their default factory settings (i.e., LTQ isolation waveform on).

Figure C-10 shows the mass spectra of cocaine (COC) with the isolation waveform toggled on (Figure C-10a) and off (Figure C-10b). COC standard was spotted (1 μL , 1 $\text{ng}/\mu\text{L}$) onto a MALDI plate and airbrushed with 2,5-dihydroxybenzoic acid as the matrix. The $[\text{M}+\text{H}]^+$ ion of cocaine at m/z 304 was isolated with a 1-Da isolation window centered at m/z 304. With the LTQ isolation waveform on (Figure C-10a), the background ions are ejected leaving a visible $[\text{COC}+\text{H}]^+$ ion at m/z 304; however, with the LTQ isolation waveform turned off (Figure C-10b) the background ions overwhelm the m/z 304 ion and it is not visible. The low mass cutoff (LMCO) is visible with the LTQ isolation waveform turned off (Figure C-10b), which is calculated to be m/z 277 based on m/z 304 being isolated at a q of 0.83, $[\text{LMCO} =$

$(0.83)(304)/(0.91) = 277$]. Figure C-11 shows the oscilloscope images of channel 1 and 2 with the trigger at isolation, AGC on, and the LTQ isolation waveform toggled on (Figure C-11a) and off (Figure C-11b). Channel 2 of Figure C-11b clearly shows that the isolation waveforms disappear from the prescan and the analytical scan when the LTQ isolation waveform is toggled off.

Figure C-12 shows the oscilloscope image of channels 1 and 2 with the trigger set at activation [trig(3,0)] and AGC on. Channel 1 shows that activation occurs between the isolation event and the scan out event of both the prescan and the analytical scan. Figure C-13 shows the oscilloscope image of channels 1 and 2 with the trigger set at scan out [trig(4,0)] and AGC on. Channel 1 shows only a single trigger pulse during the scan out of the analytical scan.

AD734 Multiplier/Divider Chips

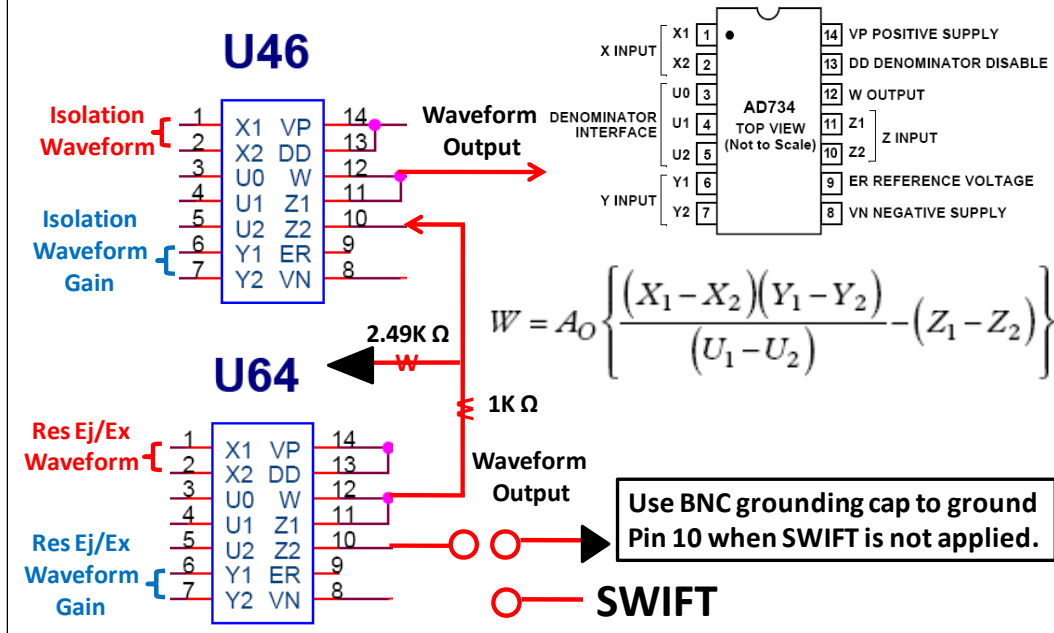


Figure C-1. Adding SWIFT waveform to AD734 chip (U64) on LTQ Analog PCB.

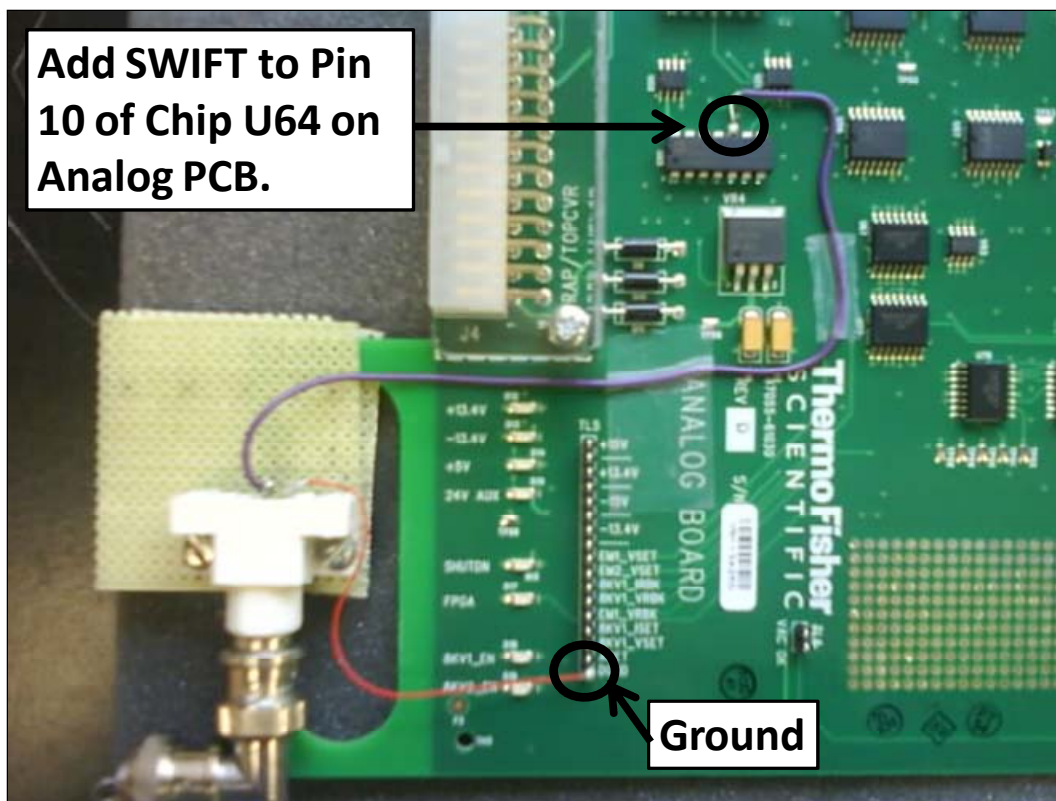


Figure C-2. Analog PCB modification to apply SWIFT waveform.

The screenshot shows the 'Diagnostics' window with the 'Triggers' menu item selected. The 'Trigger Location' is set to 'All Triggers Off' and the 'Scan Position' is set to '-1'. A 'Set' button is visible below the dropdowns.

Trigger Location Type	Full Scan	SIM (ZoomScan MS)	MS/MS (Zoom SRM)
All Triggers Off			
Beginning of Scan	0	0-9	0
Injection Period	0, 1, 2, or 3 injection periods	0-9	0
Isolation	No Trigger	0-9	0-2
Activation	No Trigger	No Trigger	0-2
Scan Out	0	0-9 SIM Windows	0-9 SRM Windows

Figure C-3. LTQ programmable trigger.

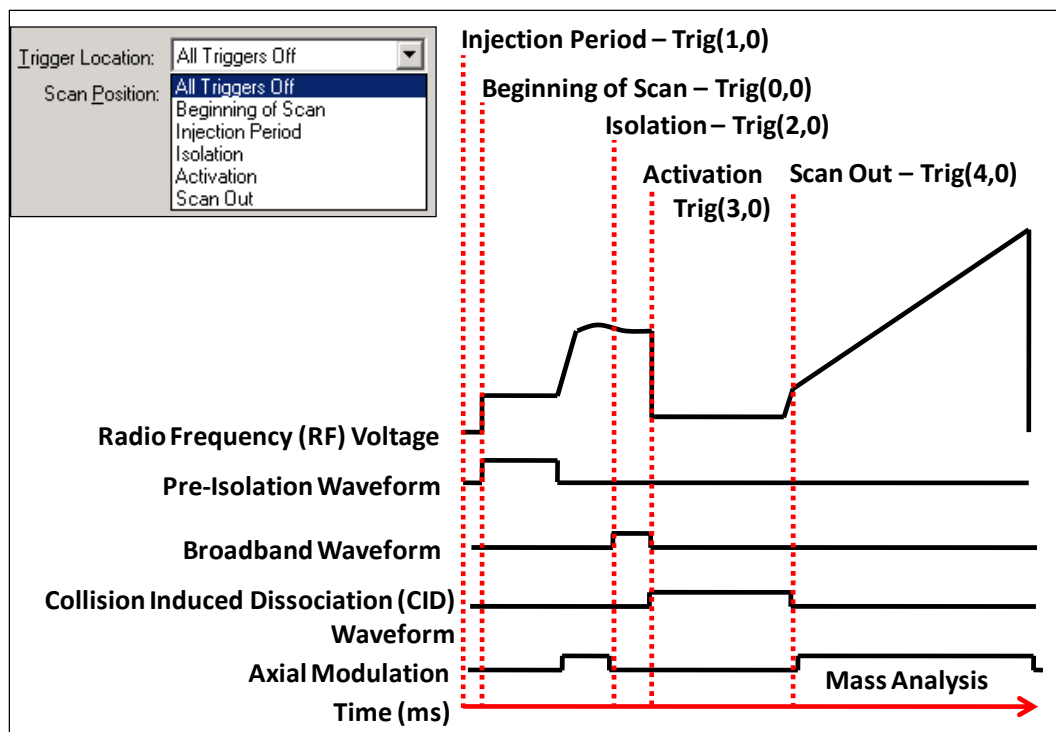


Figure C-4. Programmable trigger locations.

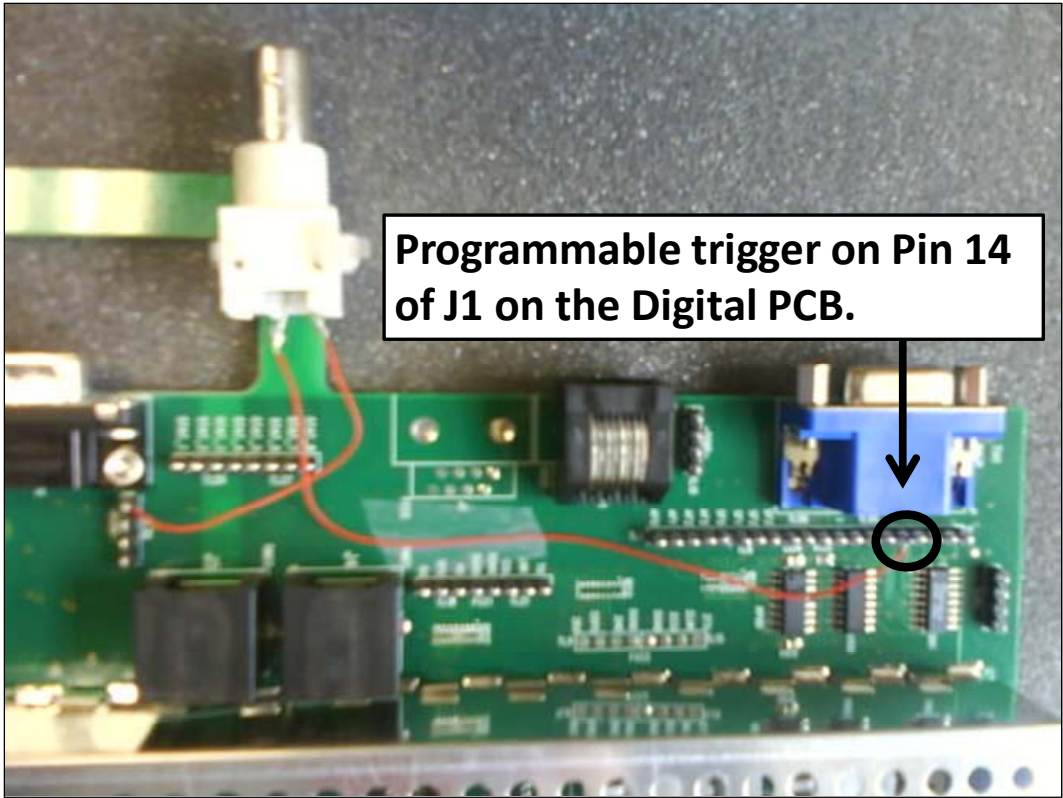


Figure C-5. Digital PCB modifications to access programmable trigger.

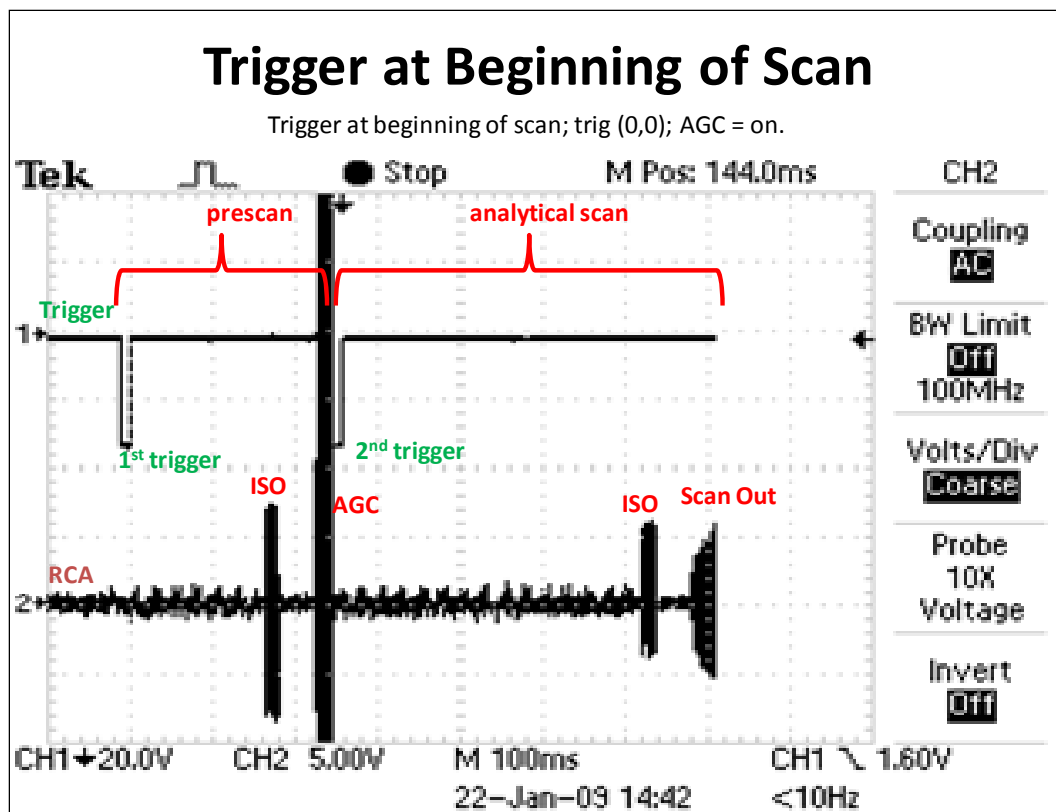


Figure C-6. Trigger at beginning of scan.

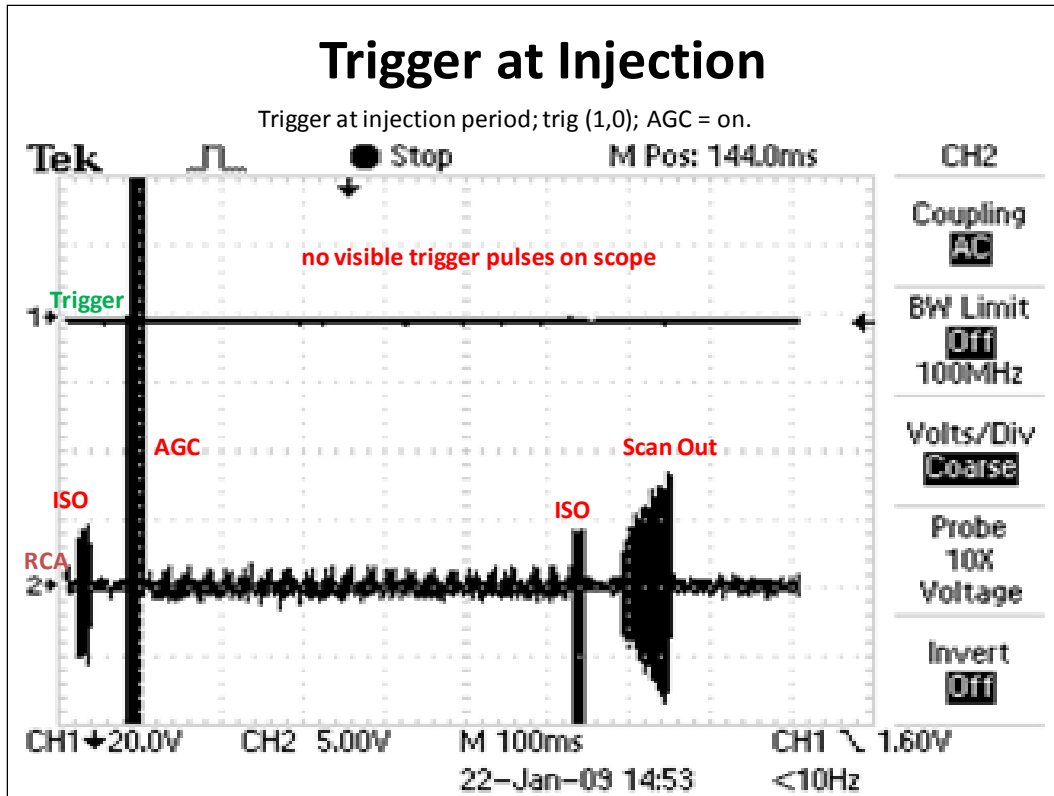


Figure C-7. Trigger at injection.

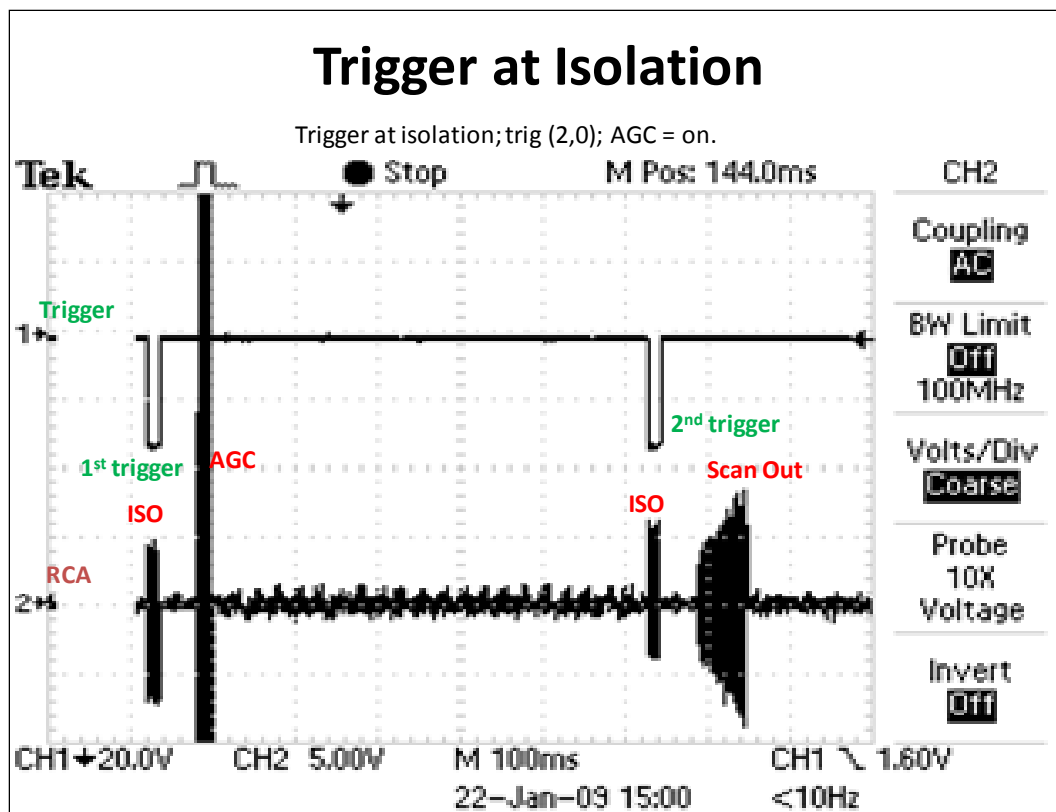


Figure C-8. Trigger at isolation.

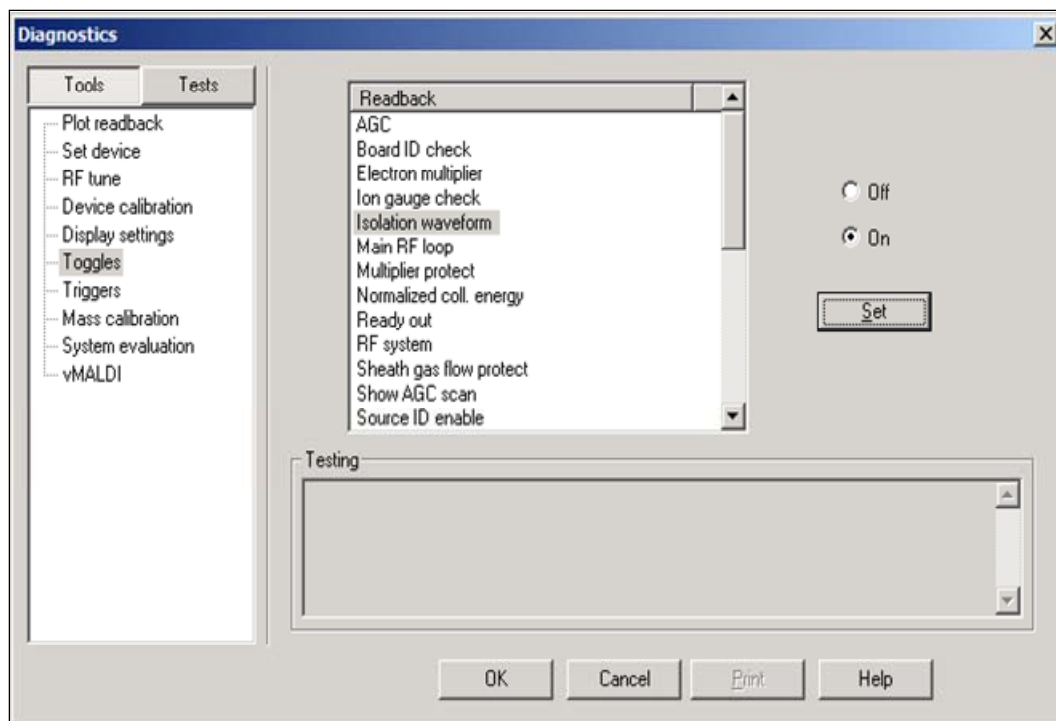


Figure C-9. Toggling LTQ isolation waveform on and off.

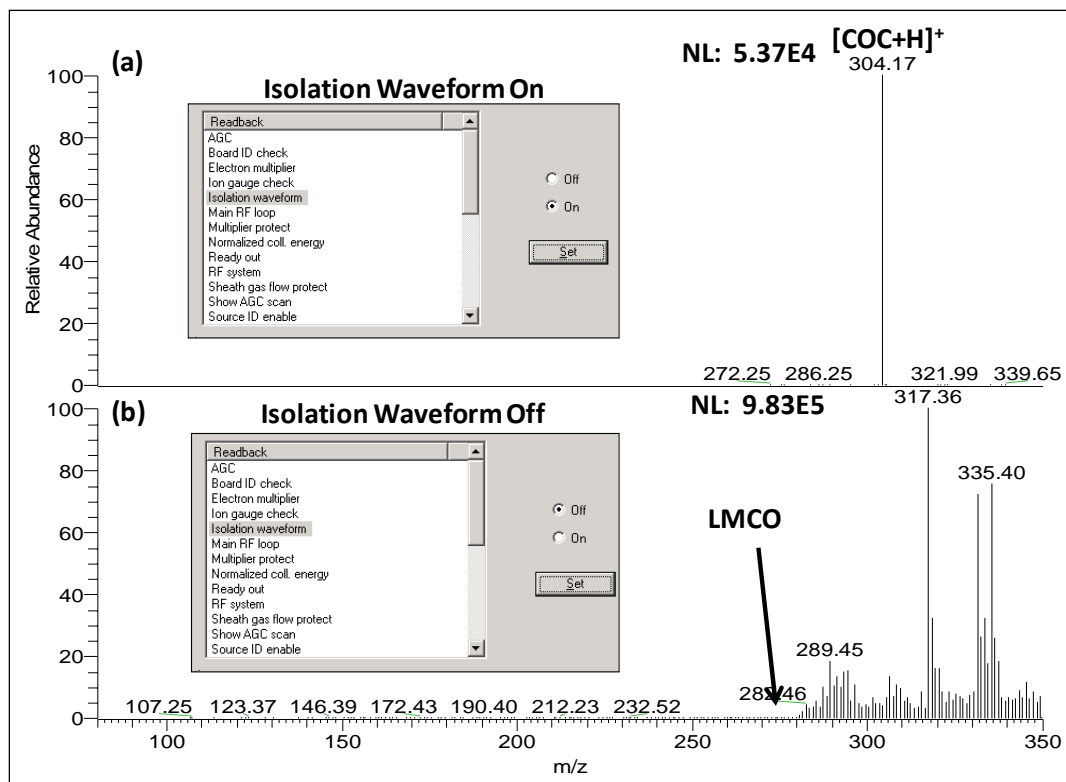


Figure C-10. Mass spectra of cocaine with isolation waveform toggled: (a) on and (b) off.

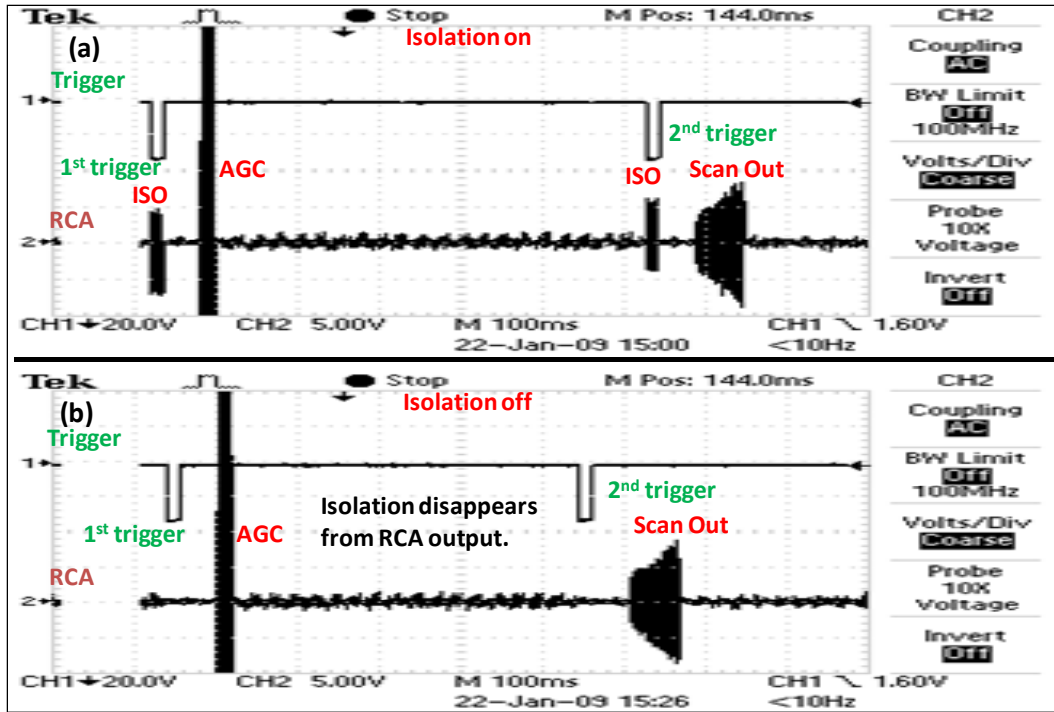


Figure C-11. Trigger at isolation with isolation toggled: (a) on and (b) off.

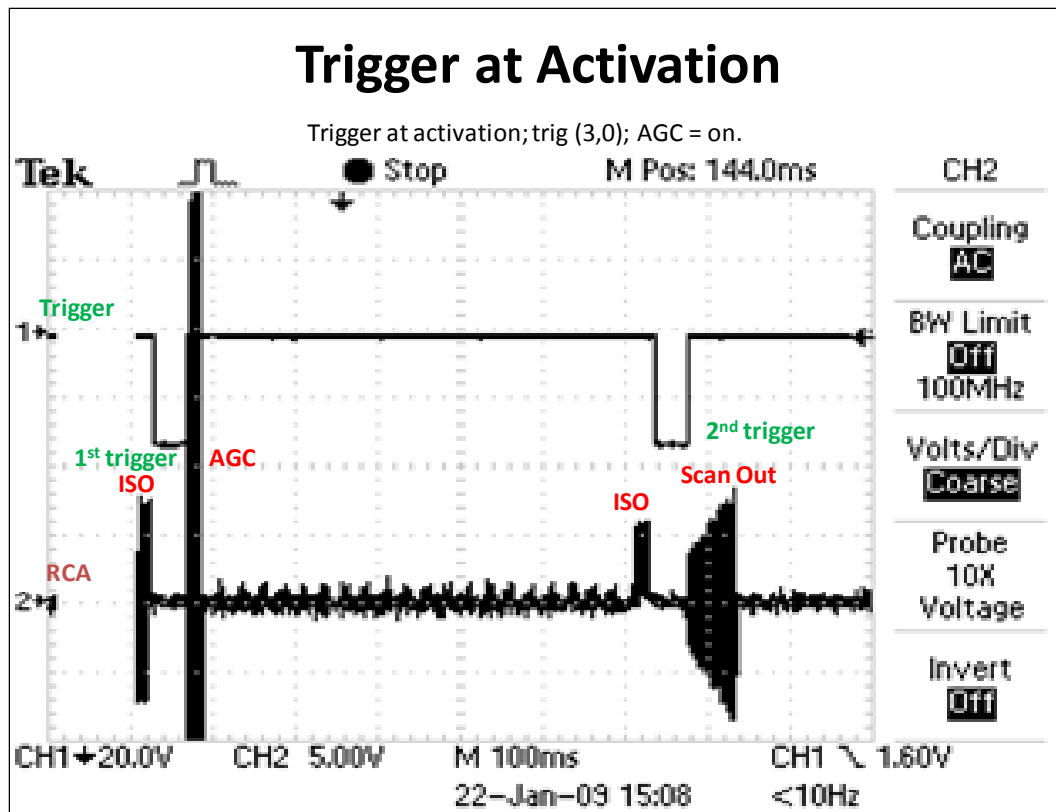


Figure C-12. Trigger at activation.

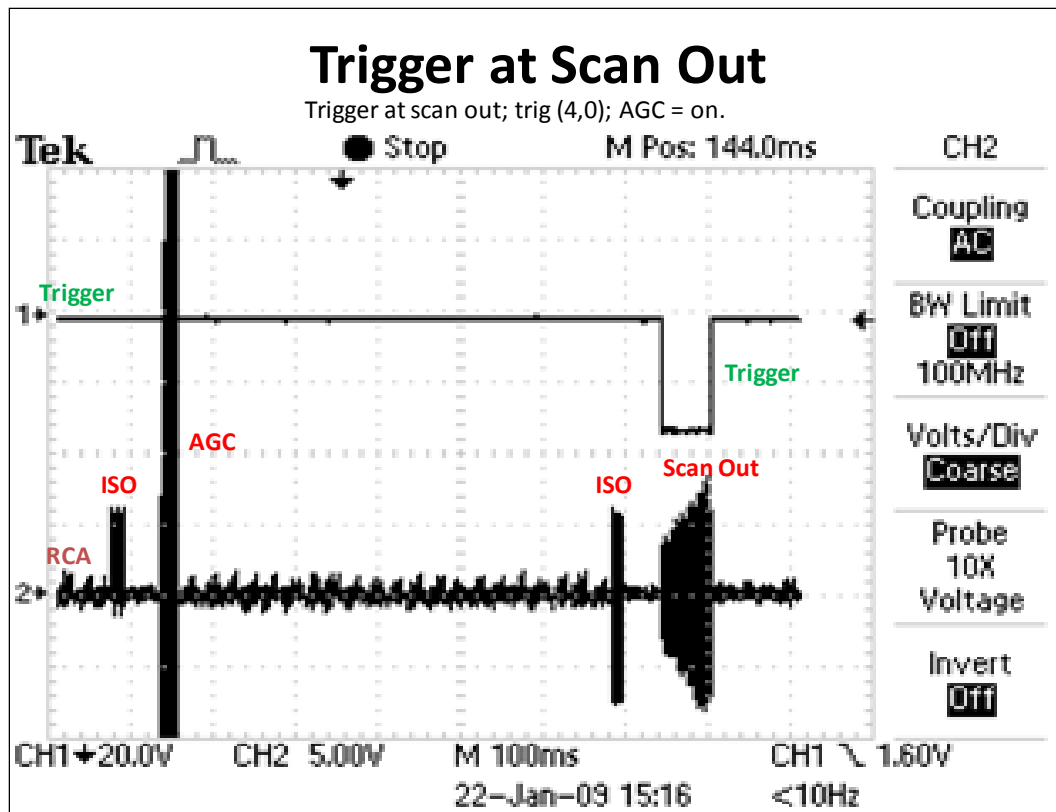


Figure C-13. Trigger at scan out.

LIST OF REFERENCES

- (1) Karch, S. B. *Karch's Pathology of Drug Abuse*, 3rd ed.; CRC Press LLC: Boca Raton, 2002.
- (2) Substance Abuse and Mental Health Services Administration, Office of Applied Studies *Drug Abuse Warning Network, 2007: Area Profiles of Drug-Related Mortality*. HHS Publication No. SMA 09-4407, DAWN Series D-31. Rockville, MD, 2009.
- (3) Human Illnesses and Behavioral Health. <http://www.humanillnesses.com> (accessed 30 June 2008).
- (4) Drummer, O. H.; Gerstamoulos, J. *Therap. Drug Monitor.* **2002**, *24*, 199-209.
- (5) Stimpfl, T.; Reichel, S. *Forensic Sci. Int.* **2007**, *170*, 179-182.
- (6) Moriya, F.; Hashimoto, Y. *J. Forensic Sci.* **1996**, *41*, 612-616.
- (7) Moriya, F.; Hashimoto, Y. *J. Forensic Sci.* **1996**, *41*, 129-133.
- (8) Spiehler, V. R.; Reed, D. J. *Forensic Sci.* **1985**, *30*, 1003-1011.
- (9) Giroud, C.; Michaud, K.; Sporkert, F.; Eap, C.; Augsburger, M.; Cardinal, P.; Mangin, P. *J. Anal. Toxicol.* **2004**, *28*, 464-474.
- (10) In *National Institute on Drug Abuse Research Monograph 163*; Majewska, M. D., Ed., 1996, pp 1-340.
- (11) Ritz, M. C.; Lamb, R. T.; Goldberg, S. R.; Kuhar, M. J. *Science* **1987**, *237*, 1219-1223.
- (12) Kalasinsky, K. S.; Bosy, T. Z.; Schmunk, G. A.; Ang, L.; Adams, V.; Gore, S. B.; Smialek, J.; Furukawa, Y.; Guttman, M.; Kish, S. J. *J. Forensic Sci.* **2000**, *45*, 1041-1048.
- (13) Alburges, M. E.; Crouch, D. J.; Andrenyak, D. M.; Wamsley, J. K. *Neurochem. Int.* **1996**, *28*, 51-57.
- (14) James, C. A.; Breda, M.; Baratte, S.; Casati, M.; Grassi, S.; Pellegatta, B.; Sarati, S.; Frigerio, E. *Chromatographia* **2004**, *59*, S149-S156.
- (15) Kusumoto, M.; Ikeda, K.; Nishiya, Y.; Kawamura, Y. *Anal. Biochem.* **2001**, *294*, 185-186.
- (16) Schiffer, W. K.; Liebling, C. N. B.; Patel, V.; Dewey, S. L. *Nucl. Med. Biol.* **2007**, *34*, 833-847.
- (17) Gatley, S. J.; Volkow, N. D. *Drug Alcohol Depend.* **1998**, *51*, 97-108.

- (18) Sosnovik, D. E.; Weissleder, R. *Curr. Opin. Biotechnol.* **2007**, *18*, 4-10.
- (19) Wang, G.; Yu, H.; De Man, B. *Med. Phys.* **2008**, *35*, 1051-1064.
- (20) Gumbleton, M.; Stephens, D. J. *Adv. Drug Delivery Rev.* **2005**, *57*, 5-15.
- (21) Contag, C. H.; Ross, B. D. *J. Magn. Reson. Imaging* **2002**, *16*, 378-387.
- (22) Denoyer, A.; Ossant, F.; Arbeille, B.; Fetissof, F.; Patat, F.; Pourcelot, L.; Pisella, P.-J. *Ophthalmic Res.* **2008**, *40*, 298-308.
- (23) Som, P.; Oster, Z. H.; Wang, G.-J.; Volkow, N. D.; Sacker, D. F. *Life Sci.* **1994**, *55*, 1375-1382.
- (24) Garidel, P.; Boese, M. *Microsc. Res. Tech.* **2007**, *70*, 336-349.
- (25) Mahmoudi, M.; Simchi, A.; Imani, M.; Hafeli, U. O. *J. Phys. Chem. C* **2009**, *113*, 8124-8131.
- (26) Niu, G.; Chen, X. *Drugs R&D* **2008**, *9*, 351-368.
- (27) Chaurand, P.; Schwartz, S. A.; Reyzer, M. L.; Caprioli, R. M. *Toxicol. Pathol.* **2005**, *33*, 92-101.
- (28) Pacholski, M. L.; Winograd, N. *Chem. Rev.* **1999**, *99*, 2977-3005.
- (29) Caprioli, R. M.; Farmer, T. B.; Gile, J. *Anal. Chem.* **1997**, *69*, 4751-4760.
- (30) Troendle, F. J.; Reddick, C. D.; Yost, R. A. *J. Am. Soc. Mass Spectrom.* **1999**, *10*, 1315-1321.
- (31) Reyzer, M. L.; Hsieh, Y.; Ng, K.; Korfmacher, W. A.; Caprioli, R. M. *J. Mass Spectrom.* **2003**, *38*, 1081-1092.
- (32) Bunch, J.; Clench, M. R.; Richards, D. S. *Rapid Commun. Mass Spectrom.* **2004**, *18*, 3051-3060.
- (33) Wang, H.-Y. J.; Jackson, S. N.; McEuen, J.; Woods, A. S. *Anal. Chem.* **2005**, *77*, 6682-6686.
- (34) Cristoni, S.; Brioschi, M.; Rizzi, A.; Sironi, L.; Gelosa, P.; Tremoli, E.; Bernardi, L. R.; Banfi, C. *Rapid Commun. Mass Spectrom.* **2006**, *20*, 3483-3487.
- (35) Crossman, L.; McHugh, N. A.; Hsieh, Y.; Korfmacher, W. A.; Chen, J. *Rapid Commun. Mass Spectrom.* **2006**, *20*, 284-290.

- (36) Hsieh, Y.; Casale, R.; Fukuda, E.; Chen, J.; Knemeyer, I.; Wingate, J.; Morrison, R.; Korfmacher, W. *Rapid Commun. Mass Spectrom.* **2006**, *20*, 965-972.
- (37) Khatib-Shahidi, S.; Andersson, M.; Herman, J. L.; Gillespie, T. A.; Caprioli, R. M. *Anal. Chem.* **2006**, *78*, 6448-6456.
- (38) Drexler, D. M.; Garrett, T. J.; Cantone, J. L.; Diters, R. W.; Mitroka, J. G.; Prieto Conaway, M. C.; Adams, S. P.; Yost, R. A.; Sanders, M. *J. Pharmacol. Toxicol. Methods* **2007**, *55*, 279-288.
- (39) Hsieh, Y.; Chen, J.; Korfmacher, W. A. *J. Pharmacol. Toxicol. Methods* **2007**, *55*, 193-200.
- (40) Stoeckli, M.; Staab, D.; Schweitzer, A. *Int. J. Mass Spectrom.* **2007**, *260*, 195-202.
- (41) Chen, J.; Hsieh, Y.; Knemeyer, I.; Crossman, L.; Korfmacher, W. A. *Drug Metab. Lett.* **2008**, *2*, 1-4.
- (42) Cornett, D. S.; Frappier, S. L.; Caprioli, R. M. *Anal. Chem.* **2008**, *80*, 5648-5653.
- (43) Hopfgartner, G.; Varesio, E.; Stoeckli, M. *Rapid Commun. Mass Spectrom.* **2009**, *23*, 733-736.
- (44) Li, F.; Hsieh, Y.; Kang, L.; Sondey, C.; Lachowicz, J.; Korfmacher, W. A. *Bioanalysis* **2009**, *1*, 299-307.
- (45) Takats, Z.; Wiseman, J. M.; Gologan, B.; Cooks, R. G. *Science* **2004**, *306*, 471-473.
- (46) Nemes, P.; Vertes, A. *Anal. Chem.* **2007**, *79*, 8098-8106.
- (47) Cooks, R. G.; Ouyang, Z.; Takats, Z.; Wiseman, J. M. *Science* **2006**, *311*, 1566-1570.
- (48) Zenobi, R.; Knochenmuss, R. *Mass Spectrom. Rev.* **1998**, *17*, 337-366.
- (49) Niu, S.; Zhang, W.; Chait, B. T. *J. Am. Soc. Mass Spectrom.* **1998**, *9*, 1-7.
- (50) Berkenkamp, S.; Menzel, C.; Karas, M.; Hillenkamp, F. *Rapid Commun. Mass Spectrom.* **1997**, *11*, 1399-1406.
- (51) Zhang, W.; Niu, S.; Chait, B. T. *J. Am. Soc. Mass Spectrom.* **1998**, *9*, 879-884.
- (52) Dreisewerd, K. *Chem. Rev.* **2003**, *103*, 395-425.
- (53) Schriver, K. E.; Chaurand, P.; Caprioli, R. M. *Proceedings of the 51st ASMS Conference on Mass Spectrometry and Allied Topics*: Montreal, Canada, 2003.

- (54) Jurchen, J. C.; Rubakhin, S. S.; Sweedler, J. V. *J. Am. Soc. Mass Spectrom.* **2005**, *16*, 1654-1659.
- (55) Cohen, S. L.; Chait, B. T. *Anal. Chem.* **1996**, *68*, 31-37.
- (56) Nakanishi, T.; Ohtsu, I.; Furuta, M.; Ando, E.; Nishimura, O. *J. Proteome Res.* **2005**, *4*, 743-747.
- (57) Baluya, D. L.; Garrett, T. J.; Yost, R. A. *Anal. Chem.* **2007**, *79*, 6862-6867.
- (58) Schwartz, S. A.; Reyzer, M. L.; Caprioli, R. M. *J. Mass Spectrom.* **2003**, *38*, 699-708.
- (59) Landgraf, R. R., Analysis of Lipids in Nerve Tissue by MALDI Tandem Mass Spectrometric Imaging. Ph.D. Dissertation, University of Florida, Gainesville, FL, 2009.
- (60) Garrett, T. J.; Yost, R. A. *Anal. Chem.* **2006**, *78*, 2465-2469.
- (61) Ayorinde, F. O.; Hambright, P.; Porter, T. N.; Keith, Q. L., Jr. *Rapid Commun. Mass Spectrom.* **1999**, *13*, 2474-2479.
- (62) Cohen, L. H.; Gusev, A. I. *Anal. Bioanal. Chem.* **2002**, *373*, 571-586.
- (63) Karas, M.; Kruger, R. *Chem. Rev.* **2003**, *103*, 427-439.
- (64) Chapman, J. R. *Practical Organic Mass Spectrometry: A Guide for Chemical and Biochemical Analysis*, 2nd ed.; John Wiley and Sons: New York, 1998.
- (65) Hensel, R. R.; King, R. C.; Owens, K. G. *Rapid Commun. Mass Spectrom.* **1997**, *11*, 1785-1793.
- (66) Nicola, A. J.; Gusev, A. I.; Proctor, A.; Jackson, E. K.; Hercules, D. M. *Rapid Commun. Mass Spectrom.* **1995**, *9*, 1164-1171.
- (67) Garrett, T. J.; Prieto-Conaway, M. C.; Kovtoun, V.; Bui, H.; Izgarian, N.; Stafford, G.; Yost, R. A. *Int. J. Mass Spectrom.* **2007**, *260*, 166-176.
- (68) Sugiura, Y.; Shimma, S.; Setou, M. *Anal. Chem.* **2006**, *78*, 8227-8235.
- (69) Hankin, J. A.; Barkley, R. M.; Murphy, R. C. *J. Am. Soc. Mass Spectrom.* **2007**, *18*, 1646-1652.
- (70) Aerni, H.-R.; Cornett, D. S.; Caprioli, R. M. *Anal. Chem.* **2006**, *78*, 827-834.
- (71) Puolitaival, S. M.; Burnum, K. E.; Cornett, D. S.; Caprioli, R. M. *J. Am. Soc. Mass Spectrom.* **2008**, *19*, 882-886.

- (72) Atkinson, S. J.; Loadman, P. M.; Sutton, C.; Patterson, L. H.; Clench, M. R. *Rapid Commun. Mass Spectrom.* **2007**, *21*, 1271-1276.
- (73) Trim, P. J.; Henson, C. M.; Avery, J. L.; McEwen, A.; Snel, M. F.; Claude, E.; Marshall, P. S.; West, A.; Princivalle, A. P.; Clench, M. R. *Anal. Chem.* **2008**, *80*, 8628-8634.
- (74) Luxembourg, S. L.; McDonnell, L. A.; Duursma, M. C.; Guo, X.; Heeren, R. M. A. *Anal. Chem.* **2003**, *75*, 2333-2341.
- (75) Lemaire, R.; Tabet, J.; Ducoroy, P.; Hendra, J. B.; Salzet, M.; Fournier, I. *Anal. Chem.* **2006**, *78*, 809-819.
- (76) Onnerfjord, P.; Ekstrom, S.; Bergquist, J.; Nilsson, J.; Laurell, T.; Marko-Varga, G. *Rapid Commun. Mass Spectrom.* **1999**, *13*, 315-322.
- (77) Sleno, L.; Volmer, D. A. *Rapid Commun. Mass Spectrom.* **2006**, *20*, 1517-1524.
- (78) Nicola, A. J.; Gusev, A. I.; Hercules, D. M. *Appl. Spectrosc.* **1996**, *50*, 1479-1482.
- (79) Ling, Y.-C.; Lin, L.; Chen, Y.-T. *Rapid Commun. Mass Spectrom.* **1998**, *12*, 317-327.
- (80) Hatsis, P.; Brombacher, S.; Corr, J.; Kovarik, P.; Volmer, D. A. *Rapid Commun. Mass Spectrom.* **2003**, *17*, 2303-2309.
- (81) Cui, M.; McCooney, M. A.; Fraser, C.; Mester, Z. *Anal. Chem.* **2004**, *76*, 7143-7148.
- (82) Gusev, A. I.; Wilkinson, W. R.; Proctor, A.; Hercules, D. M. *Fresenius. J. Anal. Chem.* **1996**, *354*, 455-463.
- (83) Kang, M.-J.; Tholey, A.; Heinzle, E. *Rapid Commun. Mass Spectrom.* **2001**, *15*, 1327-1333.
- (84) Krutchinsky, A. N.; Chait, B. T. *J. Am. Soc. Mass Spectrom.* **2002**, 129-134.
- (85) *FinniganTM vMALDI Source Hardware Manual*; Thermo Electron Corporation: San Jose, CA, 2003.
- (86) Paul, W.; Steinwedel, H. Apparatus for Separating Charged Particles of Different Specific Charges. U.S. Patent 2,939,952, June 7, 1960.
- (87) Schwartz, J. C.; Senko, M. W.; Syka, J. E. P. *J. Am. Soc. Mass Spectrom.* **2002**, *13*, 659-669.
- (88) Stafford, G. C.; Kelley, P. E.; Syka, J. E. P.; Reynolds, W. E.; Todd, J. F. J. *Int. J. Mass Spectrom. Ion Processes* **1984**, *60*, 85-98.

- (89) March, R. E.; Todd, J. F. J., Eds. *Quadrupole Ion Trap Mass Spectrometry*, 2nd ed.; John Wiley & Sons, Inc.: Hoboken, New Jersey, 2005.
- (90) Douglas, D. J.; Frank, A. J.; Mao, D. *Mass Spectrom. Rev.* **2005**, *24*, 1-29.
- (91) Cox, K. A.; Cleven, C. D.; Cooks, R. G. *Int. J. Mass Spectrom. Ion Processes* **1995**, *144*, 47-65.
- (92) Cole, R., Ed. *Electrospray Ionization Mass Spectrometry*; John Wiley & Sons, Inc.: New York, New York, 1997.
- (93) Stafford, G.; Taylor, D.; Bradshaw, S.; Syka, J., *Proceedings of the 35th ASMS Conference on Mass Spectrometry and Allied Topics*: Denver, CO, 1987.
- (94) *FinniganTM vMALDI Getting Started*; Thermo Electron Corporation: San Jose, CA, 2004.
- (95) Kishore, M.; Ghosh, P. *Int. J. Mass Spectrom. Ion Processes* **1979**, *29*, 345-350.
- (96) March, R.; Todd, T., Eds. *Practical Aspects of Ion Trap Mass Spectrometry*; CRC Press: New York, NY, 1995; Vol. 1.
- (97) Bier, M.; Schwartz, J.; Zhou, J.; Taylor, D.; Syka, J.; James, M.; Fies, W.; Stafford, G., *Proceedings of the 43rd ASMS Conference on Mass Spectrometry and Allied Topics*: Atlanta, GA, 1995.
- (98) Browne, S. P.; Moore, C. M.; Scheurer, J.; Tebbett, I. R.; Logan, B. K. *J. Forensic Sci.* **1991**, *36*, 1662-1665.
- (99) Srinivasan, K.; Wang, P.; Eley, A. T.; White, C. A.; Bartlett, M. G. *J. Chromatogr. B* **2000**, *745*, 287-303.
- (100) Sershen, H.; Reith, M. E. A.; Lajtha, A. *Neuropharmacology* **1980**, *19*, 1145-1148.
- (101) Cognard, E.; Bouchonnet, S.; Staub, C. *J. Pharm. Biomed. Anal.* **2006**, *41*, 925-934.
- (102) Ferrer, I.; Furlong, E. T. *Environ. Sci. Technol.* **2001**, *35*, 2583-2588.
- (103) Reich, R. F.; Cudzilo, K.; Levisky, J. A.; Yost, R. A. *J. Am. Soc. Mass Spectrom.* **2010**, *21*, 564-571.
- (104) Marshall, A. G.; Wang, T. C. L.; Ricca, T. L. *J. Am. Chem. Soc.* **1985**, *107*, 7893-7897.
- (105) Guan, S.; Marshall, A. G. *Anal. Chem.* **1993**, *65*, 1288-1294.
- (106) Julian, R. K., Jr.; Cooks, R. G. *Anal. Chem.* **1993**, *65*, 1827-1833.

- (107) Soni, M. H.; Cooks, R. G. *Anal. Chem.* **1994**, *66*, 2488-2496.
- (108) March, R. E. *J. Mass Spectrom.* **1997**, *32*, 351-369.
- (109) Embree, P. M.; Kimbel, B. C. *Language Algorithms for Digital Signal Processing*; Prentice Hall: Englewood Cliffs, NJ, 1991.
- (110) Chen, L.; Wang, T. C. L.; Ricca, T. L.; Marshall, A. G. *Anal. Chem.* **1987**, *59*, 449-454.
- (111) Wang, T. C. L.; Ricca, T. L.; Marshall, A. G. *Anal. Chem.* **1985**, *107*, 7893-7897.
- (112) Guan, S.; Marshall, A. G. *Int. J. Mass Spectrom. Ion Processes* **1996**, *157/158*, 5-37.
- (113) Kelley, P. E. Mass Spectrometry Method Using Notch Filter. U.S. Patent 5,134,286, July 28, 1992.
- (114) Nappi, M.; Frankevich, V.; Soni, M. H.; Cooks, R. G. *Int. J. Mass Spectrom.* **1998**, *177*, 91-104.
- (115) Popoulis, A. *The Fourier Integral and Its Applications*; McGraw-Hill: New York, 1962.
- (116) Williams, J. D.; Cox, K. A.; Cooks, R. G. *Anal. Chem.* **1994**, *66*, 725-729.

BIOGRAPHICAL SKETCH

Richard Fred Reich, Jr., graduated from the University of Arizona in December, 1995, with a B.S. in chemistry and a B.A. in German, and was commissioned in the United States Air Force.

Richard has served 14 years active duty in the Air Force as a chemical research officer. At his first assignment, he served as an explosives chemist at the Energetic Materials Branch, Munitions Directorate, Air Force Research Laboratory at Eglin Air Force Base



in Fort Walton Beach, Florida, from June 1996 – July 1999. Richard was the principal investigator of melt-cast energetics and Deputy Program Manager for the in-house High Energy Explosives Development Program. He was responsible for formulating and characterizing the sensitivity and performance of eleven explosive formulations to qualify their use in advanced Air Force munitions.

Richard was competitively selected by the Air Force to attend the Air Force Institute of Technology (AFIT) at the University of Florida in August, 1999, to pursue a Master's degree in analytical chemistry. His graduate thesis involved the trace detection of explosives using atmospheric pressure chemical ionization tandem mass spectrometry (APCI-MS/MS). He graduated from the University of Florida in February, 2001, with an M.S. in analytical chemistry.

Richard was then assigned to the Combustion Branch, Propulsion Directorate, Air Force Research Laboratory at Wright-Patterson Air Force Base in Dayton, Ohio. From February 2001 to June 2004, he served as the Deputy Branch Chief of the Combustion Branch in which he assisted the Branch Chief in leading 25 scientists and engineers in the development of state-of-the-art combustor technology for legacy and future Air Force turbine engines. He also served as

the principal chemist responsible for characterization of particulate matter from research combustors and development of fuel additives designed to mitigate soot production.

From June, 2004, to July, 2007, Richard was assigned to the Department of Chemistry at the U.S. Air Force Academy in Colorado Springs, Colorado. As Assistant Professor of chemistry, he taught general chemistry, analytical chemistry, and chemistry of weapons. He was the course director for analytical chemistry and chemistry of weapons. He also served as the executive officer of the Department of Chemistry, assisting the Department Head, Colonel Van Valkenburg, in leading a department of 65 faculty and staff.

In 2007, Richard was competitively selected to attend AFIT at the University of Florida to pursue his PhD in analytical chemistry with a completion date of August 2010. Upon graduation, Richard will be assigned to the Air Force Technical Applications Center (AFTAC) at Patrick AFB, Florida, as the Deputy Chief of the Verification Sciences Division. There he will be responsible for establishing a new radiochemistry effluent laboratory. Richard is then scheduled to return to the U.S. Air Force Academy to teach chemistry in 2013. Richard plans to retire from the Air Force in 2016 after 20 years of service.